
U ` R “T V ”

F `

D

D R A

C XXII

# Multiwavelength studies of the blazars detected by AGILE

Filippo D’Ammando

A. A. 2009/2010

Docenti Guida: Prof. Marco Tavani

Dr. Andrea Lapi

Coordinatore: Prof. Pasquale Mazzotta

# Contents

Chapter 1

# Introduction

## 1.1 A new era of $\gamma$-ray astronomy

Gamma-ray astrophysics above 100 MeV is an exciting field of astronomical sciences that received a strong impulse in recent years. Detecting $\gamma$-ray emission in the energy range from a few tens of MeV to a few tens of GeV is possible only from space instrumentation, and in the past 20 years several space missions confronted the challenge of exploring $\gamma$-rays.

After the first observations with the SAS-2 and COS-B satellites, the *Compton Gamma-Ray Observatory* (*CGRO*) in the 1990s substantially increased our knowledge of the $\gamma$-ray Universe and provided a wealth of data on a large variety of sources as well as unsolved puzzles. In particular, the Energetic Gamma-Ray Experiment Telescope (EGRET) onboard *CGRO* operating in the energy range 30 MeV–30 GeV, which carried out a complete sky survey detecting hundreds of $\gamma$-ray sources (Fichtel et al. 1997; Hartman et al. 1999). This scientific inheritance is the starting point for any high-energy astrophysics mission.

The detection of $\gamma$-ray loud AGN dates back to the dawn of $\gamma$-ray astronomy, when the European satellite COS-B detected photons in the 50–500 MeV range from 3C 273 (Swanenburg et al. 1978). However, 3C 273 remained the only AGN detected by COS-B. The discovery of emission in the $\gamma$-ray domain from many Active Galactic Nuclei (AGNs) by EGRET and the Cherenkov Telescopes was one of the most breakthrough of high energy astrophysics in the last 20 years, leading to the identification of a new class of AGN: the blazars (Punch et al. 1992; Hartman et al. 1999). However, notwithstanding the big efforts devoted to the investigation of the mechanisms responsible for the high energy $\gamma$-ray emission in blazars the definitive answer is still missing. The new generation of high-energy space missions, AGILE and *Fermi* has to address some of the fundamental issues that were left open or unresolved by EGRET.

## 1.2 The blazar phenomenon

According to the current paradigm (see Urry & Padovani 1995) Active Galactic Nuclei are galaxies whose emission is dominated by a bright central core, including a super massive black hole as central engine, surrounded by an accretion disk and by fast-moving clouds under the influence of the strong gravitational field, emitting Doppler broadened lines. More distant clouds emit narrower lines. Absorbing material in a flattened configuration, idealized as a toroidal shape, obscures the central parts so that for transverse lines of sight only the narrow-line emitting clouds are seen. In radio-loud objects we have the additional presence of a relativistic jet, roughly perpendicular to the disk. Within this scheme, blazars represent the fraction of AGNs with their jet at smaller angles with respect to our line of sight.

Blazars are the most enigmatic subclass of AGNs, characterized by the emission of strong non-thermal radiation across the entire electromagnetic spectrum, and in particular intense and variable $\gamma$-ray emission above 100 MeV (Hartman et al. 1999). The typical observational properties of blazars include irregular, rapid and often very large variability, apparent super-luminal motion, flat radio spectrum, high and variable polarization at radio and optical frequencies. These features are interpreted as the result of the emission of electromagnetic radiation from a relativistic jet that is viewed closely aligned to the line of sight (Blandford & Rees 1978).

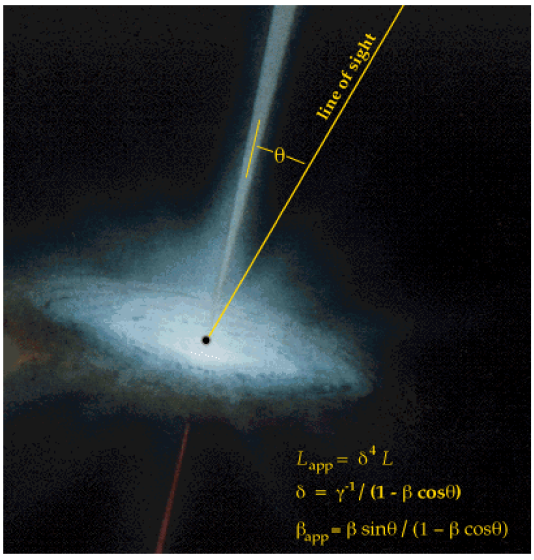


**Figure 1.1:** Schematic diagram for superluminal motion and beaming effect in blazars.

As first argued by Rees (1966), the plasma within the jets of radio-loud

AGNs moves at relativistic speed and so it transports efficiently the energy from the vicinity of the super massive black hole to the distant lobes. This has strong implications for an observer who views the jet at relatively small angles as it is believed for the blazars (see Figure 1.1). Let us assume that a source emits isotropically in its rest-frame $K'$. Then, in the observer's frame $K$, where the source moves at highly relativistic speed, three effects occur (from Rybicki & Lightman 1979):

1. *Light aberration*: the angular distribution of the radiation is highly peaked in the forward direction. In particular, since for a particle in a magnetic field the velocity and acceleration are perpendicular (in $K'$), the emitted photons are observed in $K$ to make an angle given by $\sin\theta = 1/\Gamma$, where $\Gamma = 1/\sqrt{(1-\beta^2)}$ is the Lorentz factor of the accelerated particles. This means that in $K$ half of the photons are concentrated in a cone of semi-aperture angle of $\sim 1/\Gamma$ and are not radiated over the available solid angle $2\pi$.

2. *Photons arrival times*: the emission and arrival time intervals ($\Delta t_e$ and $\Delta t_a$, respectively) of photons are different. As measured in the observe's frame $K$ we have $\Delta t_a = \Delta t_e$ (1 - $\beta \cos\theta$). If $\Delta t'_e$ is measured in $K'$, $\Delta t_e = \Gamma \Delta t'_e$ leading to $\Delta t_a = \Gamma(1 - \beta \cos\theta)\, \Delta t'_e = \Delta t'_e/\delta$, where $\delta$ is the Doppler factor.

3. *Frequencies blueshift*: since frequencies are the inverse of times, we just have $\nu = \delta\nu'$.

Owing to the first effect we observed the intensity of the jet to be dramatically enhanced if its velocity vector is closely aligned to our line of sight. This is referred to as 'beaming' or 'Doppler boosting'. An important role is played by the Doppler factor, defined as:

$$\delta = \frac{1}{\Gamma\,(1 - \beta\,\cos\theta)} \tag{1.1}$$

In particular, since $I_\nu/\nu^3$ is a relativistic invariant, we get for its observed specific intensity

$$I_\nu\,(\nu) = \delta^3 I'_{\nu'}\,(\nu') \tag{1.2}$$

and the integration over the frequencies yields

$$I = \delta^4 I' \tag{1.3}$$

Similarly, we have for the received flux, assuming the synchrotron emission spectrum which can be approximated by a power law of the form $F'_{\nu'} \propto (\nu')^{-\alpha}$

$$F_\nu = \delta^{p+\alpha} F'_{\nu'} \tag{1.4}$$

where $\alpha$ is the energy index, and $p = 3$ or 2 in the case of a moving, isotropic source or a continuous jet, respectively. Depending on the morphology of the source, i.e. whether the radiation is emitted isotropically or dependent on the angle $\theta$, the power of the Doppler factor may slightly vary. The effect of beaming is amplified for viewing angle $\theta \sim 1/\Gamma$, in which case

$$\delta \simeq 2\Gamma \tag{1.5}$$

Considering that for the observed blazars $\Gamma \sim 10$, Eqs. 1.4 and 1.5 characterize the 'blazar phenomenon', i.e. amplification by a great factor (usually in the range 1000-10000) of the observed electromagnetic emission by a relativistic jet. Therefore, the amplification due to Doppler boosting became dramatic in blazars and it is important to understand the extreme luminosity of this class of objects. The second effect predicts the observation of apparent superluminal motion for objects with their jets oriented at very small angles, like the blazars.

The blazar class includes both BL Lac objects, which have no or very weak emission lines, and the more luminous Flat Spectrum Radio Quasars (FSRQs), which have strong broad emission lines. Another difference among these two classes is that BL Lacs do not exhibit apparent cosmological evolution and are observed at redshift $z < 1$, while FSRQs are observed up to $z \simeq 5$. Because of their special properties and amplified emission, blazars offer the unique possibility to probe the central region of AGNs, and shedding light on the mechanism responsible for the extraction of non-thermal energy from the central black hole and for the acceleration and collimation of relativistic electrons into jets.

Moreover, blazars emit across several decades of energy, from radio to TeV energy bands, and thus they are the perfect candidates for simultaneous observations at different wavelengths. Multiwavelength studies of variable $\gamma$-ray blazars have been carried out since the beginning of the 1990s, thanks to the EGRET instrument onboard *CGRO*, providing the first evidence that, as shown in Figure 1.2, the Spectral Energy Distributions (SEDs) of the blazars are typically double humped with the first peak occurring in the IR/optical band in the so-called *red blazars* (including Flat Spectrum Radio Quasars, and Low-energy peaked BL Lacs, LBLs) and in UV/X-rays in the so-called *blue blazars* (including High-energy peaked BL Lacs, HBLs).

The first peak is interpreted as synchrotron radiation from high-energy electrons in a relativistic jet. On the other hand, the SED second component, peaking at MeV–GeV energies in *red blazars* and at TeV energies in *blue blazars*, is commonly interpreted as inverse Compton scattering of seed photons, internal or external to the jet, by highly relativistic electrons (Ulrich et al. 1997), although

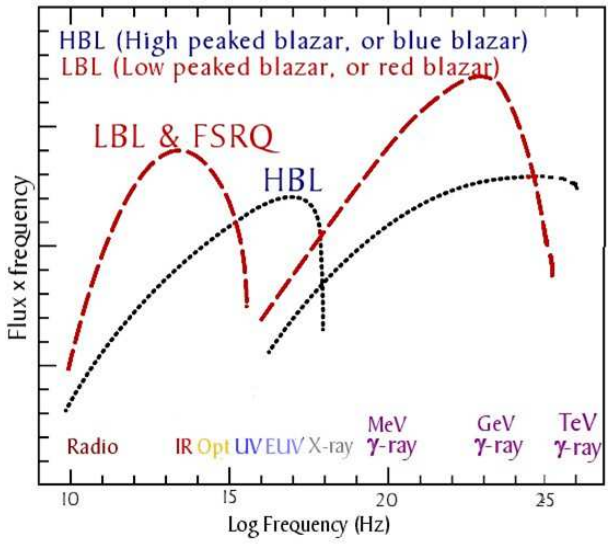


**Figure 1.2:** Spectral energy distribution of different kinds of blazars. The synchrotron power of strong emission lines blazars (FSRQs) and low-frequency peaked blazars (LBLs) peaks at submillimiter to infrared wavelengths, while that of high-frequency peaked blazars (HBLs) peak at UV to X-ray wavelengths. The Compton powers peak at GeV energies for FSRQs and LBLs and at TeV energies for HBLs [Wehrle et al. 1998].

other models involving hadronic processes have been proposed (see e.g. Böttcher 2007 for a recent review).

With the detection of several blazars in the $\gamma$-rays by EGRET (Hartman et al. 1999) the study of this class of objects has made significant progress. In fact, considering that the large fraction of the total power of blazars is emitted in the $\gamma$-rays, information in this band is crucial to study the different radiation models. 3C 279 is the best example of multi-epoch studies at different frequencies performed by EGRET during the period 1991–2000 (Hartman et al. 2001). Nevertheless, only a few objects in the EGRET *era* were detected on a time scale of two weeks or more in the $\gamma$-ray band and simultaneously monitored at different energies in order to obtain a wide multifrequency coverage.

The interest in blazars is now even more renewed thanks to the simultaneous presence of two $\gamma$-ray satellites, AGILE and *Fermi*, and the possibility to obtain $\gamma$-ray observations over long timescales simultaneously with multiwavelength data collected from radio to TeV energies allow us to reach a deeper insight on the jet structure and the emission mechanisms at work in blazars.

## 1.3 Blazars: the $\gamma$-ray view of AGILE

The $\gamma$-ray observations of blazars are a key scientific project of the AGILE (*Astrorivelatore Gamma ad Immagini LEggero*) satellite (Tavani et al. 2009a). Thanks to the wide field of view of its $\gamma$-ray imager ($\sim$ 2.5 sr), AGILE monitored tens of potentially $\gamma$-ray emitting AGNs during each pointing. In the first 2.5 years of operation, AGILE detected several blazars during high $\gamma$-ray activity and extensive multiwavelength campaign were organized for many of them, providing the possibility to monitoring on long timescales the brightest objects.

The $\gamma$-ray activity timescales of these blazars goes from a few days (e.g. S5 0716+714 and 3C 273) to several weeks (e.g. 3C 454.3 and PKS 1510−089) and the flux variability observed has been negligible (e.g. 3C 279), very rapid (e.g. PKS 1510−089) or extremely high (e.g. 3C 454.3 and PKS 1510−089). Even if at least one object for each blazar category (LBL, IBL, HBL and FSRQ) was detected, we note that only a few objects were detected more than once in flaring state by AGILE and only already known $\gamma$-ray emitting sources showed flaring activity. This evidence, together with the early results of *Fermi*-LAT (Abdo et al. 2009d), strongly constrains on the properties of the most intense $\gamma$-ray emitters. Moreover, the multifrequency campaigns organized by AGILE on the bright blazars confirm that simultaneous observation over the entire electromagnetic spectrum is fundamental to understand the structure of the inner jet, the origin of the seed photons for the IC process and the emission mechanisms at work in blazars.

## 1.4 Main results of this Thesis

This Thesis reports on the measurements of $\gamma$-rays from the brightest blazars detected by the AGILE satellite, together with the simultaneous multifrequency observations carried on these objects over the whole electromagnetic spectrum, in order to study in detail the variability correlations among the emission at different frequencies and time-resolved SEDs. These observations allowed to test the emission mechanisms of the blazars and investigate possible different behaviours and the presence of emission components in the broad band spectrum beyond the standard emission models. The main results of this Thesis could be summarized as follows.

- The $\gamma$-ray emission observed by AGILE over its 2.5 years of operation from some blazars is highly variable (e.g. PKS 1510−089, Chapter 5) until the extraordinary flare of 3C 454.3 observed in December 2009 (Chapter 7). However, the number of flaring blazars detected seems to suggest that only a few blazars are intense $\gamma$-ray emitters, and 10–15 years after the

EGRET observations about the same objects continues to be the brightest in $\gamma$-rays.

- The dominant emission mechanism in the $\gamma$-ray band for FSRQs is the inverse Compton scattering of external photons from the broad line region, but in some particular states also the contribution of seed photons from a hot corona (3C 454.3 in December 2007, Chapter 7) or the accretion disk (3C 279, Chapter 8) are shown to be important.

- The intense $\gamma$-ray flares of S5 0716+714 observed by AGILE in September and October 2007 are among the highest flux detected by a BL Lac object and considering the redshift of the source (z = 0.31) the total power transported in the jet during these episodes approaches or slightly exceeds the maximum power generated by a spinning black hole of $10^9$ $M_\odot$, challenging the Blandford-Znajek mechanism (Chapter 6).

- The possibility to obtain information over the entire electromagnetic spectrum during the multifrequency campaign organized by AGILE gave us also the opportunity to investigate in blazars the presence of Seyfert-like features, such as the little and big blue bumps (PKS 1510−089, Chapter 5) and the Compton reflection component (3C 273, Chapter 8).

- Moreover, we revealed in the FSRQ PKS 1510−089 some features typical of HBL objects, such a X-ray harder-when-brighter behaviour during March 2008 and a shift of the synchrotron peak towards higher frequencies during the huge flare of March 2009 (Chapter 5).

- Emission in optical and $\gamma$-ray bands seems to be correlated during high activity states of blazars, but not strongly, with a possible lag of the $\gamma$-ray flux with respect to optical one less than one day, both for FSRQs (e.g. 3C 454.3, Chapter 7) and BL Lacs (S5 0716+714, Chapter 6). On the other hand, during March 2009 a possible delay of the optical emission with respect to the $\gamma$-ray one is detected for PKS 1510−089 (Chapter 5), suggesting a more complex behaviour in the optical-$\gamma$ correlation, especially for FSRQs, where also a contribution of the thermal disk emission is clearly visible.

- The study of the variability of the optical/UV and X-ray light curves of S5 0716+714 collected by *Swift* during October–November 2007 and the SEDs for the flare of September and October 2007 built with AGILE, GASP-WEBT and *Swift* data seems to suggest the presence of two synchrotron self Compton components in the broad band spectrum of S5 0716+714, with different variability (Chapter 6).

The Thesis is organized as follows. An introduction to the Active Galactic Nuclei is the subject of Chapter 2, with a particular emphasis in the second part on the subclass of objects which this thesis deals with: the blazars. Chapter 3 describes the acceleration mechanisms in high-energy astrophysics and the most important emission mechanisms for the blazars. An introduction to $\gamma$-ray astrophysics is given in Chapter 4, showing in particular a description of the AGILE satellite and its detectors, the procedure for standard analysis of the $\gamma$-ray data collected by the Gamma-Ray Imaging Detector (GRID) onboard AGILE, up to a brief introduction to the multiwavelength astronomy and the AGILE multifrequency approach.

In the second part of the Thesis, I discuss the results of the analysis of $\gamma$-ray AGILE data, together with the multifrequency data collected over the electromagnetic spectrum, for specific objects: PKS 1510−089 (Chapter 5), S5 0716+714 (Chapter 6), 3C 454.3 (Chapter 7), the two brightest blazars of the Virgo region, 3C 279 and 3C 273 (Chapter 8), and the TeV blazars Mrk 421, W Comae and PG 1553+113 (Chapter 9). Finally, in Chapter 10 I will focus on the most interesting results obtained in this work.

During the period of my Ph.D. studies I have been a member of the AGILE Science Team and in particular of the AGN Working Group of AGILE; moreover, I have been an Archive Scientist at the ASI Science Data Center (ASDC) for the AGILE-GRID data. In the first part of my Ph.D. I worked on the analysis of the on-ground calibration data of the silicon tracker as well as the on-flight calibration of the GRID and the testing and verification of the AGILE Analysis pipeline. This allowed me to obtain a detailed knowledge of the $\gamma$-ray imager onboard AGILE and of the methods of reduction and analysis of the data acquired from it.

My personal direct contribution on the results of this Thesis goes from the organization and management of the multifrequency campaigns on the blazars discussed here, including the writing of several proposals on blazar observations with ground-based and space-born observatories, up to the analysis of the AGILE, *Swift*, *Suzaku*, REM, *Spitzer* data and the theoretical interpretations of the results. The original scientific results have been published in international journals, such as Astronomy & Astrophysics and Astrophysical Journal, and have been presented in several national and international conferences.

Chapter 2

# Active Galactic Nuclei

The term 'Active Galactic Nuclei' (AGNs) refers to compact regions at the center of a few percent of galaxies with a non-stellar emission much higher than the thermal emission of the entire rest of the galaxy. Indeed, this definition includes a wide variety of phenomenology. The resulting classification is very complex and mainly based on luminosity, electromagnetic spectrum and spatial morphology.

The first class of AGNs, the Seyfert Galaxies, was discovered by Karl Seyfert in the 1940s. They appeared to be spiral galaxies, but with a star-like nucleus showing broad and strong emission lines. Quasars, a subclass of AGNs with very high luminosity, were discovered in the early 1960s in radio surveys. The optical counterpart of some of the observed bright radio sources were star-like, and turned out to be the most distant sources among the known celestial objects at that time. The first quasar, 3C 273, was detected by Maarten Schmidt in 1962 and is more than 1000 times more luminous that a normal galaxy like our own. The discovery of emission in the $\gamma$-ray domain from AGNs was one of the most important breakthrough of high energy astrophysics in the last 20 years, leading to the identification of a new class of AGNs: the blazars (Punch et al. 1992; Hartman et al. 1999).

AGNs have been observed and studied extensively over the whole electromagnetic spectrum in the past 40 years and, even if the increasing knowledge about their individual and collective properties of these objects, the complete understanding of the emission mechanisms at work in AGNs is still far enough away. The first sections of this Chapter present a brief introduction on the general characteristics of AGNs, their classification and the Unification picture. Then, starting from Section 2.6 we will focus on blazars, which are the objects analyzed in this Thesis.

## 2.1 The central Black Hole and accretion

One of the main characteristics of AGNs is their extreme luminosity, typically in the range $10^{42}$–$10^{48}$ erg s$^{-1}$, in a volume much smaller than 1 pc$^3$. Whatever the emission mechanism involved, this values should not exceed the Eddington luminosity of the objects in order to keep the process effective. This consideration implies the presence of a mass of $10^6$ – $10^9$ M$_\odot$. In fact, assuming for simplicity the case of fully ionized hydrogen gas, the radiation pressure exerted on the electrons by the incident photons is

$$|F_{\rm rad}| = \sigma_T \frac{L}{4\pi r^2 c} \tag{2.1}$$

where $\sigma_T = \frac{8\pi}{3}\left(\frac{e^2}{m_e c^2}\right)^2 = 6.65 \times 10^{-25}\text{cm}^{-2}$ is the Thomson cross section. The gravitational force (considering that the particles in the gas, although completely ionized, are linked by electromagnetic forces) instead is

$$|F_{\rm g}| = \frac{GM(m_p + m_e)}{r^2} \simeq \frac{GMm_p}{r^2} \tag{2.2}$$

where since $(m_p/m_e) \simeq 1.8 \times 10^3$, we neglect $m_e$.
So that it is possible to have accretion only if

$$|F_{\rm rad}| \leq |F_{\rm g}| \tag{2.3}$$

which leads to:

$$L \leq \frac{4\pi G c m_p M}{\sigma_T} \approx 1.26 \times 10^{38} (M/M_\odot)\,\text{erg s}^{-1} \tag{2.4}$$

known as the Eddington limit. The last equation can be used to establish the mass limit, the Eddington mass $M_E$, that in appropriate units could be expressed as

$$M_{\rm E} = 8 \times 10^5 L_{44} M_\odot \tag{2.5}$$

In nearby, normal galaxies, super massive black holes (SMBHs) are revealed, and their masses are estimated, by means of technique involving stellar and gas kinematics, through the correlation between the black hole mass and the central velocity dispersion $\sigma$ of the host galaxy, the so-called '$M_{BH}$–$\sigma$ relation' (Ferrarese and Merritt 2000; Gebhardt et al. 2000). This method led to the discovery of a $\sim 10^6$ M$_\odot$ BH in our own Galaxy (Ghez et al. 1998). However, black hole mass estimates based on gas kinematics have quite large errors due to the uncertainties in the spatial distribution of the gas and the large but uncertain correction for pressure support. The range of slopes for the '$M_{BH}$–$\sigma$ relation' found

in literature appears to arise mostly from systematic differences in the velocity dispersion used by the different research groups (see Tremaine et al. 2002 and references therein).

The measure of the mass of the SMBHs has proved to be more difficult in AGNs, since the stellar dynamical searches are prevented by the strong nuclear radiation that outshine stellar light. In AGNs therefore the technique of reverberation mapping (Blandford and Mc Kee 1982; Peterson 1993; Netzer & Peterson 1997) has been used to measure the light-travel time delay over which broad emission lines flux responds to continuum luminosity variations and to deduce the characteristic size of the Broad Line Region (BLR) around the central photoionizing source. By assuming that the emission lines are broadened primarily by the virial gas motion in the gravitational potential of the central object, the BLR size and the line width then give an estimate of the mass of the central object (Peterson & Wandel 1999).

Kaspi et al. (2000) combining the measurements of 17 Seyfert galaxies from Wandel et al. (1999) and 17 high-luminosity AGNs from the Palomar-Green sample of quasars found that the BLR size scales with AGN optical luminosity as $R_{\rm BLR} \propto L^{0.70\pm0.03}$. Assuming that this scaling relation is universal at all luminosities and redshift several studies have used this relation to estimate the central masses in large AGN samples (e.g. Woo & Urry 2002; Grupe & Mathur 2004). Using the best available determinations of $R_{\rm BLR}$ for a large number of AGNs collected by Peterson et al. (2004), Kaspi et al. (2005), recalibrated the power law relation $R_{\rm BLR} \propto L^{\alpha}$, found that the best fitting value of $\alpha$ is 0.67 ± 0.05 for optical continuum and H$\beta$ luminosity, 0.56 ± 0.05 for the UV continuum luminosity and 0.70 ± 0.14 for the X-ray luminosity. The result reflects on the naive theoretical predicted slope for the relation between the BLR size and the luminosity of $\alpha = 0.5$, based on the assumption that all the AGNs have the same ionization parameter, BLR density, column density and BLR spectral energy distribution. The fact that for most energy bands the slope is quite different from $\alpha = 0.5$ indicates that for some of these characteristics the simple assumption is not valid and there is a possible evolution along the luminosity scale. The information on the BH mass and the observed variability timescale, together with the fact that the core of the emission is always unresolved in all electromagnetic bands, except for some structures in the radio waves, put tight limits on the dimensions where the large amounts of mass has to be confined. The extreme compactness (M/R) of the nuclei of active galaxies leads almost unambiguosly to postulate the presence of SMBHs.

Once accepted the presence of a SMBHs, a viable process must be provided to ensure the conversion of mass to energy. This mechanism should be very efficient in order to produce the observed luminosity. If the energy is converted so that $E = \eta mc^2$, the efficiency $\eta$ needs to be very high. This is not the case

for ordinary nuclear processes fueling stars, because in that case we can only have $\eta = 0.007$. The only possible alternative is the accretion, which involves the transformation of gravitational energy into radiation.

Let us consider an object with mass $m$ which is falling into a much more massive body with mass $M$. When the object hits the surface of the other one, at a radius $R$, its potential energy can be eventually available as thermal radiation. The efficiency of this process is proportional to the compactness of the hitten object. Indeed, the value of the parameter $\eta$ is very high for neutron stars, being around 0.1, much higher than that of nuclear fusion. It would then seem natural to assume that the accretion efficiency reaches its higher values in presence of a BH. However, this is not necessarily true, because BHs do not have a surface and the accretion mechanism must be induced by the presence of an accretion disk of gas rotating around the central BH. Moreover, it is not possible for matter to rotate around the BH beyond the so called 'radius of marginal stability' ($r_{ms}$) or 'last stable orbit'. It makes the efficiency for this process not higher than what found for a neutron star. However, if the BH has a not null angular momentum, the last stable orbits shifts to a smaller radii, allowing an efficiency up to $\eta \simeq 0.42$ for a maximally rotating Kerr BH.

## 2.2 The accretion disk

The fundamental idea behind accretion through a disk is that we can extract the gravitational energy corresponding to the lastle stable orbit around the BH by letting the gas spiraling slowly inwards. The main problem is to find a way to let the gas loose angular momentum and to convert the variation of gravitational energy into radiation. In a classical approach to accretion disk physics, both issues are resolved by assuming the viscosity arising from differential rotation of the disk annuli. The real nature of this mechanism is still under debate (see e.g. Papaloizou & Lin 1995, for a review), but useful results can be obtained adopting a dimensionless parameter $\alpha$, as first proposed by Shakura & Sunyaev (1973), to characterize a turbulent viscosity of some kind.

### 2.2.1 The standard model

In the following we will briefly describe the standard model for the accretion disk emission, as presented by Shakura & Sunyaev (1973). As well as to this paper, we will refer to the reviews made by Pringle (1981) and Beloborodov (1999).

We assume a steady disk with a constant accretion rate $\dot{m}$ and a Keplerian angular velocity around the BH, $\Omega_k = (GM/r^3)^{1/2}$. If $\dot{m}$ is neither too high or too

low compared to the critical accretion rate $\dot{m}_{cr}$ corresponding to the Eddington luminosity, the geometrical height-scale of the disk is simply regulated by the hydrostatic equilibrium between the vertical component of gravity and the internal pressure of the gas:

$$\frac{h}{r} = \frac{c_s}{v_k} \tag{2.6}$$

where $c_s^2 \equiv p/\rho$ and $v_k = \Omega_k r$. Under these conditions, the disk is geometrically thin, because $v_k \gg c_s$.
During the spiraling inward with a radial velocity $v_r$, mass and angular momentum must be conserved. The first equation, the mass conservation law, is

$$\dot{m} = 2\pi r v_r \Sigma \tag{2.7}$$

where $\Sigma$ is the disk surface density. Consequently, the second conservation law can be written as

$$\dot{J} = \dot{m} v_k r = 2\pi r^3 v_r \Sigma \omega \tag{2.8}$$

In a steady disk, the angular momentum variation is completely associated to the neat momentum of the viscosity forces in the annulus at radius $r$, so that

$$2hr f = \frac{d}{dr}\left(r^3 \Sigma v_r \omega\right) \tag{2.9}$$

where $f$ is the viscous force per unit area, completely described by the above-mentioned parameter $\alpha$. From the previous equations, it is possible to express the radial velocity in a straightforward way: $v_r \propto \frac{c_s^2}{v_k}$. This result agrees with the initial assumption of a steady disk with Keplerian rotation, since the inward accretion velocity (which must be different to zero in order to have the accretion mechanism working) is negligible with respect to the Keplerian velocity. The energy dissipated by the viscous forces, per unit time and volume, can be easily derived from energy conservation

$$\frac{dE}{dtdV} = -f\frac{d\omega}{dr}r \tag{2.10}$$

The integration of (2.10) over the whole volume of the disk can be performed taking advantage of (2.9), leading to the total dissipated luminosity

$$\frac{dE}{dt} = -\int_{r_{in}}^{\infty} f\frac{d\omega}{dr}r \cdot 4\pi h r\, dr = \frac{1}{2}\frac{GM\dot{m}}{r_{in}} \tag{2.11}$$

Thus, only one half of the available gravitational energy is effectively converted by the accretion process. The other half is possible radiated by other means or completely lost when the matter falls beyond the event horizon of the BH.

Following the prescriptions of the standard model, all the dissipated energy generated by the viscous forces is radiated away at the same radius, keeping a local equilibrium between the heating rate and the radiative losses through the surface. In this case, the disk can be considered optically thick, so that each annulus radiates a black body with a temperature which is function of the radius. This assumption makes it possible to compare the dissipated energy, per unit and surface, obtained integrating (2.10) over the disk height

$$\frac{dE}{dtdA} = -\int_{-h}^{+h} f\frac{d\omega}{dr} r\, dz = \frac{3GM\dot{m}}{4\pi r^3}\left[1-\left(\frac{r_{in}}{r}\right)^{\frac{1}{2}}\right] \tag{2.12}$$

to the same quantity emitted by a black body, that is $2\sigma T^4$, where the factor 2 is needed to take into account the two sides of the disk. This leads to the desired expression for the temperature of the emission disk at different radii:

$$T(r) = \left\{\frac{3GM\dot{m}}{8\pi\sigma r^3}\left[1-\left(\frac{r_{in}}{r}\right)^{\frac{1}{2}}\right]\right\}^{\frac{1}{4}} \tag{2.13}$$

At large radii, when $r \gg r_{in}$, this expression can be approssimated to $T(r) = T_*\,(r/r_{in})^{-3/4}$, where we have defined a characteristic temperature:

$$T_* \equiv \left(\frac{3GM\dot{m}}{8\pi\sigma r_{in}^3}\right)^{\frac{1}{4}} \tag{2.14}$$

A typical value for an AGN would be $T_* \simeq 10^5$ K, while it is higher ($\simeq 10^7$ K) for low mass X-ray binaries, containing Galactic black holes. These temperatures correspond to UV and X-ray bands, respectively, which successfully account for the observed emission of the two classes of objects. At smaller radii, the temperature keeps increasing up to a maximum value, $T_{max} = 0.488\, T_*$, which is reached at $r = (49/36)\, r_{in}$. From this radius inward, the temperature decreases to an unphysical zero value at the last stable orbit, suggesting that the model requires a detailed analysis of the boundary conditions to be consistent.

We can calculate the overall emitted spectrum. Each elemental area of the disk will radiate according to the temperature specific of its radius

$$B_\nu\,[T(r)] \propto \frac{\nu^3}{e^{\frac{k\nu}{kT(r)}} - 1} \tag{2.15}$$

Integrating this expression over the entire disk surface, we get the spectrum emitted by a geometrically thin, optically thick accretion disk

$$S_\nu \propto \int_{r_{in}}^{r_{out}} B_\nu\,[T(r)]\; 2\pi r\, dr \tag{2.16}$$

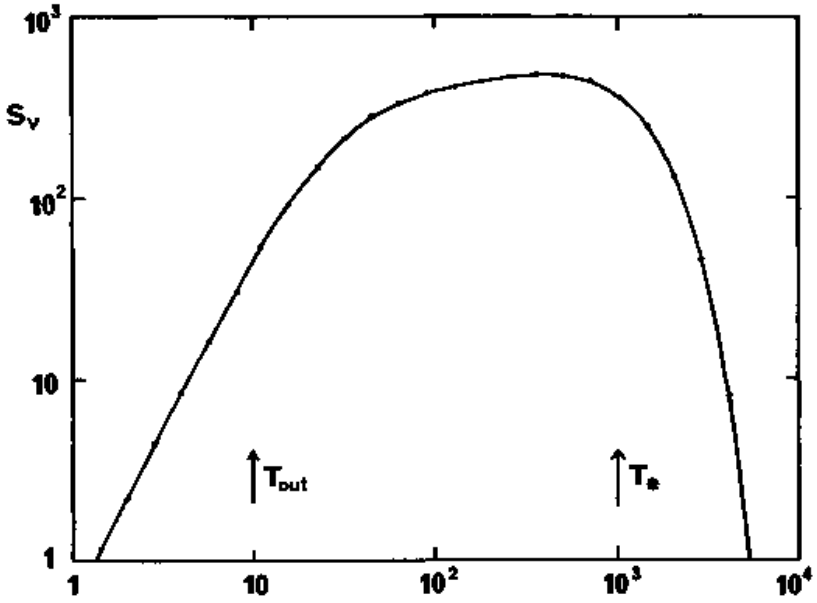


**Figure 2.1:** The integrated spectrum of an optically thick, geometrically thin accretion disk. The units are arbitrary, but the frequency corresponding to $T_{out}$ and $T_*/h$ are labelled [Pringle 1981].

where $r_{out}$ is the outer radius of the disk. The resulting spectrum is displayed in Fig. 2.1. A qualitative explanation of the shape can be achieved with easy considerations.

When $\nu \gg kT_*/h$, the spectrum falls exponentially, because the observed radiation is the high energy tail of the Planck distribution emitted by the inner region of the disk. On the other hand, when $\nu \ll kT_*/h$, the radiation comes from disk annuli with $r \gg r_{in}$, where (2.13) can be approximed as $T(r) = T_* \, (r/r_{in})^{-3/4}$. This allows us to rewrite (2.16) as

$$S_\nu \propto \nu^{\frac{1}{3}} \int_0^{x_{out}} \frac{x^{\frac{5}{3}} \, dx}{e^x - 1} \tag{2.17}$$

where we have defined $x \equiv h\nu/kT$ and consequently $x_{out} \equiv h\nu/kT_{out}$. Therefore, for frequencies between $kT_{out}/h$ and $kT_*/h$, $x_{out} \gg 1$ and the equation (2.17) leads to $S_\nu \propto \nu^{\frac{1}{3}}$, the characteristic spectrum for an accretion disk, as first calculated by Lynden-Bell (1969). Finally, for frequency lower than $kT_{out}/h$, the spectrum is dominated by the Rayleigh-Jeans tail of the outer regions of the disk, giving $S_\nu \propto \nu^2$.

### 2.2.2 Radiatively-inefficient disks

The key parameter for the so-called Shakura-Sunyaev accretion disk standard model is the accretion rate $\dot{m}$. If $\dot{m}$ is much larger or much smaller than $\dot{m}_{cr}$, then the disk cannot be considered optically thick and geometrically thin anymore. The efficiency typically becomes small, giving rise to radiatively inefficient disks. Among this class, great attention has been focused on the Advection Dominated Accretion Flows (ADAF; Narayan & Yi 1994) models. In ADAF models the accretion rate is so low that the surface density of the disk is not enough to keep ions and electrons thermally coupled via Coulomb interactions. As a consequence, the energy associated to ions, which are poor radiators, cannot be emitted locally and is advected together with the accretion flow beyond the BH event horizon. Therefore, a large fraction of the available energy turns into internal energy and the gas becomes hot and optically thin, with a very low radiative efficiency.

Such models were first proposed to explain the hard state spectrum of Cyg X-1 (Ichimaru 1977), but were later applied to AGN (Rees et al. 1982) and they have been used to model the Galactic Center (Narayan et al. 1995; Narayan et al. 1998; Quataert et al. 1999). It was later realized that the situation described by the low luminosity ADAF models was dinamically unlikely, because the viscous transport of energy within this flow could readily unbind material further out, possibly leading to a powerful wind (Blandford and Begelman 1999) or strong convection (Quataert and Gruzinov 2000). These suggestions are controversial (Balbus and Hawley 2002) and under debate (see e.g. Abramowicz et al. 2002), but in any case such a flow is likely to be extremely hot ($T_e \sim 10^9$ K) and optical thin.

For very high accretion rates, comparable to that needed to produce the Eddington luminosity, the accretion inflow time scale can become less than the time it takes for radiation to diffuse out of the disk accretion flow (Begelman 1979). The inability of these disks to radiate the gravitational potential energy, together with the viscous transport of energy and strong radiation pressure present, should lead to strong outflows. The appearence of such disks is highly uncertain, it is unclear wheter a X-ray emitting corona forms, and wheter the atmosphere of such a disk is in a state capable of producing X-ray reflection spectral signatures.

## 2.3 The AGN paradigm

Hoyle and Fowler (1963) for the first time suggested that the energy source of the AGN is gravitational and could arise from infall of matter onto an highly

collapsed object or a black hole.
The current paradigm of AGN (see Fig. 2.2) includes a spinning SMBH with mass $10^6$–$10^9$ $M_\odot$ as its central power source, whose strong gravitational potential pulls the surrounding materials inwards, forming a disc of hot plasma. The central region is surrounded by a dusty torus, located at $\sim$ 1–10 pc.
In addition, clouds of gas move in the potential well of the SMBH, showing emission lines. The broad lines observed in the optical/UV spectra of AGNs have typical widths of $\simeq$ 5000 km $s^{-1}$, but can be as large as 10000 km $s^{-1}$ or more. Such widths are due to the keplerian velocities of a large number of clouds, the Broad Line Region, rotating around the BH at a distance of 0.01–0.1 pc. The density of this gas is believed to be very high, of the order of $10^9$–$10^{11}$ $cm^{-3}$, as required by the observed ratio between forbidden and permitted emission transitions. Still under debate is the origin of these clouds. Several models have been proposed, such as the release from accretion disk instabilities (Collin & Huré 2001) or from stellar wind envelopes (Torricelli-Ciamponi & Pietrini 2002). An open problem is represented by the mechanism providing the confinement of the BLR clouds.
The narrow lines have much smaller widths, typically lower than 1000-2000 km $s^{-1}$. This is easily explained if they are produced by a material, the Narrow Line Region (NLR), farther away from the BH, extending on the 100 pc scale. That gas has a density ($10^3$–$10^6$ $cm^{-3}$) lower than that required for the BLR, and is likely composed by the inner part of the Galactic disk, photoionized by the nuclear continuum.

Finally, radio-loud AGNs are characterized by the presence of a collimated relativistic jet. The radiation produced in the jet is non-thermal, and likely produced by the interaction of an accelerated leptonic plasma with a magnetic field radiating via synchrotron and inverse Compton mechanisms (see Chapter 3 for a detailed discussion of the emission mechanisms at work in blazars). When powerful relativistic jets are formed by spinning black hole they are supposed to be collimated by surrounding disk outflow. The powerful jets terminate in 'hot spots' which are believed to be strong shock where particle acceleration and magnetic field amplification take place.

In the following part of this Section, we will briefly describe the main features of the emission of the AGNs in the different energy bands. The same considerations are valid for radio-quiet and radio-loud AGNs, even if in the latter case any differences are clearly defined in some electromagnetic bands, such as the radio emission, larger in the radio-loud objects for definition, and the $\gamma$-ray emission, typically observed only in blazars. However, even if their electromagnetic spectra are usually dominated by the jet emission, also in the blazars some features typical of radio-quiet AGNs could be important and, during low activity level of the jet, clearly visible in their spectrum.

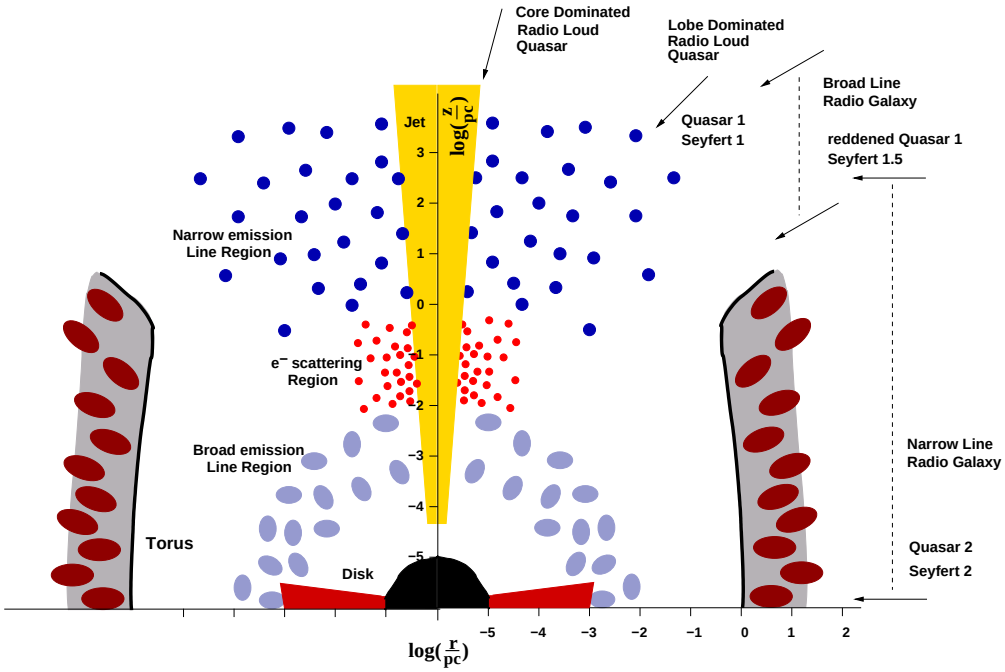


**Figure 2.2:** Artist's view of the AGN paradigm. The different region around the BH are described [adapted from Biermann et al. 2002].

We have already noted that the emission from an optically thick, geometrically thin accretion disk depends strongly on the mass of the central BH and should peak in the optical/UV band for the typical mass of a SMBH (see Section 2.2.1). The main feature observed in this band, the so-called 'Big Blue Bump', is generally associated to thermal emission from the disk (e.g. Laor 1990). However this association, though appealing, is not easily constrained, because the exact shape of the optical/UV continuum is often contamined by the host galaxies, absorption by intervening materials and reddening by dust. Moreover, the superposition of the broad emission lines makes this analysis very complex. In particular, a set of blended Balmer, Mg II, and Fe II emission lines together with the Balmer continuum make up the so-called 'Little Blue Bump', which alters the shape of the underlying continuum in the range between $\simeq$ 2000 Å and 4000 Å. A divergence between the data and the multi-black body disk emission lies in the assumption that radiation of different energy comes from region of the disk far away from each other (see (2.13)). A simple prediction is that any variabil-

ity observed in a given electromagnetic band should propagate through the disk with the sound speed, as expected in viscous disk, and so the relative variation in another band follow or preceed with a time delay. Instead, observations seem to suggest that optical and UV variability are simultaneous (see e.g. Ulrich et al. 1997), requiring propagation speeds typically higher than 0.1 $c$, very difficult to reconcile with the standard accretion disk model.

The infrared emission of AGNs is believed to be mainly of thermal origin, in terms of reprocessing of the primary radiation from dust. The presence of the 'IR bump', with a minimum around 1$\mu$m is ubiquitous in AGNs (see e.g. Sanders et al. 1989). This is interpreted as emission from dust, whose temperature does not exceed $\simeq$ 2000 K, which is exactly what expected, because at higher temperatures the dust sublimates. On the other hand, the submillimiter break at the end of the far-IR band can be easily reconciled with the rapid loss of efficiency of dust grains at long wavelengths. This would explain the sharp cut-off observed just shortward of 1mm. The infrared variability also supports the reprocessing dust model, in which an optical/UV variation should be followed by an IR variation, but with a significant time delay due to the larger scale where the dust is distributed (see e.g. Clavel et al. 1989, for the case of Fairall 9). It seems then reasonable to picture a scenario where the optical/UV continuum from the nucleus fully depletes the dust up to the sublimation radius. Beyond this radius, the same radiation heats the dust to a wide range of temperatures (depending on the distance from the central source), producing the observed IR bump. However, a significant contribution of starlight to the dust heating has been proposed, especially in the far-IR band (Prieto et al. 2001).

The radio emission constitutes a very small fraction of the total bolometric luminosity for radio-quiet AGNs, being 5–6 orders of magnitude lower than the optical/UV continuum, whereas radio-loud AGNs show an important radio emission. In the latter class the radio spectrum is typically flat, a clear sign of a non-thermal emission. Indeed, synchrotron radiation is generally invoked as the likely mechanisms responsible for the radio continuum. This interpretation is supported by the presence of low frequency cut-off in some objects, as expected for the synchrotron self absorption, even if the frequency dependence is often not as steep as it should be. It is not clear if the source of radio emission is similar in AGN radio-quiet and radio-loud and why the mechanims involving ultrarelativistic electrons in jets should be so weaker.

The X-ray spectrum of radio-quiet AGNs is dominated by a primary continuum well represented by a simple power law, with a spectral index around 1.7–1.8 and a high-energy cut-off above 100–200 keV (see e.g. Perola et al. 2002). The origin of this component is still unclear. Comptonization in a surrounding hot corona of the UV photons produced by the disk was a good mechanism for the production of the observed X-ray emission (Liang & Price 1977; Liang

1979).
The basic idea, the so-called 'two-phase model', assumes a simple sandwich geometry, where the hot corona completely embeddes the accretion disk (e.g. Haardt & Maraschi 1991). In such a scenario, the inverse Compton scattering of the UV photons emitted by the underlying disk on the hot electrons produces a X-ray power law spectrum, whose photon index is a function of the electron-positrons pairs temperature and the optical depth of the corona. However, this simple picture presents some problems when compared to the data. To reproduce the observed parameters, the model requires that most of the gravitational energy must be dissipated in the corona instead of the disk, leading to the emission of a X-ray luminosity comparable to that in UV band. This is contrary to the observations, since UV luminosities are indeed larger (Walter & Fink 1993).

A possible solution to this problem can be found in a more complex geometry of the system. In particular, a 'patchy corona' was proposed by Galeev et al. (1979) and further developed by Haardt et al. (1994), where the hot electrons are not distributed evenly around the disk, but partially cover it. In this case, the emission from the regions of the disk under the active clouds is effectively dominated by the radiation produced by the corona, but the rest of the disk simply radiates as the corona were not present. Also the observations of the fact that the photon index seems to increase as the 2–10 keV flux increases (see e.g. Perola et al. 1986; Petrucci et al. 2000) supports the thermal Comptonization models, since this behaviour is expected if the X-ray spectral variability is mainly driven by a variation of the UV flux, which in turns changes the cooling of the corona.

Finally, a substantial part of the X-ray photons falls down to the accretion disk again, are absorbed by the disk and re-emitted as black body radiation, contributing once again as the seed photons to be Comptonized by the corona. Another fraction of the X-ray radiation interacting with the disk is Compton scattered and adds to the primary spectrum emitted by the corona. The shape of the reprocessed spectrum depends strongly on the ionization state of the disk. If the matter is highly ionized, the Compton scattering becomes the principal interaction mechanism, leading to a power law spectrum indistinguishable from the primary continuum. On the other hand, if the matter is mostly neutral photoelectric absorption prevails at lower energies, producing the so-called 'Compton reflection' component, an hump peaking at 20–30 keV (see e.g. George & Fabian 1991; Matt et al. 1991). Photoelectric absorption from electrons in the K shell of the metallic elements of the disk can be followed by the emission of K$\alpha$ lines. The strongest emission line is produced by Iron, at 6.4 keV if the matter is mostly neutral, at 6.68 and 6.97 keV from more ionized material. Once escaped from the central regions, the X-ray photons can still be reprocessed by the various kinds of circumnuclear material lying farther away from the nucleus. The most striking effect is the possible absorption from intervening neutral matter.

The column density of the absorber discriminates between two kind of sources: 'Compton-thick' if it exceeds the value $\sigma_T^{-1} = 1.5 \times 10^{24}$ cm$^{-2}$ (i.e. when the optical depth for Compton scattering equals unity), completely blocking the nuclear continuum up to 10 keV or more; 'Compton-thin' if it is lower, but still in excess of the Galactic one, allowing only photons more energetic than a certain threshold to pierce through the material. The nature of this absorber comes from the Unification model as the same medium responsible for the obscuration of the nucleus and the BLR in optical band, the torus. If the torus is Compton-thick, it may be indirectly observed even if it does not intercept the line of sight. A part of the nuclear radiation hits the inner walls of the material and can be scattered towards the observer. The reprocessed spectrum has the same shape as the Compton reflection component produced by the accretion disk, but being the torus at larger distances from the nucleus the variability issue and line widths are different. On the other hand, reflection from a Compton-thin torus is quite different in shape.

An alternative mechanism to the hot corona model was proposed by Ghisellini et al. (2004). They suggest that the central BH in radio-quiet AGNs power outflows and jets intermittently, producing blobs of material. The ejection velocity may be smaller than the escape velocity, causing the blobs to fall back and eventually collide with the blobs still moving outwards produced later. In the collision, the bulk kinetic energy of the blobs is dissipated and effectively accelerates the electrons of the plasma. Their rapid cooling via inverse Compton processes leads to the production of the X-ray continuum. The main differences with the hot corona scenario, whose source energy is only accretion, is that the 'aborted jet' models provides a viable method to power high energy emission through extraction of rotational energy from the BH. It is interesting to note that this mechanism does not necessarily exclude a contribution from a hot corona.

## 2.4 The Unification Model

Thirty years after the discovery of the Seyfert Galaxies as a distant class of object by Seyfert (1943), therefore recognized as a subclass of radio-quiet AGNs, Khachikian & Weedman (1971) realized that the emission lines observed in their optical/UV spectra could be separated in two different kinds, leading to the classification of Seyfert Galaxies into type 1s and type 2s. Seyfert 1s show both the narrow lines and the broad lines; on the other hand, Seyfert 2s only show narrow lines.

When Antonucci & Miller (1985) observed the Seyfert 2 NGC 1068 in polarized light, they realized that broad line, completely absent in the total spectrum, were clearly visible and absolutely equivalent to those observed in Seyfert 1s.

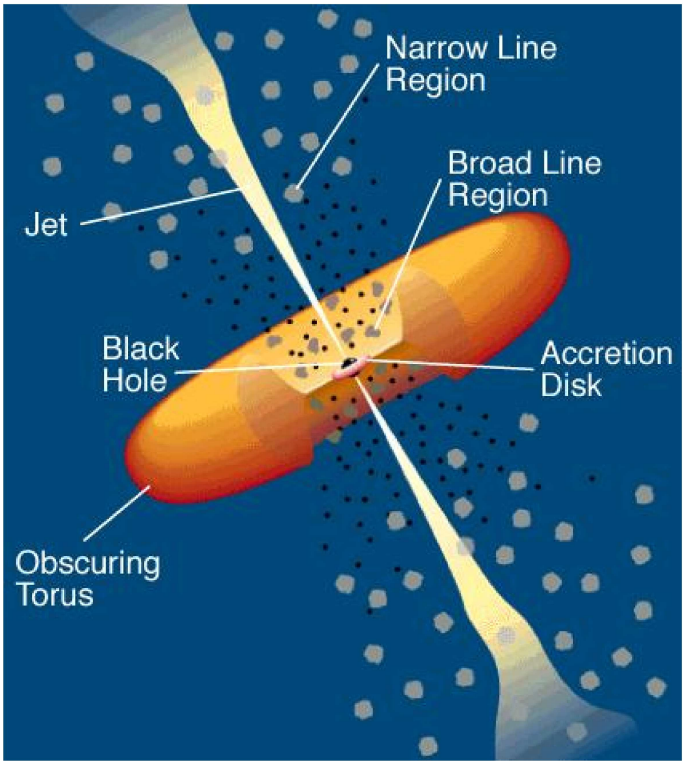


**Figure 2.3:** Pictoric illustration of the Unification Model by Urry and Padovani (1995). Surrounding the central SMBH there is a luminous accretion disk. Broad and narrow emission lines are produced in clouds closer and further away from the central source, respectively. A thick dusty torus obscures the Broad Line Region from transverse line of sight. Powerful radio jets emanated from the region near the BH are present in radio-loud AGNs.

This results led them to suggest that type 2 objects harbor a type 1 nucleus, which is obscured by intervening gas. Its presence may be indirectly observed thanks to a reflecting mirror such as a gas of electrons, which scatters part of the nuclear radiation towards the line of sight, introducing a detectable degree of polarization.

Therefore, an 'Unification Model' was proposed to explain all the different subclass of AGNs. The basic assumption of the Unification Model (see Antonucci 1993, for the archetypal review) is that type 1 and type 2 objects are absolutely equivalent, the only difference being wheter the absorbing gas intercepts the sight of the nucleus or not. The absorbing medium assumes clearly the fundamental role in this scenario. It is usually envisaged as an optically thick torus, embedding the nucleus and the BLR (see Fig. 2.3). If we observe the torus edge-

on, all the nuclear radiation, including lines from the BLR which is inside it, is completely blocked and we classify the source as a type 2. The narrow lines are still visible, because the Narrow Line Region (NLR) is located farther away from the nucleus, outside the torus. If the torus does not intercept our line of sight, we observe every component of the spectrum and the object is classified as a type 1.

The basic idea behind the Unification Model that geometrical effects play a fundamental role in the classification of AGN is probably correct, but a number of observational evidence suggests that some complications should be introduced. Since the first work by Antonucci & Miller (1985), polarized broad emission lines have been observed in several others Seyfert 2s, but there are also many examples of type 2 objects which observed in polarized light, still do not present broad lines (see e.g. Tran 2001, 2003). Moreover, simple extrapolations of the optical/UV scenario to the X-ray emission do not easily fit the observations leading sometimes to different classification of the object between the two bands. Indeed, a number of obscured objects in X-rays turn out to be type 1 AGN when observed in the optical band (Maiolino et al. 2001; Fiore et al. 2001, 2002). The only unambiguos relations between optical and X-ray classifications seem that all the X-ray unobscured objects are optically type 1s, while all type 2s are also X-ray obscured sources. However, there are also claims for the existence of unobscured Seyfert 2 (Panessa & Bassani 2002) or 'pure' Seyfert 2 galaxies in which the BLR is lack (see e.g. Ghosh et al. 2007).

## 2.5 AGN classification

Many years of observations at different wavelengths have led to the discovery of a large number of AGNs with different properties. A complex classification scheme of AGNs has evolved, based on their properties, including radio-loudness, broad and narrow line emission, continuum emission, variability and polarization.

The main distinguish features in the classification of the AGNs are the presence of emission lines in the optical/UV spectra and the intensity of the radio emission. In fact, one important distinction is based on the relative importance of the radio emission with respect to the optical one. AGNs with an intense radio emission are classified as 'radio loud', while AGNs with a weak or almost absent radio emission are classified as 'radio quiet'. Defining the radio-loudness as the ratio between the radio (5 GHz) and the optical (B band) fluxes, $R = F_{5\,\mathrm{GHz}}/F_B$ (Kellerman et al. 1994), the distinction between radio-loud and radio-quiet AGNs can be set to $R$ larger or smaller than 10, respectively. Earlier studies showed a bimodal distribution for $R$, with two peaks at $R \simeq 1$ and $R \simeq$

1000 (Kellerman et al. 1989). Although this result is possibly biased by selection effects, it is clear that the radio-loud sources are really rare, not exceeding 10–20% of the entire AGN population. Powerful relativistic jets are evident only in radio-loud objects, even if matter outflowing at sub-relativistic velocities ($\sim 0.1\ c$) seems to be present also in radio-quiet objects, as indicated by the BAL (Broad Absorption Lines) phenomenon in the optical/UV spectra.
However, historically, the first important classification criterium is based on the properties of optical/UV spectra and can be summarized as follows.

**T**ype 1 AGN: show a strong continuum emission and broad emission lines from the BLR. Radio quiet type 1 AGNs includes Seyfert 1 Galaxies at low luminosities, which are bright at UV and X-rays and are among the first AGNs to be discovered. Due to their low luminosity they are only seen nearby, making the host galaxies distinguishable from the bright core. Their high-luminosity counterparts are the Quasi Stellar Objects (QSOs), which comprise a central core so bright that the host galaxies cannot be distinguished. Instead, radio-loud type 1 AGNs consist of Broad Line Radio Galaxies (BLRGs) at low luminosities, and Flat Spectrum Radio Quasars (FSRQs) and Steep Spectrum Radio Quasars (SSRQs) at high luminosities. The difference between *steep* and $flat$ quasars is based on the value of the radio spectral index ($F_\nu \propto \nu^{-\alpha}$, where $\alpha$ is the spectral index in the 100 MHz – 30 GHz range) relative to the separation value $\alpha = 0.5$. The different radio spectra are the signature of their distinct morphologies: SSRQs have weaker radio cores and show extended radio lobes similar to the ones of radio galaxies, whereas FSRQs are generally more polarized and core dominated than SSRQs, showing an high variability.

**T**ype 2 AGN: show a weak continuum emission and narrow emission lines. The absence of broad emission lines is interpreted as low dispersion velocity or by the presence of prospectically obscuring torus that hides the BLR. Radio loud sources are classified as Narrow Line Radio Galaxies (NLRGs), and show different levels of jet collimation and morphology, including Fanaroff Riley (FR) type radio galaxies. The low luminosity FR type Is exhibit radio emission whose intensity falls off with distance from the nucleus, while the high luminosity FR type IIs display more collimated radio jets which terminate as well defined radio lobes (see Section 2.8). Radio quiet low luminosity type 2 AGNs include Seyfert 2 galaxies and narrow emission X-ray galaxies (NELG), while high luminosity radio quiet include infrared excess galaxies.

**T**ype 0 AGN: AGN with the axis of the jet close to the line of sight of the observer. Radio quiet type 0 AGNs include Broad Absorption Line (BAL) quasars, whereas radio loud include Blazars. Blazars can be divided into two subtypes: BL Lacertae objects (BL Lacs) and Flat Spectrum Radio Quasars (FSRQs). BL Lac objects, name derived from the prototype of this class BL Lacertae, are characterized by the weakness (Equivalent Width $< 5$ Å) or even absence of

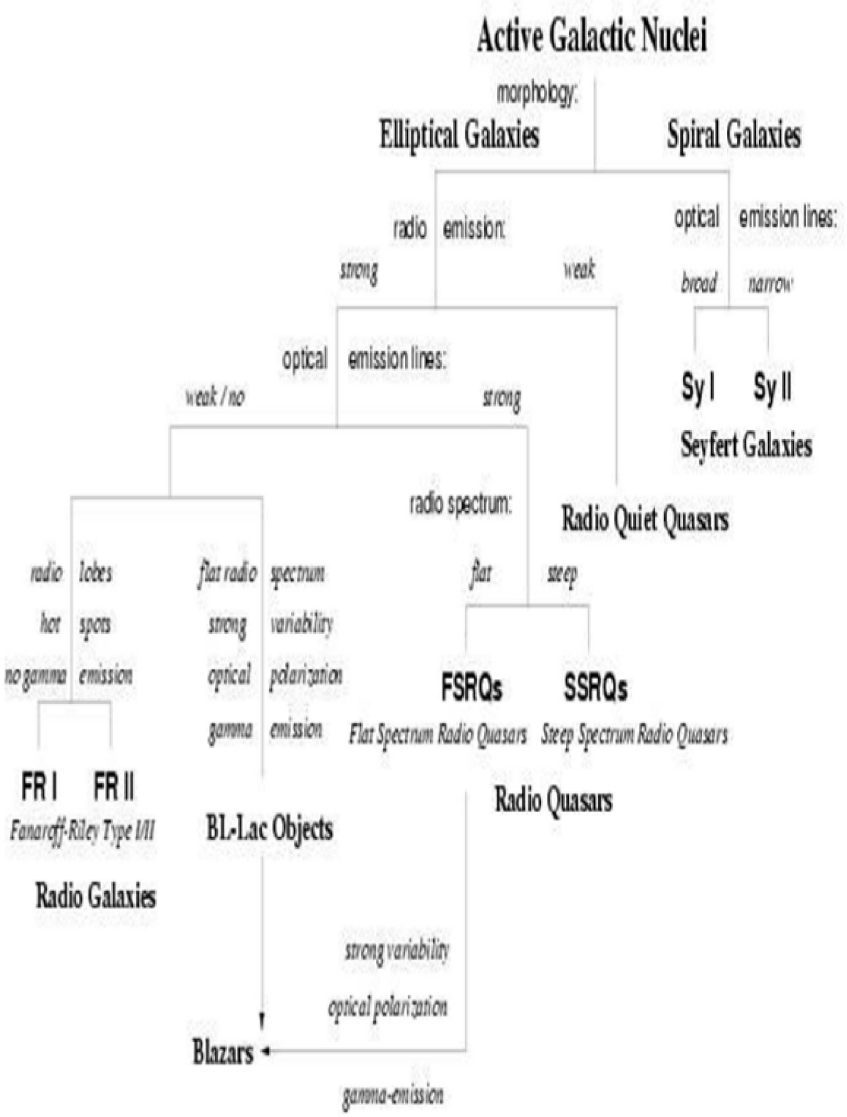


**Figure 2.4:** Schematic AGN classification, based on galaxy morphology, radio loudness, and optical emission lines properties.

emission line in their optical spectra. FSRQs include also objects empirically known, from observed properties, as Optically Violent Variable (OVV) quasars, Highly Polarized Quasars (HPQs) and Core-Dominated Quasars (CDQs). These properties often are presented together, and are also associated with superluminal motions, high brightness temperatures and a broad band emission, suggesting that they are different manifestations of a unique phenomenon now recognized in the beamed jet emission. In fact, the flat radio spectra of the compact sources are usually interpreted as being due to the superimposition of synchrotron spectra of different components along the jet, each self-absorbed at a different frequency. In the FSRQs this emission is boosted by beaming effects, and thus dominated over the extended one, characterized by a steep spectrum. BL Lacs in turns have been subdivided in three different types. When the lower peak is located in the submillimeter to optical band, the objects are classified as Low-frequency peaked BL Lacs (LBLs) while in High-frequency peaked BL Lacs (HBLs) the lower peak is located at X-ray energy. The intermediate-frequency peaked BL Lacs (IBLs) showed the synchrotron peak between UV and X-rays, promoting a smooth transition from LBLs to HBLs (see Nieppola et al. 2006).

## 2.6 Blazars: historical introduction and main characteristics

The object BL Lacertae had been in the catalogue of variable stars for much time; infact, it was originally discovered by Cuno Hoffmeister in 1929, but to understand the nature of this source it was necessary sixty years. In fact, the source showed an optical spectrum rather unusual, it was featureless and the continuum emission was steeply rising to infrared wavelengths. In 1968, Schmidt noticed that a variable radio source was located at the same position of BL Lacertae (Schmidt 1968). BL Lacertae was not a periodic variable, but rather its intensity varied irregularly with no apparent pattern of its brightening and dimming. When the spectrum of this putative 'variable star' was taken, it was discovered that in the optical emission it was featureless; there were no emission lines as from quasars, and no absorption lines as found in most stars. Peter Strittmatter in 1972 identified four objects closely similar to BL Lacertae (Strittmatter et al. 1972); and therefore the subclass is named *BL Lacertae*, from the name of the archetypal of this type of objects.

In 1974, J. E. Gunn and J. B. Oke, two Caltech astronomers, determined that BL Lacertae was actually located in a normal elliptical galaxy (Oke & Gunn 1974). By blocking the light from central region of the source, the light from the surrounding area showed absorption lines that permitted an estimation of the

redshift z $\simeq$ 0.07. This redshift corresponds to a distance at about 420 Mpc, indicating that the core of BL Lacertae shines with a luminosity $L \simeq 10^{46}$ erg s$^{-1}$. The discovery of some radio-loud quasars with a continuum similar to that of BL Lacertae, but with broad emission lines, led to the definition of a new class of sources. Ed Spiegel jokingly referred to these objects as *blazars* (Blandford & Rees 1978). The word *blazar* is a combination of two words: BL Lac and quasar, and also connected with the term *blazing*. In 1981 Moore and Stockman performed a polarization survey in which they discovered 17 high polarization quasars (HPQs) and discussed their link to BL Lac objects, establishing the division of this new class of AGN in two main subgroups: the BL Lac objects and the Flat Spectrum Radio Quasars.

Blazars are the most extreme class of Active Galactic Nuclei, characterized by the emission of strong non-thermal radiation across the entire electromagnetic spectrum, from radio to very high $\gamma$-ray energies. The typical observational properties of blazars include irregular, rapid and often very large variability, apparent superluminal motion of the jet at VLBI scales, flat or inverted radio spectrum, high and variable polarization at radio and optical frequencies. These features are interpreted as the result of the emission of electromagnetic radiation from a relativistic jet that is viewed closely aligned to the line of sight, thus causing strong relativistic amplification (Blandford & Rees 1978; Urry & Padovani 1995).
In the following, we will discuss some typical characteristics of blazars: the superluminal motion, the variability, the presence of the jet and their Spectral Energy Distribution.

### 2.6.1 Superluminal motion

There are many observational evidences of superluminal motion in the VLBI observation of radio jets of the blazars (see Fig. 2.5). Superluminal motions can be explained in terms of an emitting region with a relativistic bulk velocity subtending small angles with the observer line of sight (Rees 1966). The apparent velocity seen by the observer is:

$$\beta_a = \frac{v_a}{c} = \frac{\beta sin\theta}{1 - \beta cos\theta} \tag{2.18}$$

where $\theta$ is the angle between the bulk motion velocity and the observer line of sight and $\beta$ is the bulk motion velocity of the emitting region. One of the main implications of superluminal motion is the relativistic beaming. Due to this effect isotropic emission in the rest frame of the source is seen by the observed beamed into a small cone. In the case of bulk motion toward the observer, the observed flux is enhanced with respect to the emitted one. A second consequence is that

the differences between the emission and arrival time in the observer frame are shortened, and being the frequency the inverse of times follows that the observer will see the frequencies blueshifted with respect to those emitted in the source rest frame. The flux amplification is important in order to explain $\gamma$ transparency and to avoid inverse Compton catastrophe.

In order to estimate the $\gamma$ transparency at the threshold energy for pair production the *compactness* parameter was introduced by Cavaliere & Morrison (1980). This parameter is defined as:

$$C = \frac{L_\nu \sigma_T}{4\pi R m_e c^3} \tag{2.19}$$

where $L_\nu$ is the specific $\gamma$-ray luminosity of the source, $\sigma_T$ is the Thomson cross section, $c$ is the velocity of the light and $R$ the radius of the source. The problem of the $\gamma$-ray transparecy arose from the observation of many bright $\gamma$-ray blazars detected by EGRET, and now confirmed by AGILE and *Fermi*.

For these sources the size inferred by the time scale variability, $R = ct_{var}$ / (1+z), where z is the redshift, implied a compactness >> 1 with the resulting $\gamma$-rays destruction and electron-positron production. The observed transparency to the $\gamma$–$\gamma$ pair production is explainable if the rest frame luminosity is lower than the inferred from observed flux and the size is greater than that inferred from the observed time scale. In fact, in the case of a beamed emission, $L_{\nu_{obs}} \sim \delta^3 L_{\nu_{em}}$ and the observed time-scale variability is related to that in the source rest frame by $t_{obs} = t_{src}/\delta$, where $\delta$ is the beaming factor, so that the relation between the variability time scale and typical source size are: $R = ct_{var}\delta/(1+z)$. Consequently the compactness to the source respect to that inferred from observation will be $C_{src} = C_{obs}/\delta^4$ and for typical value of the beaming factor $\delta \sim 10$ results $C_{src} < 1$.

From an historical point of view the problem of the compactness of these sources arose since the first radio observation of compact objects, and was referred as the 'inverse Compton catastrophe'. The problem of the inverse Compton catastrophe is originated by the ratio between the synchrotron and the Compton cooling rates in compact radio-sources. In the case of synchrotron self absorbed sources this ratio can be expressed as:

$$\eta = \frac{\dot{\gamma}_{IC}}{\dot{\gamma}_{sync}} = \frac{U_{ph}}{U_B} \sim \nu T_e^5 \tag{2.20}$$

where $T_e$ is the temperature of the relativistic electrons that for synchrotron self-absorbed source is equal to the brightness temperature $T_b$. If the value of $\eta > 1$ then radio flux should be very suppressed in favour of higher energy emission. To keep $\eta < 1$ in the observed compact radio sources, $T_b$ should be lower than $\sim 10^{12}$ K. Typical observed values of $T_b$ are in the order of $10^{11}$ K, but taking

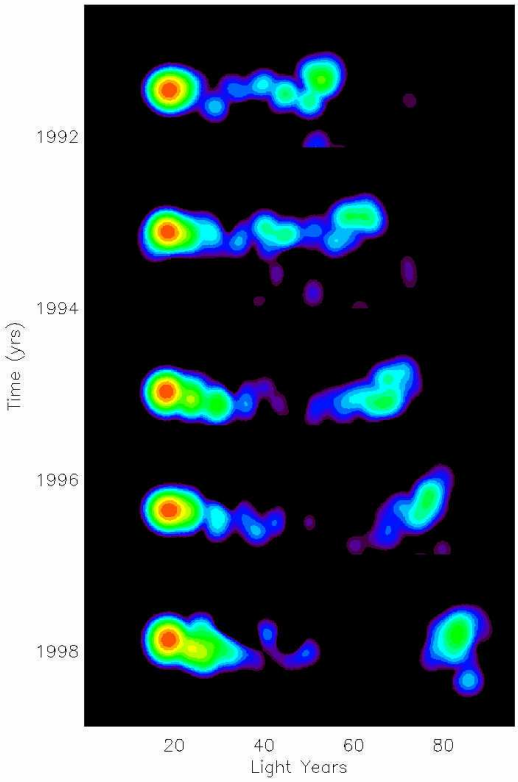


**Figure 2.5:** A sequence of VLBI observations of 3C 279. Apparently superluminal motion of the radio components in the blazar 3C 279. The bright component at the left is taken to be fixed radio core, and the bright spot at the right appears to have moved 25 light years on the plane of the sky between 1991 and 1998 [Wehrle et al. 2001].

into account the size of the radio source estimated by time-scales variability $T_b$ exceeding $10^{12}$ are found. Also in this case if one considers relativistic beaming effects follows that the observed brightness temperature is related to that in the source by $T_b^{obs} = \delta\, T_b^{src}$ and $\nu_{obs} = \delta\nu_{em}$. It results that the observed cooling ratio $\eta_{obs} = \delta^6\, \eta_{src}$, with the source brightness temperature $T_b^{obs} = \delta^5\, T_b^{src}$, that is far from the catastrophe limit also if $T_b^{obs}$ exceeds $10^{12}$ K.

### 2.6.2 Variability

Extreme variability, both in amplitude and timescales, is one of the main characterizing features of the blazars. In fact, blazars are known to display strong

variability over the whole electromagnetic spectrum, from radio to TeV energy. A dramatic example of large variability amplitude on long timescale is offered by the $\gamma$-ray emission of 3C 279 in the EGRET *era*. The flux was observed to change by more than two orders of magnitude between two observations performed in 1993 and 1996. This aspect is very complex and closely related to the physics of the emission and the acceleration processes and to the geometry of the emitting region. The emission level of blazars is highly variable on all timescales, with changes of the emission level of the electromagnetic radiation by more than one order of magnitude. The timescales range from years down to minutes, with the longer ones being typical for the radio to optical part of the spectrum, where they are observed to be of the order of days up to several years (see Ulrich et al. 1997). On the other hand, X-rays and $\gamma$-rays can vary in flux in a matter of hours, with the TeV flares being the most dramatic ones, with flux doubling time as short as half an hour. Often short time scale variability is superimposed to a long trend one. Some sources also seem to produce Intra-Day Variability (IDV) in all wavebands, even if it is more simple to be observable at the lowest energies (see Wagner & Witzel 1995).

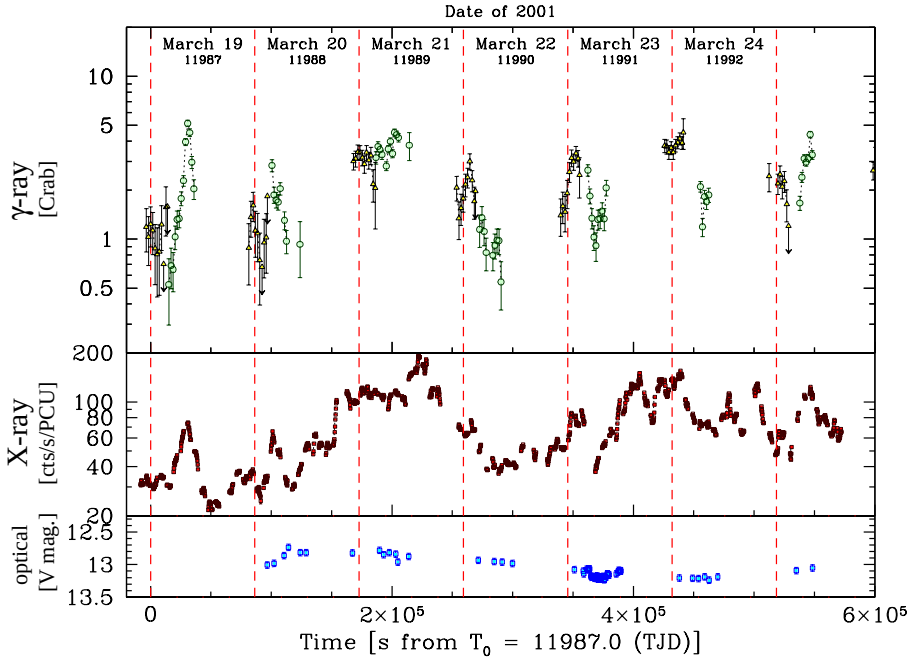


**Figure 2.6:** Simultaneous optical (V band, bottom panel), X-ray (2–10 keV, middle panel), and TeV (E > 0.4 TeV, top panel) light curves for Mrk 421 in 2001 March 18–25. Variations in X-rays and TeV bands are clearly correlated [Fossati et al. 2008].

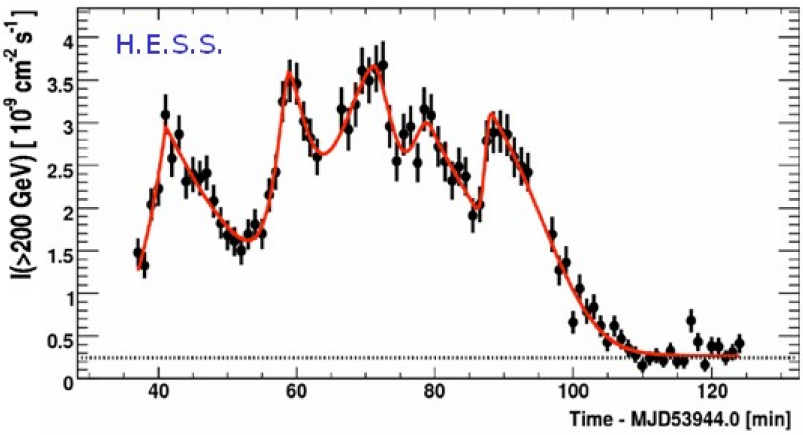


**Figure 2.7:** TeV light curve obtained for the BL Lac PKS 2155−304 by H.E.S.S. in July 2006. Variations of the flare on timescales of 200 seconds are observed [Aharonian et al. 2007].

While many of the emission models are able to describe the observed SED to a certain degree, the observation of a rapid, large scale flares should enable discerning constraints to be put on the different models, as the models respond differently to changes in the source injections parameters. During the flares, blazars are observed to have greater amplitudes in the high-energy spectral component than in the low-energy one (e.g. Wehrle et al. 1997). In addition, the flux changes are energy dependent within each of the two spectral components, having the greater amplitude increase with the higher photon energy (Sikora et al. 1997). Moreover, coordinated variations in different spectral bands indicate that the emission is produced in a single region and that the same electrons could be radiating both the components (e.g. see Fig. 2.6).

Rapid variations in the blazars SED imply a very compact emission region that is moving toward the observer with highly relativistic speeds (Blandford & Königl 1979). The observed timescales put constraints on the size and the location of the emitting region, which corrected for the Doppler boosting, turns out to be surprisingly small, of the order of light hours and in some cases less than an hour. The most extreme cases observed were the very rapid TeV flare of Mrk 501 detected by MAGIC during 2005 (Albert et al. 2007c) and that of PKS 2155−304 observed by H.E.S.S. during 2006 (Aharonian et al. 2007; Fig. 2.7), where the variability timescales were of the order of only few minutes. These variability timescale much shorter than the inferred light crossing times at the black hole horizon put extreme requirements of the bulk Lorentz factor of $\sim$ 50–

100. This value of the Lorentz factor is clearly in excess of the jet Lorentz factor $\Gamma_{\rm jet} \sim 10$ measured for these two sources (Giroletti et al. 2004). Even accounting for the effects of relativistic beaming such shorter timescales are challenging conventional emitting models. This contradiction can be avoided if the jet is efficiently decelerated on sub-parsec scales after the TeV flare (Georganopoulos & Kazanas 2003) that could also be due to radiative feedback in a spine/layer configuration (Ghisellini and Tavecchio 2008). An alternative scenario is the jet-in-a-jet model proposed by Giannios et al. (2009), with a compact emitting region that move relativistically within a jet of bulk $\Gamma_{\rm jet} \sim 10$ in a Poynting-flux dominated jet.

### 2.6.3 Jets

Jets are ubiquitous phenomena in the Universe, found in AGNs, Gamma-Ray Bursts, young stellar objects, protoplanetary nebula, microquasars and X-ray binaries. The physical mechanisms behind the production of jets in AGNs, and thus at the base of the radio-loud/radio-quiet division is still unclear, though there is consensus that the production of the jets can be related to the spin of the black hole (see e.g. Blandford 1990).

Radio-loudness is associated to the existence of jets expelled from the innermost regions of the AGNs, propagating for kpc or even Mpc from the central regions (Begelman, Blandford & Rees 1984). It is widely believed that the relativistic jet is the key element of the observed blazar emission. Acceleration processes in the jet generate non-thermal highly variable emission over an energy range spinning up to 20 orders of magnitude (Fig. 2.8) . The jets are beamed by strong magnetic fields and oriented perpendicular to the accretion disc. The jets themselves seem to be stable up to kpc scales, being a strong source of the non-thermal radiation from radio to VHE $\gamma$-rays. As already noted, the jets are often characterized by a highly polarized radiation, short variability time scale and an apparent superluminal motion. It is believed that the twisting of magnetic fields in the accretion disk collimates the outflowing along the rotation axis of the central object, so when conditions are suitable, a jet will emerge perpendicular to the plane of the accretion disk.

While the physical conditions inside the jet are currently mainly unknown, the general popular believe is that detailed magnetohydrodynamic (MHD) models of the accretion disk/black hole system should be able to reproduce jet collimation and particle acceleration mechanisms (see e.g. Meier et al. 2001). Such models account for jet collimation and accelerations in the accretion framework: jets seem to be a natural consequence of a rotating disk in presence of a magnetic field (Kudoh et al. 1999). The magnetic field is frozen in the outflowing plasma, allowing particles to escape along the magnetic field lines. Requirements for

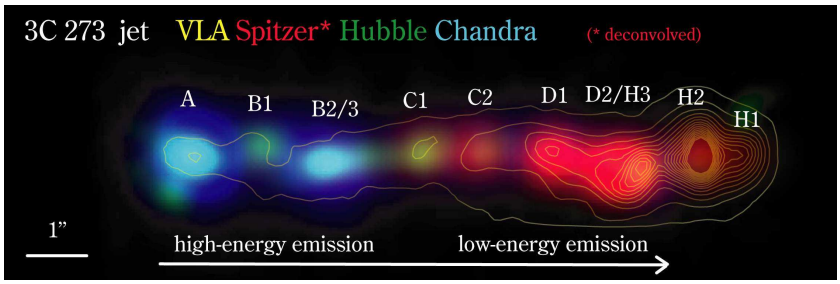


**Figure 2.8:** Multiwavelength image of the jet of the blazar 3C 273 from radio to X-rays, with VLA, *Spitzer*, Hubble Space Telescope and *Chandra* observations [Uchiyama et al. 2006].

jet formation are a compact object to collect material to be ejected, a magnetic field anchored in it, and differential rotation to form the helical magnetic field structures. Numerical simulations have shown that tightly collimated jets along the rotational axis are a general feature of rotating, gravitational confined plasmas. Such calculations show that a very fast rotating Kerr black hole is able to accelerate material in the jets up to Lorentz factor of $\Gamma = 10$. At the beginning, the jets as a total are magnetically driven (Poynting flux dominates over the kinetic matter flux) and collimated due to a toroidal component of the magnetic field (Sikora et al. 2005). Further down the jet, on sub-parsec scales, the energy density of non-thermal particles is much higher than the energy density of the magnetic field. However, the strength of the magnetic field as well as the composition of the jets are still unclear. The acceleration mechanism is indeed a matter of debate. The accelerated plasma could originate from the outer halo of the accretion disk (Marscher et al. 2002). Other models assume that the charged black hole acts as as giant dynamo (Kirk and Mastichiadis 1999). Also in these models magnetic fieds are naturally given.

## 2.7 Spectral energy distribution and the blazar sequence

Considering that the blazars emit in all bands of the electromagnetic spectrum it is essential to consider and study their entire emission in a global way. The main tool is provided by the so-called Spectral Energy Distribution (SED), in which the data are plotted as $log\ (\nu)$ versus $log\ (\nu f_\nu)$, giving the source power per logarithmic frequency interval and thereby directly shows the relative energy output in each frequency band.

The SEDs of blazars are typically double-humped with the first peak occurring in the IR/optical band for the so-called *red blazars* (including Flat Spectrum Radio Quasars and Low-energy peaked BL Lacs) and at UV/X-rays for the so-called *blue blazars* (including High-energy peaked BL Lacs). The first peak is commonly interpreted as synchrotron radiation from high-energy electrons in a relativistic jet. The SED second component, peaking at MeV–GeV energies in *red blazars* and at TeV energies in *blue blazars*, is commonly interpreted as inverse Compton scattering of seed photons, internal or external to the jet, by relativistic electrons (Ulrich et al. 1997), although other models have been proposed (see e.g. Böttcher 2007 for a recent review). The emission mechanisms at work in blazars is shown in detail in Chapter 3.

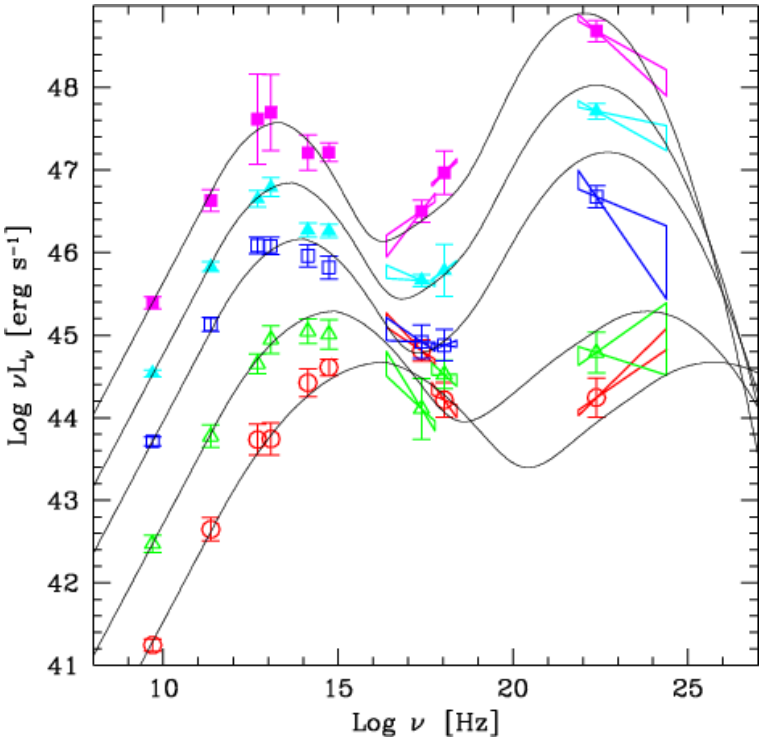


**Figure 2.9:** The average SED of the blazars studied by Fossati et al. (1998), including also the average values of the hard X-ray spectra collected by *Beppo*SAX. The thin solid lines are the spectra constructed following the parametrization proposed by Fossati et al. [Donato et al. 2001].

The statics of blazars found since the end of 1990s allowed to make several phenomenological studies about their properties. In particular, Fossati et al. (1998) studied 126 blazars from three samples of blazars: the *Einstein* Slew

Survey (Elvis et al. 1992), the 1-Jy samples of BL Lacertae (Kühr et al. 1982) and the FSRQs extracted by Padovani & Urry from the 2-Jy sample of Wall & Peacock (1985). 33 of these blazars were also detected in $\gamma$-ray by the EGRET instrument on board *CGRO*. Fossati et al. computed average SED for group of blazars binned according to radio luminosity and a sequence with remarkably features appeared. The blazar sequence is shown in Fig. 2.9. The first peak occurs in different frequency ranges for different luminosity classes: blazars with greater bolometric luminosity have smaller peak frequencies and 'redder' SEDs, while blazars of lower bolometric luminosity have higher peak frequencies and then are 'bluer'. Moreover, the higher energy peak component correlates positively with the peak frequency of the lower energy one and the luminosity ratio of the high to the low frequency components increases with bolometric luminosity. These features cannot be explained solely by the orientation effect of the jet as argued in the Unification model mentioned in the previous section.

The spectral sequence was interpreted by Ghisellini et al. (1998) as consequence of the different radiative cooling suffered by the emitting electrons of blazars of different power. Moreover, it is evident the increasing importance of an external radiation field along the sequence from HBLs to FSRQs. Within the FSRQs Ghisellini et al. found a hint of a further subdivision between low-polarized quasars (LPQs) and high-polarized quasars (HPQs), with a tendency for LPQs to be more extreme. The sequence shown in Fig. 2.10 corresponds to an increase on the external radiation field, the total energy density and the injected power going from HBLs to LPQs. These in turn result in a decrease of $\gamma_{\rm peak}$ and an increase in the Compton dominance. The sequence was later confirmed when the Cherenkov Telescopes allowed us the detection of an increasing number of BL Lacs (Ghisellini, Celotti & Costamante 2002; Celotti & Ghisellini 2008). An interpretation of these findings is possible within the internal shock scenario (Ghisellini 1999; Spada et al. 2001; Guetta et al. 2004), which could account for the radiative efficiency location of the dissipation region and spectral trend if the particle acceleration process is balanced by the radiative cooling. In this scenario the energetics on scales of $10^2$–$10^3$ Schwarzschild radii is dominated by the power associated to the bulk motion of the plasma. This is in contrast with the electromagnetically dominated flow (Blandford 2002).

The blazar sequence found a wide popularity because just a single parameter, the bolometric luminosity, seems to govern the physical properties and radiation mechanisms in the relativistic jets present in blazars. This sequence was examined lately with different tests taking an advantage of a higher statistics of detected blazars, in order to check the claimed correlation and at detecting the 'forbidden objects' and it appears to be clear that it could partially suffer from selection effect because these studies consider the brightest blazars and the phenomenological blazar sequence had an incomplete SED coverage (only 33

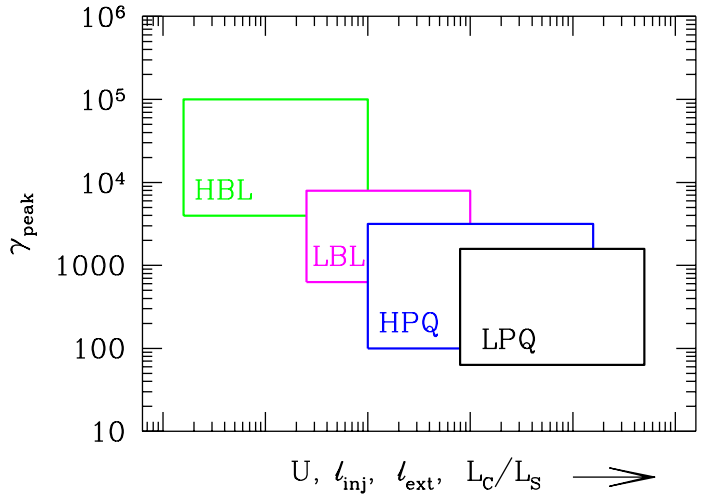


**Figure 2.10:** Schematic representation of the unifing scheme of the different types of blazars. The behaviour of these class of objects in function of different parameters (external radiation field [$l_{ext}$], total energy density [U], injected power [$l_{inj}$], the Compton dominance [$L_c/L_s$] on x-axis, the $\gamma_{peak}$ on y-axis) is shown [Ghisellini et al. 1998].

sources were observed also in $\gamma$-ray) that probably describes active states of the sources, not necessarily their averaged status.

Padovani (2007) presented a critical review of the blazar sequence, pointing three main tests for the validation of the blazar sequence: existence of an anticorrelation between the synchrotron peak frequency and the bolometric observed luminosity, non-existence of 'blue' powerful objects and the fact that 'blue' sources should be more numerous than 'red' ones. The first point is related to observed properties and considering that red low-luminosity blazars could be slightly misaligned, the existence of red blazars with small observed luminosity is not invalidating the sequence, that even predicts them.
Instead, some possible example of High-frequency peaked FSRQ (HFSRQ, i.e. FSRQ with SED similar to that of HBLs, but with $\nu_{\rm peak}$ at frequency 10 times smaller than that of typical HBLs; Perlman et al. 2001, Padovani et al. 2003) are found: RGB J1629+4008 (Padovani et al. 2002), RXJ1456.0+5048 (Maraschi et

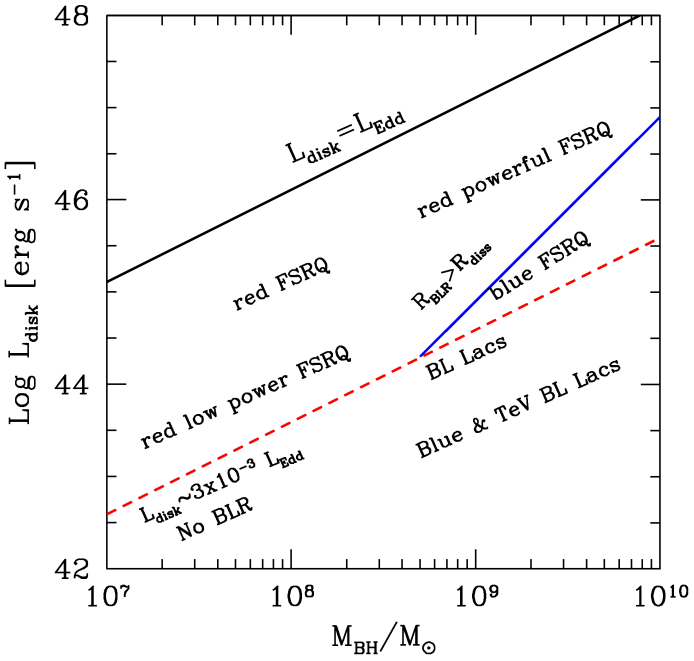


**Figure 2.11:** The disk luminosity versus black hole mass plane. Different blazar classes occupy different regions of this plane. The dashed line corresponds to a disk luminosity equals to $3 \times 10^{-3}$ of the Eddington one. Below this line the BRL does not exist or it is very weak. Another important dividing line correponding to where $R_{diss} > R_{BLR}$ [Ghisellini et al. 2008].

al. 2008), SDSS J081009.94+384757.0 (Giommi et al. 2007) and IGR J22517+2218 (Bassani et al. 2007). The presence of these tentative HFSRQs are not predicted by the blazar sequence, therefore the confirm of their nature and existence could bring it up for discussion the picture of the sequence. However, as pointed in Ghisellini et al. (2008) these sources are not powerful quasars, but the extreme manifestation of the blazar sequence: high-energy peak increasingly dominating increasing the observed luminosity (see also Maraschi et al. 2008). Concerning the third point, Padovani pointed out that the ratio of blue/red BL Lacs in deeper radio and X-ray samples of blazars disagrees with the prediction made by the blazar sequence, especially for radio surveys down to the 50 mJy flux, but if red blazars are intrinsically more powerful than blue BL Lacs they can enter in a flux limited sample even if the jet is slightly misaligned, while blue BL Lacs cannot. This selection effect could make red blazars to be overrepresented in the sample.

All the subsequent studies, from the surveys that were not subject to select effect, have shown very large scatter and some possible outliers, but no strong outliers have been found and after ten years of investigations it seems that the anti-correlation between the peak frequencies and the bolometric luminosity found by Fossati et al. (1998) is a good approximation of average SEDs. Nieppola et al. (2008) indicate that the blazar sequence seems to be an observational phenomenon, by accounting for the different Doppler factors across the sequence. They study the correlation between the de-bosted synchrotron peak position and luminosity, deriving the Doppler factors from variability timescales from brightness temperatures at high radio frequencies. The blazar sequence seems to disappear when the intrinsic Doppler corrected values are considered. However, the technique used gives information on the Doppler factor for radio emitting regions in AGNs. Considering that the jet strongly decelerates from the blazar region to the VLBI scale, from which most of the radio emission originates (Ghisellini et al. 2005), the Doppler factor obtained by Nieppola et al. (2008) for the radio jet emitting regions is probably much smaller than the Doppler factor in optical-to-$\gamma$-ray emitting region, especially in HBLs.

Ghisellini and Tavecchio (2008) proposed a new blazar sequence, in which the power of the jet is linked to the two main parameters of the accretion process: the mass of the black hole and the accretion rate. This new blazar sequence could have implications on the possible cosmic evolution of blazars. In fact, if the accretion rate in blazars evolves in redshift we should have larger accretion rates in the past, therefore BL Lac objects, whose accretion rate is less than a critical value, should be rarer in the past implying a negative evolution. On the other hand, FSRQs should be more common in the past, since a large fraction of massive black holes accretes at rates larger than the critical one. This is in agreement with the scenario proposed by Cavaliere & D'Elia (2002), in which blazars are born initially as powerful at high accretion rate and transform themself into BL Lacs when the accretion rate decreases.

Recently, Ghisellini et al. (2009b) perform a systematic study of all blazars of known redshift detected by *Fermi*-LAT during its first three months survey and with a reasonable data coverage of their SED, confirming the previous findings concerning the relation of the physical parameters with the source luminosity which are the origin of the blazar sequence. Moreover, their study confirms the divide between FSRQs and BL Lac objects in terms of accretion rate, already investigated in Ghisellini, Maraschi & Tavecchio (2009a). It occurs when the accretion rate become smaller than 10% of the Eddington one (or equivalently when the disc luminosity became smaller than 1% Eddington luminosity). Finally, for more powerful blazars a positive correlation between the jet power and the disk luminosity is found, confirming the relation between the power carried out by the jet, in the form of bulk motion of particles and magnetic fields and of

the luminosity associated to the accretion.

## 2.8 Radio galaxies and blazars

Historically, radio galaxies have been classified in two different morphological types by Fanaroff and Riley (1974): Fanaroff–Riley type I (FRI) and Fanaroff–Riley type II (FRII). Also a physical division was suggested by Fanaroff and Riley that found a correlation between the morphology and the radio power of these galaxies: radio galaxies are characterized by luminosities below and above a 'luminosity break' of $L_{178\,\mathrm{MHz}} \sim 2 \times 10^{25}$ W Hz$^{-1}$. The FRI/FRII division seems to be related to the speed and the propagation of the jet: the present evidence suggests that FRI jets become trans-relativistic quite early, within a few kiloparsec, while for FRII midly or even highly relativistic speeds are required. The FRI/FRII division could be ultimately related to the different regimes of the accretion flow: radiatively inefficient/efficient (Ghisellini & Celotti 2001). FRI galaxies are characterized by symmetric radio jets with the highest intensity near the nucleus and decreasing intensity in outer regions untill fading into a weak diffuse nebulosity, while FRII show usually highest radio emission far from the nucleus with well collimated jets leading to sharp edge lobes which embed prominent bright zone, the 'hot spots'. Their jets are often too faint to be observed. It was later realized that the critical radio luminosity separating FRIs and FRIIs increases with the optical luminosity of the host elliptical galaxy (Owen and Ledlow 1994). FRI sources generally lack strong emission lines, while FRII comprises objects with clear emission lines such as NLRG and BLRG.

The current Unification scheme attemps to combine the radio galaxies (the so-called 'parent population') with FSRQs and BL Lacs assuming that the blazars are radio galaxies with the jet axis close to the line of sight of the observer. Relativistic effects amplify the non-thermal jet emission, producing all the peculiar characteristics observed in these sources. In particular, BL Lacs should be beamed FRI radio-galaxies and FSRQs beamed FRII. Since the Unification scheme is based on the anisotropy of the jet emission induced by the relativistic beaming, it directly implies that all the isotropic properties of blazars, such as extended radio emission, luminosity of narrow emission lines, luminosity and type of the host galaxy, and environment have to be similar to those of their assumed parent population of radio galaxies. In this respect, radio loud AGNs are usually hosted in luminous elliptical galaxies (e.g. McLure et al. 1999; Urry et al. 2000). Morphology, luminosity and size of the host galaxies of blazars are similar to those of the host galaxies of FRI and FRII, which supports the unification of blazars and radio galaxies, but conclusive results on the BL Lac/FRI and

FSRQ/FRII association do not exist.

Studies of the environmental properties of radio loud AGNs are somewhat inconclusive. Quasars and FRIIs are found to reside in clusters of similar richness (e.g. Wold et al. 2000). On the other hand, Wurts et al. (1997) for a sample of 45 BL Lac objects found that their environments are more similar to those of quasars and FRIIs rather than FRIs. Prestage and Peacock (1988) found that for a sample of $\sim 200$ radio sources with redshift $z < 0.25$, FRI galaxies are in rich clusters than FRII galaxies, but at higher redshift ($z \simeq 0.5$) their environments were found to be similar (Hill and Lilly 1991). More recent studies seems to indicate that also at low redshift ($z \simeq 0.2$) they have similar cluster environments (Mc Lure and Dunlop 2001). Regarding the extended radio emissions and narrow line luminosities there is a discrepancy. Quasars are found to have extended radio powers typical of FRII radio galaxies (e.g. Murphy et al. 1993; Fernini et al. 1997), BL Lac objects can have extended radio powers typical both of FRI and FRII galaxies (e.g. Kollgaard et al. 1992; Cassaro et al. 1999; Rector and Stocke 2001). Narrow emission lines are weak or absent in FRI as for BL Lacs. On the contrary, narrow emission line characteristic of FSRQs in FRIIs can be both strong and weak (e.g. Laing et al. 1994; Tadhunter et al. 1998).

Another important prediction of the Unification scheme is that the statistical properties of the parent population must be similar to the properties of the beamed population, once the beaming is taken into account. In particular, due to the small viewing angle needed for the beaming effect, the total number of beamed objects must be small compared with the number of the parent objects. Therefore the luminosity function of the parent population under the effects of the beaming transforms into the luminosity function of the expected beamed population. Urry and Padovani (1995), calculating the beaming properties of the blazar populations, found that the Lorentz factor $\Gamma$, both in FRI and FRII, lies in the range $5 < \Gamma < 40$. This result is in agreement with the values found with the measures of the superluminal motion (Vermulen and Cohen 1994). Urry and Padovani (1995) have successfully applied this model also to the observed radio luminosity functions of quasars (FSRQs and SSRQs) and FRII radio galaxies from the 2 Jy sample. Even if with more uncertainties, comparison of luminosity function of BL Lacs and FRI radio galaxies at radio, optical and X-rays showed a quite good agreement with the beaming hypothesis (Padovani and Urry 1990, 1991; Urry et al. 1991). On the basis of overlapping properties between FRI and FRII, and BL Lac and FSRQ, seems to be likely the Unification scheme that relates the population of the radio galaxies to that of blazars.

Recently, *Fermi*-LAT detected $\gamma$-ray emission from 3 radiogalaxies: M87 (Abdo et al. 2009b), Cen A (Abdo et al. 2009a) and Perseus A/NGC 1275 (Abdo et al. 2009c). Moreover, other objects with possible association with EGRET detection, like NGC 6251 (Mukherjee et al. 2002) and 3C 111 (Sguera et al. 2005;

Hartman et al. 2008) await confirmation with *Fermi*. In contrast with the blazars, most radio galaxies have large inclination angles and hence there is no significant amplification of their emission due to Doppler beaming. However, if the jet has a velocity gradients, as suggested by recent radio/X-ray observations (see e.g. Kataoka et al. 2006), it is possible to produce $\gamma$-ray emission from the nucleus of radio galaxies via inverse Compton process, where the emission from the slow part is amplified in the rest frame of the faster part and viceversa (see Ghisellini et al. 2005; Georganopoulos & Kazanas 2003). These detections show the strict relation between the blazars and their parent populations, the radio galaxies, and the correctness of the Unification scheme. Further detection in $\gamma$-ray band will allow us systematic studies of relativistic jets with a wide range of viewing angles and therefore investigate in more detail differences and similarity between blazars and radio galaxies.

Chapter 3

# Acceleration and emission mechanisms in blazar

## 3.1 Acceleration mechanisms

One of the most intriguing problems in high energy astrophysics is the mechanisms by which high energy particles are accelerated to ultrarelativistic energies. A great variety of astrophysical phenomena are based on the presence of plasma or particles, accelerated up to relativistic velocities. The class of blazars gets into this context. One of the common feature of the particle acceleration is that the electron energy spectrum of many non-thermal sources have the form

$$dN(E) \propto E^{-x}\, dE \tag{3.1}$$

where the exponent $x$ lies in the range roughly 2.2–3. The question we ask at this point is how these particles are accelerated. The answer ranges in different fields of the physics. After some general principles of acceleration, we will discuss the mechanisms that are considered the most plausible to explain acceleration of plasma in the jets of blazars.

The acceleration mechanisms may be classified as dynamic, hydrodynamic and electromagnetic. In many cases, there is no firm distinction between them because, being charged, the particles are closely coupled to magnetic field lines. In some models, the acceleration is purely dynamical; for example when the acceleration takes place through the collision of particles with clouds. Hydrodynamic models can involve the acceleration of whole layers of plasma to high velocities. The electromagnetic processes include those in which particles are accelerated by electric fields, for example, in neutral sheets, in electromagnetic or plasma waves and in the magnetospheres of neutron stars.

The general expression for the acceleration of a charged particle in electric and magnetic fields is

$$\frac{d}{dt}(\gamma\, m\, \mathbf{v}) = \frac{e}{c}(\mathbf{E} + \mathbf{v} \times \mathbf{B}) \tag{3.2}$$

Also in order to explain the observed features of the blazar emission is necessary that radiating particles are accelerated to relativistic energies. An acceleration process was originally considered by Fermi in 1949, in which it was assumed that collisions with interstellar clouds would be the main source of energy for the particles. However, this mechanism is very inefficient and it cannot explain the 'universal' spectral index observed in different astrophysical environments. To solve these problems, new versions of the Fermi acceleration mechanism was proposed by several authors. In recent years, intense theoretical efforts have been spent to produce a framework for the particle acceleration. We look at these mechanisms in some detail in the next sections, based mainly on the results reported in Longair (2000).

### 3.1.1 First and second order Fermi acceleration

The Fermi mechanism was first proposed by Fermi in 1949 as a stochastic means by which particles colliding with clouds in the interstellar medium could be accelerated to high energies. In Fermi's original picture, charged particles are reflected from 'magnetic mirrors' associated with irregularities in the Galactic magnetic fields. These magnetic irregularities are assumed to move randomly with typical velocity $V$ and the particles gain energy statistically in these reflections. If the particles only remain within the acceleration region for some characteristic time $\tau_{esc}$, a power law distribution of particle energies is found.

The collision between the particle and the 'mirror', or massive cloud, takes place such that the angle between the initial direction of the particle and the normal to the surface of the mirror is $\theta$. Let us work out the change of energy of the particle in a single collision. We suppose the cloud is infinitely massive, so that its velocity is unchanged in the collision. The center of momentum frame is therefore that of the cloud moving at velocity $V$. The energy of the particle in this frame is

$$E' = \gamma_V (E + Vp\cos\theta) \tag{3.3}$$

where $\gamma_V = \left(1 - \frac{V^2}{c^2}\right)^{-1/2}$.
The $x$ component of the relativistic three-momentum in this frame is

$$p'_x = p' \cos\theta' = \gamma_V \left(p\, \cos\theta + \frac{VE}{c^2}\right) \tag{3.4}$$

In the collision, the particle's energy is conserved ($E'_{\rm before} = E'_{\rm after}$) but the momentum in x direction is reversed, $p'_x \rightarrow -p'_x$. Therefore, transforming back to the observe's frame, we find

$$E'' = \gamma_V (E' + V\, p'_x) \tag{3.5}$$

Substituting equations (3.3) and (3.4) into equation (3.5) and recalling that $p_x/E = v\,\cos\theta/c^2$, we find the change in energy of the particle

$$E'' = \gamma_V^2 E \left[1 + \frac{2Vv\cos\theta}{c^2} + \left(\frac{V}{c}\right)^2\right] \tag{3.6}$$

Expanding to second order in $V/c$, we find

$$E'' - E = \Delta E = \frac{2Vv\cos\theta}{c^2} + 2\left(\frac{V}{c}\right)^2 \tag{3.7}$$

Because of scattering by hydromagnetic waves or irregularities in the magnetic field, it is likely that the particle is randomly scattered in pitch angle between encounters with the clouds, and we can therefore work out the mean increase in energy by averaging over the angle $\theta$ in the expression (3.7). A crucial point is that there is a slightly greater probability of head-on collisions as opposed to the following collisions: v + Vcos$\theta$ versus v - Vcos$\theta$. For simplicity, let us consider the case of a relativistic particle with $v \simeq c$, in which case the probability of a collision at angle $\theta$ is proportional to $\gamma_V[1 + (V / c) \cos\theta]$. Recalling that the probability of the pitch angle lying in the angular range $\theta$ to $\theta + {\rm d}\theta$ is proportional to $\sin\theta\ {\rm d}\theta$, we find on averaging over all angles in the range 0 to $\pi$ that the first term in expression (3.7) in the limit $v \rightarrow c$ becomes

$$\left\langle \frac{2V\cos\theta}{c} \right\rangle = \left(\frac{2V}{c}\right) \frac{\int_{-1}^{1} x[1 + (V/c)x]dx}{\int_{-1}^{1} x[1 + (V/c)x]dx} = \frac{2}{3}\left(\frac{V}{c}\right)^2 \tag{3.8}$$

where $x = \cos\theta$. Thus, in the relativistic limit, the average energy gain per collision is

$$\left\langle \frac{\Delta E}{E} \right\rangle = \frac{8}{3}\left(\frac{V}{c}\right)^2 \tag{3.9}$$

This is the famous result derived by Fermi that the average increase in energy is only *second order* in $V/c$. It is also immediately apparent that this results leads to an exponential increase in the energy of the particle since the same fractional increase occurs per collision.

If the mean free path between clouds along a field line is $L$, the time between collisions is $2L/c$ (where the factor 2 is due to the average on the pitch angles).

Therefore, we find a typical rate of energy increase

$$\frac{dE}{dt} = \frac{4}{3}\left(\frac{V^2}{cL}\right)E = \alpha E \tag{3.10}$$

We search the solution of the diffusion-loss equation for $N(E)$ in equilibrium, assuming that the particle remains in the accelerating region for a characteristic time $\tau_{esc}$ (see e.g. Ginzburg and Syrovaitskij 1964)

$$\frac{dN}{dt} = D\,\nabla^2 N + \frac{\partial}{\partial E}[b(E)N(E)] - \frac{N}{\tau_{esc}} + Q(E) \tag{3.11}$$

We are interested in the steady-state solution and hence $dN/dt = 0$. We are not interested in diffusion, thus $D\,\nabla^2 N = 0$, and assuming that there are no sources, $Q(E) = 0$. The energy loss term is $b(E) = -\,dE/dt = -\alpha E$. Therefore, the equation (3.11) reduces to

$$-\frac{d}{dE}[\alpha E N(E)] - \frac{N(E)}{\tau_{esc}} = 0 \tag{3.12}$$

Differentiating and rearranging this equation, we find

$$\frac{dN(E)}{dE} = -\left(1 + \frac{1}{\alpha\tau_{esc}}\right)\frac{N(E)}{E} \tag{3.13}$$

from which we obtain

$$N(E) = constant \times E^{-\left(1+\frac{1}{\alpha\tau_{esc}}\right)} \tag{3.14}$$

We have succeded in deriving a power law energy spectrum.
In the Fermi's original paper, it was assumed that collisions with interstellar clouds would be the main source of energy for the particles. However, there are some important problems to take into account.

(i) The random velocities of interstellar clouds in the Galaxy are very small in comparison with the velocity of light, $V/c \leq 10^{-4}$. Furthermore, considering a mean-free path of cosmic rays in the interstellar medium of the order of 1 pc, the number of collisions would be roughly one per year, resulting in a very slow gain of energy by the particles. Therefore from the original Fermi mechanism no significant acceleration is gained.

(ii) We have not considered the effect of energy losses upon the acceleration process. In particular, ionisation losses hamper the acceleration of particles from low energies. If the acceleration mechanism is to be effective, the particles must either be injected into the acceleration region with energies greater than the corresponding to the maximum energy loss rate, or else the initial acceleration process must be sufficiently rapid to overcome the energy losses.

(iii) This theory does not explain why the slope of the energy spectrum should be roughly 2.5 in different astrophysical contests. In fact the exponent of the power law depends by the product of $\alpha$ and $t_{esc}$, two parameters largely indipendent.

This simplified version of the second order Fermi acceleration disguises a key aspect of the acceleration process. Inspection of the expression (3.7) shows that, to first order in $V/c$, the particles does not gain energy. The particle's energy is changing all the time stochastically and if we were to inject particles with a single energy, the energy distribution would be broadened by random collisions with interstellar clouds. In fact, the typical root mean square change of energy of the particle on average is $O(V/c)$, whereas the systematic energy is only $O(V/c)^2$. In a proper calculation, we have to take account of the statistical nature of the acceleration process as well as the average systematic increase in energy. The full treatment has to take account explicitely of the stochastic nature of the acceleration process and the spreading of the energy spectrum by scattering. This is accomplished by developing a Fokker-Planck equation for the diffusion of the particles in momentum space, similar to

$$\frac{dN}{dt} = D\,\nabla^2 N + \frac{\partial}{\partial E}[b(E)N(E)] - \frac{N}{\tau_{esc}} + Q(E) + \frac{1}{2}\frac{\partial^2}{\partial E^2}[d(E)\,N(E)] \qquad (3.15)$$

where $d(E)$ is the mean square change in energy per unit time

$$d(E) = \frac{d}{dt}\left\langle (\Delta E)^2 \right\rangle \qquad (3.16)$$

From the expression (3.7) we can find an expression for the average value of $(\Delta E)^2$. To second order in $V/c$, the only term which survives, averaging also over angles, is

$$\left\langle (\Delta E)^2 \right\rangle = \frac{4}{3} E^2 \left(\frac{V}{c}\right)^2 \qquad (3.17)$$

Thus, there is a very close relation between the mean square energy change and the average increase in energy per collision. Comparing the last equation with the equation (3.9) we see that d(E) = –E b(E)/2 = $\alpha$ E$^2$/2. We seek again steady-state solution of the equation (3.15), but including the stochastic term, that is

$$\frac{\partial}{\partial E}[b(E)N(E)] - \frac{N}{\tau_{esc}} + \frac{1}{2}\frac{\partial^2}{\partial E^2}[d(E)\,N(E)] = 0 \qquad (3.18)$$

The solution for a value x of the power law form $N \propto E^{-x}$ is

$$x = \frac{3}{2}\left(1 + \frac{16}{9\,\alpha\,\tau_{esc}}\right)^{1/2} - \frac{1}{2} \qquad (3.19)$$

which is exactly the result derived by Blandford & Eichler (1987) if we adopt the expression $\alpha = \frac{4}{3}\,(V^2/cL)$. The importance of including the diffusion term can be appreciated by comparing the expressions (3.19) and (3.14), showing that, in these second order acceleration mechanisms, the value of $\alpha$ to be used in the formulae for $b(E)$ and $d(E)$ is model dependent. In the modern version of the Fermi second order acceleration, the particles interact with various types of plasma wave and gain energy by being scattered stochastically by these waves.

We can rewrite the Fermi mechanism in a rather simpler fashion if we let $E = \beta E_0$ be the average energy of the particle after one collision and $P$ be the probability that the particle remains within the accelerating region after one collision. Then, after $k$ collisions, there are $N = N_0 P^k$ particles with energies $E = E_0 \beta^k$. If we eliminate $k$ between these two quantities,

$$\frac{\ln\,(N/N_0)}{\ln\,(E/E_0)} = \frac{\ln\,P}{\ln\,\beta} \tag{3.20}$$

and hence

$$\frac{N}{N_0} = \left(\frac{E}{E_0}\right)^{\ln\,P/\ln\,\beta} \tag{3.21}$$

In fact, this value of $N$ is $N(\geq E)$ since this number reaches energy $E$ and some fraction of them go on to higher energies. Therefore

$$N(E)dE = \text{constant} \times E^{-1+(\ln\,P/\ln\,\beta)}dE \tag{3.22}$$

and also in this formulation we have again recovered a power law.

In the original version of the Fermi mechanism (see (3.9)) $\alpha$ is proportional to $(V/c)^2$, because of the decelerating effect of the following collisions. The original version of Fermi's theory is therefore known as *second order* Fermi acceleration and clearly is a very slow process. We would do much better if there were only head-on collisions. The equation (3.7) shows that, in this case, the energy increase is $\Delta E/E \propto 2V/c$, that is first order in $V/c$ and therefore called *first order* Fermi acceleration.

A very attractive version of first order Fermi acceleration in the presence of strong shock waves was discovered indipendently by a number of authors in the late 1970s (Axford, Leer & Skadron 1977; Krimsky 1977; Bell 1978; Blandford and Ostriker 1978). There are two different ways of tackling the problem, one starting from the diffusion equation for the evolution of the momentum distribution of high energy particles in the vicinity of a strong shock (e.g. Blandford and Ostriker 1978) and a more physical approach, in which the behaviour of individual particles is followed (e.g. Bell 1978).

We adopt Bell's version of this theory. To illustrate the basic physics of the accelerated process, let us consider the case of a strong shock that propagates through the interstellar medium. A flux of high energy particles is assumed to be present both in front and behind the shock front. The particles are considered to be of very high energy, and so the velocity of the shock is very much less than the velocities of the high energy particles. The key point of the acceleration mechanism is that the high energy particles hardly notice the shock at all, since its thickness will normally be very much smaller than the gyroradius of a high energy particle. Because of turbulence behind the shock front and irregularities ahead of it, when the particles pass through the shock in either direction, they are scattered so that their velocity distribution rapidly becomes isotropic on either side of the shock front. The key point is that the distributions are isotropic with respect to the frames of reference in which the fluid is at rest on either side of the shock.
In the case of a strong shock, the shock wave travels at a highly supersonic velocity $U >> c_s$, where $c_s$ is the sound speed in the ambient medium. It is convenient to transform into the frame of reference in which the shock front is at rest, and then the upstream gas flows into the shock front at velocity $v_1 = U$ and leaves the shock with a downstream velocity $v_2$. The equation of continuity requires mass to be conserved through the shock, then

$$\rho_1 v_1 = \rho_2 v_2 \tag{3.23}$$

In the case of strong shock, $\rho_2 / \rho_1 = (\gamma + 1) / (\gamma - 1)$, where $\gamma$ is the ratio of specific heats of the gas. Taking $\gamma = \frac{5}{3}$ for a monoatomic or fully ionised gas, we find $\rho_2 / \rho_1 = 4$, and therefore $v_2 = \frac{1}{4} v_1$.
Let us consider the high energy particles ahead of the shock. Scattering ensures that the particle distribution is isotropic in the frame of the reference in which the gas is at rest. Considering the upstream particles first, the shock advances through the medium at velocity $U$, but the gas behind the shock travels at a velocity $\frac{3}{4} U$ relative to the upstream gas. When a high energy particle crosses the shock front, it obtains a small increase in energy of the order $\Delta E/E \sim U/c$. The particles are then scattered by the turbulence behind the shock front so that their velocity distributions become isotropic with respect to that flow.

Considering instead the case of the particle diffusing from behind the shock to the upstream region in front of the shock, the velocity distribution of the particles is isotropic behind the shock and when they cross the shock front, they encounter gas moving towards the shock front, again with the same velocity, $\frac{3}{4} U$. Therefore, the particle undergoes exactly the same process of receiving a small increase in energy $\Delta E$ on crossing the shock from downstream to upstream as from upstream to downstream. Every time the particle crosses the

shock front it receives an increase of energy and the increment in energy is the same going in both directions. Thus, unlike the standard Fermi mechanism in which there are both head-on and following collisions, in the case of the shock front the collisions are always head-on and energy is transferred to the particles. This mechanism has a completely symmetry between the passage of the particles from upstream to downstream and viceversa through the shock wave.

Now we evaluate, by simple arguments due originally to Bell (1978), the average increase in energy of the particle on crossing from upstream to downstream sides of the shock. The gas on the downstream side approaches the particle at a velocity $V = \frac{3}{4}\, U$ and performing a Lorentz transformation, the particle's energy when it passes into the downstream region is

$$E' = \gamma_V \,(E + p_x\, V) \tag{3.24}$$

where we take the $x$ coordinate to be perpendicular to the shock. We assume that the shock is non-relativistic, $V << \mathrm{c}$, $\gamma_V = 1$, but the particles are relativistic, thus $E = pc$, $p_x = (E/c)\cos\theta$. Therefore,

$$\Delta E = p\, V\, \cos\theta \;\; ; \;\; \frac{\Delta E}{E} = \frac{V}{c}\cos\theta \tag{3.25}$$

The number of particles within the angles $\theta$ to $\theta + \mathrm{d}\theta$ is proportional to $\sin\theta$ $\mathrm{d}\theta$, but the rate at which they approach the shock front is proportional to the $x$ component of their velocities, $c\,\cos\theta$. Therefore the probability of the particle crossing the shock is proportional to $\sin\theta\,\cos\theta\,\mathrm{d}\theta$. Normalising so that the integral of the probability distribution over all the particles approaching the shock is equal to unity, we find

$$p\,(\theta) = 2\sin\theta\cos\theta\, d\theta \tag{3.26}$$

Therefore, the average gain in energy on crossing the shock is

$$\left\langle \frac{\Delta E}{E} \right\rangle = \frac{V}{c}\int_0^{\pi/2} 2\cos^2\theta\sin\theta\, d\theta = \frac{2}{3}\frac{V}{c} \tag{3.27}$$

The particle's velocity vector is randomised without any energy loss by scattering in the downstream region and it then recrosses the shock, when it gains another fractional increase in energy $\frac{2}{3}\,(V/c)$, so that in making one round trip across the shock and back again, the fractional energy increase is, on average,

$$\left\langle \frac{\Delta E}{E} \right\rangle = \frac{4}{3}\frac{V}{c} \tag{3.28}$$

Consequently, in one round trip

$$\beta = \frac{E}{E_0} = 1 + \frac{4V}{3c} \tag{3.29}$$

Bell (1978) use a clever argument to obtain the escape probability $P$. According to classical kinetic theory, the number of particles crossing the shock is $\frac{1}{4}\,Nc$, where $N$ is the number density of particles. This is the average number of particles crossing the shock in either direction, since the particles scarsely notice the shock. Downstream the particles are swept away or 'advected' from the shock because the particles are isotropic in that frame. The particles are removed from the region of the shock at a rate $NV = \frac{1}{4}NU$. Thus, the fraction of the particles lost per unit time is $\frac{1}{4}\,NU\,/\,\frac{1}{4}\,Nc = U/c$. Since we assume that the shock is non-relativistic, it can be seen that only very small fraction of the particles is lost per cycle. Thus, $P = 1 - (U/c)$. This solves the problem since we need $\ln\beta$ and $\ln\,P$ to insert into expression (3.17). Therefore, since

$$\ln\,P = \ln\left(1 - \frac{U}{c}\right) = -\frac{U}{c} \tag{3.30}$$

$$\ln\,\beta = \ln\left(1 + \frac{4V}{3c}\right) = \frac{4V}{3c} = \frac{U}{c} \tag{3.31}$$

we find

$$\frac{\ln\,P}{\ln\,\beta} = -1 \tag{3.32}$$

and, hence, the differential energy spectrum of the high energy particles is

$$N(E)dE \propto E^{-2}dE \tag{3.33}$$

This is the result we have been seeking. It has been obtained a value of 2 rather than 2.5 for the exponent of the differential energy spectrum, but the reason that this mechanism has excited so much interest is that, for the first time, there are excellent physical reasons why power law energy spectra with a unique spectral index should occur in diverse astrophysical environments. In the simplest version of the theory, the only requirements are the presence of strong shock waves and that the velocity vectors of the high energy particles be randomised on either side of the shock. It is entirely plausibile that there are strong shocks in most sources of high energy particles, such as Active Galactic Nuclei, supernova remnants and the diffuse components of extended radio sources.

One important feature of the model is that the particles must be scattered in both the upstream and downstream regions. Behind the shock, it is plausibile that there are turbulent motions which can scatter the particles. In Bell's original proposal, the particles which recross the shock from downstream to upstream

result in bulk streaming of the relativistic particles through the unperturbed interstellar medium and consequently argued that the particles are scattered by the generation of Alfven and hydromagnetic waves. It is therefore expected that the high energy particles will be confined within some characteristic distance in front of the shock. The number of high energy particles is expected to decrease exponentially ahead of the shock wave.

The subject of particle acceleration in strong shocks has developed dramatically since the results derived by Fermi. Detailed reviews have been presented by Drury (1983), Blandford & Eichler (1987) and Völk (1987). In the diffusive shock acceleration scenario proposed by Blandford & Eichler (1987) a particle that crosses the shock front gains energy via a first order process. To cross the shock many times the particles has to be diffused from downstream to upstream the shock. The diffusion may be the result of the interaction of the particles with the disturbances in the magnetic field of the plasma. The probability of the particle to undergo an accelerative step is set by a competition between acceleration and escape. Also in this scenario a power law energy spectrum is obtained.

However, this result is not universal. It has been successfull applied to the observed cosmic ray energy spectra, but several astrophysical scenarios existing where acceleration processes can results in an electron distribution deviating slightly from a power law. For example, Massaro et al. (2004) have shown that if the acceleration probability is energy dependent the power law turn into a curved distribution with a log-parabolic shape. Moreover, it has to be taken into account the role of stochastic acceleration that results from second order mechanism. Historically, the importance of the second order process has been neglected to explain the acceleration in astrophysical jets due to the quadratic dependence in the relative energy gain respect to the velocities ratio, but Schlickeiser et al. (1993) realized that second order process is not negligible behind the shock and Jones (1994) shown that for non-relativistic shocks first or second order process are not very different in terms of efficiency and in a blazar jet, the resulting particle distribution may show signature of both the presences. In particular, stochastic acceleration may induce an intrinsic curvature in the particle energy distribution as shown by Kardashev (1962), who found an analytic solution for stochastic acceleration resulting in curved electron spectra with a log-parabolic shape.

## 3.2 Radiation mechanisms

In this Section a short review of the most important emission processes acting in the blazar jet is given: effects from relativistic beaming, synchrotron and inverse Compton emission are discussed. This brief summary is based on Rybicky &

Lightman (1979), Blumenthal & Gould (1970), Pacholczyk (1970), and Longair (2000).

### 3.2.1 Relativistic beaming and transformation rules

Transformations rules between reference systems where the emitting source has a relativistic motion with respect to the observer result from Lorentz equations and relativistic aberration are given. Be R the frame where the emitting source is at rest and L is the frame where the source has a velocity $\beta = v/c$ with corresponding bulk Lorentz factor $\Gamma = (1 - \beta^2)^{-1/2}$. Quantities in the R-frame is primed.

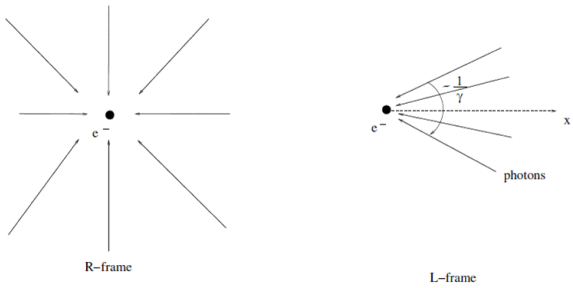


**Figure 3.1:** An isotropic emission in the R-frame is beamed in the L-frame.

Assume that a photon is emitted in R-frame at an angle $\theta$ to the velocity. The direction of light velocity will transform according to:

$$\tan\,\theta = \frac{\sin\,\theta'}{\Gamma(\cos\,\theta' + \beta)} \tag{3.34}$$

$$\cos\,\theta = \frac{\cos\,\theta' + \beta}{1 + \beta\cos\,\theta'} \tag{3.35}$$

For an isotropic emission in the R-frame the transformation of the angle $\theta' = \pi/2$ implies that $\tan\,\theta = 1/(\Gamma\,\beta)$ and $\sin\theta = 1/\gamma$. This means that in the L-frame the observer sees half of the emitted photons concentrated in a cone of half angle $\theta \simeq 1/\Gamma$ (see Fig 3.1).
The time interval will transform according to:

$$dt' = dt/\Gamma \tag{3.36}$$

The difference in time of photon arrival ($\Delta t_a$) in the L-frame is related to that of photon emission in the R-frame ($\Delta t'_e$) by the Doppler formula:

$$\Delta t_a = \Delta t'_e \Gamma(1 - \beta\mu) = \Delta t'_e/\delta \tag{3.37}$$

where $\mu$ is the cosine of the angle between the direction of the bulk motion of the R-frame and the direction to the observer line sight, and $\delta$ is the so-called *beaming factor* defined as

$$\delta = \Gamma(1 + \beta\mu') = \frac{1}{\Gamma(1 - \beta\mu)} \tag{3.38}$$

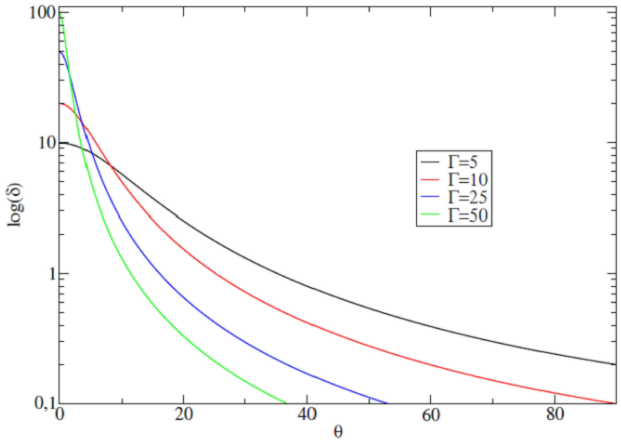


**Figure 3.2:** The beaming factor as a function of the viewing angle for different values of $\Gamma$.

The Figure 3.2 shows the variation of the beaming factor as a function of the angle $\theta$ and the different Lorentz factor values.

The solid angle $d\Omega$' subtended in the direction making an angle $\cos^{-1}\mu$ with the R-frame velocity vector, trasforms according to the relation:

$$d\Omega = \Gamma^2(1 - \beta\mu)^2 d\Omega' = (2\pi/\delta^2)d\mu' \tag{3.39}$$

For the frequency $\nu$, being the inverse of the time one has:

$$\nu = \frac{\nu'}{\Gamma(1 - \beta\mu)} = \nu'\delta \tag{3.40}$$

Since the quantity $I_\nu/\delta^3$ is Lorentz invariant, the transformation of specific intensity $I_\nu$ will be

$$I_\nu = \frac{I'_\nu}{\Gamma^3(1 - \beta\mu)^3} = I'_\nu\delta^3 \tag{3.41}$$

and similarly for the emission and absorption coefficient

$$j_\nu = j'_\nu \delta^2, \quad \alpha_\nu = \alpha'_\nu \delta^2 \tag{3.42}$$

The differential cross section will transform as:

$$\left(\frac{d\sigma}{d\Omega}\right)' = \left(\frac{d\sigma}{d\Omega}\right) \frac{(1-\beta\mu_{\rm f})^2}{1-\beta\mu_{\rm i}} \Gamma^2 \tag{3.43}$$

where the photon incident and scattered direction cosine in the L-frame are denoted by $\mu_{\rm f}$ and $\mu_{\rm i}$ respectively.

### 3.2.2 Synchrotron emission

The synchrotron radiation is the emission process of relativistic particles centripetally accelerated in a magnetic field. A brief summary of synchrotron emission process here is given. For a more detailed discussion we refer to Blumenthal & Gould (1970), Pacholczyk (1970), Rybicki & Lightman (1970), Longair (2000) and the reference therein.

**Synchrotron emission from a single electron**

The motion of an electron of mass $m$ and charge $e$ in an uniform magnetic field $B$ (Fig. 3.3), is described by the relativistic equations

$$\frac{d}{dt}(\gamma m v) = \frac{e}{c}\,\mathbf{v} \times \mathbf{B} \tag{3.44}$$

$$\frac{d}{dt}(\gamma m c^2) = e\,\mathbf{v} \times \mathbf{E} \tag{3.45}$$

The Eq. (3.45) implies that, for small radiated power, $\gamma$ can be considered as a constant. It follows

$$m\gamma \frac{d\mathbf{v}}{dt} = \frac{e}{c}\,\mathbf{v} \times \mathbf{B} \tag{3.46}$$

Separating the velocity components along the line of the magnetic field, $\mathbf{v}_\parallel = \beta_\parallel \mathrm{c}$, and in the plane orthogonal to the B direction $\mathbf{v}_\perp = \beta_\perp \mathrm{c}$, and indicating with $\alpha$ the pitch angle between the velocity direction and the magnetic field line, the Eq. (3.46) can be written as

$$\frac{dv_\parallel}{dt} = 0 \tag{3.47}$$

$$\frac{d\mathbf{v}_\perp}{dt} = \frac{e}{\gamma m c^2} \mathbf{v}_\perp \times \mathbf{B} \tag{3.48}$$

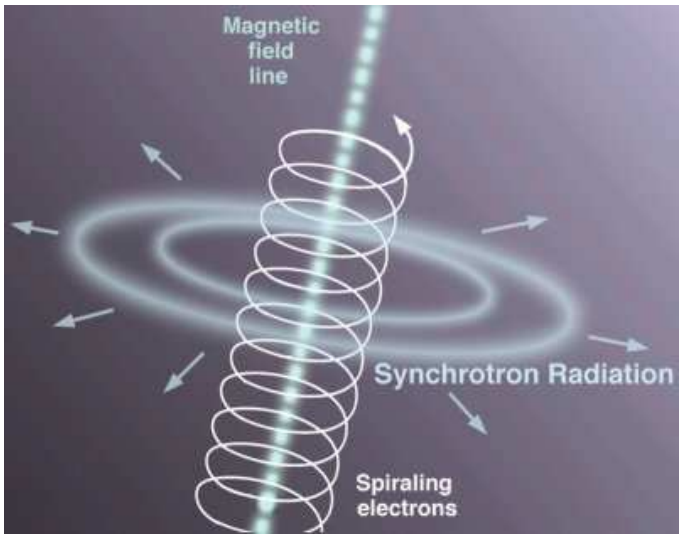


**Figure 3.3:** A schematic picture of the synchrotron emission.

It follows that $\mathbf{v}_{\parallel}$ is constant, and since also $\gamma$ is constant $\mathbf{v}_{\perp}$ is constant. The solution to this equation is an helical motion of the electron around the field line. The frequency of rotation is

$$\nu_B = \frac{eB}{2\pi\gamma mc} = \frac{\nu_L}{\gamma} \tag{3.49}$$

where $\nu_L = \frac{eB}{2\pi mc}$ is the Larmor frequency. The motion in the plane perpendicular to the magnetic field line is circular with the Larmor radius

$$r_L = \frac{mc^2}{eB}\gamma\beta \sin\alpha \tag{3.50}$$

The acceleration is perpendicular to the velocity and, from the Larmor formula, the total emitted power is

$$P_s = \frac{dE}{dt} = \frac{2}{3} r_e^2 \, c\beta^2\gamma^2 B^2 sin^2\alpha = 2\sigma_T \, c\beta^2\gamma^2 \frac{B^2}{8\pi} \sin^2\alpha \tag{3.51}$$

For an isotropic distribution of velocities it is necessary to average this value over all the pitch angles, obtaining

$$\langle P_s \rangle = \frac{4}{3}\sigma_T \, c\beta^2\gamma^2 u_B \tag{3.52}$$

where $u_B = \mathrm{B}^2/8\pi$ is the magnetic energy density and $\sigma_T$ is the Thomson cross section.

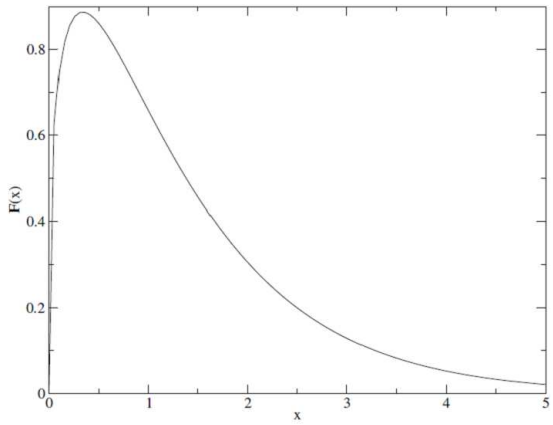


**Figure 3.4:** The function $F(x)$.

The synchrotron spectrum for the single ultrarelativistic ($\beta \sim 1$) electron is

$$\frac{dP}{dn}(\nu, \gamma) = \frac{\sqrt{3}e^3 B sin\alpha}{2m_e c^2} F(x) \tag{3.53}$$

where $e$ and $m_e$ are the charge and the rest mass of the electron respectively and $x = \nu/\nu_c$, with the critical frequency $\nu_c$ given by:

$$\nu_c = \frac{3\gamma^2 qB \sin\,\alpha}{4\pi m_e c} \tag{3.54}$$

The function F(x) is the synchrotron kernel, defined as:

$$F_x \equiv x \int_x^\infty K_{5/3}(x')dx' \tag{3.55}$$

where $K_{5/3}$ is the modified Bessel function of 5/3 order.

$$K_n(\eta) = \frac{\delta(n+\frac{1}{2})(2\eta)^n}{\sqrt{\pi}} \int_0^\infty \frac{\cos y}{(y^2+\eta^2)^{n+\frac{1}{2}}} dy \tag{3.56}$$

The function $F(x)$, plotted in Fig. 3.4, peaks at $x \simeq 0.29$ with the following asymptotic behaviour:

$$F(x) \simeq \frac{4\pi}{\sqrt{3}\Gamma(1/3)} \left(\frac{x}{2}\right)^{1/3}, \quad x << 1 \tag{3.57}$$

$$F(x) \simeq \frac{\pi}{2}^{\frac{1}{2}} e^{-x} x^{\frac{1}{2}}, \quad x >> 1 \tag{3.58}$$

Since $F(x)$ has the maximum at $x \simeq 0.29$, it follows that the peak frequency of synchrotron emission for an electron with a Lorent factor $\gamma$ in a magnetic field B is about at:

$$\nu_p \simeq 1.22 \times 10^6 B \gamma^2 \sin\alpha \,\mathrm{Hz} \tag{3.59}$$

Integrating the Eq. (3.53) over the frequencies the total emitted power for a single electron is

$$P_S = \int \frac{dP}{d\nu} d\nu = 2\sigma_T \, c\beta^2\gamma^2 u_B \tag{3.60}$$

The synchrotron emission cooling rate is

$$-\frac{dE}{dt} = \dot{\gamma} m_e c^2 = \frac{4}{3}\sigma_T \, c\gamma^2 u_B \tag{3.61}$$

**Synchrotron emission from an electron distribution**

We consider the case of the synchrotron emission from an electron population with a distribution N($\gamma$) representing the number density of electrons per unit of volume and energy. The value of $\gamma_{\min}$ and $\gamma_{\max}$ define the electrons energy range. Under the assumption that the electrons are uniformely distributed in the space and that the velocities are isotropically distributed the emission coefficient is given by:

$$j_\nu^S(\nu) = \frac{1}{4\pi} \int_{\gamma_{\min}}^{\gamma_{\max}} \frac{dP(\gamma)}{d\nu} N(\gamma) d\gamma \tag{3.62}$$

and substituing the expression for $\frac{dP(\gamma)}{d\nu}$ one obtains:

$$j_\nu^S(\nu) = \frac{\sqrt{3} e^3}{4\pi m_e c^2} B \sin\alpha \int_{\gamma_{min}}^{\gamma_{max}} F(x) N(\gamma) d\gamma \tag{3.63}$$

**Synchrotron Self Absorption**

Synchrotron emission is accompanied by absorption, in which a photon interacts with an electron in the magnetic field and it is absorbed, giving up its energy to the particle. Another process that can occur is the stimulated emission or negative absorption, in which a charge is induced to emit more strongly into a direction and at a frequency where photons are already present. These processes can be interrelated by means of the Einsteins coefficients, generalized to continuum states. Following Rybicki & Lightman (1979) one obtains:

$$\alpha_\nu(\nu) = -\frac{\sqrt{3}e^3 B \sin\alpha}{8\pi m_e^2 c^2 \nu^2} \int_{\gamma_{\min}}^{\gamma_{\max}} \gamma^2 \frac{\partial}{\partial\gamma}\left[\frac{N(\gamma)}{\gamma^2}\right] F(x) d\gamma \tag{3.64}$$

### 3.2.3 Inverse Compton emission

The Compton scattering is the interaction between photons and particles, in particular electrons in high energy astrophysical processes. For low photons energies ($h\nu << m_e c^2$) the scattering of radiation from free charges reduced to the classical case of the Thomson scattering, in which the incident photons are approximed as a continuous electromagnetic wave. In this case, the energy of scattered photons is conserved and the scattering is called elastic. Quantum effects of the interaction between electrons and photons appear in two ways: first, through the kinematics of the scattering mechanism and, second, through the change of the cross section. In this case the process is more generally indicated as Compton scattering. In the astrophysical framework, the so-called inverse Compton scattering occurs when in the scattering, scattered photons gain energy from electrons. In the following it is shown the case of the scattering of a single photon from a single electron. Finally the general case of interaction of photon distribution with an electron population.

**Scattering from a single electron in the electron rest frame**

Let $\epsilon_i'$ and $\epsilon_f'$ the energies of the photons in the electron rest frame before and after the collision, respectively. Both energies are expressed in units of $m_e c^2$ by

$$\epsilon' = \frac{h\nu'}{m_e c^2} \tag{3.65}$$

From Compton kinematics it follows:

$$\epsilon_f' = \frac{\epsilon_i'}{1 + \epsilon_i'(1 + cos(\lambda))} \tag{3.66}$$

where $\cos(\lambda)$ is the scattering angle. Two approximations depending on the value of $\epsilon'$ follow

- $\epsilon_i' << 1$ (Thomson limit), there is no change in the scattered photon energy ($\epsilon_f' \simeq \epsilon_i'$).
- $\epsilon_i' >> 1$, one can distinguish two range: for small angles $\theta$ (forward diffusion), $\epsilon_f' \simeq \epsilon_i'$, while for large angles the value of $\epsilon_f$ is the order of unity.

The differential scattering cross section is given by the Klein Nishina formula that for not polarized incident radiation is:

$$\frac{d\sigma_{KN}}{d\Omega} = \frac{3}{16\pi}\sigma_T \frac{1}{[1+\epsilon_i'(1-\lambda)]^2}\left[\frac{(\epsilon_i')^2}{(1-\lambda)} + \epsilon_i'(1-\lambda) + 1 + \lambda^2\right] \tag{3.67}$$

where $\sigma_T = \frac{8\pi}{3}(\frac{e^2}{m_e c^2})^2 = 6.65 \times 10^{-25}$ cm$^2$ is the Thomson cross section. For low values of photon energies Eq. (3.67) become the classical Thomson scattering:

$$\frac{d\sigma_{KN}}{d\Omega} = \frac{3}{16\pi}\sigma_T(1+\lambda^2) \tag{3.68}$$

When the Compton scattering is viewed in the frame where the electrons are relativistic ($\gamma >> 1$, L-frame) it is generally refered as 'inverse Compton scattering'. When the electrons are ultrarelativistic the rule for the angle transformations implies that $\mu_i' \rightarrow -1$, i.e. the collision in the electron rest frame (R-frame) are almost head-on. Under this approximation it follows that the energy of the scattered photon in the L-frame will be given by:

$$\epsilon_f = \gamma^2 \epsilon_i \frac{(1-\beta\cos\theta)\,[1+\beta\cos(\phi'+\theta')]}{1+\gamma\epsilon(1-\beta\cos\phi)(1-\cos\theta')} \tag{3.69}$$

In the ultrarelativistic limit the minimum and maximum value for the final photon energy are

$$\epsilon_i \leq \epsilon_f \leq \frac{4\epsilon_i\gamma^2}{1+4\gamma\epsilon_i} \tag{3.70}$$

It is possible to distinguish the maximum energy gained in the inverse Compton scattering in the Thomson and Klein Nishina regime, respectively:

$$\epsilon_{f,\max} \simeq 4\epsilon_i\gamma^2, \;\; 4\epsilon_i\gamma << 1 \tag{3.71}$$

$$\epsilon_{f,\max} \simeq \gamma, \;\; 4\epsilon_i\gamma >> 1 \tag{3.72}$$

Finally, the differential cross section for the Compton scattering for unpolarized incident radiation is the Klein-Nishina formula:

$$\frac{d\sigma_{KN}}{d\Omega} = \frac{r_e^2}{2}\left[\frac{\epsilon_f'^{\,2}}{\epsilon_i'} + \frac{\epsilon_f'^{\,2}}{\epsilon_i'} + \cos^2(\lambda)\right] \tag{3.73}$$

**Inverse Compton spectrum**

To obtain the spectrum emitted by an arbitrary electron distribution, N($\gamma$), upscattering an arbitrary photon distribution, $j_\nu(\nu_i)$, the derivation given by Blumenthal & Gould (1970) is followed. This derivation is accurate for highly energetic electrons ($\gamma >> 1$), and for isotropic electrons and photons distributions. The emission coefficient is given by:

$$\int d\gamma\, N(\gamma) f(\epsilon_i, \epsilon_f, \gamma) \tag{3.74}$$

where f($\epsilon_i, \epsilon_f, \gamma$) is the Compton kernel of Jones (1968) given by

$$f(\epsilon_i, \epsilon_f, \gamma) = \frac{K}{\nu_i \gamma^2}[2q\ \ln\ q + (1+2q)(1-q) + \frac{(4\epsilon_i \gamma q)^2}{2(1+4\epsilon_i \gamma q)}(1-q)] \tag{3.75}$$

where

$$K = \frac{h\sigma_T 3c}{16\pi} \tag{3.76}$$

$$q = \frac{\epsilon_f}{4\epsilon_i \gamma(\gamma - \epsilon_i)} \tag{3.77}$$

For a given $\epsilon_i$ the kinematic constraint of Eq.(3.70) gives the integration range for the Eq. (3.74).

**Cooling rates**

In the case of Thomson scattering limit, the energy of the scattered photon in the L-frame after electron collision is much larger than that before. Then it is possible to rewrite the electron energy loss rate:

$$-\frac{dE_e}{dt} = \frac{d\epsilon_f^L}{dt} \tag{3.78}$$

both sides of the equation are Lorentz invariant and for isotropic photon distribution from

$$-\frac{dE_e}{dt} = c\,\sigma_T \gamma^2 \int < (1 - \beta\cos\theta) > \epsilon_i\, n_{\nu_i}(\nu_i) d\nu_i U_{ph} = c\,\sigma_T \gamma^2 (1 + \frac{1}{3}\beta^2) U_{ph} \tag{3.79}$$

where cos $\theta$ is the cosine of the angle between the electron velocity and the incident photon direction in the L-frame and $U_{ph}$ is the total photon energy density:

$$U_{ph} = m_e c^2 \int \nu_i \, n_{\nu_i}(\nu_i) \, d\nu_i \tag{3.80}$$

The net energy loss rate is

$$-\frac{dE_e}{dt} \, |_{IC} = \dot{\gamma}_{IC} \, m_e c^2 = \frac{4\sigma_T \gamma^2 U_{ph}}{3} \tag{3.81}$$

Comparing Eq. (3.81) and Eq. (3.61) the relation between synchrotron and inverse Compton loss rate in Thomson regime immediately follows:

$$\frac{\dot{\gamma}_{IC}}{\dot{\gamma}_{synch}} = \frac{U_{ph}}{U_B} \tag{3.82}$$

In the general case, the inverse Compton cooling rate is given by:

$$\dot{\gamma}_{IC} = \int \nu_f \, d\nu_f \int d\nu_i \, n_{\nu_i} f(\nu_i, \nu_f, \gamma) \tag{3.83}$$

Due to Klein Nishina suppression in the cross section generally results that the ratio of Eq. (3.82) in will be lower in the Klein Nishina regime respect to the Thomson one. This means that when IC emission happens for $\epsilon_i \gamma$ increasing, the ratio of Compton losses respect to synchrotron losses decreases.

## 3.3 Emission models

As demonstrated by the high degree of polarization the first spectral component of blazars is synchrotron emission from a population of relativistic electrons in the jet. The origin of the high energy component is more debated. In general the model for the production of high energy radiation in blazars can be divided in leptonic and hadronic models.

At present, the measured SEDs of blazars can be successfully explained in first approximation by the leptonic origin scenario. Instead, no observational result has confirmed the hadronic origin scenario yet. In this Section the two emission origin scenarios are briefly described.

### 3.3.1 Leptonic origin scenarios

Leptonic models consider the inverse Compton scattering of soft photons by the same electrons responsible for the synchrotron emission. Different sources of soft photons can be considered and depending on the population of soft photons dominating the IC process two classes of models are generally discussed: the synchrotron self Compton (SSC) and the external Compton (EC) models.

In the synchrotron self Compton model (SSC; e.g. Marscher & Gear 1985; Maraschi et al. 1992) it is assumed that target photons are dominated by those produced through synchrotron by the same relativistic electrons. Synchrotron and IC emissions are strongly linked; this gives the possibility to find robust constraints on the basic physical quantities of the jet (e.g. Tavecchio, Maraschi & Ghisellini 1998).

The simplest homogeneous SSC model assumes the blazar emissions to be produced in a blob of radius $R$, containing relativistic electrons in a combination of tangled and uniform magnetic field. The emitters move toward the observer with bulk Lorentz factor $\Gamma$. We assume the emitters to emerge from the injection/acceleration phase with a jet-frame distribution of the random energies $\gamma mc^2$ in the form of a standard broken power-law

$$n_e(\gamma) = \frac{K\,\gamma_b^{-1}}{(\gamma/\gamma_b)^{\zeta_1} + (\gamma/\gamma_b)^{\zeta_2}} \tag{3.84}$$

where $\zeta_1$ and $\zeta_2$ are the spectral indices for $\gamma < \gamma_b$ and $\gamma > \gamma_b$, respectively, where $\gamma_b$ is the Lorentz factor at the break. These electrons emit a primary synchrotron spectrum; a second contribution is then produced by IC as the primary synchrotron photons scatter off the same electron population. The SED behaves as $\epsilon F(\epsilon) \propto \epsilon^{1-\alpha}$, where $\epsilon$ is the energy of the received photons, and $\alpha = (\zeta - 1)/2$. For electrons in a magnetic field $B$, the synchrotron SED peaks around

$$\epsilon_s = h\,\frac{3.7 \times 10^6 B\,\gamma_b^2\,\delta}{1+z} \tag{3.85}$$

where $h$ is Planck's constant, $z$ is the redshift of the source, and $\delta = [\Gamma(1 - \beta\cos\theta)]^{-1}$ is the bulk Doppler factor due to the flow of emitters toward the observer at an angle $\theta$ relative to the line of sight; the SED at the synchrotron peak is

$$\epsilon_s\,F(\epsilon_s) \propto \delta^4 R^3 B^2 K\,\gamma_b^2 \tag{3.86}$$

As to the IC component, its SED contribution peaks at

$$\epsilon_c = \frac{4\gamma_b^2 \epsilon_s}{3} \tag{3.87}$$

with a peak value of

$$\epsilon_c\,F(\epsilon_c) \propto \delta^4 R^4 B^2 K^2 \gamma_b^4 \tag{3.88}$$

if the scattering takes place in the Thomson regime with the density of target photons scaling as $n_{ph} \propto F_s R/c$. The relativistic motion toward the observer amplifies the emitted power by the factor $\delta^4$, and allows it to vary on a timescale

$$t_{var} \gtrsim \frac{t_{cr}(1+z)}{\delta} \tag{3.89}$$

close to or shorter than the crossing-time $t_{cr} = R/c$.
Due to the synchrotron and IC losses the electrons cool with timescale

$$\tau_{cool}(\gamma) = \frac{3mc}{4\beta^2\sigma_T\gamma\,(U_B + U_r)}$$

where $\sigma_T$ is the Thomson cross section, $U_B = B^2/8\pi$ and $U_r$ is the energy density of radiation before scattering. This sets a typical cooling break at $\gamma_{cool} = 3mc^2/4\sigma_T\,R\beta^2(U_B + U_r)$ beyond which the electrons cool rapidly.

For $\gamma_b > 10^4$ the scattering approaches the Klein-Nishina (KN) regime with a blob-frame photon energy $> m_ec^2/\gamma_b$. In the extreme KN regime the IC SED peaks at $\epsilon_c \sim \gamma_b m_e c^2\delta/(1+z)$; the dependence on $B$ and $\gamma_b$ progressively weakens as the two latter parameters grow. In the simplest SSC models there are 7 free parameters: the size of the emitting region, the density of relativistic particles, the Doppler factor of the blob, the magnetic field strength in the blob, the spectral index of the injected electron spectrum, and the lowest and highest energy of the injected electrons. Theoretically, these 7 parameters can be determined by means of the knowledge of 7 observational parameters: the synchrotron and IC peak frequencies and luminosities, the minimum variability timescales, and the electron distribution spectral indexes.

In the external Compton it is assumed that soft photons coming from the central region of the AGN, produced by the accretion disk around the central BH or reprocessed by the gas in the BLR, dominate over the synchrotron photons. The first version of this model proposed by Dermer & Schlickeiser (1993) considered the direct UV emission from the accretion disk as the principal source of soft photons. However, as pointed out by Sikora, Begelman & Rees (1994), the debeaming suffered by the radiation directly coming from the disk in the reference frame of the jet causes a strong depression of this contribution. On the other hand, the primary disk radiation reflected or reprocessed by the gas of the BLR and beamed in the jet frame can provide an important contribution to the emission: this radiation can be considered isotropic in the BLR rest frame and is strongly amplified in the rest frame of the emitting source. Blazejowski et al. (2000) pointed out that IC scattering of the thermal near-IR radiation emitted by the dust of the torus could provide the dominant contribution to the high energy emission, especially in the energy band 10 keV – 100 MeV. In the case of EC, the SED now peaks at energies

$$\epsilon_c = \frac{4\gamma_b^2\epsilon'_{ext}\,\delta}{3(1+z)} \tag{3.90}$$

and the corresponding SED value is

$$\epsilon_c\,F(\epsilon_c) \propto \delta^4 R^3 K\,\gamma_b^2 N'_{ext}\epsilon'_{ext} \tag{3.91}$$

In this EC process two new ingredients enter: $\epsilon'_{ext}$ and $N'_{ext}$, the energy and the density at peak of the external photons as seen by the moving blob, respectively. This has two main consequences:
**i**) The model contains two further degrees of freedom and the parameter evaluation may be degenerate.
**ii**) These news quantities are related to $N_{ext}$ and $\epsilon_{ext}$ in the observer frame by means of the bulk Lorentz factor $\Gamma$ in a manner that depends on the geometry of the system (Dermer & Schlickeiser 2002), causing an additional dependence on $\Gamma$ in the EC spectra. Dermer & Schlickeiser (1993) discuss SED dependences on $\Gamma$ varying from $\propto \Gamma^3$ to $\propto \Gamma^6$, for photons entering into the blob from behind or head-on, respectively.

Another possibility, alternative to SSC and EC models, is the so-called 'Mirror model' (Ghisellini & Madau 1996). The beamed synchrotron emission from the jet can be reflected by the BLR and go back into the jet. The double change of frame (source $\rightarrow$ lab frame $\rightarrow$ source) translates in a great amplification of the energy density of the soft radiation. However, when the constraints posed by the travel time of the radiation are taken into account, the relative contribution of this mechanism to the total emission is severely suppressed.

### 3.3.2 Hadronic origin scenarios

The hadronic models assume that a high energy protonic component contributes to the high-energy bump, while the low-energy bump is explained by synchrotron radiation of co-accelerated electrons. The energy of relativistic protons can be converted into high energy radiation via the following processes: (1) direct synchrotron radiation of protons, (2) photomeson production ($p + \gamma \rightarrow p + k\pi$), and (3) nuclear collisions ($p + p \rightarrow \pi$ + X). The first two processes are known to be very inefficient, and they can become important in AGN jets only for proton energies $\geq 10^8 - 10^{10}$ GeV. Only for such high energies the time scales of the proton energy losses can become comparable to or shorter than the propagation time scale of the AGN jets. Energy losses of such energetic protons are dominated by photomeson production, and this process was used for explaining $\gamma$-ray production in blazars by the so-called proton-induced cascade model (e.g. Mannheim 1993).

In that model, the radiation target of photomeson production is dominated by near/mid-IR radiation. In blazars, such radiation is provided by hot dust at distances of $\sim 1 - 10$ pc from the central engine and/or by the synchrotron radiation due to relativistic electrons in the jet. The main outputs of the photomeson processes are pions. The pions take about 1/3 of the energy of the protons and convert it in photons, neutrinos, and through muons, in electrons and positrons. The photons injected by neutral pions are immediately absorbed by soft photons in

the pair production process. Most of this radiation is so energetic that it produces two more generations of photons and pairs. The final output of the sycnhrotron-supported pair cascade is the high energy component, enclosed within or cutoff at energies above which photons are absorbed by a $\gamma\gamma$-pair production process. This maximum energy can be at $\sim$ 30 GeV in FSRQs, as determined by external UV radiation, and $\sim$ 1 TeV in BL Lac objects, as determined by infrared radiation of dust.

Much less extreme proton energies are required in models based on the assumption that the protron energy losses are dominated by collisions with the ambient gas. The final output of these collisions is the same as in the photomeson process, i.e. relativistic electrons/positrons, photons and neutrinos. The process can be efficient only if the column density of the target is $n_H \geq 10^{26}$ cm$^{-2}$. Bednarek (1993) proposed as target the funnels formed around the black hole by a geometrically thick disk, while Dar and Laor (1997) suggested interactions of jet with cloud and/or stellar winds. The disadvantage of this model is that relativistic protons, before colliding with the nuclei, may easily suffer deflections by magnetic fields; this general results in a lack of collimation of the radiation.

Another model belonging to this class has been proposed by Aharonian (2000). The author argues that in the physical condition of blazars direct synchrotron emission from high energy protons (with $E = 10^{19}$–$10^{20}$ eV) could be preferred to the proton intiated cascade process, provided that the magnetic field intensity is relatively large (30–100 G).

### 3.3.3 Hybrid scenarios

Even if the leptonic scenario is more likely for representing the SEDs of the blazars, it is not possible that in realistic case a mix of the model could be more satisfactory. In fact there are claims that if the blazar sequence is real, then it may be that a mix of SSC and EC models would explain it gradually increasing the importance of the external component along the progression HBL–LBL–FSRQ. A similar explanation for the sequence can also be given by a mixing of the different versions of the hadronic model. Hybrid leptonic-hadronic models might be more satisfactory to explain the observations of the correlated flares at X-ray and TeV energies that are followed by orphan TeV flares.

Clearly, more studies need to be done to properly understand the blazar emission mechanisms. One thing that stand out is the importance of multiwavelength campaign; in fact, broad band shape of the SED is needed to compare the models. Not only the broad-band SED is crucial, but also variability information is needed as well to understand how the high states of emission can occur and how they differ from the low/quiescent states. This may help in discriminating between models. However, to obtain simultaneous observation of blazars over

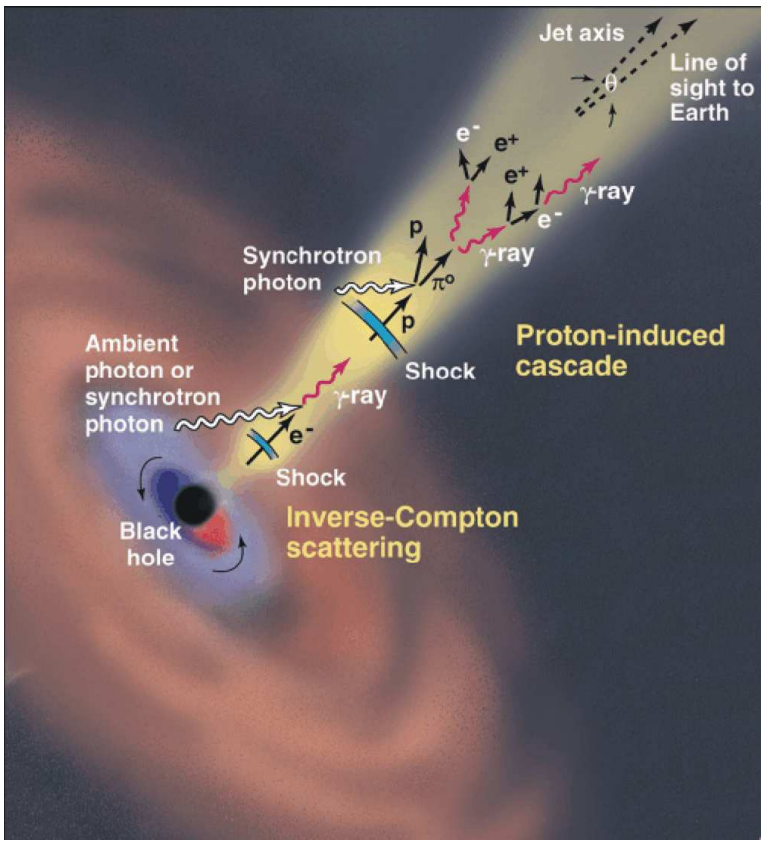


**Figure 3.5:** Different emission mechanisms in the jet of blazar.

the entire electromagnetic spectrum is not simple and it represents a considerable effort from the community. Figure 3.5 summarizes the different possible emission processes discussed in this Section.

Chapter 4

# $\gamma$-ray astrophysics and the multifrequency approach

## 4.1 The $\gamma$-ray astrophysics: from Explorer XI to AGILE and *Fermi*

Cosmic $\gamma$-rays represent the high-energy end of the electromagnetic spectrum and provide insight into some of the most dynamic processes in the Universe. Depending on their energy, $\gamma$-rays interact with matter in different predominant ways. Typically, below a few hundred keV the photoelectric effect is dominant. Above that and up to tens of MeV, the Compton scattering is the most important process. Beyond that energy, pair production dominates. Above $10^6$ eV the photons are $\gamma$-ray, even if the line between X-rays and $\gamma$-rays is not so sharp. Often X-rays are considered to be those photons produced by atomic or thermal processes, while $\gamma$-rays are those involving nuclear or nonthermal processes. The $\gamma$-rays are produced by energetic phenomena in different astrophysical settings including supernovae, pulsars, AGNs, as well as the interstellar and intergalactic medium. The Earth's atmosphere is opaque to all radiation above 10 eV, meaning that to observe $\gamma$-rays directly requires placement of a detector in the space. The Universe is largely transparent to these high-energy photons out to high redshift; thus $\gamma$-rays provide a valuable probe of the largest energy transfers throughout much of the Universe.

Since the discovery by Victor Hess in 1912 that the Earth is continuosly bombarded by a population of high-energy particles, much efforts has been expended in attempt to elucidate their origins. The potential for studying the sky with $\gamma$-rays was identified fifty years ago (Morrison 1958). A decade later the first definitive detections of $\gamma$-rays from space came from data recorded in 1965

by the Explorer XI telescope (Clark et al. 1968). However the telescope, with its small collection area and poor angular resolution, observed a flux of $\gamma$-rays from space but could not pinpoint its location. The third Orbiting Solar Observatory (OSO-3) contained a $\gamma$-ray detector similar to the one of Explorer XI, but slightly more sophisticated. After Explorer XI and OSO-3 some balloon-borne and satellite missions began to investigate the $\gamma$-ray sky.

Browning, Ramsada and Wright (1971) found pulsed $\gamma$-ray radiation from the Crab pulsar, using a $\gamma$-ray telescope on a balloon. Then a shift in $\gamma$-ray astronomy, from using balloon-based detectors to satellite-based ones, was instigated by the launch in 1972 of the NASA mission Small Astronomy Satellite (SAS-2, Fichtel et al. 1975), that showed that the $\gamma$-rays trace the structure of the Milky Way (Hartman et al. 1979) and discovered the second $\gamma$-ray pulsar, Vela (Thompson et al. 1975) and the first unidentified $\gamma$-ray source, $\gamma$195+5 (Kniffen et al. 1975), later identified like Geminga (Bignami et al. 1983).

The first catalogue of $\gamma$-ray source was produced by the European COS-B satellite (Bignami et al. 1975), most of which were not identified with objects known at other wavelengths (Hermsen et al. 1977; Swanesburg et al. 1981). COS-B found the first extragalactic source in $\gamma$-rays, 3C 273 (Swanenburg et al. 1978), and made the first $\gamma$-ray observations of molecular clouds as spatially-extended source (Caraveo et al. 1980). Previously the Vela satellite operated by the U.S. military to detect clandestine muclear test around the globe, discovered short-duration cosmic $\gamma$-ray bursts (Klebesadel et al. 1973). Instead, the Third High Energy Astrophysical Observatory (HEAO-3) carried a low-energy $\gamma$-ray telescope with high spectral resolution (Mahoney et al. 1980) that detected the 0.5 MeV positron-electron annihilation line from the Galactic center region (Riegler et al. 1981), confirming previous observation from balloon (Leventhal et al. 1978).

In the same period, a parallel branch of very high $\gamma$-ray astrophysics using ground based detectors was developing. At $\gamma$-ray energies above about $10^{11}$ eV, photons are too scarce to be detected by on-space satellite detectors. The Earth's atmosphere can be used as a detector for these very high energy (VHE) photons. When such photons collide with the material at the top of the atmosphere, they produce showers of particles moving faster than the local speed of light, thereby emitting Cherenkov radiation in the optical and ultraviolet. The flashes of light from these interactions can be detected with Atmospheric Cherenkov Telescopes on the ground, providing an indirect way to conduct $\gamma$-ray astrophysics. The first milestone in VHE astrophysics is the high-confidence detection of the Crab Nebula (but not pulsar) in 1989 with the Whipple Observatory (Weekes et al. 1989). Since then, the Imaging Atmospheric Cherenkov Technique (IACT) has proven itself as the most powerful technique for the detection of VHE $\gamma$-ray sources. The technique has developed significantly since the initial Crab Nebula detec-

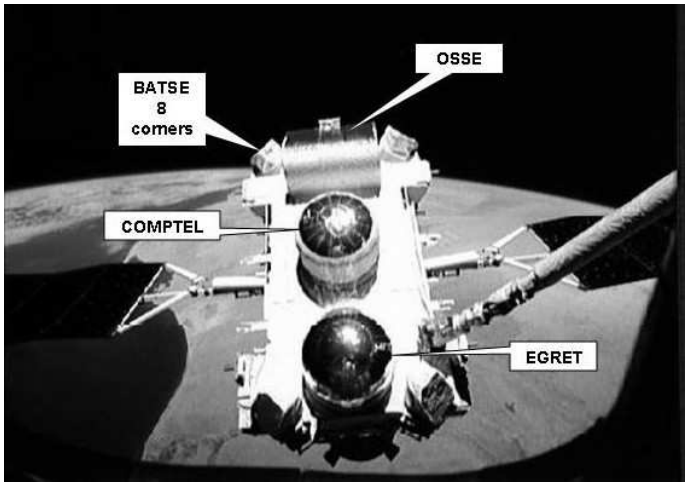


**Figure 4.1:** The Compton Gamma-Ray Observatories just before its release by the Shuttle in April 1991 [Thompson 2008].

tion and many observatories have been built to detect and monitor objects at these energies. Stereo observatories (two or more IAC telescopes observing contemporaneously as an array), such as VERITAS and H.E.S.S., have added power to the technique, increasing collection area as well as improving sensitivity and angular resolution. Larger aperture IAC telescopes, such as MAGIC, also have lower energy thresholds so that more of the object's spectrum may be studied. Recent summaries of results obtained at VHE are summarized in Chadwick et al. (2008) and Aharonian et al. (2008a).

A strong impulse in the excited field of the $\gamma$-ray astrophysics has received in the recent years, starting from the EGRET instrument on board the *Compton Gamma Ray Observatory* until the launch of the AGILE and *Fermi* satellites.

## 4.2 The *Compton Gamma Ray Observatory*

The success of SAS-2 and COS-B missions prompted efforts to commission a new experiment, with great collection area and flux sensitivity. The *Compton Gamma Ray Observatory (CGRO)*, shown in Figure 4.1, was the second of NASA's Great Observatories, following the Hubble Space Telescope. The original plane was to have four observatories operating simultaneously, but the launch of the *Chandra* X-ray Observatory (formely AXAF) and the *Spitzer* Space Telescope (formely SIRTF) are delayed. CGRO was launched on the Space Shuttle Atlantis on 5 April 1991 and operated successfully until it was de-orbited on 4 June 2000.

CGRO carried four $\gamma$-ray telescopes that covers six orders of magnitude in the electromagnetic spectrum from less than 15 keV to more than 30 GeV. The three lower-energy telescopes were:

- Burst and Transient Source Explorer (BATSE). BATSE consists of one module located on each corner of the spacecraft. Each BATSE unit included a large flat NaI(Yl) scintillator and a smaller thicker scintillator for spectral measurements, combining to cover an energy range from 15 keV to 1 MeV. BATSE discovered over 2700 Gamma-Ray Bursts (GRBs), showing that the distribution on the sky of GRBs is isotropic. A summary of the BATSE results is given by Fishman (1995).

- Oriented Scintillation Spectrometer Experiment (OSSE). OSSE used four large, collimated scintillator detectors to study the energy range 60 keV – 10 MeV. OSSE mapped the 0.5 MeV line from positron annihilation and provided detailed measurements of many hard X-ray/soft $\gamma$-ray sources. Kurfess (1996) summarized the most important results from OSSE.

- Imaging Compton Telescope (COMPTEL). COMPTEL detected $\gamma$-rays, using a Compton scattering technique, between 0.8 MeV and 30 MeV. COMPTEL mapped the distribution of radioactive Aluminium-26 in the Galaxy, showing the locations of newly formed material. The summary by Schönfelder et al. (1996) describes many of the COMPTEL results.

### 4.2.1 EGRET

The Energetic Gamma Ray Experiment Telescope (EGRET) is the CGRO experiment of most interest to the $\gamma$-ray community, since it operated at the high end of the energy spectrum covered by the instruments onboard CGRO. In the energy range above 10 MeV, the principal interaction process for $\gamma$-rays is the pair production. The photon energy is converted into an electron and positron. This process can take place in the field of an atomic nucleus or in a strong magnetic field, but not in free space, in order to conserve energy and momentum. The Anticoincidence System consists of a single dome of plastic scintillator, read out by 24 photomultiplier tubes mounted around the bottom. The Tracker is made of 36 wire grid spark chambers with active area of 81 cm $\times$ 81 cm, interleaved with the converter plates. The time-of-flight (TOF) trigger system has two four by four arrays of plastic scintillator tiles, each read out by a single photomultiplier tube. The Calorimeter was made of 36 NaI crystals bonded together and read out by 16 photomultiplier tubes.

EGRET covered the energy range 20 MeV to 30 GeV (Hughes et al. 1980; Fichtel et al. 1983). The operational concept of EGRET is shown in Figure 4.2.

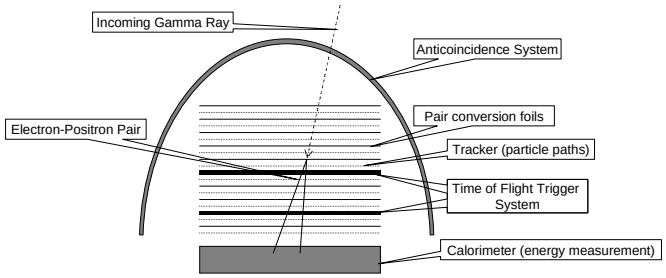


**Figure 4.2:** Schematic diagram of the EGRET telescope [Thompson 2008].

The key challenges for such telescopes are identify the $\gamma$-ray in presence of a huge background and measure the $\gamma$-ray arrival time, arrival direction and energy.
The process works as follows:

(1) A $\gamma$-ray enters in EGRET. It first passes through the Anticoincidence System without producing a signal.

(2) The $\gamma$-ray interacts in one of the 28 thin tantalum sheets. This interaction converts the $\gamma$-ray into an electron and positron via pair production.

(3) The spark chamber tracker records the paths of the electron and positron, allowing EGRET to see the pair interaction and to determine the arrival direction of the $\gamma$-ray.

(4) The electron and positron pass through two scintillator detectors operated in a TOF configuration. The TOF signal confirms the direction of the particles and triggers the readout of the spark chambers.

(5) The electron and positron enter in the Calorimeter, producing an electromagnetic shower, which measures the energies of the particles and therefore the energy of the original $\gamma$-ray.

(6) Unwanted cosmic-ray particles produce signals in the Anticoincidence System, which tell the electronics not to trigger the spark chamber. The Anticoincidence System rejects nearly all unwanted signals produced by cosmic-rays that enter in EGRET.

Observations of the CGRO ranged in duration from a few days to a few weeks, reflecting the paucity of cosmic $\gamma$-ray photons. Because the EGRET spark chambers were gas detectors, their performance deteriorated with time due to gas aging. In its nine-year lifetime, EGRET detected over $1,500,000$ celestial $\gamma$-rays. One photon at a time, EGRET built up a picture of the entire high-energy $\gamma$-ray sky. Figure 4.3 shows the summed map collected by EGRET above 100 MeV, in Galactic coordinates.

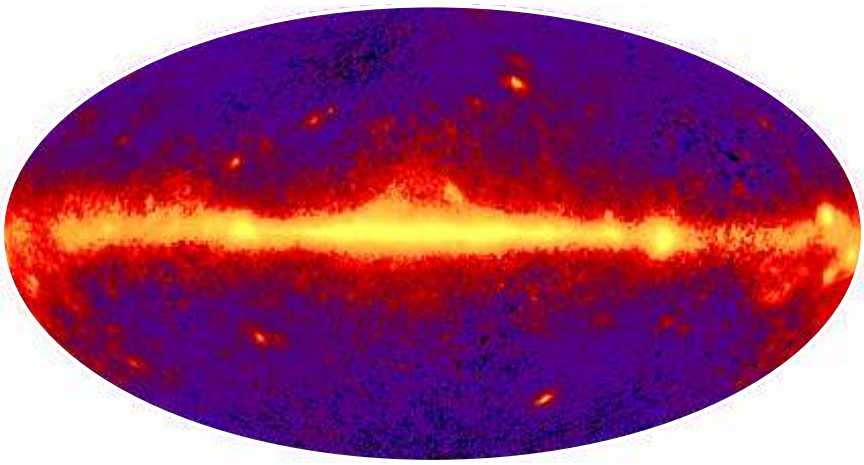

**Figure 4.3:** The $\gamma$-ray sky observed by EGRET during the entire mission, in Galactic coordinates [Thompson 2008].

The key results obtained by EGRET are:

- The detection of diffuse $\gamma$-ray emission from the galactic plane.
- The brightest persistent sources are pulsars.
- Many of the bright sources away from the Galactic plane belong to a new subclass of Active Galactic Nuclei: the blazars.
- Many of the sources detected in $\gamma$-rays are not identified with known objects.
- The detection of six GRBs at $\gamma$-rays.
- The detection of high-energy emission from region spatially coincident with supernova remnants.

EGRET provided a dramatic new view of the high-energy Universe, including the first all-sky mapping of the Universe at energies above 30 MeV. The EGRET observations revealed a wealth of information about Galactic and extragalactic $\gamma$-ray radiation from both individual and diffuse sources. One of the most striking characteristic of the EGRET $\gamma$-ray sky is its variability, ranging from the extremely rapid flaring of GRBs to the long-term variations seen in some sources such as blazars. Since CGRO was taken out of orbit in 2000, a gap

in the coverage of the high-energy $\gamma$-ray sky was opened. This gap was recently filled thanks to the launch of two $\gamma$-ray satellites, AGILE and *Fermi*. With AGILE and *Fermi* now in operation, the time has come to seek out the solutions to some of these mysteries left behind by EGRET.

## 4.3 The AGILE satellite

AGILE (*Astrorivelatore Gamma ad Immagini LEggero*) is an Italian Space Agency (ASI) mission devoted to high-energy astrophysics, with detectors capable of observing cosmic sources simultaneous in X-rays and $\gamma$-rays. AGILE was successfully launched by the Indian PSLV-C8 rocket from the Sriharikota base on 23 April 2007. AGILE has a quasi-equatorial orbit with the smallest inclination ($\sim$ 2.5 degrees) ever archievied by a high-energy space mission. The satellite's commisioning phase was carried out during the period May–June 2007. The scientific verification phase and the in-orbit calibration were carried out during the period July–November 2007. The nominal scientific observation phase and the Cycle 1 started on 1 December 2007.

The AGILE instrument design is based on solid-state Silicon detector technology. The instrument is light ($\sim$ 100 kg) and very compact ($\sim$ 0.25 m$^2$). The total satellite mass is about 350 kg. The AGILE scientific payload is made of three detectors combined into one instrument with broad band detection and imaging capabilities. The payload is surrounded by an anticoincidence system to screen out the charged particle background. Figure 4.4 shows a schematic view of the intrument, and Table 4.3 summarizes the main instrument's scientific performance.
The Gamma-Ray Imaging Detector (GRID) is sensitive in the energy range 30 MeV – 50 GeV, and consists of a silicon tracker, a Cesium Iodide calorimiter, and an anticoincidence system of plastic scintillators. The GRID trigger logic and data acquisition system allows us for an efficient background discrimination and inclined photon acceptance. The hard X-ray detector (SuperAGILE) is a coded-mask imager placed on top of the $\gamma$-ray detector and sensitive in the 18–60 keV band. A mini-calorimiter operating in the burst mode it is part of the GRID, but also capable of indipendetly detecting GRBs and other transients in the 350 keV – 100 MeV energy range with excellent timing capabilities.

### 4.3.1 The anticoincidence system

The anticoincidence system (AC) is aimed at a very efficient charged particle background rejection (Perotti et al. 2006). Moreover, it allows us a preliminary direction reconstruction for triggered photon events through the data handling

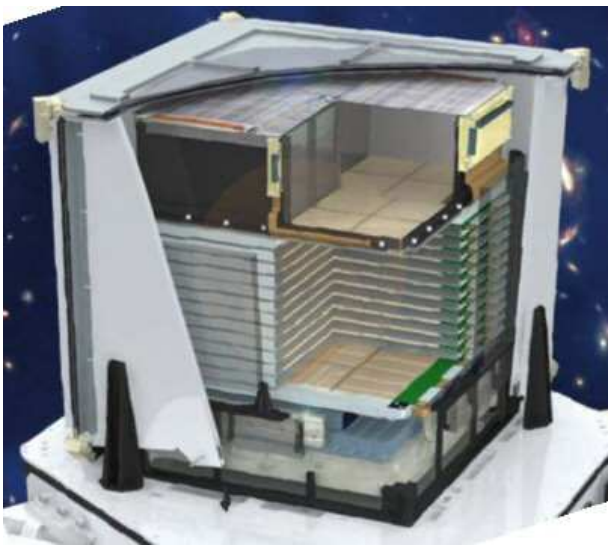

**Figure 4.4:** The AGILE scientific instrument showing the hard X-ray imager, the $\gamma$-ray silicon tracker, and the calorimeter. The anticoincidence system is partially displayed, and no lateral electronic boards and harness are shown for simplicity. The AGILE instrument 'core' is approximately a cube of about 60 cm size and of weight approximately equal to 100 kg [Tavani et al. 2009a].

logic. The AC system completely surrounds all the other AGILE detectors. Each lateral face is segmented in three plastic scintillator layers connected to photomultipliers placed at the bottom of the panels. A single plastic scintillator layers constitutes the top-AC, whose signal is read by four light photomultipliers placed at the four corners of the structure frame.

### 4.3.2 The silicon tracker

The silicon tracker (ST) is the AGILE $\gamma$-ray imager based on photon conversion in the Tungsten layers into electron-positron pairs, measuring the trajectories of the $e^+/e^-$ by means of the silicon strips (Prest et al. 2003; Barbiellini et al. 2001). The silicon tracker consists of a total of 12 trays with distance between middle-planes equal to 1.9 cm. The distance between mid-planes has been optimized through extensive Montecarlo simulations. The first 10 trays are capable of converting $\gamma$-rays by a Tungsten layer. Tracking of charged particles is ensured by silicon microstrip detectors that provide the two othogonal coordinates for each element along the track. The individual silicon detector element is a tile of area $9.5 \times 9.5$ cm$^2$, microstrip pitch of 121 $\mu$m, and 410 $\mu$m thickness. Four silicon tiles are bonded together to provide a ladder and 4 ladders constitute a ST plane.

**Table 1 - The AGILE Scientific Performance**

| **Gamma-ray Imaging Detector (GRID)** | |
|---|---|
| Energy range | 30 MeV – 50 GeV |
| Field of view | ~ 2.5 sr |
| Flux sensitivity ($E > 100$ MeV, 5-$\sigma$ in $10^6$ s) | $3 \times 10^{-7}$ (ph cm$^{-2}$ s$^{-1}$) |
| Angular resolution at 100 MeV (68% cont. radius) | 3.5 degrees |
| Angular resolution at 400 MeV (68% cont. radius) | 1.2 degrees |
| Source location accuracy (high Gal. lat., 90% C.L.) | ~15 arcmin |
| Energy resolution (at 400 MeV) | $\Delta$E/E ~1 |
| Absolute time resolution | ~ 2 $\mu$s |
| Deadtime | ~ 100 – 200 $\mu$s |
| **Hard X–ray Imaging Detector (SuperAGILE)** | |
| Energy range | 18 – 60 keV |
| Single (1-dim.) detector FOV (FW at zero sens.) | 107°× 68° |
| Combined (2-dim.) detector FOV (FW at zero sens.) | 68°× 68° |
| Sensitivity (18–60 keV, 5$\sigma$ in 1 day) | ~ 15 mCrab |
| Angular resolution (pixel size) | 6 arcmin |
| Source location accuracy (S/N~10) | ~1–2 arcmin |
| Energy resolution (FWHM) | $\Delta$E ~ 8 keV |
| Absolute time resolution | ~ 2 $\mu$s |
| **Mini-Calorimeter** | |
| Energy range | 0.35 – 50 MeV |
| Energy resolution (at 1.3 MeV ) | 13% FWHM |
| Absolute time resolution | ~ 3 $\mu$s |
| Deadtime (for each of the 30 CsI bars) | ~ 20 $\mu$s |

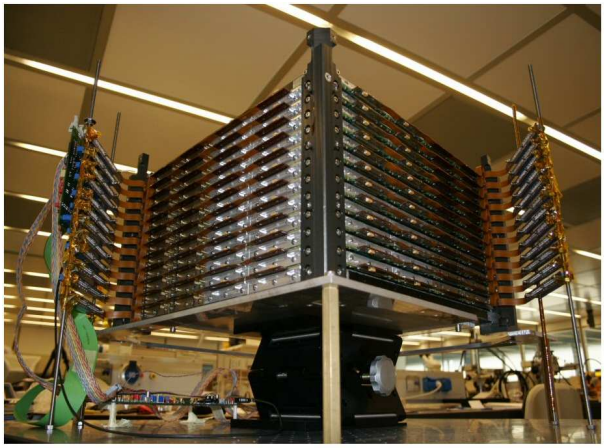

**Figure 4.5:** The assembled silicon tracker before being integrated with the rest of the AGILE payload [Tavani et al. 2009a].

The AGILE ST readout system is capable of detecting and storing the energy deposited in the Silicon microstrips by the penetrating particles. The readout signal is processed for half of the microstrips by an alternating readout system characterized by 'readout' and 'floating' strips. The analog signal produced in the readout strips is read and stored for further processing. Each Silicon ladder has a total of 384 readout channels (242 $\mu$m readout pitch) and 3 TAA1 chips are required to process independently the analog signal from the readout strips. Each tracker layer is then made of $4 \times 4$ Si-tiles, for a total geometric area of $38 \times 38$ cm$^2$. The first 10 trays are equipped with a Tungsten layer of 245 $\mu$m (0.07 $X_0$) positioned in the bottom part of the tray. The two orthogonal coordinates of particle hits in the ST are provided by two layers of Silicon detectors properly configured for each tray that therefore has $2 \times 1536$ readout microstrips. Since the ST trigger requires a signal from at least three contiguous planes, two more trays are inserted at the bottom of the tracker without the Tungsten layers. Therefore only the first 10 trays are capable of converting $\gamma$-rays through a Tungsten layer. The total readout channel number for the GRID tracker is then $36,864$. The ST has an *on-axis* total radiation length near 0.8 $X_0$, for an interaction probability above 1 GeV above 35%. Special trigger logic algorithms implemented onboard (Level-1 and Level-2) lead to a substantial particle/albedo-photon background subtraction and a preliminary onboard reconstruction of the photon incidence angle.

The $\gamma$-ray direction reconstruction is obtained from the identification and the analysis of the $e^+/e^-$ tracks stemming from the conversion vertix. At each plane the microstrip on the silicon layers measure separately the coordinates X and Y

of the hits. The track parameters are fitted by a Kalman filter smooth algorithm (Früwirth 1987). A special implementation of the filter (Giuliani et al. 2004) exploits the measurements of the angular scattering of the electrons due to the interaction with the material to estimate the track energies. Combining the track energies the $\gamma$-ray energy is estimated.

The silicon tracker calibration was carried out at the INFN Laboratories in Frascati during the period 2005 November 1–25. A beam of $\gamma$-ray photons in the energy range 20–700 MeV was produced by Bremsstrahlung of electrons and tagged by a dedicated set-up in the Beam Test Facility of the INFN Laboratori Nazionali di Frascati based on the measurement with silicon strip detectors of the electron trajectory in a magnetic field. A total of $100,000$ tagged events was accumulated for several incidence directions and instrument configurations. Both the GRID spectral and PSF response were carefully studied and compared with results of extensive simulations. Furthermore, the leptonic background was studied by using the direct electron and positron beams interacting with the GRID for different geometries. A sequence of runs was obtained for both direct incidence on the instrument as well as for events originating by interactions with the spacecraft. During the first six months of my Ph.D. studies I have dealt the analysis of the on-ground calibration data of the AGILE silicon tracker. Preliminary results are presented in Cattaneo et al. (2009).

### 4.3.3 SuperAGILE

SuperAGILE (SA), the compact and light hard X-ray imager of AGILE (Feroci et al. 2007) is a coded-mask system made of a Silicon detector plane and a thin Tungsten mask positioned 14 cm above it. The detector plane is organized in four independent square Silicon detectors ($19 \times 19$ cm$^2$ each) plus dedicated front-end electronics based on the XAA1.2 chips suitable to the SA energy range (Del Monte et al. 2007). The total number of SA readout channels is $6,144$. The detection cabability of SA includes: (1) photon-by-photon transmission and imaging of sources in the energy range 18–60 keV, with a large field of view (FOV $\sim$ 1 sr); (2) an angular resolution of 6 arcmin; (3) a good sensitivity ($\sim$ 15 mCrab between 18–60 keV for 50 ksec integration, and $<$ 1 Crab for a few seconds integration). SA is aimed at the hard X-ray detection simultaneously with $\gamma$-ray detection of high-energy sources with excellent timing capabilities (a few microseconds). The SA acquisition logic produces on-board essential GRB quantities such as time, coordinates and preliminary flux estimates.

### 4.3.4 The Mini-Calorimeter

The mini-calorimeter (MCAL) is made of 30 Caesium Iodide (CsI(Tl)) bars arranged in two planes, for a total (on-axis) radiation length of 1.5 $X_0$. A detailed description of the MCAL detector can be found in Labanti et al. (2006, 2009). The signal from each CsI bar is collected by two photodiodes placed at both ends. The MCAL aims are: *(i)* obtaining information on the energy deposited in the CsI bars by particles produced in the silicon tracker (and therefore contributing to the determination of the total photon energy); *(ii)* detecting GRBs and other impulsive events with spectral and intensity information in the energy band $\sim 0.35 - 100$ MeV. An independent burst search algorithm is implemented onboard with a wide range of trigger timescales for an MCAL independent GRB detection. Following a GRB trigger, MCAL is indeed able to store photon-by-photon information for a duration dynamically determined by the onboard logic. The MCAL segmentation and the photon-particle hit positioning along the bars allow to obtain the general configuration of 'hits' across the calorimeter volume. This information is used by the onboard trigger logic for background discrimination and by the ground processing to obtain a preliminary determination of GRB direction.

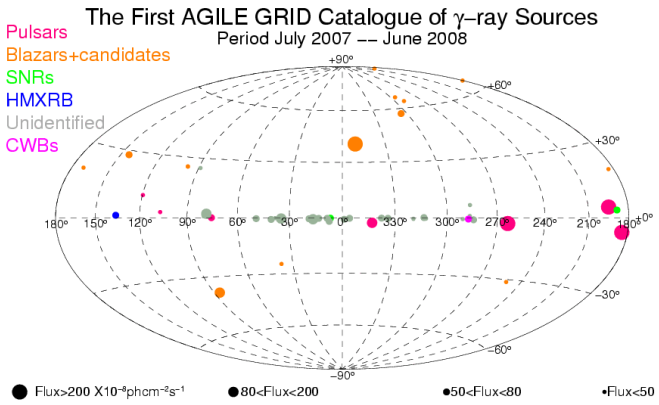


**Figure 4.6:** First AGILE-GRID Catalog of high-confidence $\gamma$-ray sources detected during the first 12 months of operation. The sources were obtained by integrating all data during the period July 2007 to June 2008. The color code refers to the average $\gamma$-ray intensity [Pittori et al. 2009].

### 4.3.5 AGILE: main scientific results

AGILE provides crucial data for the study of Active Galactic Nuclei, Gamma-Ray Bursts, pulsars, unidentified gamma-ray sources, Galactic compact objects,

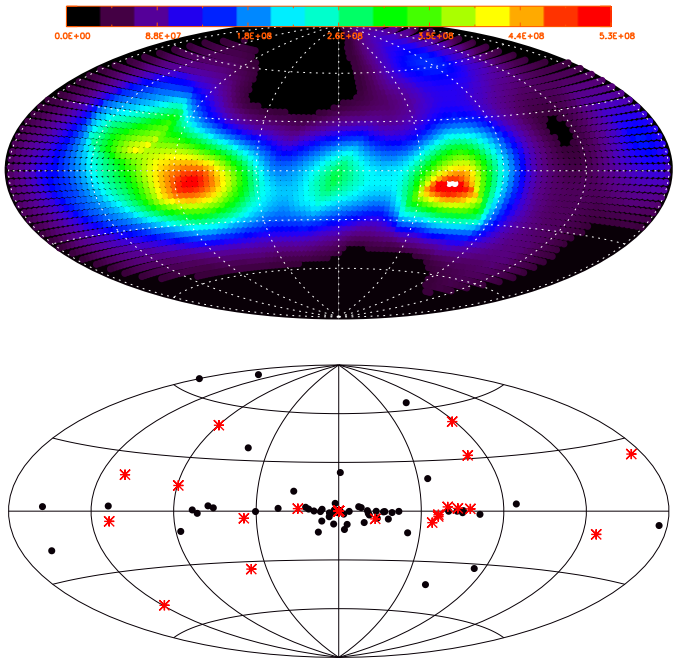

**Figure 4.7:** *Top panel*: integrated exposure map, in units of effective area times exposure time, to any region of the sky, over the time period July 2007 – April 2009. *Bottom panel*: distribution of the sources detected by SuperAGILE in galactic coordinates over the first AGILE two years in orbit. Red asterisks show the sky distribution of the localized GRBs [Feroci et al. 2009].

supernova remnants, TeV sources and fundamental physics by microsecond timing. During the first 2.5 years of operation AGILE surveyed the $\gamma$-ray sky and detected many Galactic and extragalactic sources with important results. Figures 4.6, 4.7 show the high-confidence sources detected in $\gamma$-rays by GRID during the first year of operation and in hard X-rays by SuperAGILE over its first two years of operation, respectively. Moreover, in Fig. 4.8 is shown the $\gamma$-ray sky observed by AGILE in 2 years. In the following we briefly summarize some of the most important results obtained by AGILE (except for the results on blazars that are discussed in detail in the second part of this Thesis).

- Discovery of several new $\gamma$-ray pulsars such as PSR B1509-58, the millisecond PSR in the Globular Cluster M28, and the PSR J2021+3651 in the Cygnus region (Pellizzoni et al. 2009a) and detection of important features of the $\gamma$-ray emission from the well-known Vela, Crab, and Geminga pulsars (Pellizzoni et al. 2009b).

- A comprehensive monitoring of a large number of microquasars and Galac-

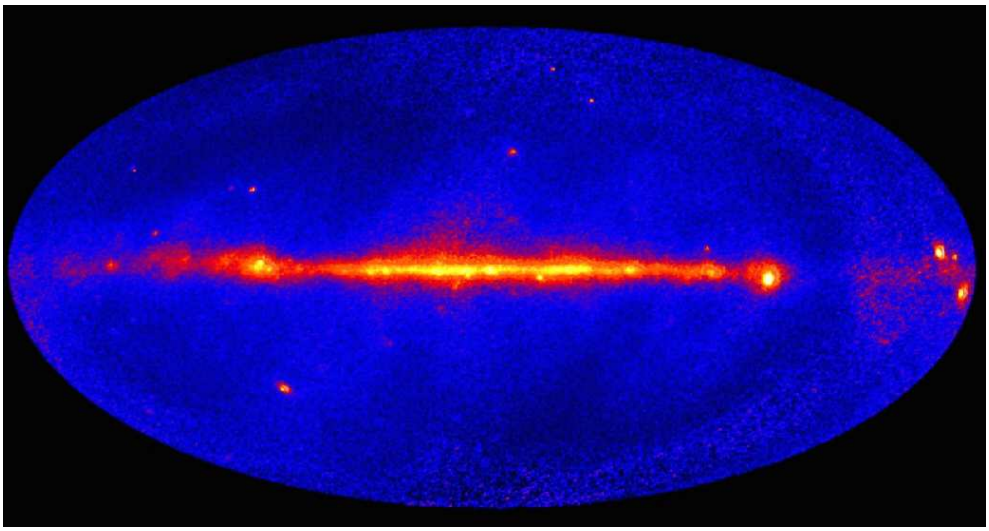

**Figure 4.8:** The $\gamma$-ray sky observed by AGILE during the first 2.5 years of mission.

tic compact sources simultaneously in the $\gamma$-ray and hard X-ray energy ranges, with the detection of transient $\gamma$-ray emission above 100 MeV from the microquasar Cygnus X-3, an exceptional X-ray binary which sporadically produces powerful radio jets (Tavani et al. 2009c).

- Detection of $\gamma$-ray emission from the Vela Pulsar Wind Nebula (Pellizzoni et al. 2009c).
- The first remarkable detection of a colliding wind system, Eta Carinae ($\eta$ Car), at hundreds of MeV energies (Tavani et al. 2009b).
- Detection of delayed $\gamma$-ray emission from GRB 080514B (Giuliani et al. 2008) and from the short GRB 090510 (Giuliani et al. 2010), suggesting that the same process responsible for high energy $\gamma$-ray production takes place, in both long and short GRBs, independently from the central engine.
- High-resolution imaging of several SNRs (e.g. IC 443, Tavani et al. 2009d).
- Detection of Terrestrial Gamma-Ray flashes (Marisaldi et al. 2009).
- Discovery of a class of $\gamma$-ray transients in the Galactic plane (characterized by the remarkable absence of strong hard X-ray emission).

### 4.3.6 AGILE-GRID data analysis procedure

In this Section is described the procedure of the AGILE-GRID data analysis and the source detection method used in the following Chapters for analyzing the GRID $\gamma$-ray data.
Level-1 AGILE-GRID data are analyzed using the AGILE Standard Analysis Pipeline. The first step is to align all data times to terrestrial time (TT) on a contact-by-contact basis, and it performs preliminary calculations and units convertions. In the second step, an ad-hoc implementation of the Kalman Filter technique is used for track identification and event-direction reconstruction in detector coordinates. Subsequently, a quality flag is assigned to each GRID event: Gamma (G), Particle (P), Single (S), and Limbo (L), depending on whether it is recognised as a confirmed $\gamma$-ray event, a charged particle event, a single-track event, or its nature is uncertain, respectively. The (L) event class includes events typically affected by an order of magnitude higher of particle contamination than (G). The single-track (S) event class includes events for which only one track is reconstructed in the two orthogonal views of the tracker. Then, an AGILE logfile is created, containing all the spacecraft information relevant to computating the effective exposure and live time. The third step is to create the AGILE event files, excluding events flagged as particles. This step also reconstructs the event direction in sky coordinates.
Once the above steps are completed, the AGILE Scientific Analysis Package can be run. Counts, exposure and Galactic background $\gamma$-ray maps were created.

In the data analysis we use the diffuse emission model developed for AGILE (Giuliani et al. 2004) for diffuse $\gamma$-ray background counts predictions. Diffuse $\gamma$-ray emission includes a combination of two components: (1) diffuse emission from the Galactic interstellar medium and (2) an approximately isotropic extragalactic component, plus possible contributions from unresolved and faint point sources. Diffuse emission coming from the Galactic plane dominates other components and, as in the EGRET model (Hunter et al. 1997), it is assumed to be produced by the interaction of cosmic rays with the interstellar medium through three physical processes: proton-proton collision, Bremsstrahlung and inverse Compton emission.

The AGILE diffuse emission model substantially improves the previous EGRET model by using state-of-the-art neutral hydrogen (HI) and CO updated maps in order to model the matter distribution in the Galaxy. It is based on a 3-D grid with $0.25^\circ \times 0.25^\circ$ square binning in Galactic longitude and latitude, and a 0.2 kpc step in distance along the line of sight. Concerning the distribution of neutral hydrogen, we used the Leiden-Argentine-Bonn (LAB) Survey of Galactic HI (Kalberla et al. 2005). The LAB survey improves previous results especially in terms of sensitivity (by an order of magnitude), velocity range and resolution.

In order to properly project the velocity-resolved radio data, we used the Galactic rotation curves parameterized by Clemens et al. (1985). The detailed and relatively high-resolution distribution of molecular hydrogen is obtained from the CO observations described in Dame et al. (2001). The CO is assumed to be a tracer of molecular hydrogen, through a known ratio between hydrogen density and CO radio emissivity. Cosmic rays can emit $\gamma$-rays through the inverse Compton mechanism due to their interaction with photons of the cosmological background and of the interstellar radiation field (ISRF). In order to account for this component we use the analytical model proposed by Chi & Wolfendale (1991). It describes the ISRF as the result of three main contributions: far infrared (due to dust emission), near infrared, and optical/UV (due to stellar emission). The distribution of cosmic rays (both protons and electrons) in the Galaxy is obtained using the GALPROP cosmic-ray model (Strong. et al. 2004; Strong 2007).

The AGILE source detection method is based on a Maximum Likelihood (ML) analysis to derive, for each candidate source, the source significance, $\gamma$-ray flux, and source location. The ML statistical technique, already used in the past in the analysis of $\gamma$-ray data (Mattox et al. 1996), compares measured counts in each pixel with the predicted counts derived from the diffuse $\gamma$-ray model to find statistically significant excesses consistent with the instrument point spread function.

The Likelihood ratio test is then used to compare the null (diffuse background-only) hypothesis with the possible presence of point-source components. According to Wilks'theorem (Wilks 1938), the point source 'Test Statistic' (TS), defined as:

$$TS = -2\,(\ln L_0 - \ln L_1) \tag{4.1}$$

is expected to behave as $\chi^2_1$ in the null hypothesis, plus terms of order $O(N^{-1/2})$, where N is the number of counts. In practice for a number of AGILE counts $N > 20$, the significance of a source detection at a certain position is given by a number of standard deviations $\sigma$ equal to $\sqrt{TS}$.

## 4.4 The *Fermi* satellite

The *Fermi* Gamma ray Space Satellite (formely GLAST) was launched by NASA on 2008 June 11 on a Delta II Heavy launch vehicle. *Fermi* has an imaging $\gamma$-ray telescope, the Large Area Telescope (LAT; Atwood et al. 2009), with superior area, angular resolution, field of view, and deadtime that together will provide a great advance in sensitivity as well as provide capability for study of transient phenomena, and a secondary instrument for the study of the GRBs, the GLAST Burst Monitor (GBM; Charles et al. 2009). With the LAT and GBM, *Fermi* is a

flexible observatory for investigating the great range of astrophysical phenomena best studied in high-energy $\gamma$-rays.

### 4.4.1 Large Area Telescope

As for the silicon tracker onboard AGILE, the primary interaction of photons in the *Fermi* energy range with matter is pair conversion. Incident radiation first passes through an anticoincidence shield, which is sensitive to charged particles, then through conversion foils. Photon conversions are facilitated in the field of a heavy nucleus. After a conversion, the trajectories of the resulting electron and positron are measured by particle tracking detectors, and their energies are then measured by a calorimeter. The characteristic $\gamma$-ray signature in the LAT is therefore (1) no signal in the anticoincidence shield, (2) more than one track starting from the same location within the volume of the tracker, and (3) an electromagnetic shower in the calorimeter.

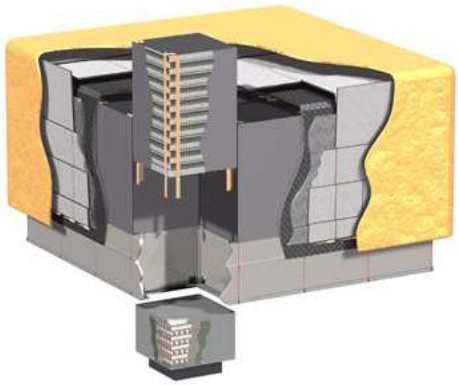

**Figure 4.9:** Cut-away image of the Large Area Telescope onboard *Fermi*. The detector is comprised of an array of 16 columnar silicon strip detectors. These are used to obtain highly accurate 2-dimensional coordinates on the arrival of a high energy $\gamma$-ray by tracking the electron-positron pair that results from pair production in thin tungsten conversion foils between the columns. The third coordinate is obtained using adjacent towers to calculate the arrival direction. These silicon strip detectors sit on top of a calorimeter. The entire detector is encased in an anticoincidence shield [Credit: NASA].

The baseline LAT (see Fig. 4.9) is modular, consisting of a 4 x 4 array of identical towers. Each $40 \times 40$ cm$^2$ tower comprises a tracker, calorimeter and data acquisition module. Each tracker module has a vertical stack of 18 *x*,*y* tracking planes, including two layers (*x* and *y*) of single sided silicon strip detectors and high-Z converter material (tungsten) per tray. The calorimeter in

each tower consists of eight layers of 12 CsI bars in a hodoscopic arrangement, read out by photodiodes, for a total thickness of 10 radiation lengths. Owing to the hodoscopic configuration, the calorimeter can measure the three-dimensional profiles of showers, which permits corrections for energy leakage and enhances the capability to discriminate hadronic cosmic rays. The anticoincidence shield, which covers the array of towers, employs segmented tiles of scintillator, read out by wavelength-shifting fibers and miniature phototubes. The LAT is self triggered: events that cause detector hits in three planes automatically trigger readouts of each tower and the anticoincidence system. Efficient rejection of the charged particle background, which is thousands of times more intense than the celestial $\gamma$-ray radiation, is essential for *Fermi* to function.

### 4.4.2 GLAST Burst Alert

The GBM includes two sets of detectors: twelve sodium iodide (NaI) scintillators, each 12.7 cm in diameter by 1.27 cm thick, and two cylindrical bismuth germanate (BGO) scintillators, each 12.7 cm in diameter and 12.7 cm in height. The NaI detectors are sensitive in the lower end of the energy range, from a few keV to about 1 MeV and provide burst triggers and locations. The BGO detectors cover the energy range 150 keV to 30 MeV, providing a good overlap with the NaI at the lower end and with the LAT at the high end. The GBM detectors will view the entire sky not occulted by Earth, and are expected to pick up about 200 GRBs per year, as well as solar flares and other transient events. The combination of the GBM and the LAT provides a powerful tool for studying GRBs over a very wide range of energies.

## 4.5 Multiwavelength astronomy and the AGILE approach

In the beginning astronomy meant optical astronomy, because all observations were made in the visible range of the electromagnetic spectrum, the discovery of other parts of the spectrum enlarged the observation window providing an enormous amount of information, not previously available from ground-based observations made in the visible wavelength region only, and changing significantly the appearence of the sky.

In fact, although astronomy is a very old branch in science, it was restricted for a long time to the part of the electromagnetic spectrum visible by eye. Already ancient civilizations in Mesopotamia, Egypt, Persia, Middle and South America, Greece and India made astronomical observations. For example in 1054 Chinese and Arab astronomers recorded the observation of the Supernova

leaving as well-known remnant the Crab Nebula. A great problem for extending the observations to a wider range of frequencies came from the transparency of the atmosphere to radiation at different wavelengths. In fact, due to its composition, the opacity of the Earth's atmosphere depends on the wavelength of the radiation. As shown in Fig. 4.10, there are only a few windows in which ground-based observations are possible: the optical window (300 nm to 1100 nm), the radio window (1 cm to 11 m) and several windows in the infrared. For observations in other ranges ballon experiments and space telescopes have to be launched. New techniques and telescopes for making observation both from the ground and space have been developed in the last 50 years to explore the Universe in all wavelengths, allowing us to make great leaps in our understanding of the Universe.

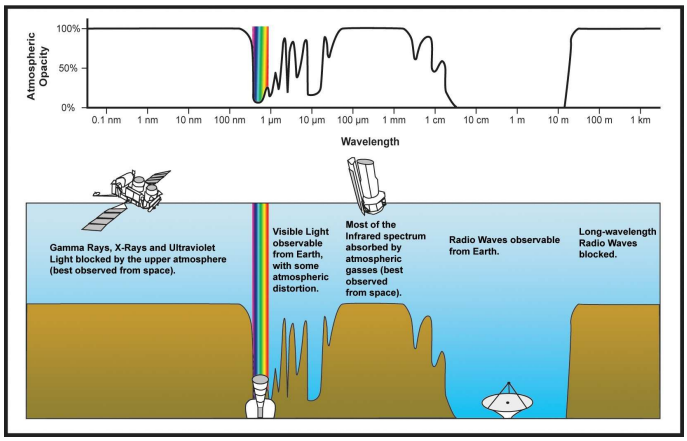


**Figure 4.10:** Opacity of the Earth's atmosphere in function of the wavelength [Credit: NASA/JPL-Caltech].

A new and exciting time for $\gamma$-ray space observations started in April 2007 with AGILE, and was consolidated by the launch and operations of the *Fermi* mission in June 2008. Considering that AGILE is most effective in the low-energy range of the $\gamma$-ray domain (50–400 MeV), whereas *Fermi* is currently optimized above 400 MeV, the two missions are complementary and joint scientific investigations by the two satellites could give important information for the study of extragalactic and Galactic sources. However, a wide multiwavelength coverage is needed to obtain a complete knowledge of the emission mechanisms of these sources, in particular for the class of blazar studied in this Thesis. In fact, because of their emission over the entire electromagnetic spectrum, multiwavelength observations of blazars are crucial to constrain the emission mechanisms, structure, and physical quantities of the inner jet on parsec and sub-parsec scales.

Therefore, considering the importance to obtain information over the entire electromagnetic spectrum for studying blazars, most of the AGILE campaigns were coordinated with other observatories at different wavelengths, such as *Spitzer*, *Swift*, *Suzaku*, INTEGRAL, RXTE, MAGIC, VERITAS, the WEBT Consortium, and REM.

This approach, based on pre-approved target of opportunity (ToO) guest investigator (GI) proposals, Director discretionary time (DDT) requests, monitoring programs, and bilateral agreements, allowed the AGILE Team to obtain truly simultaneous data on specific sources, covering the entire spectral energy distribution of blazar, from $10^9$ to $10^{26}$ Hz.

In particular, in order to obtain an as dense as possible optical coverage of $\gamma$-ray sources during the AGILE observations, we established a tight and fruitful collaboration with the GLAST-AGILE Support Program (GASP) organized within the Whole Earth Blazar Telescope (WEBT), which provides radio-to-optical long-term continuous monitoring of a list of selected $\gamma$-ray-loud blazars. Moreover, in order to monitor the synchrotron to inverse Compton region of the SED, the most effective satellite in orbit is *Swift*, because of its rapid reaction to ToO requests and its broad-band coverage, from optical/UV up to the hard X-rays. Several GI programs and ToO observations were performed, for a total of a few hundreds ksec.

The synergy between the AGILE wide field of view, its fast response to sudden changes in blazar activity state at over wavelengths and to alert other telescopes quickly in reponse to changes in the $\gamma$-ray fluxes, together with the availability of a network of ground-based telescopes, allowed us to obtain a multiwavelength coverage for almost all the detected sources, giving us the opportunity to study the spectral energy distributions from radio to $\gamma$-rays and to investigate the physics of different classes of blazars. In the second part of this Thesis I present and discuss the most interesting results obtained during the AGILE multiwavelength campaigns on blazars in which I was personally involved.

Chapter 5

# PKS 1510−089

## 5.1 Introduction

PKS 1510−089 is a nearby (z=0.361) radio-loud highly polarized quasar (HPQ), belonging to the class of the Flat Spectrum Radio Quasars (FSRQs) with radiative output dominated by the $\gamma$-ray emission, while the synchrotron emission peaks around IR frequencies, below a pronunced UV bump, likely due to the thermal emission from the accretion disk (Malkan & Moore 1986; Pian & Treves 1993).

Its radio emission exhibited very rapid, large amplitude variations in both total and polarized flux (Aller, Aller, & Hughes 1996). Moreover, the radio jet shows superluminal motion up to 20 *c*, with the parsec and kiloparsec scale jets misaligned of 177 degrees (Wardle et al. 2005).

PKS 1510−089 has been extensively observed in the X-rays in the last three decades, since the observation by the satellites *Einstein* (Canizares and White 1989), EXOSAT (Singh, Rao & Vahia 1990; Sambruna et al. 1994), GINGA (Lawson & Turner 1997), ROSAT (Siebert et al. 1998), and ASCA (Singh, Shrader & George 1997). The observed X-ray spectrum by ASCA in the 2–10 keV band was very flat with photon index of $\Gamma \simeq 1.3$, but steepened ($\Gamma \simeq 1.9$) in the ROSAT bandpass (0.1–2.4 keV), suggesting the possible presence of a spectral break around 1–2 keV, associated with the existence of a soft X-ray excess. Observations by *Beppo*SAX (Tavecchio et al. 2000) and *Chandra* (Gambill et al. 2003) confirm the presence of a soft X-ray excess below 1 keV. Evidence of a similar soft X-ray excess has been detected in other blazars such as 3C 273, 3C 279, AO 0235+164, and 3C 454.3, even if the origin of this excess is still an open issue, not only for blazars but for all AGNs (see e.g. D'Ammando et al. 2008a for a discussion on the soft X-ray excess problem in the radio-quiet AGNs).

A monitoring campaign on this source was organized during August 2006 by *Suzaku* and *Swift*. The *Suzaku* observations confirm the presence of a soft X-ray excess, suggesting that it could be a feature of the bulk Comptonization, whereas the *Swift*/XRT observations reveal significant spectral evolution of the X-ray emission on timescales of a week: the X-ray spectrum becomes harder as the source gets brighter (Kataoka et al. 2008).

$\gamma$-ray emission from PKS 1510−089 was detected in the past by EGRET during low/intermediate states, with an integrated flux above 100 MeV varying between $(13 \pm 5)$ and $(49 \pm 18) \times 10^{-8}$ photons cm$^{-2}$ s$^{-1}$, and an energy spectrum, integrated over all the EGRET observations, modeled with a power law with photon index $\Gamma = 2.47 \pm 0.21$ (Hartman et al. 1999).

In the last two years, PKS 1510−089 showed high variability over all the electromagnetic spectrum and in particular very high $\gamma$-ray activity was detected by the AGILE and *Fermi* satellites. The Gamma-Ray Imaging Detector on board the AGILE satellite detected flaring episodes in August 2007 and March 2008. Moreover, an extraordinary activity was detected in March 2009 with several flaring episodes and a flux that reached $600 \times 10^{-8}$ photons cm$^{-2}$ s$^{-1}$.
In this Chapter we discuss the results of the analysis of the multiwavelength data collected by GASP-WEBT, REM, *Swift* and AGILE during these $\gamma$-ray flares and the theoretical implications for the emission mechanisms. The results presented in this Chapter are published in Pucella et al. (2008), D'Ammando et al. (2009a), D'Ammando et al. (2009b), D'Ammando et al. (2009c).

## 5.2 The 2007 observations

PKS 1510−089 was detected for the first time by AGILE in high $\gamma$-ray activity during August 2007. The AGILE observations of PKS 1510–089 were performed from 23 August 2007 12:00 UT to 1 September 2007 12:00 UT, for a total of 84 hours of effective exposure time. In the first period, between 23 and 27 August, the source was located $\sim 50^\circ$ off the AGILE pointing direction. In the second period, between 28 August and 1 September, after a satellite re-pointing, the source was located at $\sim 35^\circ$ off-axis.

Level–1 AGILE-GRID data were analysed using the AGILE Standard Analysis Pipeline (see Section 4.3.6). Counts, exposure, and Galactic background $\gamma$-ray maps are created with a bin-size of $0.5^\circ \times 0.5^\circ$ for photons with energy over 100 MeV. To reduce the particle background contamination, we selected only events flagged as confirmed $\gamma$-ray events, and all events collected during the South Atlantic Anomaly were rejected. We also rejected all the $\gamma$-ray events whose reconstructed directions form angles with the satellite-Earth vec-

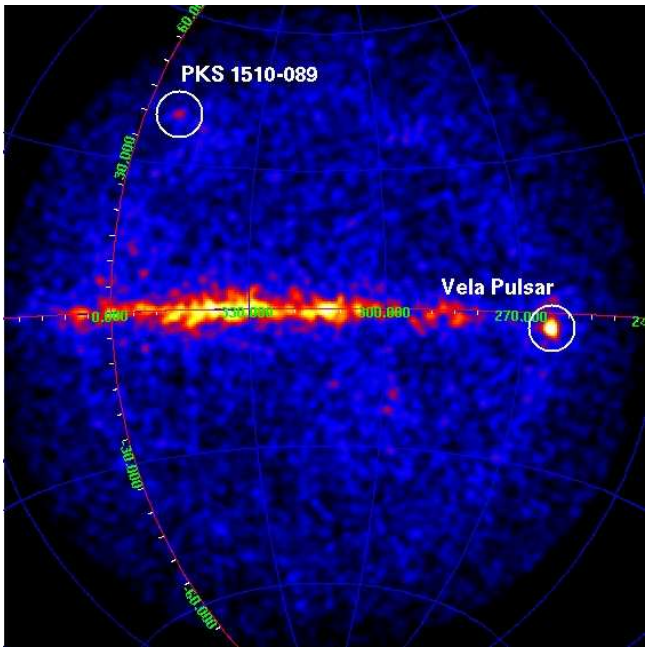


**Figure 5.1:** Gaussian-smoothed count map ($\sim 140^\circ \times 140^\circ$) in Galactic coordinates integrated over the observing period 2007 August 23 – August 27. The circles are located at the PKS 1510−089 and Vela Pulsar coordinates. Only photons with energy greater than 100 MeV have been included [Pucella et al. 2008].

tor smaller than 80°, reducing the $\gamma$-ray Earth albedo contamination by excluding regions within $\sim 10^\circ$ from the Earth limb.

During the observing period 2007 August 23–27, AGILE detected $\gamma$-ray emission for photon energies over 100 MeV from a position consistent with the quasar PKS 1510−089 at a significance level of 5.6-$\sigma$, as derived from a maximum likelihood analysis (Fig. 5.1). During this period the source was located $\sim 50^\circ$ off the AGILE pointing direction, therefore considering the early phase of on-flight calibration of the GRID intrument, in particular at high off-axis angle, and thanks to fact that the satellite simultaneously also detected the $\gamma$-ray activity of the Vela Pulsar, about 90 degrees from PKS 1510−089, we use the flux of Vela Pulsar for a direct calibration of the flux of PKS 1510−089. In fact, the two sources were characterized by an almost equal angular distance from the AGILE boresight and therefore the instrument response in the estimation of the flux of the two sources are compatible. In this way, the average flux (E > 100 MeV) of PKS 1510−089 estimated for this first period was $(270 \pm 65) \times 10^{-8}$ photons cm$^{-2}$ s$^{-1}$. The reduced effective area and the consequently reduced count statistics for these large off-axis angles makes it difficult to create a light curve and an average

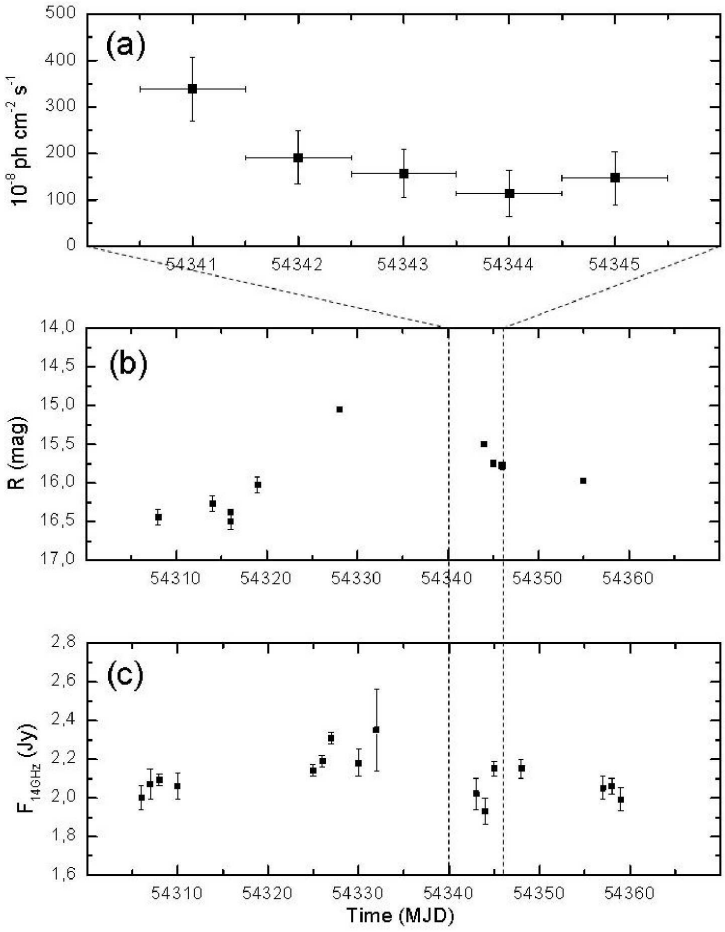


**Figure 5.2:** a) AGILE-GRID $\gamma$-ray light curve, with a 1-day resolution, for the observation period 2007 August 28 – September 1, for photons with E > 100 MeV in units of $10^{-8}$ photons cm$^{-2}$ s$^{-1}$. b) *R*-band optical light curve as observed by the GASP-WEBT for the observation period 2007 July 26 – September 11. c) UMRAO radio light curve at 14.5 GHz for the observation period 2007 July 24 – September 15 [Pucella et al. 2008].

energy spectrum.

In the period 2007 August 27 – September 1, AGILE-GRID detected the source, observed at 35° off-axis, at a significance level of 10.6-$\sigma$. With the likelihood method, the best position for the $\gamma$-ray emission above 100 MeV is l = 350.89°, b = 40.34°, with an average flux (E > 100 MeV) over the entire period of $(195 \pm 30) \times 10^{-8}$ photons cm$^{-2}$s$^{-1}$. In Fig. 5.2 the $\gamma$-ray light curve for

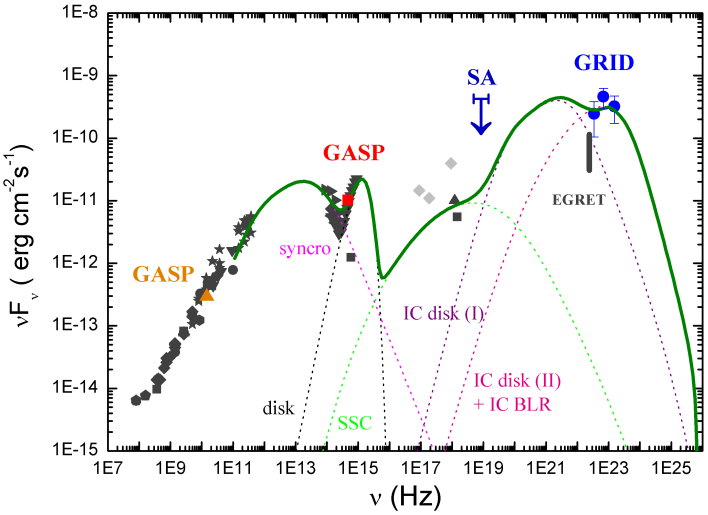


**Figure 5.3:** Spectral energy distribution of PKS 1510−089 for the GRID observation period 28 August – 1 September 2007 (blue dots), including simultaneous GASP optical (red square) and radio (orange triangle) data and the 3-$\sigma$ SuperAGILE upper limit (blue arrow). Non-simultaneous historical data (from 1969 to 2007) taken from NASA Extragalactic Database (NED) and Kataoka et al. (2008) over the entire electromagnetic spectrum are represented in dark grey and light grey, respectively [Pucella et al. 2008].

this period with a 1-day resolution, the *R*-band optical light curve as observed by the GASP-WEBT for the observation period between 26 July and 11 September 2007, and the UMRAO radio light curve at 14.5 GHz for the observation period between 24 July and 15 September 2007 are reported. We calculated the $\gamma$-ray average energy spectrum for this second period, when only three energy bins were taken into account for the fit: 100–200 MeV, 200–400 MeV, and 400–1000 MeV. A simple power-law model can fit the data. With the weighted least squares method we obtain a photon index $\Gamma = 1.98 \pm 0.27$.

SuperAGILE observed PKS 1510−089 for a total on-source effective exposure time of 200 ks. The source was not detected above 5-$\sigma$ by the SuperAGILE Iterative Removal Of Sources (IROS) applied to the image, in the 20–60 keV energy range. A 3-$\sigma$ upper limit of 45 mCrab was obtained from the observed count rate by a study of the background fluctuations at the position of the source and a simulation of the source and background contributions with IROS.

During the AGILE observation period, the PKS 1510−089 optical flux appears to be decreasing in the range $R \sim 15.5$–$15.8$, following a bright state that reached at least $R = 15.0$ (see Fig. 5.2, panel b). The contemporaneous $\gamma$-ray flux

decrease of about a factor 3 suggests that the two flux variations may be correlated. Finally, in Fig. 5.3 the spectral energy distribution (SED) is shown for the GRID observation period 2007 August 28 – September 1, including simultaneous GASP optical and radio data and the 3-$\sigma$ SuperAGILE upper limit. Also non-simultaneous historical data over the entire electromagnetic spectrum are represented. To model the SED we used a homogeneous one-zone synchrotron self Compton (SSC) model, plus the contribution of external seed photons originating both from the accretion disc and the Broad Line Region (BLR). We consider a relativistic moving spherical blob of radius $R = 2.5 \times 10^{16}$ cm and an electron energy distribution described by a double power law:

$$n_e(\gamma) = \frac{K\gamma_b^{-1}}{(\gamma/\gamma_b)^{p_1} + (\gamma/\gamma_b)^{p_2}} \tag{5.1}$$

for electron Lorentz factor $40 < \gamma < 4 \times 10^3$ with spectral indices pre- and post-break $p_1 = 2.0$ and $p_2 = 4.5$, a normalization factor $K = 80$ cm$^{-3}$ and the break energy Lorentz factor $\gamma_b = 400$. We assumed a magnetic field $B = 3$ Gauss and a Doppler factor $\delta = 9$ for the blob.

In order to interpret the AGILE $\gamma$-ray data, an accretion disc characterised by a blackbody spectrum with a luminosity of $10^{46}$erg s$^{-1}$ at 0.1 pc from the blob is assumed as the source of external target photons. Even if the contribution of the IC from the disc is calculated up to the second order, it is not enough to account for the high $\gamma$-ray state observed by AGILE. The addition of the IC emission from a BLR, represented by a spherical layer extending between 0.1 pc and 0.4 pc from the central black hole, reprocessing a 10% of the irradiating continuum can explain the high state observed by AGILE compared to the historical EGRET observations (see Fig. 5.3), and it reflects on the different photon index obtained in the AGILE and EGRET observations. In this model, the IC contribution from the BLR can explain the observed hard $\gamma$-ray spectrum. However, considering the sparse multifrequency coverage simultaneously to the $\gamma$-ray observation and the lack of informations in X-ray band (except for the upper limit estimated by SuperAGILE), the model is not strongly constrained by the available observations and the choice of parameters is not unique.

## 5.3 The 2008 observations

During a pointing toward the Galactic Center region, between 1 and 30 March 2008, AGILE detected a rapid $\gamma$-ray flare from PKS 1510−089. This source has been continuosly monitored between January and April 2008 in the radio-to-optical bands by the GASP-WEBT. Moreover, the $\gamma$-ray flaring episode triggered

three Target of Opportunity (ToO) observations by the *Swift* satellite in three consecutive days, starting from 20 March 2008.

The quasi-simultaneous radio-to-optical, UV, X-ray and $\gamma$-ray coverage allows us to make a detailed study of the multifrequency time evolution, the spectral energy distribution of this source, and its theoretical interpretation based on the synchrotron and IC emission mechanisms.

### 5.3.1 AGILE observations

The AGILE observations of PKS 1510−089 were performed from 1 March 2008 12:45 UT to 21 March 2008 2:04 UT, for a total of 211 hours of effective exposure time. In the first period, between 1 and 16 March, the source was located $\sim 50^\circ$ off the AGILE pointing direction. In the second period between 17 and 21 March, after a satellite re-pointing, the source was located at $\sim 40^\circ$ off-axis. Finally, after a gap of 4 days of observation due to technical maintenance of the satellite, the source was observed at $\sim 50^\circ$ off axis between 25 March 13:09 UT and 30 March 10:29 UT. Unfortunately, during the observation the source was substantially off-axis in the field of view of SuperAGILE.

AGILE-GRID data were analyzed, starting from the Level–1 data, using the AGILE Standard Analysis Pipeline (see Section 4.3.6). After the creation of the event files, the AGILE Scientific Analysis Package can be run. Counts, exposure, and Galactic background $\gamma$-ray maps were generated with a bin size of $0.25^\circ \times 0.25^\circ$ for photons with energies E > 100 MeV. To reduce the particle background contamination, we selected only the events flagged as confirmed $\gamma$-ray events, so all events collected during the South Atlantic Anomaly were rejected. We also rejected all the $\gamma$-ray events whose reconstructed directions form angles with the satellite-Earth vector smaller than $80^\circ$, in order to reduce the $\gamma$-ray Earth albedo contamination.

During the period 1–16 March 2008, AGILE-GRID detected $\gamma$-ray emission from a position consistent with the powerful $\gamma$-ray quasar PKS 1510−089 at a significance level of 6.2-$\sigma$ with an average flux over the entire period of $(84 \pm 17) \times 10^{-8}$ photons cm$^{-2}$ s$^{-1}$ for photon energies above 100 MeV. Instead, in the period 17–21 March 2008, AGILE detected $\gamma$-ray emission from a position consistent with the source at a significance level of 7.3-$\sigma$. The AGILE 95% maximum likelihood contour level baricenter of the source is $l = 351.49^\circ, b = 40.07^\circ$, with a distance between this position and the radio position ($l = 351.29^\circ, b = 40.14^\circ$) of $0.17^\circ$. The overall AGILE error circle, taking both statistical and systematic effects into account, has a radius $r = 0.50^\circ$. The average $\gamma$-ray flux above 100 MeV during this second period, with the source located $\sim 40^\circ$ off the AGILE pointing direction, was $(134 \pm 29) \times 10^{-8}$ photons cm$^{-2}$ s$^{-1}$. The peak level of activity with daily integration was $(281 \pm 68) \times 10^{-8}$

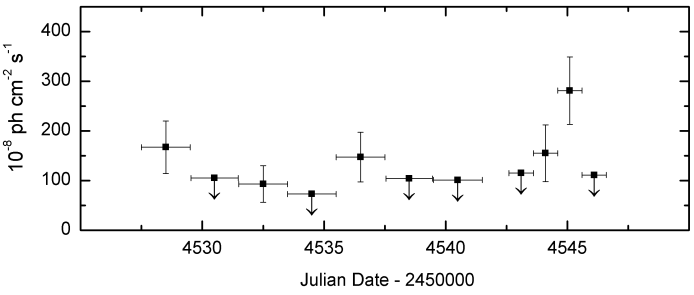


**Figure 5.4:** AGILE-GRID $\gamma$-ray light curve between 1 and 21 March 2008 at 1-day or 2-day resolution for E > 100 MeV with fluxes in units of $10^{-8}$ photons cm$^{-2}$ s$^{-1}$. The downward arrows represent 2-$\sigma$ upper limits [D'Ammando et al. 2009a].

photons cm$^{-2}$ s$^{-1}$, showing an increase of a factor two in one day and at least three in two days, as the source had not been detected for some days after two episodes of medium intensity. After the sudden increase, the flux rapidly decreased around 19 March 2008.

When fitting the data relative to the period 17–21 March with a simple power law model, we obtain a photon index of $\Gamma = 1.81 \pm 0.34$. This photon index is calculated with the weighted least squares method, considering for the fit three energy bins: 100–200 MeV, 200–400 MeV, and 400–1000 MeV. The photon index obtained for this second period is consistent within the errors with the one observed by AGILE in August 2007 ($\Gamma = 1.98 \pm 0.27$).

Figure 5.4 shows the $\gamma$-ray light curve between 1 and 21 March 2008, with 2-day resolution for the first period and 1-day for the second period, for photons of energy above 100 MeV. The downward arrows represent 2-$\sigma$ upper limits. Upper limits are calculated when the analysis provides a significance of detection < 3-$\sigma$ (see Mattox et al. 1996). Finally, in the third period between 25 and 30 March 2008 the source was not detected by the GRID and an upper limit with 95% confidence level of 54 $\times 10^{-8}$ photons cm$^{-2}$ s$^{-1}$ is provided.

During August–October 2008, *Fermi*-LAT detected the source with an average flux for E > 100 MeV of (55.8 ± 3.3) $\times 10^{-8}$ photons cm$^{-2}$ s$^{-1}$ and a peak of intensity of (165.9 ± 11.7) $\times 10^{-8}$ photons cm$^{-2}$ s$^{-1}$ (Abdo et al. 2009d). The peak of $\gamma$-ray emission corresponds to the first flare observed by *Fermi*-LAT at the end of September 2008 (Tramacere 2008), and together with the average flux value confirms the flaring state observed by AGILE in mid-March 2008.
Moreover, *Fermi*-LAT observed a softer photon index for this source in August–October 2008, $\Gamma = 2.48 \pm 0.05$ (Abdo et al. 2009d), but this value corresponds to an average value over three months of observation in which the source flux was

variable, whereas the value reported by us refers to a rapid flaring episode. The value obtained by *Fermi*-LAT is very similar to what was measured by EGRET averaging over all the observations ($\Gamma = 2.47 \pm 0.21$), confirming that the average spectral indexes are softer than those measured during short flaring states. The difference between the value obtained by AGILE and *Fermi* could also be partially due to the different bandpasses of the two intruments.

### 5.3.2 *Swift* observations

The NASA *Swift* gamma-ray burst mission (Gehrels et al. 2004), performed three ToO observations of PKS 1510–089 in three consecutive days with the first occurring on 20 March 2008. The three observations of $\sim 2$ ksec each were performed using all three onboard experiments: the X-ray Telescope (XRT; Burrows et al. 2005, 0.2–10 keV), the UV and Optical Telescope (UVOT; Roming et al. 2005, 170–600 nm) and the coded-mask Burst Alert Telescope (BAT; Barthelmy et al. 2005, 15–150 keV). The hard X-ray flux of this source is below the sensitivity of the BAT instrument for so short exposure, so the data from this instruments will not be used.

#### 5.3.2.1 *Swift*/XRT data

The XRT data were processed with standard procedures (`xrtpipeline` v0.12.0), and the filtering and screening criteria were applied by means of the FTOOLS in the `Heasoft` package v6.5. Given the low count rate of PKS 1510–089 during the three observations ($< 0.5$ count $s^{-1}$ in the 0.2–10 keV range), we only considered photon counting (PC) data for our analysis, and further selected XRT grades 0–12 (according to *Swift* nomenclature, see Burrows et al. 2005). No pile-up correction was necessary. The ancillary response files were generated with the task `xrtmkarf`, applying corrections for the PSF losses and CCD defects, and we used the latest spectral redistribution matrices (RMF, v011) in the calibration database maintained by HEASARC. The adopted energy range for spectral fitting is 0.3–10 keV, and all data were rebinned with a minimum of 20 counts per energy bin to use the $\chi^2$ minimization fitting technique. An exception is the observation of 21 March 2008, when the number of counts was so low that the Cash statistic (Cash 1979) on ungrouped data was used. *Swift*/XRT uncertainties are given at 90% confidence level for one interesting parameter, unless otherwise stated.

Spectral analysis was performed using the `XSPEC` fitting package 12.4.0 (Arnaud et al. 1996). We fitted the spectra with a power-law model with Galactic absorption fixed to $N_{\rm H} = 6.89 \times 10^{20}$ cm$^{-2}$ (Kalberla et al. 2005). Table 5.1 sum-

**Table 5.1:** Observation log and fitting results of *Swift*/XRT observations of PKS 1510−089. Power-law model with $N_{\rm H}$ fixed to Galactic absorption is used.

| Obs. Date | Counts (0.2–10 keV) | Flux 0.3–10 keV[a] erg cm$^{-2}$ s$^{-1}$ | Ph. Index $\Gamma$ | $\chi^2_{\rm red}$ (d.o.f.) |
|---|---|---|---|---|
| 20-Mar-2008 | 306 | $12.20^{+1.65}_{-1.65}$ | $1.16 \pm 0.16$ | 0.87 (13) |
| 21-Mar-2008 | 189 | $8.77^{+1.33}_{-1.39}$ | $1.53 \pm 0.17$ | 467 (48.2)[b] |
| 22-Mar-2008 | 261 | $9.48^{+1.13}_{-1.14}$ | $1.41 \pm 0.19$ | 1.34 (11) |

[a]Unabsorbed flux in units of $10^{-12}$. [b]Cash statistic (C-stat) and percentage of Montecarlo realizations that had statistic < C-stat, performing $10^4$ simulations.

marizes the most important information on XRT observations and the relative spectral fit parameters.

A variability of about 30% in the X-ray flux of the source was observed on a timescale of one day. Notwithstanding the uncertainties due to the errors on fluxes and photon indexes, the XRT data seem to indicate that the X-ray spectrum becomes harder when the source gets brighter, confirming the behavior already observed in this source by Kataoka et al. (2008) during the *Swift*/XRT observations carried out in August 2006. This is a trend often observed in HBL (see e.g. Massaro et al. 2008; Tramacere et al. 2007a; Kataoka et al. 1999), but quite rare for quasar-hosted blazars such as PKS 1510−089.

#### 5.3.2.2 *Swift*/UVOT data

During the three *Swift* pointings, the UVOT instrument (Poole et al. 2008) observed PKS 1510−089 in all its optical (*V*, *B*, and *U*) and UV (UV*W*1, UV*M*2, and UV*W*2) photometric bands. Data were reduced with the `uvotmaghist` task of the HEASOFT package. Source counts were extracted from a circular region of 5 arcsec radius, centered on the source, while the background was estimated from a surrounding annulus with 8 and 18 arcsec radii. In the first two days, only one exposure per filter was available, while three exposures per filter were acquired on the last day. With the only exception of UV*M*2, the source brightness turned out to be quite stable in all the UVOT bands, with variations of a few hundredth of mag, well inside the typical UVOT data uncertainty of 0.1 mag due to both systematic and statistical errors. Average values are: $V = 16.94$, $B = 17.19$, $U = 16.31$, UV$W1 = 16.64$, and UV$W2 = 16.55$. The UV*M*2 frames have low signal-to-noise ratios, thus the source magnitude in this band presents a larger dispersion. The average value is UV$M2 = 16.47 \pm 0.14$.

### 5.3.3 Radio-to-optical observations by the GASP-WEBT

PKS 1510–089 is one of the 28 $\gamma$-ray-loud blazars that are regularly monitored by the GLAST-AGILE Support Program (GASP) of the Whole Earth Blazar Telescope (WEBT). Optical and near-IR data are collected as already calibrated magnitudes, according to a common choice of photometric standards from Raiteri et al. (1998). Radio data are provided as calibrated flux densities. The reference optical band for the GASP is the *R* band. The corresponding light curve in January–April 2008 is shown in the Fig. 5.5, with the data provided by the following observatories: Abastumani, Calar Alto[1], Crimean, Lowell (Perkins), Lulin, Roque de los Muchachos (KVA and Liverpool), San Pedro Martir, St. Petersburg, Torino. The source showed intense activity during the entire considered period, with several episodes of fast variability. At the beginning of the optical observing season, the January observations indicate that the source was in a faint state, around $R = 16.6$ mag. A fast brightening of $\sim 1.3$ mag in 8 days led the source to $R = 15.3$ mag on 15 February. This was followed by a $\sim 0.6$ mag dimming in 4 days. Other minimum brightness states were observed on 23 March and in late April, while peaks were detected on March 29 and April 11.

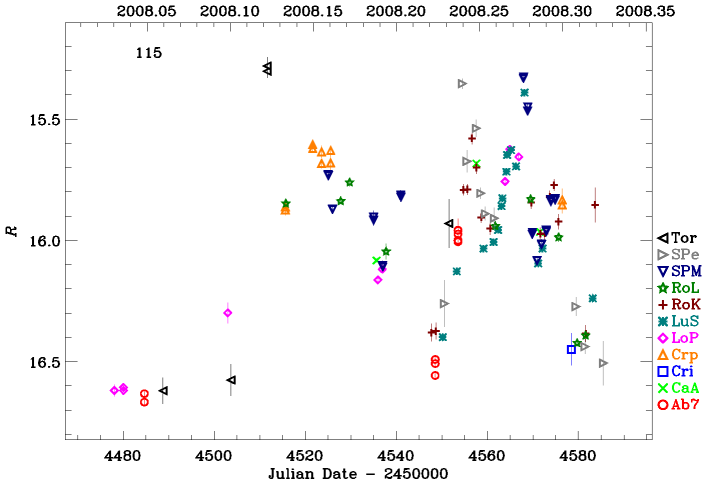


**Figure 5.5:** Optical light curve of PKS 1510−089 obtained by the GASP–WEBT during the period January–April 2008. The different symbols refer to different observatories [D'Ammando et al. 2009b].

Near-IR data in the *JHK* bands were taken at Campo Imperatore and Roque de los Muchachos (Liverpool). Millimetric flux densities at 345 and 230 GHz

[1]Calar Alto data were acquired as part of the MAPCAT (Monitoring AGN with Polarimetry at the Calar Alto Telescopes) project.

came from the SubMillimeter Array (SMA) on Mauna Kea. Centimetric radio data were acquired at Medicina (22 and 8 GHz), Noto (43 GHz), and UMRAO (14.5, 8.0, and 4.8 GHz). In Fig. 5.6 the source radio behavior in different bands is compared to the optical one (top panel). The light curve at high radio frequencies (230–345 GHz) suggests that the mechanism producing the flaring events observed in the optical band in the second half of February and in late March–April 2008 also interested the millimetric emitting zone, with some delay. An estimate of this delay is hampered by the limited data sampling. At lower radio frequencies (22–43 GHz), a hint of flux increase is visible in the second part of the light curve, while the radio flux at 5–15 GHz shows no trend at all. This suggests that the jet regions that are responsible for the emission at the longest radio wavelengths are not affected by the flaring mechanism.

### 5.3.4 Modeling the spectral energy distribution

Figure 5.7 shows the SED for the AGILE-GRID observation period 17–21 March 2008, including quasi-simultaneous optical and radio data by GASP and optical/UV and X-ray data by *Swift*. Since the source brightness over the three days of UVOT observations remained stable, we built a unique SED for the whole period, including contemporaneous data at other frequencies, in particular radio-to-optical data from the GASP. The optical and near-IR data were acquired exactly in the period of the UVOT observations: one *R*-band datum from Roque (KVA) and *J*, *H*, and *K* data from Campo Imperatore. The UVOT and GASP magnitudes were corrected for Galactic extinction by adopting $A_B = 0.416$ mag, and deriving the values in the other bands according to Cardelli et al. (1989). To convert magnitudes into fluxes, we assumed the zero-mag fluxes by Poole et al. (2008) and Bessel et al. (1998).

Radio light curves are less well-sampled than the *R*-band one (see Fig. 5.6), therefore in the SED we show the high-frequency radio data (43–345 GHz) taken within a week from the UVOT observations, while the low-frequency data points were obtained by interpolating between the closest data preceeding and following the UVOT observations. This is justified by the smooth behavior of the low-frequency radio light curves.

The dip in the SED corresponding to the UV*W*1 frequency must be regarded with caution, since it is also found for other blazars with different redshifts and could be systematic. Observations performed by *Swift* and the GASP in March and June 2007, when the source was nearly at the same brightness level, showed the same shape in the near-IR-to-UV part of the SED. A similar trend characterized the optical/UV SED of August 2006 shown by Kataoka et al. (2008). We notice that the shape of the SED in the optical band may be affected by the flux contribution of broad emission lines, including the little blue bump (Neugebauer

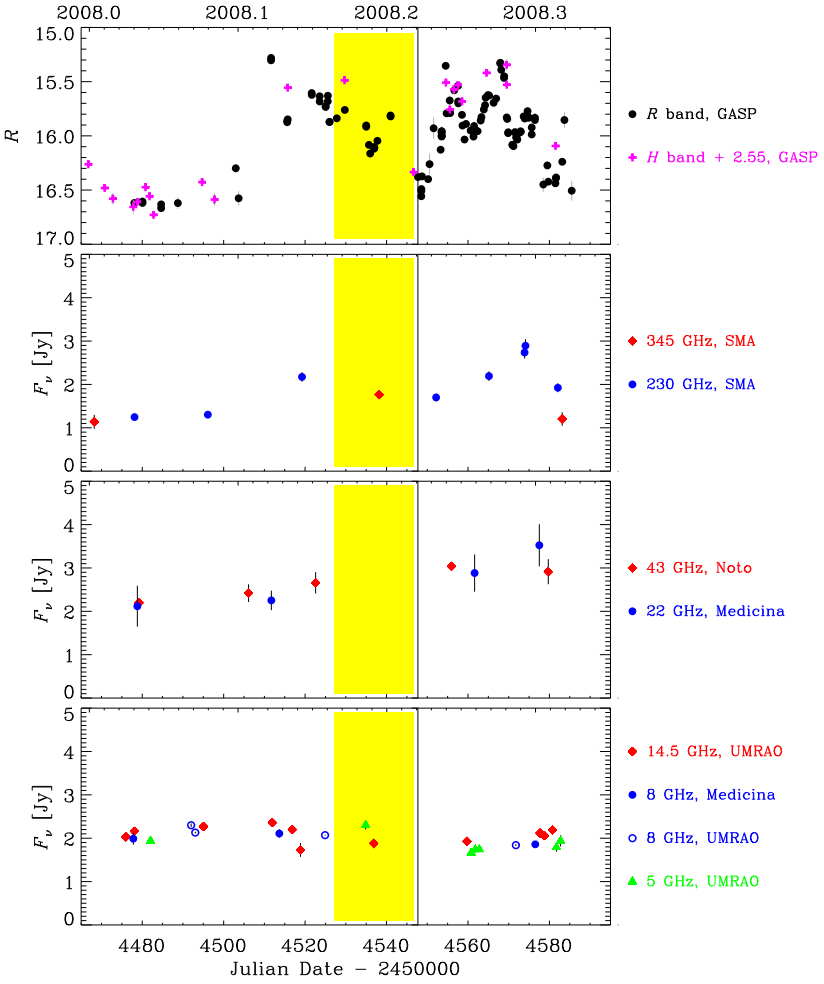


**Figure 5.6:** Optical light curve of PKS 1510−089 (top panel) obtained by the GASP–WEBT during the period January–April 2008 compared to its radio flux densities at different frequencies. The vertical bar indicates the time of the *Swift* observations. The yellow shaded region marks the period also covered by the AGILE observation [D'Ammando et al. 2009a].

et al. 1979; Smith et al. 1988). For the SED we used the *Swift*/XRT data collected on 20 March, the observation closest to the $\gamma$-ray flare and during which the higher X-ray flux was observed.

To model the SED we used a homogeneous one-zone synchrotron self Compton (SSC; Marscher & Gear 1985; Maraschi et al. 1992; Bloom & Marscher 1996) model, plus the contribution of external Compton scattering of both direct-

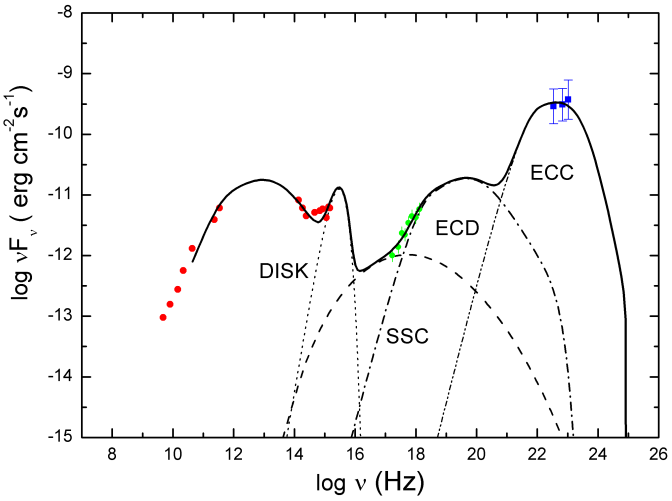


**Figure 5.7:** Spectral energy distribution of PKS 1510−089 for the AGILE-GRID observation of 17–21 March 2008, including quasi-simultaneous GASP radio-to-optical data, the *Swift*/UVOT data of 20–22 March and the *Swift*/XRT data of 20 March. The dotted, dashed, dot–dashed, and double–dot–dashed lines represent the accretion disk black body, the SSC, the ECD, and the ECC radiation, respectively [D'Ammando et al. 2009a].

disk radiation (ECD; Dermer et al. 1992) and photons from the BLR clouds (ECC; Sikora et al. 1994). The strong thermal features usually observed in FSRQs (and in this blazar in particular, see Neugebauer et al. 1978; Smith et al. 1988) at optical/UV frequencies suggest that the environment is rich in the soft photons produced by the accretion disk and/or reprocessed by the BLR. This implies that the energy density of the external soft radiation is much higher than for the synchrotron radiation; therefore, during the $\gamma$-ray flares in FSRQs, the most important processes are the ECC and ECD, and the $\gamma$-ray photon index could be determined by the dominant contribution of the two.

We consider a moving spherical blob of radius $R$, filled by relativistic electrons and embedded in a random magnetic field. We assume that the electron energy density distribution is described by a broken power law:

$$n_e(\gamma) = \frac{K\gamma_b^{-1}}{(\gamma/\gamma_b)^{p_1} + (\gamma/\gamma_b)^{p_2}} \tag{5.2}$$

where $\gamma$ is the electron Lorentz factor assumed to vary between $\gamma_{min}$ and $\gamma_{max}$, $p_1$ and $p_2$ are pre- and post-break electron distribution spectral indexes, respectively,

**Table 5.2:** Parameters for the model used to explain the SED of PKS 1510−089 during the $\gamma$-ray flare of 18–19 March 2008.

| Parameter | Value | Units |
|---|---|---|
| $p_1$ | 2.2 | |
| $p_2$ | 4.6 | |
| $\gamma_{\rm min}$ | 30 | |
| $\gamma_{\rm b}$ | 290 | |
| $\gamma_{\rm max}$ | 5200 | |
| $K$ | 75 | $\rm cm^{-3}$ |
| $R$ | 10 | $10^{15}$ cm |
| $B$ | 3.5 | G |
| $\delta$ | 20.26 | |
| $L_{\rm d}$ | 5 | $10^{45}$ erg $\rm s^{-1}$ |
| $\theta$ | 2.86 | degrees |
| $\Gamma$ | 18 | |

and $\gamma_{\rm b}$ is the break energy Lorentz factor. We assume that the blob contains a comoving random average magnetic field $B$ with a bulk Lorentz factor $\Gamma$ at an angle $\theta$ with respect to the line of sight. The relativistic Doppler beaming factor is then $\delta = [\Gamma(1\text{-}\beta\cos\theta)]^{-1}$, and $K$ is the normalization density parameter into the blob.

We have chosen an angle of view of 0.05 rad in agreement with both the apparent jet velocities derived from multiepoch Very Long Baseline Array (VLBA) observations of the source (Homan et al. 2001; Wardle et al. 2005; Jorstad et al. 2005a; Lister et al. 2009) and the value used by Kataoka et al. (2008).

The short time variability observed in $\gamma$-ray band constrains the size of the emitting region to $R < {\rm c}\,\Delta{\rm t_{var}}\delta/(1+{\rm z}) = 3.86 \times 10^{16}$ cm, where $\Delta t_{\rm var}$ is the observed variation time. An accretion disk characterized by a black body spectrum with a luminosity of $5 \times 10^{45}$ erg $\rm s^{-1}$, as estimated with UV observations by Pian & Treves (1993), at 0.05 pc from the blob is assumed as one of the sources of external target photons. We also assumed a BLR at 0.2 pc, reprocessing 10% of the irradiating continuum. The IC spectra derived from the approximation of the BLR radiation as a black body reproduces quite well more refined spectra calculated by Tavecchio et al. (2008) taking into account a more accurate shape of the BLR.

Assuming a model with synchrotron, SSC and EC components plus the contribution from the accretion disk radiation, the SED of mid-March 2008 can be represented well with input parameters summarized in Table 5.2. In the choice of

the parameters we were guided by the knowledge of the angle of view, the disk luminosity and the simultaneous observations of the synchrotron and IC peak regions (therefore of the synchrotron and IC peak frequencies and luminosities). In addition, the minimum variability timescale gives an indication of the size of the emitting region. However, even if these quantities are quite tightly constrained by fitting the whole SED, the choice of some parameters is not unique because the simultaneous presence of the synchrotron, SSC, ECC, and ECD components leads to a possible partial degeneration of the parameters.

### 5.3.5 X-ray spectral evolution

The spectral evolution detected in X-rays by *Swift* in just two days, soon after the $\gamma$-ray flaring episode is another hint of the rapid change in activity by this source. Usually in FSRQs as PKS 1510–089 only little variability is observed in X-rays on short timescales from hours to days, and also on longer timescales the X-ray spectral shape is almost constant with only small variations. The photon indexes measured by *Swift*/XRT in March 2008, in particular during the first observation, tend to be lower than usually observed in FSRQs ($<\Gamma_{[0.1-2.4\,\mathrm{keV}]}>$ = 1.76 ± 0.06 and $<\Gamma_{[2-10\,\mathrm{keV}]}>$ = 1.65 ± 0.04, Donato et al. 2001) and are more like those observed in some high-redshift quasars (such as RBS 315, Tavecchio et al. 2007a, and Swift J0746+2548, Sambruna et al. 2007). The hard photon indexes of high-redshift blazars could be interepreted in terms of absorption by warm plasma in the region surrounding the source, in agreement with a scenario where in the early evolution phases the quasars are substantially obscured by gas subsequently expelled from the host galaxy by powerful winds (see e.g. Fabian 1999). However, considering the low redshift, this interpretation is unlikely for this source.

Instead, the X-ray spectral evolution observed by *Swift*/XRT could be caused by the contamination of an additional component below ∼2 keV: the soft X-ray excess. In fact, previous observations with *Chandra* (Gambill et al. 2003) and *Suzaku* (Kataoka et al. 2008) seem to indicate the presence of soft X-ray excess in the spectrum of PKS 1510–089. The soft X-ray excess is an emission in excess of the extrapolation of the power law component dominating at higher energies, but the origin of this excess in AGNs is still an open issue (see e.g. D'Ammando et al. 2008a for a discussion of the origin of the soft X-ray excess in radio-quiet AGNs). In the past, it was often associated with the thermal emission of the accretion disk and then related to the big blue bump. However, it has recently been shown that modeling the soft X-ray excess in non-blazar AGNs with a thermal component yields a remarkably constant disk temperature, around 0.1–0.2 keV, regardless of the central black hole mass and luminosity (Gierlinsky & Done 2004; Crummy et al. 2006). Also in Kataoka et al. (2008) the soft X-ray

excess is tentatively described by a black body with temperature kT $\simeq$ 0.2 keV. This result is difficult to explain in any model for the soft excess related to disk continuum emission, as the temperature in any disk model is expected to vary with both the black hole mass and the accretion rates (see Section 2.2).

For FSRQs one possible theoretical explanation is that the soft X-ray excess is a bulk Comptonization feature produced by cold plasma accelerated in a jet (Celotti et al. 2007), even if this feature has never been positively observed until now. In BL Lac objects the radiative environment is instead too weak to produce the soft X-ray excess via bulk Compton and the soft X-ray excess is likely related to the high-energy tail of the synchrotron emission.

The change in the photon index observed during the *Swift*/XRT observations could stem from the spectral shape of the inverse Compton component in X-ray remaining roughly constant, but the amount of contamination from the soft excess emission varies. The contribution of the soft X-ray excess would be more significant when the source gets fainter, affecting the spectrum at higher energies. Unfortunately, the brief exposure of the *Swift* observation does not allow a detailed spectral modeling of this feature.

One possibility for the origin of this hard power law in PKS 1510−089 is that the photon index observed in X-rays results from the combination of the synchrotron self Compton and external Compton emission, hence from the mismatch of the spectral slopes of these two components, not to a real soft X-ray excess. This is the solution that the data presented in this paper would favor. In this context, the spectral evolution during the three *Swift*/XRT observations could come from the change in contribution of one of the two components and therefore from a different variability of the SSC and EC components.

### 5.3.6 Thermal emission components

Even if the SED of the blazars are usually dominated by the beamed nonthermal jet radiation, some of them show the signature of Seyfert-like features such as the little and the big blue bumps. The little blue bump is usually observed in quasars between $\sim$ 2000 Å and $\sim$ 4000 Å in the rest frame and likely stems from the contribution of Fe II and Mg II emission lines and the Balmer continuum produced in the broad line region (Wills et al. 1985). The big blue bump instead is associated with a rise in the UV band commonly interpreted as thermal emission from the accretion disk (see e.g. Laor 1990). Evidence of these thermal components has been found in other quasar-like blazars, such as 3C 273 (Grandi and Palumbo 2004; Türler et al. 2006), 3C 279 (Pian et al. 1999) and 3C 454.3 (Raiteri et al. 2007).

The presence of the emission by the accretion disk is consistent with the scenario in which the seed photons for the IC producing the $\gamma$-rays are external

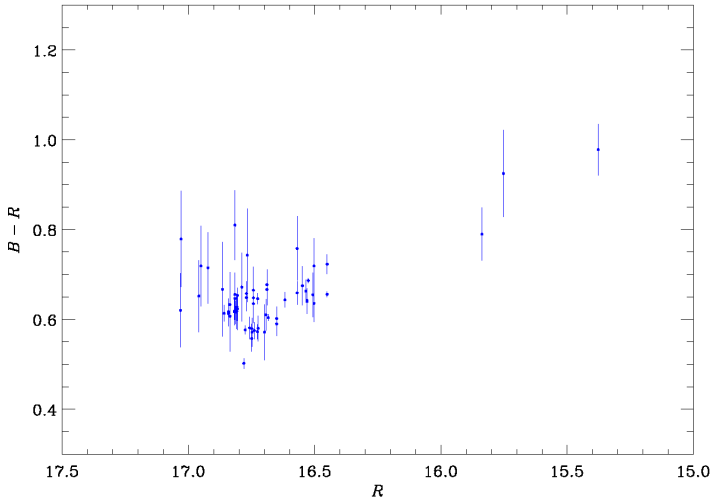


**Figure 5.8:** $B - R$ color index versus $R$ band magnitude for PKS 1510–089 obtained with archive data of the Torino Observatory [D'Ammando et al. 2009a].

to the relativistic jet, but it is usually not observed because hidden by the beamed variable synchrotron emission. The fact that the synchrotron component of PKS 1510−089 peaks around $10^{13}$ Hz (see Bach et al. 2007; Nieppola et al. 2008) allows us to observe these thermal features in this source. In fact, around $10^{15}$ Hz, a rising emission is visible in the spectrum and is likely a manifestation of the big blue bump produced by the accretion disk, as already discussed for this source by Malkan & Moore (1986) and Pian & Treves (1993); moreover, a hint of the little blue bump seems to appear in the SED of the source at $10^{14.5}$ Hz.

Given the redshift of PKS 1510–089, the H$\alpha$, H$\beta$, Fe II, and Mg II lines mostly contribute to the observed spectrum between $10^{14.2}$ and $10^{14.8}$ Hz, and together with the disk emission, could explain the excess of emission observed around $10^{14.5}$ Hz and not modeled from the other components represented in the SED. Moreover these non-jet components in the blue part of the spectrum of this blazar have already been observed by Neugebauer et al. (1979) and Smith et al. (1988) and it agrees with the redder-when-brighter behavior shown by the $B - R$ index versus $R$ band plot in Fig. 5.8. The plot has been obtained with archive data stored at the Torino Observatory.

### 5.3.7 Energetics and alternative model

Finally, to estimate the energetics of PKS 1510–089, we computed the isotropic luminosity in the $\gamma$-ray band, comparing it with the Eddington and bolometric luminosity and the total power transported by the jet. For a given source with redshift $z$, the isotropic emitted luminosity in the energy band $\epsilon$ is defined as

$$L(z)_{\epsilon} = \frac{4\pi F d_{\rm l}^2(z)}{(1+z)^{(1-\alpha_\gamma)}}\,, \tag{5.3}$$

where, in our case, $\epsilon$ is the $\gamma$-ray energy band with $E_{\rm min} = 100$ MeV and $E_{\rm max} = 10$ GeV, $\alpha_\gamma = \Gamma - 1$, $F$ the $\gamma$-ray energy flux between $E_{\rm min}$ and $E_{\rm max}$, calculated from the photon flux $F_\gamma$ ($E > 100$ MeV) as suggested by Ghisellini et al. (2009a):

$$F = 1.6 \times 10^{-12} \frac{\alpha_\gamma F_\gamma}{1-\alpha_\gamma}[100^{1-\alpha_\gamma} - 1]\,. \tag{5.4}$$

The luminosity distance is given by

$$d_{\rm l}(z_1, z_2) = (1+z_2)^2 \times \frac{c/H_0}{1+z_2} \int_{z_1}^{z_2} [E(z)]^{-1} dz\,, \tag{5.5}$$

where $z_1 = 0$, $z_2 = z_{\rm src}$, and

$$E(z) = \sqrt{\Omega_{\rm m}(1+z)^3 + (1-\Omega_{\rm m}-\Omega_\Lambda)(1+z)^2 + \Omega_\Lambda} \tag{5.6}$$

where $H_0$ is the Hubble constant, and $\Omega_{\rm m}$ and $\Omega_\Lambda$ are the contribution of the matter and of the cosmological constant, respectively, to the density parameter. Using a luminosity distance $d_L = 1915$ Mpc, a $\Lambda$CDM cosmology with $H_0 = 71$ km s$^{-1}$ Mpc$^{-1}$, $\Omega_{\rm m} = 0.27$, $\Omega_\Lambda = 0.73$ and the average $\gamma$-ray flux observed by the AGILE-GRID during 17–21 March 2008, we obtained an isotropic luminosity $L_\gamma^{\rm iso} = 5.3 \times 10^{47}$ erg s$^{-1}$ for PKS 1510–089 ($z = 0.361$).

The power carried by the jet in the form of magnetic field ($L_{\rm B}$), cold protons ($L_{\rm p}$), relativistic electrons ($L_{\rm e}$), and produced radiation ($L_{\rm rad}$), are

$$L_{\rm p} = \pi R^2 \Gamma^2 c \int [N(\gamma)\, m_p\, c^2\, d\gamma] = 3.6 \times 10^{45}\ {\rm erg\ s^{-1}} \tag{5.7}$$

$$L_{\rm e} = \pi R^2 \Gamma^2 c \int [N(\gamma)\, \gamma\, m_e\, c^2\, d\gamma] = 1.5 \times 10^{44}\ {\rm erg\ s^{-1}} \tag{5.8}$$

$$L_{\rm B} = \pi R^2 \Gamma^2 c\, U_{\rm B} = 1.5 \times 10^{45}\ {\rm erg\ s^{-1}} \tag{5.9}$$

$$L_{\rm rad} \simeq L_{\rm iso}\Gamma^2/\delta^4 = 5.3 \times 10^{45}\ {\rm erg\ s^{-1}}\,, \tag{5.10}$$

where $U_B$ is the magnetic energy density. Therefore the total power transported by the jet is $P = L_B + L_p + L_e + L_{rad} = 1.1 \times 10^{46}$ erg s$^{-1}$.

Assuming a black hole mass $M_{BH} = 4.5 \times 10^8$ M$_\odot$ for the source (Woo & Urry 2002), we obtain an Eddington luminosity

$$L_{Edd} = \frac{4\pi G c m_H}{\sigma_T} M_{BH} = 5.7 \times 10^{46} \text{ erg s}^{-1} \tag{5.11}$$

to be compared with the bolometric luminosity $L_{bol} = 2.4 \times 10^{46}$ erg s$^{-1}$ reported in Woo & Urry (2002).

An alternative theoretical model has recently been proposed by Kataoka et al. (2008) to interpret the data of PKS 1510–089 collected during August 2006, with the high-energy emission originated by the Comptonization of infrared radiation produced by the molecular torus surrounding the central engine and suggesting that the soft X-ray excess could be produced by the IC scattering of external photons by a population of cold electrons, as discussed by Begelman et al. (1997) and Celotti et al. (2007). Our data do not seem to rule out this alternative model, but this is not the best situation for testing this hypothesis. In fact, we do not have simultaneous observations in FIR band that can confirm the excess detected by IRAS (Tanner et al. 1996), interpreted by Kataoka et al. (2008) as due to dust radiation from the nuclear torus and assumed to be the main source of seed photons for the IC mechanism. Moreover, the bulk Comptonization feature should not be observable during a high activity state of the source, such as observed in mid-March 2008, because overwhelmed by the SSC and ECD emission.

Further X-ray observations with XMM-*Newton* and *Suzaku*, simultaneously with the optical monitoring by means of the REM Telescope and WEBT Consortium, could give strong indications of the emission mechanisms involved in this source, in particular of the real nature of the soft X-ray excess, Seyfert-like features in the spectrum, and the possibility of the bulk Comptonization feature.

Finally, with two $\gamma$-ray satellites, AGILE and *Fermi*, in orbit at the same time, we will be able to study the source behavior at high energies in detail on a long timescale, even if a wide multiwavelength coverage is needed to achieve a complete understanding of the structure of the jet, the origin of the seed photons for the inverse Compton process, and all the emission mechanisms working in this blazar.

## 5.4 The 2009 observations

After the rapid flaring episodes detected by AGILE and *Fermi* in the period 2007–2008, an extraordinary $\gamma$-ray activity from PKS 1510−089 was detected

by AGILE during March 2009, with several flaring episodes over three weeks. This high $\gamma$-ray activity triggered several *Swift* ToO observations, starting from 11 March 2009. Moreover, the monitoring by GASP-WEBT provided important information from radio-to-optical band and, together with the data collected by REM in near-IR and optical bands, allowed us to obtain a very good coverage in the low-energy part of the broad band spectrum of the source.

### 5.4.1 AGILE observations

The AGILE satellite observed PKS 1510−089 between 1 March 2009 00:01 UT and 31 March 2009 11:41 UT, with the source initially located at $\sim 30^\circ$ off the AGILE pointing direction until to be located at $\sim 50^\circ$ off-axis at the end of the observation period. AGILE-GRID data were analyzed, starting from the Level–1 data, using the AGILE Standard Analysis Pipeline and the AGILE Scientific Analysis Package, with counts, exposure, and Galactic background $\gamma$-ray maps generated with a bin size of $0.25^\circ \times 0.25^\circ$ for photons with energies E > 100 MeV. We selected only the events flagged as confirmed $\gamma$-ray events, and not collected during the South Atlantic Anomaly or with reconstructed directions that form angles with the satellite-Earth vector smaller than $80^\circ$, in order to reduce the $\gamma$-ray Earth albedo contamination.

PKS 1510−089 was detected over the period 1–30 March 2009 at a significance level of 19.9-$\sigma$, with an average $\gamma$-ray flux of $F_{\mathrm{E>100\,MeV}} = (162 \pm 12) \times 10^{-8}$ ph cm$^{-2}$ s$^{-1}$, as derived from a maximum likelihood analysis. Figure 5.9 shows the $\gamma$-ray light curve of March 2009 with 1-day resolution for photons with energy higher than 100 MeV. From a first look to the light curve it is clear that in the first period the source was not active in $\gamma$-rays. In fact, AGILE-GRID did not detect PKS 1510−089 between 1 and 9 March 2009 and only upper limits at 95% confidence level are obtained. Instead, in the period 9–30 March 2009 different flaring episodes were detected and these flares could be an overlapping of different events. The peak level of activity with daily integration was $F_{\mathrm{E>100\,MeV}} = (702 \pm 131) \times 10^{-8}$ ph cm$^{-2}$ s$^{-1}$ on 25 March 2009. This is the highest $\gamma$-ray flux observed by this source and one of the highest from a blazar. We note that the increasing of the error on the flux estimation throughout the whole observation period is related to the fact that with the increase of the off-axis angle between the center of the FoV of the GRID and the position of the source, the possible background contamination and the GRID calibration uncertainties become higher.

The $\gamma$-ray spectrum during the first period of activity detected by AGILE (9–16 March 2009) can be fitted with a power law of photon index $\Gamma = 2.08 \pm 0.15$, while considering only the period of highest activity (24–27 March) the photon index is $\Gamma = 1.80 \pm 0.17$. The photon index is obtained with the least

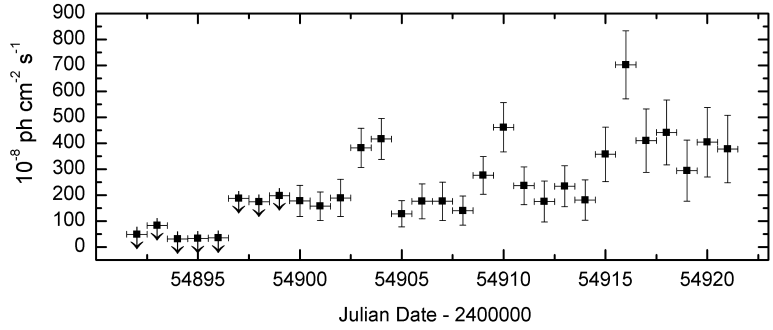


**Figure 5.9:** AGILE $\gamma$-ray light curve between 1 and 30 March 2009 at 1-day resolution for E > 100 MeV. The downward arrows represent 2-$\sigma$ upper limits [D'Ammando et al. 2009b].

squares method by considering four energy bins: 100–200 MeV, 200–400 MeV, 400–1000 MeV, 1–3 GeV. Comparing also with the photon index measured by *Fermi*-LAT over the first three months of observations ($\Gamma = 2.48 \pm 0.05$; Abdo et al. 2009d), these values confirm a possible hardening of the $\gamma$-ray spectrum during the very high activity detected around 25–26 March 2009. Moreover, we note that the photon index obtained for the period 24–27 March 2009 is very similar to that observed by AGILE during the rapid flare of 17–21 March 2008 ($\Gamma = 1.81 \pm 0.34$).

## 5.4.2 *Swift* observations

The *Swift* satellite performed 14 ToO observations of PKS 1510−089 between 11 and 30 March 2009. The observations were performed with all the three onboard instruments: the X-ray Telescope (XRT; 0.2–10.0 keV), the UltraViolet Optical Telescope (UVOT; 170-600 nm), and the Burst Alert Telescope (BAT; 15–150 keV).

### 5.4.2.1 *Swift*/XRT data

The XRT data were processed with standard procedures (`xrtpipeline` v0.12.1), filtering, and screening criteria by using the `Heasoft` package (v.6.6.1). The source count rate was low during the whole campaign (count rate < 0.5 counts $s^{-1}$), so we only considered photon counting (PC) data and further selected XRT

event grades 0–12. Pile-up correction was not required. Source events were extracted from a circular region with radius of 20 pixels (1 pixel $\sim$ 37″), while background events were extracted from a circular region with radius 60 pixels away from background sources. Ancillary response files were generated with `xrtmkarf`, and account for different extraction regions, vignetting and PSF corrections. We used the spectral redistribution matrices v011 in the Calibration Database maintained by HEASARC. All spectra were rebinned with a minimum of 20 counts per energy bin to allow $\chi^2$ fitting within XSPEC (v12.4.1).

We fit the individual spectra with a simple absorbed power law, with a neutral hydrogen column fixed to its Galactic value ($6.89 \times 10^{20}$ cm$^{-2}$; Kalberla et al. 2005). The fit results are reported in Table 5.3.

**Table 5.3:** Observation log and fitting results of *Swift*/XRT observations of PKS 1510−089 during March 2009. Power law model with $N_{\rm H}$ fixed to Galactic absorption is used.

| Obs. Date | Exp. Time (sec) | Ph. Index $\Gamma$ | Flux 2–10 keV ($\times 10^{-12}$ erg cm$^{-2}$ s$^{-1}$ ) | $\chi^2_{\rm red}$ (d.o.f.) |
|---|---|---|---|---|
| 11-Mar-2009 | 4890 | $1.59 \pm 0.10$ | $5.90^{+0.42}_{-0.52}$ | 0.94 (36) |
| 12-Mar-2009 | 4842 | $1.53 \pm 0.09$ | $6.98^{+0.36}_{-0.50}$ | 0.92 (41) |
| 17-Mar-2009 | 4869 | $1.56 \pm 0.11$ | $5.59^{+0.58}_{-0.38}$ | 0.99 (31) |
| 18-Mar-2009 | 4777 | $1.42 \pm 0.10$ | $6.35^{+0.46}_{-0.57}$ | 1.12 (30) |
| 19-Mar-2009 | 2501 | $1.63 \pm 0.15$ | $5.42^{+0.71}_{-0.58}$ | 1.07 (16) |
| 20-Mar-2009 | 2010 | $1.39 \pm 0.21$ | $6.43^{+0.81}_{-1.00}$ | 1.21 (9) |
| 22-Mar-2009 | 2242 | $1.47 \pm 0.17$ | $5.97^{+0.69}_{-0.58}$ | 0.95 (13) |
| 22-Mar-2009 | 2580 | $1.64 \pm 0.19$ | $7.41^{+1.07}_{-0.97}$ | 1.00 (9) |
| 23-Mar-2009 | 2640 | $1.51 \pm 0.16$ | $5.46^{+0.70}_{-0.63}$ | 0.95 (15) |
| 24-Mar-2009 | 1972 | $1.53 \pm 0.16$ | $5.52^{+0.70}_{-0.84}$ | 0.88 (11) |
| 25-Mar-2009 | 2447 | $1.51 \pm 0.12$ | $6.64^{+0.60}_{-0.76}$ | 1.22 (18) |
| 27-Mar-2009 | 2599 | $1.46 \pm 0.19$ | $5.88^{+0.77}_{-0.82}$ | 0.83 (9) |
| 28-Mar-2009 | 2657 | $1.30 \pm 0.14$ | $7.64^{+0.70}_{-0.84}$ | 1.11 (16) |
| 30-Mar-2009 | 2544 | $1.40 \pm 0.13$ | $8.00^{+0.87}_{-0.67}$ | 0.63 (15) |

During the 14 ToO observations performed in March 2009, *Swift*/XRT observed the source in an intermediate state with a 2.0–10.0 keV flux in the range $(5.4 - 8.0) \times 10^{-12}$ erg cm$^{-2}$ s$^{-1}$ [$(7.5 - 10.8) \times 10^{-12}$ erg cm$^{-2}$ s$^{-1}$ in the 0.3–10 keV energy range]. Compared to the optical and $\gamma$-ray activity, the X-ray flux observed by XRT is not much variable and seems not to be strongly correlated with the high optical and $\gamma$-ray activity, even if an increase of the X-ray flux after 27 March 2009, with a hint of hardening of the spectrum, is observed. A similar harder-when-brighter behaviour in X-rays was observed for PKS 1510−089

in August 2006 and March 2008. The lack of X-ray/$\gamma$-ray correlation could be justified by the fact that the X-ray photons are likely to originate mostly in the low-energy part of the external Compton emission component. Therefore the X-ray spectral index seems to reflect the change in the low-energy tail of the electron distribution.

#### 5.4.2.2 *Swift*/UVOT data

During the *Swift* pointings, the UVOT instrument (Poole et al. 2008) observed PKS 1510−089 in all its optical ($V$, $B$, and $U$) and UV (UV$W1$, UV$M2$, and UV$W2$) photometric bands. Data were reduced with the `uvotmaghist` task of the HEASOFT package. Source counts were extracted from a circular region of 5 arcsec radius, centered on the source, while the background was estimated from a surrounding annulus with 8 and 18 arcsec radii. In Figure 5.13 the magnitude collected by UVOT are reported with blue circles.

#### 5.4.2.3 *Swift*/BAT data

As part of its normal operations, the BAT onboard *Swift* collects data over a wide area of the sky in its survey mode. The survey data in the 15–50 keV band is used to produce sky images in which hard X-ray sources can be detected using the standard *Swift* analysis software. During March 2009, we detected two short flaring episodes from PKS 1510−089. The first covered approximately 2 days beginning MJD 54898 (8 March 2009), with an average count rate of (0.006 ± 0.002) cnt/s/cm$^2$ (15–50 keV), which corresponds to 28 mCrab and peaking on 9 March 2009 at 40 mCrab (Krimm et al. 2009a). A second weaker episode occurred on MJD 54919 (29 March 2009), where the average count rate was (0.003 ± 0.001) cnt/s/cm$^2$, corresponding to 15 mCrab. Since this time, we have seen flares of at least 20 mCrab and 3-$\sigma$ significance on two other days: MJD 55057 (14 August 2009) and 55063 (20 August 2009).

As comparison we report that during March 2008, *Swift*/BAT recorded flaring episodes from PKS 1510−089 on MJD 54512 (16 February 2008), 54517 (21 February 2008) and 54520 (24 February 2008), with count rates of approximately (0.005 ± 0.0015) cnt/s/cm$^2$ on each of those observations.

It is interesting to note that the outburst detected by *Swift*/BAT in the 15–50 keV energy band occurred on 9 March 2009 (Fig 5.10), just at the beginning of the $\gamma$-ray activity observed by AGILE. On other hand, no significative sign of activity is detected by BAT simultaneously with the highest $\gamma$-ray flare detected by AGILE.

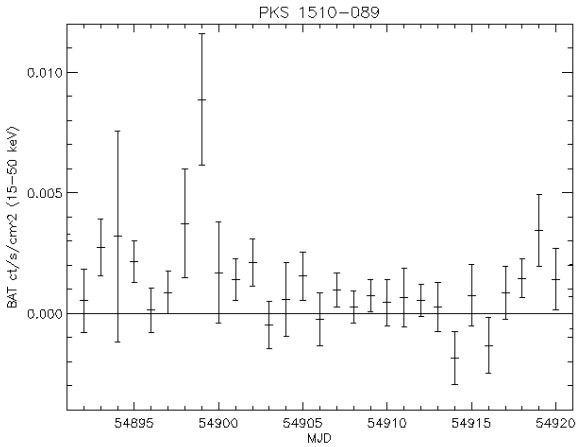


**Figure 5.10:** *Swift*/BAT light curve of PKS 1510−089 in the energy range 15–50 keV between 2 and 30 March 2009.

### 5.4.3 Radio, near-IR and optical observations

PKS 1510−089 is continuosly monitored by the GASP-WEBT Consortium and, considering the high activity observed in the past two years, this source is one of the high priority target of their monitoring program. Optical and near-IR data are collected as already calibrated magnitudes, according to a common choice of photometric standards from Raiteri et al. (1998). The reference optical band for the GASP is the *R*-band. The data are provided by the following GASP observatories: Abastumani, Calar Alto, Castelgrande, L'Ampolla, La Silla (MPG/ESO), Lulin (SLT), Roque (KVA and LT), San Pedro Martir, St. Petersburg, Valle d'Aosta. Conversion of magnitudes into de-reddened flux densities was obtained by adopting the Galactic absorption value $A_B = 0.416$ from Schlegel et al. (1998), the extinction laws by Cardelli et al. (1989) and the magnitude-flux calibrations by Bessell et al. (1998).

The GASP observation in *R*-band showed that after a low intensity period in February 2009, the optical activity of the source is greatly increased in March 2009 with an intense flare on 26–27 March (Fig. 5.11). Near-IR data in the *JHK* bands were taken at Campo Imperatore and Roque de los Muchachos (Liverpool), whereas WEBT data in *BVI* bands were taken at Castelgrande, La Silla and St. Petersburg. Data collected by GASP and WEBT observatiories during March 2009 are reported in Figure 5.13 with red diamonds and magenta triangles, respectively.

Millimetric flux densities at 230 GHz came from the SubMillimiter Array (SMA) on Mauna Kea. Centrimetric radio data were acquired at Metshäovi (37

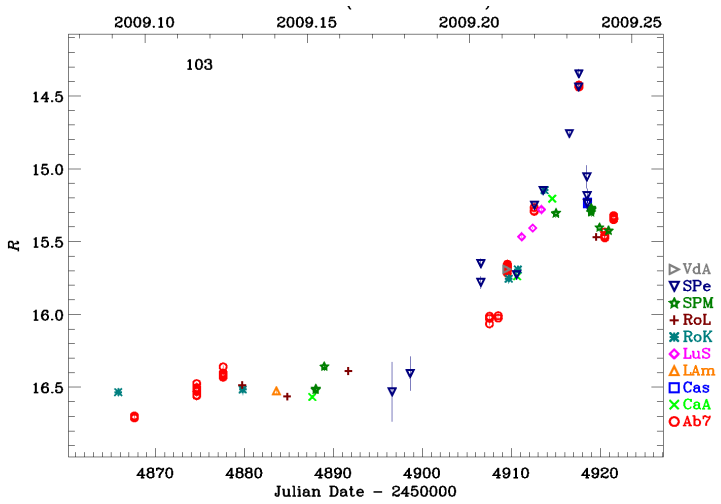


**Figure 5.11:** *R*-band light curve obtained by GASP during the period February–March 2009. Different symbols refer to different observatories [D'Ammando et al. 2009b].

GHz), Medicina (22 GHz), and UMRAO (14.5, 8 and 5 GHz). Figure 5.12 show the optical light curve of PKS 1510−089 compared with the radio data of March 2009. Taking into account also the sparse radio coverage no clear sign of activity in radio bands is observed during March 2009. However, the radio data acquired at Metshäovi at 37 GHz in April–May 2009 showed that the increase of activity marginally observed also in Fig 5.12 and starting at the beginning of March 2009 (JD $\sim$ 2454905) has continued gradually in April–May 2009, reaching a flux density of 3.47 mJy on 29 April 2009 (JD 2454951.5) and peaking at 4.02 mJy on 15 May 2009 (JD 2454969.4). The increase of flux density observed at 37 GHz confirms that the mechanism producing the $\gamma$-ray flaring events also interested the mm/cm emitting region, as already observed in March–April 2009 during the period soon after the previous $\gamma$-ray flare of PKS 1510−089 detected by AGILE. The delay between the $\gamma$-ray and radio emission peaks is not simple to be estimated because, considering the high number of flares observed in $\gamma$-rays in the first half of 2009 by AGILE and *Fermi*, it is not simple to associate the radio outburst with a specific $\gamma$-ray event.

Moreover, in the same period of the GASP observations photometric optical and near-IR observations were carried out with REM (Zerbi et al. 2004), a robotic telescope located at the ESO Cerro La Silla observatory (Chile). The REM telescope has a Ritchey-Chretien configuration with a 60 cm f/2.2 primary and an overall f/8 focal ratio in a fast moving alt-azimuth mount providing two stable Nasmyth focal stations. At one of the two foci, the telescope simultane-

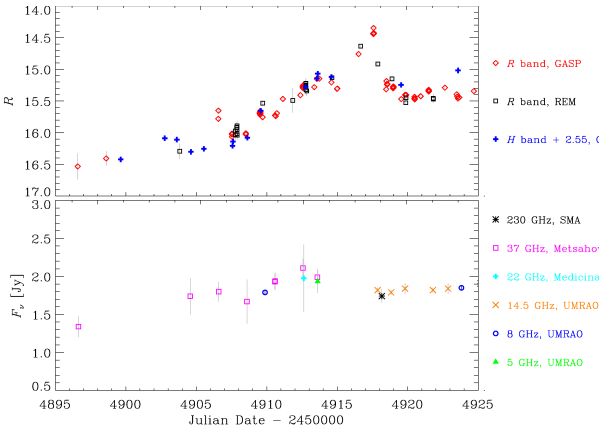


**Figure 5.12:** *R*-band light curve of PKS 1510−089 obtained by GASP and REM during March 2009, together with the *H* band data by GASP (top panel) compared with the radio flux densities at different frequencies (bottom panel).

ously feeds, by means of a dichroic, two cameras: REMIR for the NIR (Conconi et al. 2004) and ROSS (Tosti et al. 2004) for the optical. Both the cameras have a field of view of 10 × 10 arcmin and imaging capabilities with the usual NIR (z', J, H, and K) and Johnson-Cousins VRI filters. The REM software system (Covino et al. 2004) is able to manage complex observational strategies in a fully autonomous way. All raw optical/NIR frames obtained with REM telescopes were then corrected for dark, bias, and flat field following standard recipes. Instrumental magnitudes were obtained via aperture photometry and absolute calibration has been performed by means of secondary standard stars in the field. A similar behaviour of the optical light curve collected by GASP-WEBT was observed by the REM telescope (reported in Figure 5.13), with an achromatic variation in the second half of March in the near-IR (*JHK*) and optical (*BVR*) bands, suggesting that a unique mechanism is responsible of the flux enhancement observed from near-IR to optical.

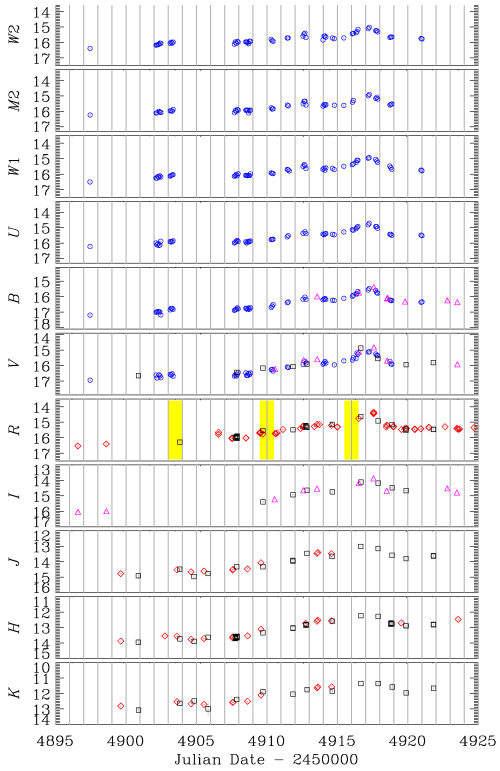


**Figure 5.13:** Light curves collected in NIR, optical and UV bands, between 1 and 31 March 2009. Blue circles represent the UVOT data in *U*, *B*, *V*, UV*W*2, UV*M*2, UV*W*1 filters. Red diamonds represent GASP data in *R, J*, *H*, and *K* bands. Magenta triangles represent WEBT data in *B*, *V*, *I* bands. REM data in *V*, *R*, *I*, *J*, *H*, *K* bands are reprented with black squares. Yellow regions in *R*-band light curve indicate the periods of high activity observed in $\gamma$-rays by AGILE [D'Ammando et al. 2009c].

### 5.4.4 Optical/$\gamma$-ray correlation

In Figure 5.14 we compare the light curve collected in $\gamma$-rays by AGILE with the one collected in *R*-band by GASP-WEBT and REM during March 2009. While the $\gamma$-ray light curve show three different flaring episodes of increasing entity, the optical light curve seems to show a gradual increase in time with a single major outburst on 26–27 March 2009. Unfortunately, the main $\gamma$-ray peak lacks strictly simultaneous optical observations, therefore either a very rapid optical flare occurred simultaneously to the $\gamma$-ray one and we missed it or alternatively the optical peak is delayed with respect to the maximum $\gamma$-ray flare of 1–2 days, suggesting a more complex correlation between the optical and $\gamma$-ray emission, particularly in the FSRQs in which the optical emission could be due to the contribution both of the synchrotron emission and the thermal accretion disk emission.

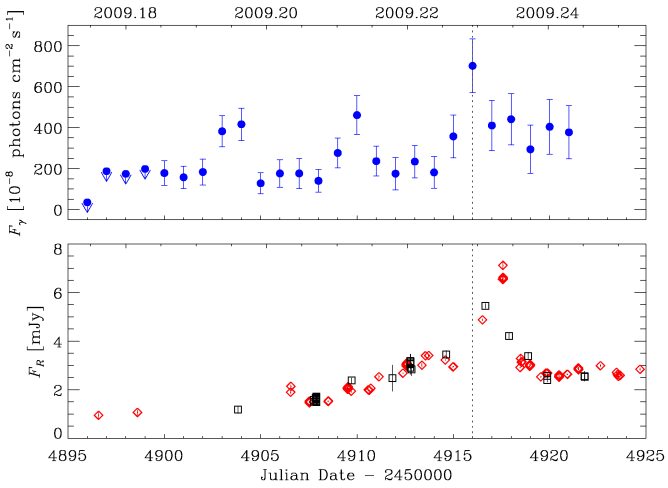


**Figure 5.14:** Comparison between the $\gamma$-ray light curve collected by AGILE in the period 5–30 March 2009 (top panel) with the *R*-band light curve collected by GASP-WEBT and REM in the same period (bottom panel) [D'Ammando et al. 2009c].

### 5.4.5 Broad band spectrum from radio-to-UV

Finally, we built the SED from radio-to UV of PKS 1510−089 for 25–26 March 2009 with the radio data collected by GASP, the optical spectrum in *BVRI* of St. Petersburg, the REM data in *JHK* bands and the data collected by *Swift*/UVOT. In Figure 5.15 this SED is compared with those collected on 20–22 March 2008 and 18 March 2009. We note that the dip at the UV*W*1 frequency it is also found in UVOT observation of other blazars with different redshift and could be due

to a systematic intrumental origin and not an astrophysical signature. In fact, it could be due to the fact that the count rate to flux conversion factor (CF) used in the UVOT reduction is obtained from GRB models (see Poole et al. 2008), valid only for a maximum reddening B-V of 0.03. For blazars with a larger reddening B-V (like PKS 1510−089) some systematics effects could arise.

Leaving the dip at the UV$W1$ frequency out of consideration, the broad band spectrum of PKS 1510−089 from radio-to-UV during 25-26 March 2009 seems to show a flat spectrum in the optical/UV energy band, suggesting an important contribution of the synchrotron emission in this part of the spectrum during the huge flaring episode and therefore a possible shift of the synchrotron peak, usually observed in this source in the infrared band. The increase of the synchrotron emission leads to the decrease of the evidence of the little and big blue bumps observed in the other SEDs. As for the harden-when-brighter behaviour observed in X-ray during March 2008, this is a behaviour typical of HBL objects and not so common in a FSRQ such as PKS 1510−089.

Moreover, as shown in Figure 5.15, comparing the optical/UV data collected by UVOT on 25 March 2009, during the first UVOT exposure (orange squares), with the data collected on 25-26 March 2009, during the third UVOT exposure (green triangles), a significative flux variation is observed in only 10 hours. Considering that the accretion disk is slowly variable on so short timescales this is another hint of the fact that the optical flare of 26 March is due mainly to the synchrotron emission.

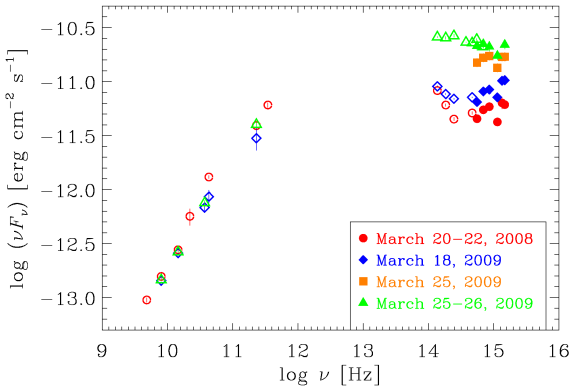


**Figure 5.15:** SED of low-energy part of the spectrum constructed with data collected by GASP-WEBT and *Swift*/UVOT during March 2008 and March 2009 [D'Ammando et al. 2009c].

## 5.5 Summary and remarks

1. In the last two years PKS 1510−089 showed high variability over all the electromagnetic spectrum, and in particular very high $\gamma$-ray activity.

2. AGILE detected rapid flaring episode from PKS 1510−089 in August 2007 and March 2008. Moreover an extraordinary $\gamma$-ray activity was detected in March 2009, with several flaring episodes and a flux that reached $600 \times 10^{-8}$ ph cm$^{-2}$ s$^{-1}$.

3. Observations at optical/UV in March 2008 and March 2009 indicate the presence of Seyfert-like features in the broad band spectrum of PKS 1510−089, such as little blue bump and big blue bump, interpreted as thermal emission from the BLR and the accretion disk, respectively.

4. X-ray observations by *Swift*/XRT in March 2008, soon after a rapid $\gamma$-ray flare showed a harder-when-brighter behaviour usually not observed in FSRQs. A hint of a similar behaviour is observed also during the *Swift*/XRT monitoring of the source in March 2009.

5. The SED from radio-to-UV on 25–26 March 2009 seems to show a flat spectrum in the optical/UV, suggesting an important contribution of the synchrotron emission in this part of the spectrum during the huge flare observed in $\gamma$-rays and therefore a possible shift of the synchrotron peak, usually observed in infrared in this source. The significative flux variations in 10 hours observed among the different UVOT exposures on 25–26 March confirms the hypothesis that the main contribution of the optical/UV flare observed on 26–27 March is due to the synchrotron radiation and not to the accretion disk emission.

6. The comparison of the optical and $\gamma$-ray light curve collected during the very high activity of March 2009 showed a possible delay of the optical emission of 1–2 days with respect to the main $\gamma$-ray peak of 25 March 2009.

7. The spectral indexes measured by AGILE during the March 2008 and March 2009 flares show a hardening of the $\gamma$-ray spectrum with respect to the quiescient state observed in past by EGRET and *Fermi*.

8. After the $\gamma$-ray flare of March 2008 and March 2009 a significant increase in the flux density was observed also at high radio frequencies, suggesting that the same mechanism produces the flaring episodes in radio and $\gamma$-rays, at different times.

Chapter 6

# S5 0716+714

## 6.1 Introduction

S5 0716+714 was discovered in 1979 as the optical counterpart of an extragalactic radio source (Kühr et al. 1981a). Two years later, it was classified as a BL Lac object (Biermann et al. 1981) because of its featureless optical spectrum and high linear polarization. The optical continuum is so featureless that every attempt to determine the spectroscopic redshift of the source has failed. However, by optical imaging of the underlying galaxy in the *I*-band during the quiescent state of the active nucleus, using it as a standard candle, Nilsson et al. (2008) derived a redshift of z = 0.31 ± 0.08. This value is consistent with the redshift z = 0.26 determined by spectroscopy for 3 galaxies close to the location of S5 0716+714 (Stickel et al. 1993).

According to its spectral energy distribution and the classification scheme proposed by Padovani & Giommi (1995), the source belongs to the Intermediate BL Lac (IBL) subclass. In fact, observations by *Beppo*SAX (Tagliaferri et al. 2003; Giommi et al. 1999) and XMM-*Newton* (Foschini et al. 2006; Ferrero et al. 2007) provide evidence for a concave X-ray spectrum in the 0.1–10 keV band, a signature of the presence of both the steep tail of the synchrotron emission and the flat part of the inverse Compton spectrum. The detection in the X-ray band of fast variability only in the soft X-ray component can be interpreted as the contemporary presence of a slowly variable Compton component and a fast and erratic variable tail of the synchrotron component.

S5 0716+714 has been studied intensively at all frequency bands and showed strong variability on both long and short timescales from radio to X-rays (e.g. Wagner et al. 1996; Raiteri et al. 2003, and the references therein). Intra-Day Variability (IDV) was detected in this source in the optical, millimiter and radio bands (e.g. Montagni et al. 2006; Agudo et al. 2006, and the references

therein). The IDV in the different bands seems strongly correlated (Quirrenbach et al. 1991; Wagner & Witzer 1995; Führmann et al. 2008), suggesting that the radio and optical emissions could have a common and intrinsic origin. Radio monitoring by the Very Long Baseline Array (VLBA) telescope of S5 0716+714 showed the presence of more superluminal components during the active state of 2003–2004 (Rastorgueva et al. 2009).

A substantial fraction of the power of S5 0716+714 is emitted in the energy range 0.1–10 GeV and the EGRET instrument onboard the *CGRO* (Hartman et al. 1999) detected the source several times in the $\gamma$-rays (Lin et al. 1995; von Montigny et al. 1995). The integrated flux above 100 MeV varied between (13 ± 5) and (53 ± 13) x $10^{-8}$ photons $cm^{-2}$ $s^{-1}$.

During the first three months of operation *Fermi*-LAT detected the source with an average flux for E > 100 MeV of (16.4 ± 1.4) $\times 10^{-8}$ photons $cm^{-2}$ $s^{-1}$ and a weekly averaged peak of intensity of (29.0 ± 4.2) $\times 10^{-8}$ photons $cm^{-2}$ $s^{-1}$ (Abdo et al. 2009d). Moreover, during the first year of all-sky $\gamma$-ray monitoring no evidence of very significant activity was observed by *Fermi*-LAT. Instead, in April 2008, the MAGIC telescope discovery high flux of VHE $\gamma$-rays from S5 0716+714 (Anderhub et al. 2009b).

S5 0716+714 was observed by AGILE in two different epochs: September–October 2007 and March–May 2008. In particular, during the observations in the period September–October 2007, two $\gamma$-ray flaring episodes were detected by AGILE: the first in mid-September, the other one on 2007 October 22–23. For the first time a bright $\gamma$-ray flare was observed from this source.

In this Chapter we present the analysis of the AGILE data of S5 0716+714 in these two epochs, together with the multiwavelength data collected by *Swift* and GASP-WEBT, with the aim of investigating the correlated variability in different bands, the theoretical interpretation of the spectral energy distributions and the energetics of the source.
The analysis and the results shown are published in Chen et al. (2008), D'Ammando et al. (2008b), Giommi et al. (2008a) and Vittorini et al. (2009).

## 6.2 The 2007 observations

In September 2007, the AGILE satellite was performing its Science Verification Phase and devoted three weeks to the observation of S5 0716+714 between 2007 September 4 14:58 UT and September 23 11:50 UT, for a total pointing duration of ∼16.9 days[1]. In October, following a high flux state in the optical band,

[1]Between 2007 September 15 12:52 UT and September 16 12:42 UT AGILE performed a calibration test on the Crab pulsar and S5 0716+714 was out of the field of view of GRID for two days.

AGILE repointed toward the source and observed S5 0716+714 between 2007 October 24 9:47 UT and November 1 12:00 UT, for a total pointing duration of ~ 8.1 days. Level-1 AGILE-GRID data were analyzed using the AGILE standard Analysis Pipeline, following the procedure described in detail in Section 4.3.6. Counts, exposure, and Galactic background $\gamma$-ray maps were created with a bin-size of $0.3^\circ \times 0.3^\circ$ for photons of energies higher than 100 MeV.

S5 0716+714 was detected by the GRID instrument onboard AGILE in the period 7–12 September 2007, with the source at about 15° off-axis, at a significance level of 9.6-$\sigma$ with an average $\gamma$-ray flux of $(97 \pm 15) \times 10^{-8}$ photons cm$^{-2}$ s$^{-1}$ for E > 100 MeV, as derived from a maximum likelihood analysis (Fig. 6.1) . The peak level of the $\gamma$-ray flux is $(193 \pm 42) \times 10^{-8}$ photons cm$^{-2}$ s$^{-1}$, showing an increase of the flux by a factor four within three days (see Fig. 6.3, top panel). The peak $\gamma$-ray flux observed in mid-September 2007 by AGILE is the highest flux observed from this source and one of the highest ever detected from a BL Lac object.

SuperAGILE observed the source between 7 and 12 September for a total on-source net exposure time of 335 ksec. The source was not detected above 5-$\sigma$ by the SuperAGILE Iterative Removal Of Sources (IROS) algorithm, which was applied to the image in the 20–60 keV energy range. A 3-$\sigma$ upper limit of 10 mCrab was estimated from the observed count rate by a study of the background fluctuations at the position of the source and a simulation of the source and background contributions with IROS.

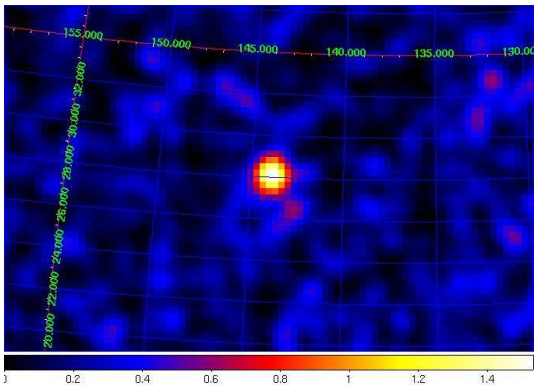


**Figure 6.1:** Gaussian-smoothed counts map of S5 0716+714 in Galactic coordinates integrated over the observing period of most intense activity (2007 September 7–12) [Chen et al. 2008] .

During September–October 2007, S5 0716+714 showed intense activity with strong flaring episodes also in optical band. Moreover, a rare roughly contemporaneous optical-radio outburst was detected by GASP-WEBT, even if seen in

detail the event in the two bands showed a different behaviour: the optical flux presents stronger and faster variations, whereas the radio flux rises and falls in a much smoother way (Villata et al. 2008). The intense $\gamma$-ray flare detected by AGILE in mid-September 2007 triggered optical observations by the GASP-WEBT. S5 0716+714 brightened from $R$ = (12.92 ± 0.01) mag on September 8 to $R$ = (12.58 ± 0.04) mag on September 12 and faded to $R \sim$ 13.01-13.03 mag on September 15 (Carosati et al. 2007). About one month later, the GASP-WEBT observed a bright phase of the source, triggering AGILE and *Swift* ToO observations. In particular, after a rather variable phase, the optical flux in mid-October started to rise, reaching a peak of $R$ = (12.15 ± 0.01) mag ($F_R$ = 45.7 mJy) on October 22.2 (see Fig. 6.3, bottom panel; Chen et al. 2008; Villata et al. 2008). This is the highest optical brightness level ever observed from this source.

At that time S5 0716+714, even if rather off-axis ($\sim 50^\circ$ from the axis), was observed by AGILE and detected in a high $\gamma$-ray state. In particular, between 2007 October 22 12:33 UT and October 23 12:06 UT, the maximum likelihood analysis measured a flux of $F_{\mathrm{E}>100\,\mathrm{MeV}} = (203 \pm 75) \times 10^{-8}$ photons cm$^{-2}$ s$^{-1}$ at a significance level of 4.0-$\sigma$. We note that the large error in the flux estimation is justified by the fact that AGILE has a higher particle background at high off-axis angles, and that the exposure time of the observation is relatively short. After this flaring episode, AGILE observed the source with a dedicated repointing, at an off-axis angle of $\sim 15^\circ$, between October 24 9:47 UT and November 1 12:00 UT. During the ToO period, the AGILE-GRID detected a $\gamma$-ray flux above 100 MeV at a significance level of 6.0-$\sigma$ with an average flux of $F_{\mathrm{E}>100\,\mathrm{MeV}} = (47 \pm 11) \times 10^{-8}$ photons cm$^{-2}$ s$^{-1}$, a factor of four lower than the peak flux of the two flaring episodes observed in mid-September and on 22-23 October. At the start of the AGILE repointing the optical level of S5 0716+714 observed by GASP-WEBT, after a sudden drop of 0.73 mag in 2 days, was relatively low. It confirms the decrease of the activity source observed in $\gamma$-ray band.

Therefore, during 2007 September–October observations AGILE detected S5 0716+714 at two different levels of activity. The $\gamma$-ray spectrum during the high activity state of mid-September can be fitted with a power law of photon index $\Gamma$ = 1.56 ± 0.30, while during the AGILE October ToO the source was in an intermediate $\gamma$-ray activity state and the photon index of the energy spectrum was $\Gamma$ = 1.95 ± 0.54 (Fig. 6.2). The photon index was obtained with the least squares method by considering only three energy bins: 100–200 MeV, 200–400 MeV and 400–1000 MeV.

Notwithstanding the large uncertainties due to the low photon statistics, the different spectral indexes seem to reflect the different levels of activity of the source.

## 6.3 Light curves studies

A comparison between the $\gamma$-ray and optical light curves of S5 0716+714 in September–October 2007 is reported in Fig. 6.3: the top panel shows the $\gamma$-ray light curve with 1 or 2 day resolution for photons above 100 MeV, the bottom panel shows the *R*-band optical light curve as obtained by the GASP-WEBT.

To analyze the $\gamma$-optical correlation, we have applied the Discrete Correlation Function (DCF; see Edelson & Krolick (1988); Hufnagel & Bregman (1992); Peterson (2001)) to the $\gamma$-ray and *R*-band light curves. The DCF is a statistical method developed to analyze unevenly sampled data sets. The *R*-band flux densities were averaged over 0.1 day bins to smooth the intraday variability. The result is shown in Fig. 6.4. The DCF displays a significant peak (DCF $\sim$ 0.9) for a time-lag of –1 day. Notwithstanding the large uncertainty due to poor $\gamma$-ray sampling, this result suggests a possible delay in the $\gamma$-ray flux variations with respect to optical variations of the order of 1 day. The uncertainty in the delay can be estimated by Monte Carlo simulations based on the 'flux randomization / random subset selection' method (see Peterson et al. (2001) and Raiteri et al. (2003)). By performing 2000 simulations we derived a 1-$\sigma$ uncertainty level in the lag of 1.1 days.

Looking at Fig. 6.3, one can see that most of the DCF signal originates from the quasi-simultaneity of the $\gamma$-ray and optical peaks of late October (JD $\sim$ 2454396-397). As for the September AGILE detection, the strong $\gamma$-ray flare lacks strictly simultaneous optical observations since it occurred at both the start of the GASP operation and the optical observing season. However, we notice that when the $\gamma$-ray fluxes are $\leq 120 \times 10^{-8}$ photons cm$^{-2}$ s$^{-1}$, the correspond-

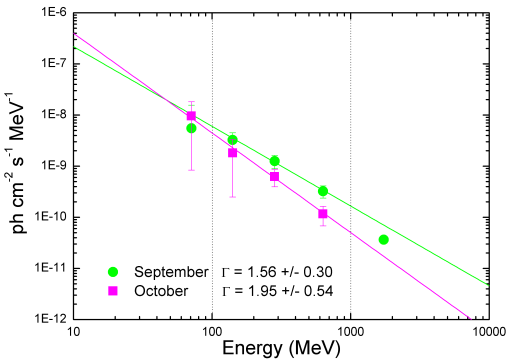


**Figure 6.2:** $\gamma$-ray photon spectrum of S5 0716+714 during the high state of mid-September (green line) and the intermediate state of end of October (magenta line) [Chen et al. 2008].

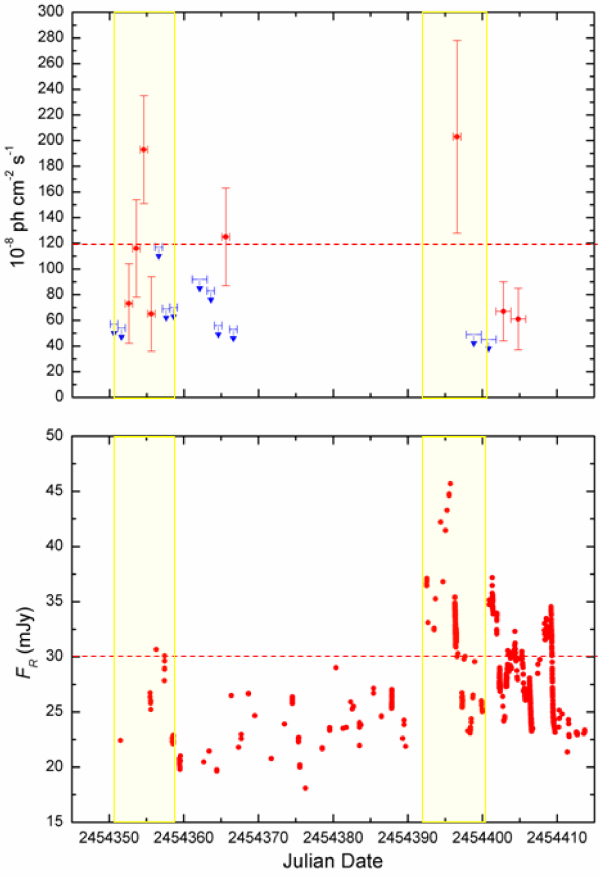


**Figure 6.3:** In the top panel, the AGILE–GRID $\gamma$-ray light curve with 1-day or 2-day resolution for fluxes in units of $10^{-8}$ photons cm$^{-2}$ s$^{-1}$ for E > 100 MeV. The downward arrows represent 2-$\sigma$ upper limits. In the bottom panel, the *R*-band optical light curve as observed by GASP-WEBT. In both panels, the mean flux level is highlighted with horizontal red dashed lines and the yellow shaded regions indicate the two high-activity periods in the $\gamma$-ray band [D'Ammando et al. 2008b].

ing optical flux densities are around 25–30 mJy. In contrast, the October $\gamma$-ray peak reaching $\sim 200 \times 10^{-8}$ photons cm$^{-2}$ s$^{-1}$ has an optical counterpart of 40–45 mJy (see Fig. 6.3). This suggests that a significant optical event could have occurred at the same time as the $\gamma$-ray flare also in September and it was missed.

Moreover, while the ratio between the high and low $\gamma$-ray flux levels is about 2.5, in the optical band the same ratio is of the order of 1.5. Hence, the $\gamma$-ray variability seems to depend on the optical flux density changes roughly quadratically. This would favour a SSC process in the Thomson regime and, together

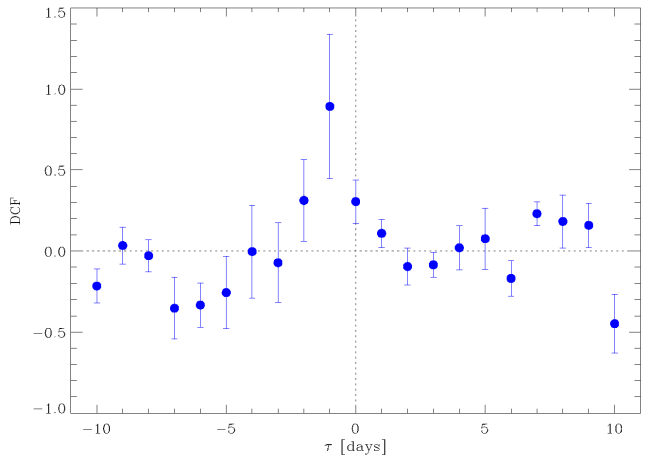


**Figure 6.4:** Discrete correlation function between the $\gamma$-ray and *R*-band light curves for S5 0716+714 in September–October 2007 [Chen et al. 2008].

with the lack of emission lines and the Big Blue Bump in the optical/UV spectrum, concurs to rule out the contribution of an EC process. In case of SSC process, the 1-day time-lag in the $\gamma$-ray emission with respect to the optical emission suggested by the DCF could be due to the light travel time of the synchrotron seed photons that scatter the energetic electrons.

The optical flare detected on 22 October 2007, also triggered 10 *Swift* ToO observations of 2-3 ks each, performed between 23 October and 13 November 2007. The observations were carried out using all three instruments on board *Swift*, even if the hard X-ray flux of the source above 15 keV is below the sensitivity of the BAT instrument for such a short exposure. The average photon index detected in the entire XRT energy range 0.3–10 keV is steeper than 2, showing that the X-ray spectrum is dominated by the synchrotron radiation. However, dividing the energy range in 0.3–4.0 keV and 4.0–10.0 keV bands a different variability is observed, suggesting that the high energy part of the spectrum is due to the rise of the inverse Compton component. The light curves in 0.3–4.0 keV, 4.0–10.0 keV and U bands collected by XRT and UVOT are shown in Fig. 6.5. S5 0716+714 show strong variability (up to a factor $\approx 4$) in the soft-X-ray band, more moderate variations (less than a factor 2) at optical/UV frequencies, and an approximately constant hard X-ray flux. The different variability observed in optical/UV, soft X-ray and hard X-ray seems to suggest the presence of two emission components. Instead, no significant variability is detected in the $\gamma$-ray band by AGILE between 24 October and 1 November 2007.

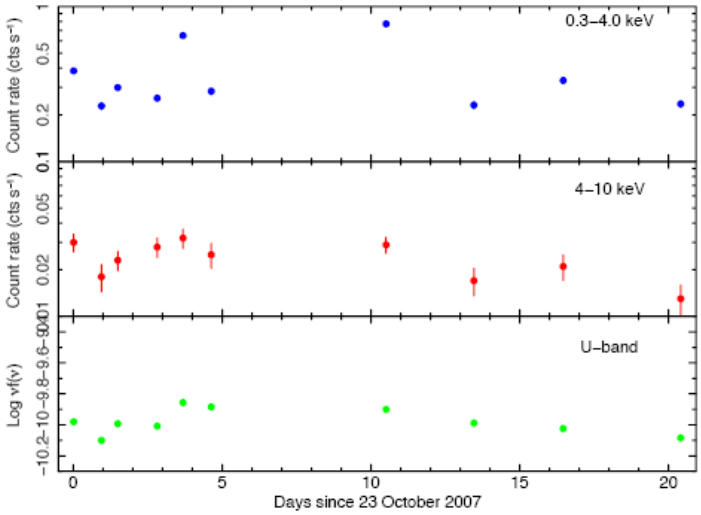


**Figure 6.5:** The light curves of S5 0716+714 in the soft XRT band (0.3–4.0 keV), hard XRT band (4.0–10.0 keV) and in the UVOT U filter, from top to bottom panels. The vertical axis is logarithmic with the same range for all the energy bands [adapted from Giommi et al. 2008a].

## 6.4 Modeling the spectral energy distributions

The multiwavelength data collected by AGILE, *Swift*, and GASP-WEBT during September–October 2007 allowed us to build the Spectral Energy Distribution (SED) and investigate the emission mechanisms at work in this blazar in different periods. The SED with the AGILE and GASP-WEBT data of mid-September 2007 is shown in Fig. 6.6 as green dots. The blue dotted line shows a simple SSC model that fits simultaneous observations of a ground state (Tagliaferri et al. 2003, and references therein) and non-simultaneous EGRET data (empty blue triangles; Lin et al. 1995). Because of the hardness of the $\gamma$-ray spectrum of mid-September 2007 the SED cannot be fitted by a standard one-zone SSC model alone, hence we used a model with two SSC components.

Together with the first SSC component that is slowly variable and reproduces the ground state, we add a faster second SSC component dominating in the optical and $\gamma$-ray bands. Both components are reproduced with a double power law electron distribution: the spectral index is $p_{\rm low}$ from $\gamma_{\rm min}$ to $\gamma_{\rm break}$ and $p_{\rm high}$ above $\gamma_{\rm break}$. The parameters of the two SSC components are reported in detail in Table 6.4. A viewing angle $\theta \sim 2^\circ$ is adopted, according to Bach et al. (2005). The absence of the signatures of IC catastrophe in previous multifrequency observa-

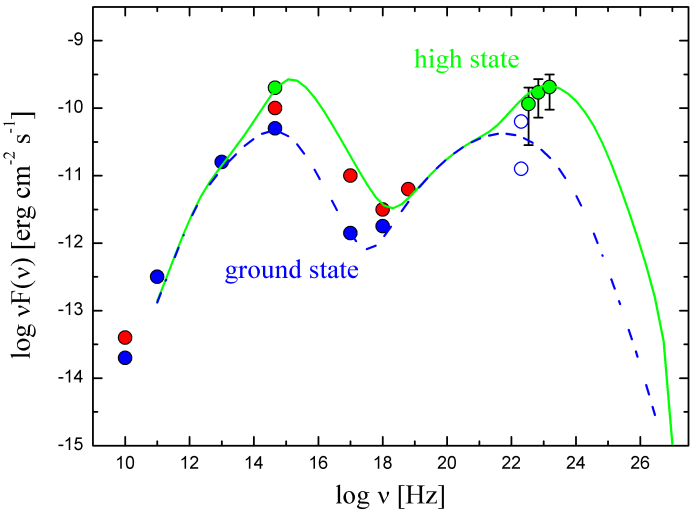


**Figure 6.6:** The SED of S5 0716+714, including GASP-WEBT optical data quasi-simultaneous with a AGILE-GRID $\gamma$-ray observation in September 2007 (green dots). Historical data over the entire electromagnetic spectrum relative to a ground state of the source together with EGRET non-simultaneous data are represented with blue dots. Red dots represent historical data simultaneous with a high X-ray state [Chen et al. 2008].

**Table 6.1:** Parameters for the two SSC components of the SED of mid-September 2007.

| Parameters | 1$^{st}$ SSC comp | 2$^{nd}$ SSC comp | Units |
|---|---|---|---|
| $\delta$ | 14 | 25 | |
| $\Gamma$ | 7.5 | 15 | |
| $R$ | 40 | 40 | [$10^{15}$ cm] |
| $B$ | 1 | 0.5 | [G] |
| $\gamma_{\rm min}$ | 200 | 3 x $10^3$ | |
| $\gamma_{\rm break}$ | 4 x $10^3$ | 6 x $10^3$ | |
| $p_{\rm low}$ | 2.0 | 2.0 | |
| $p_{\rm high}$ | 4.8 | 4.8 | |
| $n_{\rm e}$ | 2.2 | 0.8 | [cm$^{-3}$] |
| $\theta$ | 2 | 2 | [deg] |

tions during states of extreme apparent brightness temperatures provide a lower limit $\delta \geq 14$ for the Doppler factor (Führmann et al. 2008; Ostorero et al. 2006). The faster SSC component is marked by high electron energies with a sharp low energy cut-off. Moreover, high bulk Lorentz factor $\Gamma = 15$ is used in agreement

with Wagner et al. (1996).

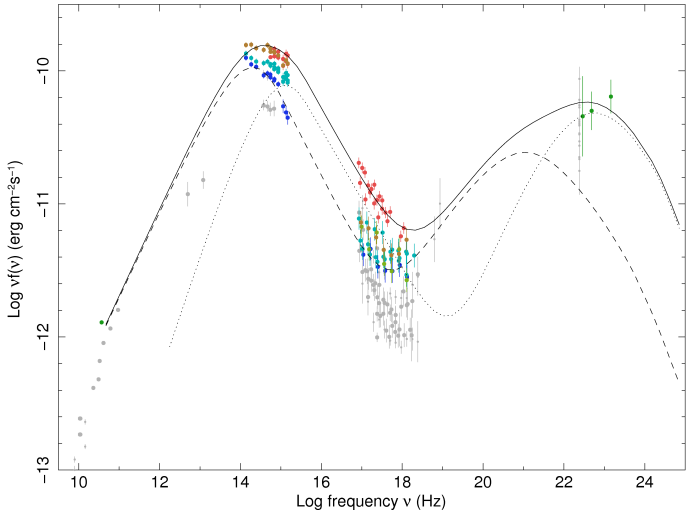


**Figure 6.7:** The SED of S5 0716+714, including *Swift* XRT and UVOT data taken simultaneously with AGILE-GRID $\gamma$-ray data and optical and radio data from Villata et al. 2008 (color) together with non-simultaneous archival data (light grey points). The dashed and dotted lines represent the two SSC components, while the continuous line is their sum [Giommi et al. 2008a]

.

The SED built with all the 10 *Swift* XRT and UVOT observations and the AGILE-GRID data averaged over the period 24 October – 1 November 2007 is shown in Fig. 6.7, together with non-simultaneous archival data. Considering two separate energy bands, 100–400 MeV and 400–1000 MeV, the flux detected by AGILE are $(23 \pm 9) \times 10^{-8}$ photons cm$^{-2}$ s$^{-1}$ and $(6 \pm 2) \times 10^{-8}$ photons cm$^{-2}$ s$^{-1}$, respectively. A rough spectral fitting analysis indicates a spectral index of $\sim 1.8$. The low counting statistic does not allow us to detect small amplitude variability in the $\gamma$-ray band. Instead, the spectral variation of S5 0716+714 observed by *Swift* among the different observations cannot be the result of simple changes in the magnetic field or of the beaming factor in a one-zone homogeneous SSC model. In this case the emission in different bands is expected to vary in a highly correlated way, contrary to what is observed in the optical and X-ray light curves. The different flux variations observed could instead be explained by the presence of two SSC components, one of which constant over the entire period, while the second one highly variable and possibly due to a secondary blob of relativistic plasma including fresh and more energetic particles.
We assumed SSC models with broken power law spectrum for both particle com-

ponents and constant density within a blob of radius $R$. The spectral indexes for the stationary component are $p_{\rm low} = 1.7$ and $p_{\rm high} = 4.2$ and a break Lorentz factor $\gamma_{\rm b} = 2.5 \times 10^3$, the second SSC components have similar spectral indices ($p_{\rm low} = 1.1$ and $p_{\rm high} = 4.05$) with a larger break Lorentz factor $\gamma_{\rm b} = 6.0 \times 10^3$. The magnetic field and the Doppler factor are the same for the two components, $B = 1.1$ G and $\delta = 20$, while the first component has a higher normalization and larger radius ($K = 630.96$ cm$^{-3}$ and $R = 3 \times 10^{16}$ cm) with respect to the second component ($K = 8.91$ cm$^{-3}$ and $R = 1.5 \times 10^{16}$ cm).

Finally, we note that also modeling the SED relative to the flare episode that occurred in October 22 including GASP-WEBT, *Swift* (UVOT and XRT) and AGILE data with a one-zone SSC model fails to reproduce the simultaneous radio, optical, X-ray and $\gamma$-ray observations. Also in this case it is required a two-components model: the first produces the slowly variable radio and hard X-ray emission, whereas the second is responsible for the faster variability in optical/UV, soft X-ray and $\gamma$-ray (see Vittorini et al. 2009). This is in agreement with what found for the SED of mid-September, and also with the different flux variations observed by *Swift*.

## 6.5 Energetics of S5 0716+714

Considering the intense flares detected in September and October 2007, we study its extreme energetics and the possible implications on energy extraction from a rotating black hole (BH). Assuming an isotropic emission, the observed power radiated from a source with luminosity distance $D_L(z)$ is

$$L_{\rm obs} = 4\pi D_L(z)^2 \int d\epsilon F(\epsilon) \tag{6.1}$$

The total power transported by the jet is the sum of contributions by intrinsic radiated power, kinetic energy flow of electrons and cold protons (assuming one proton per emitting electron), and Poynting flux, respectively (see Vittorini et al. 2009; Celotti and Ghisellini 2008):

$$L_{\rm r} = L_{\rm obs}\Gamma^2/\delta^4 = 2 \times 10^{-3}(\delta/15)^{-4}\Gamma_1^2 L_{\rm obs} \text{ erg s}^{-1} \tag{6.2}$$

$$L_{\rm e} = 0.8 \times 10^{43} R_{16}^2 \Gamma_1^2 \ < n_e\gamma >_4 \text{ erg s}^{-1} \tag{6.3}$$

$$L_{\rm p} = 1.4 \times 10^{43} R_{16}^2 \Gamma_1^2 \ < n_p >_1 \text{ erg s}^{-1} \tag{6.4}$$

$$L_{\rm B} = 3.8 \times 10^{43} R_{16}^2 \Gamma_1^2 B^2 \text{ erg s}^{-1} \tag{6.5}$$

Considering the redshift of the source (z = 0.31), the intrinsic radiative luminosity is of the order of $L_r \sim 2 \times 10^{45}$ erg s$^{-1}$. Celotti and Ghisellini (2008) show that in BL Lacs $L_r$ tends to match the contribution of kinetic energy flow of electrons and cold protons plus the Poynting flux. The total power transported by the jet for the two SSC components model, using the parameters in Table 6.4, is

$$P_{\rm tot,flare} = (3.5 \pm 1.0) \times 10^{45} {\rm erg\ s^{-1}} \tag{6.6}$$

with $L_r \geq (L_e + L_p + L_B)$, as proposed by Celotti and Ghisellini (2008). Under this assumption, the total jet power is minimized and the details of cooling do not affect the global energies, being the radiated luminosity mainly contributed by peaks emission. Moreover, the uncertainty in $P_{\rm tot,flare}$ is mainly due to the observed $\gamma$-ray flux error.

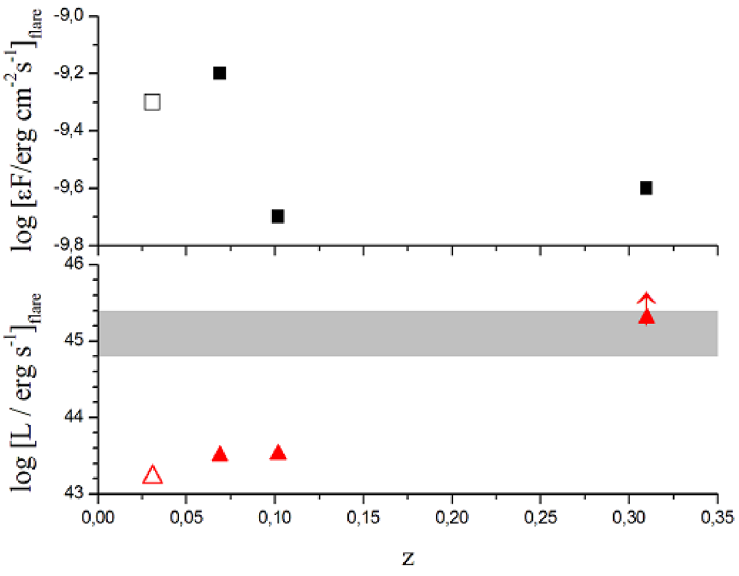


**Figure 6.8:** Observed high-energy peak fluxes (top panel) and the corresponding intrinsic peak luminosities (bottom panel) for 4 BL Lacs in flaring states, in increasing order of redshift: Mrk 421 (open symbols, Donnarumma et al. 2009a), BL Lacertae (Ravasio et al. 2002), W Comae (Böttcher et al. 2002a) and S5 0716+714 (Chen et al. 2008). The shaded area represents the BZ limiting luminosity range for BH masses in the range $3 \times 10^8$–$10^9$ $M_\odot$ [Vittorini et al. 2009].

This total power may exceed the maximum power generated by a spinning BH of $10^9$ $M_\odot$ in most widely known models. In fact the power extractable from a rotating BH with the Blandford-Znajek (BZ) mechanism is

$$P_{\rm BZ} \simeq 2 \times 10^{45}\, M_9 \,{\rm erg\ s^{-1}} \tag{6.7}$$

and assuming a BH of $10^9$ $M_\odot$ and a conservative value of B $\sim 10^4$ G (see discussion in Cavaliere & D'Elia 2002, and the reference therein) we obtain $P_{\rm BZ} \sim 2 \times 10^{45}$ erg s$^{-1}$. Therefore, the total power of the flaring episode of mid-September approached or just exceeded the upper limit set by the BZ mechanism for a maximally rotating BH of $10^9$ $M_\odot$. This output is significantly large with respect to the other BL Lacs. In Fig 6.8 we show for comparison the intrinsic radiated power for other three BL Lacs during intense $\gamma$-ray and TeV emissions: BL Lacertae (Bloom et al. 1997), Mrk 421 (Donnarumma et al. 2009a) and W Comae (Böttcher et al. 2002a).

S5 0716+714 is the first BL Lac object that approached the limit of the BZ mechanism and eventually exceeded it. If the violation is confirmed, it could be explained in terms of the alternative Blandford-Payne mechanism (Blandford & Payne 1982) that, however, requires an ongoing accretion not supported by the observations of S5 0716+714. Alternatively, a so high power could be due to a less conservative value of the magnetic field, up to $B^2/4\pi \leq \rho c^2$, related to particle orbits plunging from the disk toward the BH horizon (Meier 2002) into a region fully related by strong gravity effects.

As discussed in Vittorini et al. (2009) a very similar total jet power is obtained for the flaring episode of S5 0716+714 during 22–23 October 2007, and also in that case the SED is modeled by two SSC components with different variability with a set of parameters consistent with those used for the SED of mid-September 2007.

## 6.6 The 2008 observations

During the first half of 2008, AGILE observed S5 0716+714 in two different periods: 30 March – 10 April and 30 April – 9 May 2008. The GRID data were analyzed using the AGILE Standard Analysis Pipeline. Only events flagged as confirmed $\gamma$-rays and not recorded while the satellite crossed the South Atlantic Anomaly were accepted. We also rejected all the events with reconstructed direction within 10° from the Earth limb, in order to reduce the contamination from Earth's $\gamma$-ray albedo. After the selection, the total effective observation time of the source is 147 hours and 110 hours for the first and second period, respectively. Counts, exposure and Galactic background $\gamma$-ray maps were created with a bin-size of $0.25^\circ \times 0.25^\circ$ for E > 100 MeV. The average $\gamma$-ray flux was derived from a maximum likelihood procedure according to Mattox et al. (1993).

During the period 30 March – 10 April, the source, observed at about 45°off-axis with respect to the AGILE boresight, was detected by the GRID at a signif-

icance level of 4.1-$\sigma$ with an average flux of (36 ± 12) $\times 10^{-8}$ photons cm$^{-2}$ s$^{-1}$ for E > 100 MeV. Instead, in the period 30 April – 9 May 2008, with the source at about 35° off-axis, the GRID detected $\gamma$-ray emission from S5 0716+714 at a significance level of 4.3-$\sigma$ with an average flux of (31 ± 10) $\times$ $10^{-8}$ photons cm$^{-2}$ s$^{-1}$ for E > 100 MeV.

The $\gamma$-ray flux observed by AGILE in these two periods is a factor of two higher than the average flux observed by *Fermi*-LAT over the first three months of operation, and comparable to the weekly averaged peak flux, suggesting that the source was in an intermediate activity state during April–May 2008.

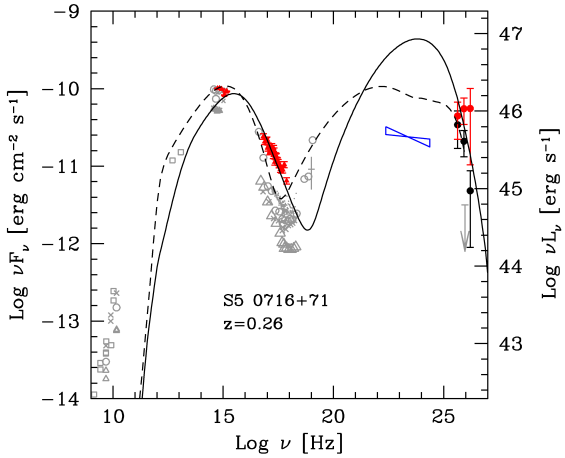


**Figure 6.9:** SED of S5 0716+714 during April 2008 with KVA (from 23 April 2008) *Swift*/UVOT and *Swift*/XRT (from 29 April 2009) and deasorbed MAGIC data. The solid line shows the one-zone SSC model, the dashed line the spine-layer model [Anderhub et al. 2009b].

It is interesting to note that during 22–24 April 2008, the MAGIC telescope, triggered by a high optical state observed by the KVA telescope, detected S5 0716+714 in VHE $\gamma$-rays (Anderhub et al. 2009b). This suggests a possible correlation between VHE $\gamma$-rays and optical bands, aleady observed in other BL Lacs objects such as Mrk 180 (Albert et al. 2006), 1ES 1011+ 496 (Albert et al. 2007a), and BL Lacertae (Albert et al. 2007b), at least in high activity states. In the same period, the source was detected by *Swift*/XRT in a very high X-ray state (Giommi et al. 2008b) and the positional angle of optical polarization started to rotate immediately after the optical maximum (Larionov et al. 2008).

This may correspond to the propagation of a polarized knot spiraling down in the jet, similar to what seen in BL Lacertae (Marscher et al. 2008), attributed to an emission feature moving in helical path upstream of the VLBA core. The SED of this optical, X-ray and VHE flare modeled with a one-zone SSC model predicts a very high $\gamma$-ray flux, more than 10 times larger than the average flux observed by *Fermi*-LAT, and not plausible (see Fig. 6.9). An alternative model proposed is a structured jet model, with a spine surrounder by a slower moving layer (Ghisellini et al. 2005).

Unfortunately, during the VHE flare detected by MAGIC no strictly simultaneous observations were carried in $\gamma$-ray band, but the AGILE observation in the periods 30 March – 10 April and 30 April–9 May indicate an intermediate $\gamma$-ray activity of the source before and after this flare, suggesting a possible very high flux also in $\gamma$-rays simultaneously with the optical, X-ray and VHE flare, even if probably not so high as predicted by the one-zone SSC model.

The study of the light curves in radio, optical, X-ray, $\gamma$-ray and VHE bands as well as VLBA maps and optical polarization relative of the first half of 2008 is under investigation. Preliminary light curves of S5 0716+714 in *B*, *V*, *R*, and *I* bands between January and June 2008 (Fig. 6.10) shows that the variations seem to be quite simultaneous in all the optical bands. In the Fig. 6.11 showing only the *R*-band data (which is the best sampled one), it is evident the huge flare of April 2008 observed also by MAGIC and *Swift*, whereas in the period when AGILE was observing the source (30 April – 9 May) the optical activity had already decayed. A comparison between optical *R*-band and 37 GHz light curves (Fig. 6.12) shows that in the mm-band not a significative activity was observed simultaneously to the optical, contrary to what observed for S5 0716+714 during the 2007 flare.

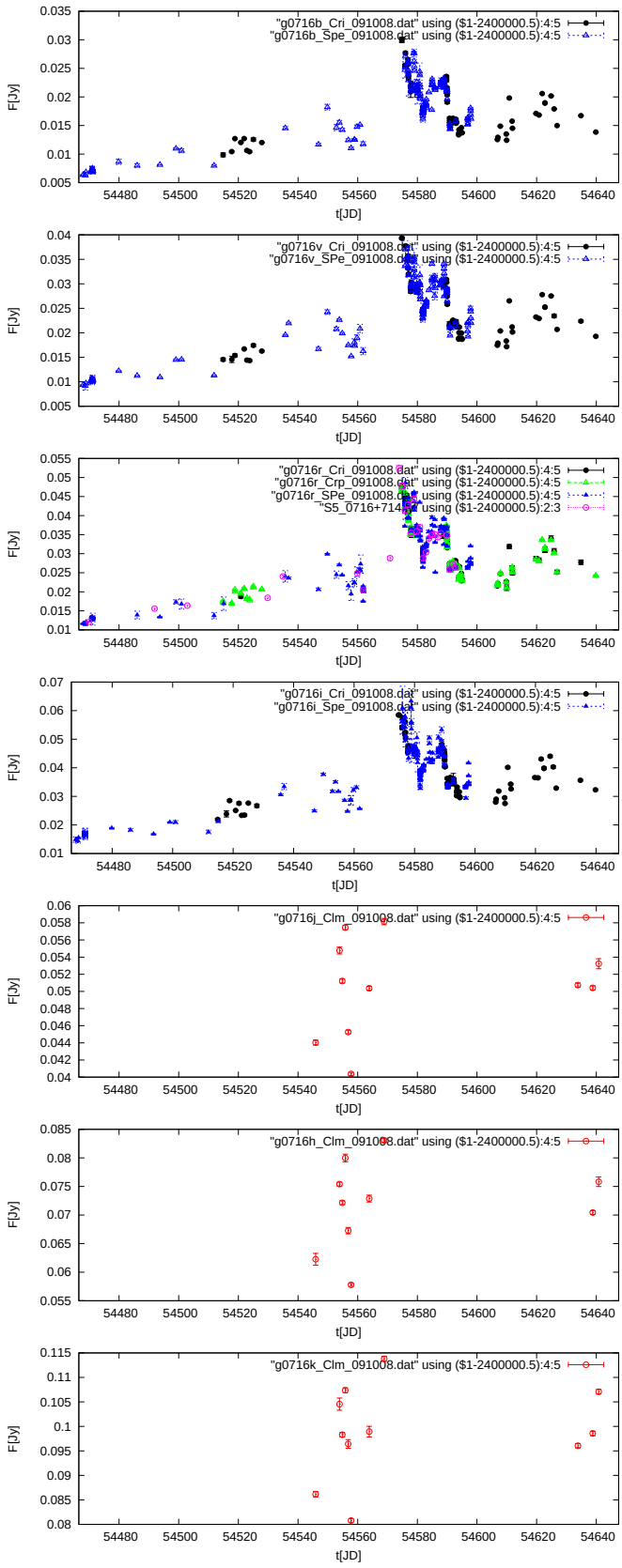




**Figure 6.10:** Preliminary light curves of S5 0716+714 in *B*, *V*, *R*, *J*, *H*, and *K* bands between January and June 2008.

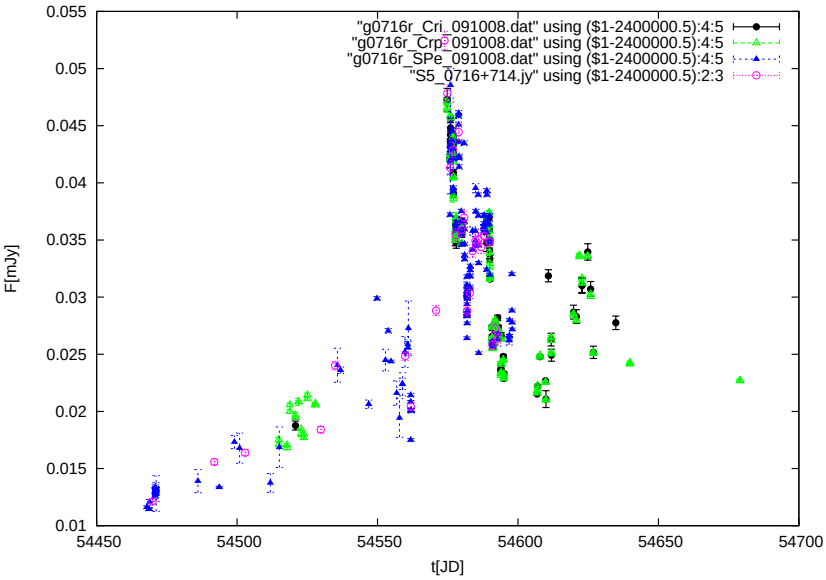


**Figure 6.11:** Preliminary light curve of S5 0716+714 in *R*-band between January and June 2008.

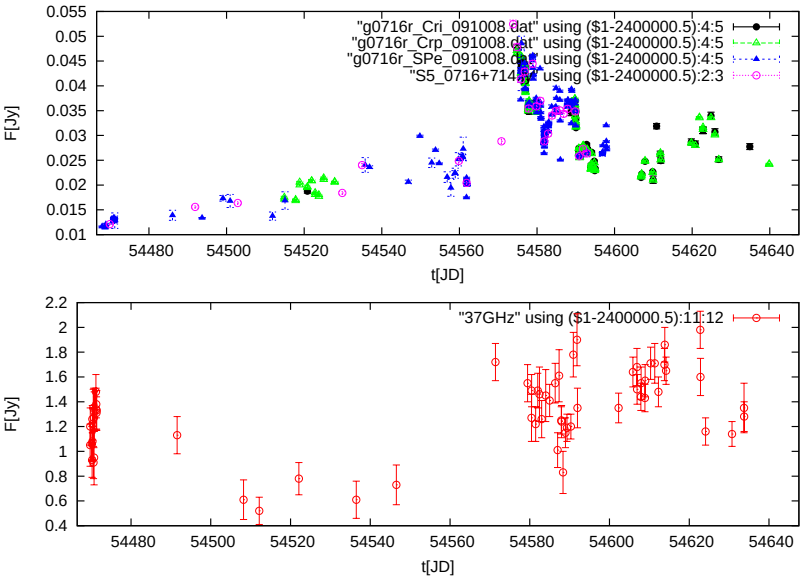


**Figure 6.12:** Comparison between the optical (*R*-band) and mm-band (37 GHz) light curves of S5 0716+714 between January and June 2008.

## 6.7 Summary and remarks

1. Two very intense $\gamma$-ray flares of S5 0716+714 were detected by AGILE during September–October 2007 with a flux of the order of 200 $\times 10^{-8}$ ph cm$^{-2}$ s$^{-1}$ for E > 100 MeV. This is one of the most intense flares detected by a BL Lac object.

2. The total power transported in the jet during these flares approach or slightly exceeds the limit of the Blandford-Znajek mechanism for a BH of $10^9$ M$\odot$.

3. Optical and $\gamma$-ray light curves collected by GASP-WEBT and AGILE show that the $\gamma$-ray variability appears to depend on the square of changes in optical flux density, and together with no evidence of thermal disk emission and emission lines, seems to rule out EC model.

4. The different variability observed in soft X-ray, hard X-ray and optical/UV by *Swift* in October 2007 is compatible with the presence of two SSC components.

5. The SED of S5 0716+714 of September and October 2007 seems to be consistent with a SSC emission model, but only by including two SSC components with different variability: the first slowly variable that emit in radio and hard X-ray, whereas the second responsible for the faster variability in optical/UV, soft X-ray and $\gamma$-ray.

Chapter 7

# 3C 454.3

## 7.1 Introduction

Among the Flat Spectrum Radio Quasars (FSRQs) class of blazars, 3C 454.3 (PKS 2251+158; z = 0.859) is one of the brightest source. 3C 454.3 has been detected significantly at almost all the wavelengths from radio to $\gamma$-rays and its spectral energy distribution (SED) has the typical double-humped shape of blazars, with the synchrotron peak at infrared frequencies, while the inverse Compton (IC) emission reaches the maximum at MeV–GeV energies.

3C 454.3 exhibited radio superluminal motion and a radio and X-ray jet (Lobanov et al. 2000; Marshall et al. 2005). Multi-epoch VLBI observations indicate a jet Lorentz factor of $\Gamma_{\rm jet} = (15.6 \pm 2.2)$, corresponding to an angle of sight of $\theta = (1.3^\circ \pm 1.2^\circ)$ and a Doppler factor of $\delta \sim 25$ (Jorstad et al. 2005). These values are consistent with the recent results obtained by Lister et al. (2009).

Historically the source was detected above 100 MeV by EGRET (Hartman et al. 1999) and in the softer $\gamma$-ray bands by OSSE (McNaron-Brown et al. 1995) and COMPTEL (Zhang et al. 2005). In particular, the source was detected by EGRET in 1992 during an intense $\gamma$-ray flaring episode (Hartman et al. 1992b, 1993) when the blazar flux (E > 100 MeV) was observed to vary within the range (0.4–1.4) $\times 10^{-6}$ photons cm$^{-2}$ s$^{-1}$. In 1995, a 2-week EGRET campaign detected a $\gamma$-ray flux < 1/5 of its historical maximum (Aller et al. 1997).

Recently, the source entered a high-flux phase in 2000 and was remarkably active in 2005. In particular during May 2005, 3C 454.3 was reported to undergo a very strong optical flare with a remarkable flux increase of about four magnitudes compared to previous observations (Balonek 2005), reaching the maximum at $R = 12.0$ mag (Villata et al. 2006). During the same period, RXTE recorded a flux over 10 mCrab, suggesting that 3C 454.3 was extremely active

also at X-ray frequency when it had become one of the brightest extragalactic sources in the sky (Remillard 2005). This exceptionally high state triggered observations by high-energy satellites (*Chandra*: Villata et al. 2006; INTEGRAL: Pian et al. 2006; *Swift*: Giommi et al. 2006) which confirm an exceptionally high flux also in X-ray band. INTEGRAL detected during 2005 May 15–18 the source at a flux level of $\sim 5 \times 10^{-10}$ erg cm$^{-2}$ s$^{-1}$ in the 3–200 keV energy band (Pian et al. 2006), a factor of 2–3 higher than the previous flux level observed by *Beppo*SAX in the same energy band (Tavecchio et al. 2002). A huge mm outburst followed the optical one, peaking in June–July 2005. In the meantime the high frequency radio flux (43–37 GHz) started to increase, reaching the maximum flux level in late February 2006 (Villata et al. 2007).

Subsequently, WEBT and XMM-*Newton* followed 3C 454.3 during the post-outburst phase, when the source was in a faint state and the contribution of the synchrotron emission from the jet was low; it allowed to recognise some Seyfert-like features in its optical/UV spectrum: the little blue bump, due to line emission from the Broad Line Region (BLR), and the big blue bump, due to the thermal emission from the accretion disk (Raiteri et al. 2008a).

Unfortunately, at the time of the bright flare of 2005 no high $\gamma$-ray satellite was operational and considering that, especially for FSRQs, the major of the radiative output is emitted in that energy band simultaneous observations in $\gamma$-rays were been crucial to precisely locate the inverse Compton peak and to constrain the physical mechanisms operating in blazars. However, since the detection of the exceptional 2005 outburst, several monitoring campaigns were carried out to investigate the source multifrequency behavior (Villata 2006; Villata et al. 2007; Raiteri et al. 2007; Raiteri et al. 2008b). During the last of these campaigns, 3C 454.3 underwent a new optical brightening in mid-July 2007, which triggered observations at all frequencies, including a Target of Opportunity (ToO) by the AGILE $\gamma$-ray satellite.

That was the beginning of an extraordinary long-term $\gamma$-ray activity of this source. In fact, 3C 454.3 is the blazar which exhibited the most variable activity in the $\gamma$-ray sky in the last two years and therefore it was always detected during AGILE pointings, until the huge $\gamma$-ray flare observed in early December 2009 (Striani et al. 2009a,b). In the period July 2007–January 2009 the AGILE satellite monitored intensively 3C 454.3 together with *Spitzer*, GASP-WEBT, REM, MITSuME, *Swift*, RXTE, *Suzaku* and INTEGRAL observatories, yielding the longest multiwavelength coverage of this $\gamma$-ray quasar so far. The source underwent an unprecedented long period of very high $\gamma$-ray activity, showing flux levels variable on short timescales of 24–48 hours and reaching on daily timescale a $\gamma$-ray flux higher than $500 \times 10^{-8}$ photons cm$^{-2}$ s$^{-1}$.

In this Chapter, we present the AGILE data collected between July 2007 and December 2009 and the results of the multifrequency data collected from

radio to hard X-rays during these $\gamma$-ray observations, and in particular the campaign organized by AGILE during November 2007, December 2007, May–June 2008, July–August 2008 and October 2008–January 2009. The broadband coverage obtained in different epochs allowed us to study in detail the $\gamma$-optical correlation and, modelling the single-epoch SEDs, the different emission mechanisms of 3C 454.3. The analysis and results presented are published in Vercellone et al. (2008), Raiteri et al. (2008b), Vercellone et al. (2009a), Anderhub et al. (2009a), D'Ammando et al. (2009d), Donnarumma et al. (2009b), Vercellone et al. (2009b).

## 7.2 AGILE data

The AGILE satellite observed the bright blazar 3C 454.3 in $\gamma$-rays during different epochs between July 2007 and January 2009, for a total exposure on the source of $\sim$ 6.5 Ms, and considering also the source activity, AGILE detected always it in $\gamma$-ray band. Table 7.1 shows the AGILE-GRID observation log of 3C 454.3.

AGILE detected 3C 454.3 for the first time during a dedicated ToO activated immediately after an extremely bright optical flare in mid-July 2007. Subsequently, 3C 454.3 underwent an unprecedented long period of very high $\gamma$-ray activity and two multiwavelength campaigns on the source were organized during November 2007 and December 2007. The source has been monitored continuously for more than 1 month, except between 2007 November 25 10:57 UT and November 28 12:05 UT when the data are not collected due to a pre-planned GRID calibration activity. Instead, the AGILE observation during May–June 2008 was split into different periods: May 10–June 9 (P1) and June 15–30 (P2) because of a ToO re-pointing towards W Comae (see Section 9.3). The AGILE observation in July–August 2008 started immediately after the *Fermi*-LAT detection of a very high $\gamma$-ray activity in the period 2008 July 10–21 (Tosti 2008), which reached, on July 10, a $\gamma$-ray flux of $F_{E>100\,\mathrm{MeV}} = 1200 \times 10^{-8}$ ph cm$^{-2}$ s$^{-1}$ (Abdo et al. 2009e). Finally, the source has been monitored by AGILE between October 2008 and January 2009 in order to follow and investigate the decreasing of the long-lasting $\gamma$-ray activity.

Level–1 AGILE-GRID data were analyzed using the AGILE Standard Analysis Pipeline (see 4.3.6). Counts, exposure, and Galactic background $\gamma$-ray maps were created with a bin-size of $0.25^\circ \times 0.25^\circ$ for E > 100 MeV. We selected only events flagged as confirmed $\gamma$-ray events, and not collected during the South Atlantic Anomaly. We rejected also all $\gamma$-ray events whose reconstructed directions form angles with the satellite-Earth vector smaller than 85°, reducing the $\gamma$-ray

Earth albedo contamination by excluding regions within $\sim 15^\circ$ from the Earth limb.

**Table 7.1:** AGILE-GRID observation log of 3C 454.3.

| Epoch | Start Time (UTC) | End Time (UTC) | Exposure (Ms) |
|---|---|---|---|
| 1 | 2007-07-24 14:30 | 2007-07-30 11:40 | 0.22 |
| 2 | 2007-11-10 12:16 | 2007-12-01 11:38 | 0.64 |
| 3 | 2007-12-01 11:39 | 2007-12-16 12:09 | 0.56 |
| 4 | 2008-05-10 11:00 | 2008-06-09 15:20 | 1.03 |
| 5,6 | 2008-06-15 10:46 | 2008-06-30 11:14 | 0.54 |
| 7 | 2008-07-25 19:57 | 2008-08-14 21:08 | 0.70 |
| 8 | 2008-10-17 12:51 | 2009-01-12 14:30 | 2.86 |

We ran the AGILE Source Location task in order to derive the most accurate location of the source. Then, we ran the AGILE Maximum Likelihood Analysis using a radius of analysis of $10^\circ$, and the best guess position derived in the first step. The average $\gamma$-ray flux as well as the daily values were derived according to the procedure described in Mattox et al. (1993): first, the entire period was analyzed to determine the diffuse emission parameters, then the source flux density was estimated independently for each of the 1-day periods with the diffuse parameters fixed at the values obtained in the previous step. The procedure is repetead for each epoch separately, in order to take into account the possible variation of the $\gamma$-ray extragalactic background in the different periods.

Figure 7.1 shows the AGILE-GRID light curve between July 2007 and January 2009 at $\sim$ 3-day resolution for E > 100 MeV in units of $10^{-8}$ ph cm$^{-2}$ s$^{-1}$. The light curve shows several $\gamma$-ray flares, with a dynamical range of a factor of 3–4 on a time scale of about ten days and a factor $\sim$ 10 over the entire period. Moreover, a clear dimming trend in the long-term light curve is present.

We calculated also the average energy spectrum for each AGILE observing epoch, obtained by computing the $\gamma$-ray flux in five energy bins: 50–100 MeV, 100–200 MeV, 200–400 MeV, 400–1000 MeV, 1000–3000 MeV. Considering that the current GRID intrument response is accurately calibrated in the energy range 100 MeV–1 GeV, and that the flux above 1 GeV is likely understimated by a factor of about 2, we fit the data by a simple power law taken into account for the fit only three energy bins: 100–200 MeV, 200–400 MeV, and 400–1000 MeV. The photon indexes, estimated with the weighted least squares method, are reported in Table 7.2. In Fig. 7.2, 7.3, and 7.4 are shown the average $\gamma$-ray

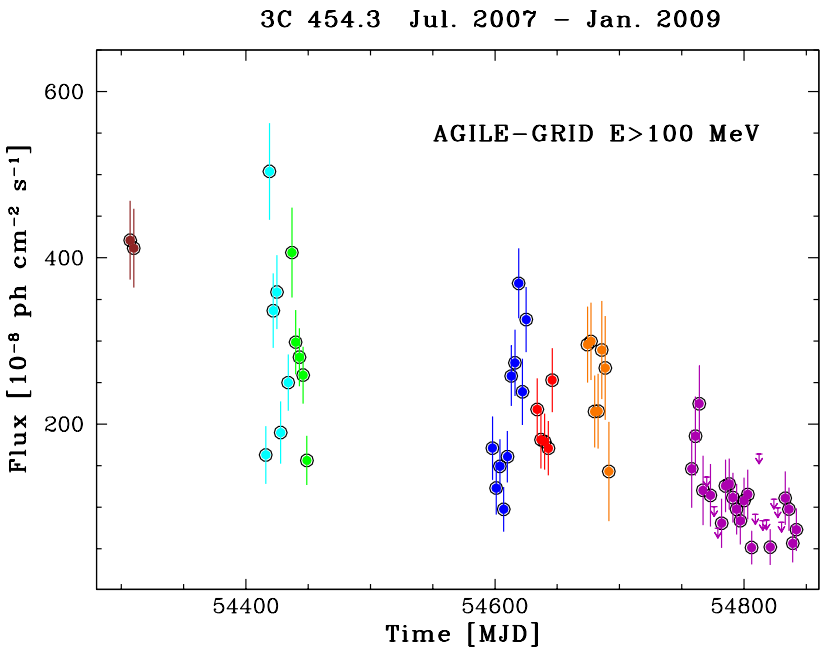


**Figure 7.1:** AGILE-GRID light curve at ~ 3-day resolution for E > 100 MeV in units of $10^{-8}$ ph cm$^{-2}$ s$^{-1}$. Different colors correspond to different observing periods [Vercellone et al. 2009b].

**Table 7.2:** AGILE-GRID $\gamma$-ray flux for E > 100 MeV, significance of detection and spectral index calculated between 100 MeV and 1 GeV in the different periods.

| Start Date | End Date | $F_{E>100\,MeV}$ $\times 10^{-8}$ ph cm$^{-2}$ s$^{-1}$ | Significance $\sigma$ | $\Gamma$ |
|---|---|---|---|---|
| 2007-07-24 | 2007-07-30 | 416.2 ± 36.0 | 17.4 | 1.74 ± 0.16 |
| 2007-11-10 | 2007-12-01 | 224.2 ± 15.3 | 21.7 | 1.91 ± 0.14 |
| 2007-12-01 | 2007-12-16 | 265.7 ± 17.5 | 22.5 | 1.86 ± 0.12 |
| 2008-05-10 | 2008-06-09 | 218.5 ± 12.2 | 25.6 | 2.05 ± 0.10 |
| 2008-06-15 | 2008-06-30 | 198.5 ± 17.1 | 16.3 | 1.98 ± 0.16 |
| 2008-07-25 | 2008-08-14 | 254.8 ± 20.6 | 17.5 | 2.11 ± 0.14 |
| 2008-10-17 | 2009-01-12 | 77.0 ± 5.5 | 17.9 | 2.21 ± 0.13 |

spectrum of the period May–June 2008 (subdivided in two sub-periods P1 and P2), July–August 2008 and October 2008 – January 2009.

We note that in the first three months of observation, *Fermi*-LAT detected a significant softening of the photon spectral index by $\Delta\Gamma \sim 1.2$ towards higher

energies, with a break in the $\gamma$-ray spectrum of 3C 454.3 at energy $E_{break}$ = 2.4 $\pm$ $0.3_{stat}$ $\pm$ $0.3_{syst}$ GeV (Abdo et al. 2009e). The softening is not consistent with a spectral change of $\Delta\Gamma = 0.5$ due to the cooling break associated with radiative losses, instead this spectral break could be due to an intrinsic break in the electron spectrum around energies $\sim 10^3$ $m_e$ $c^2$ and from subsequent investigations it seems to be a common features observed by *Fermi*-LAT in many other luminous blazars. The possible uncertainties of calibration of the AGILE-GRID instrument in the energy range 1–3 GeV prevented us from discussing the presence of a possible spectral break in our data and its theoretical interpretation.

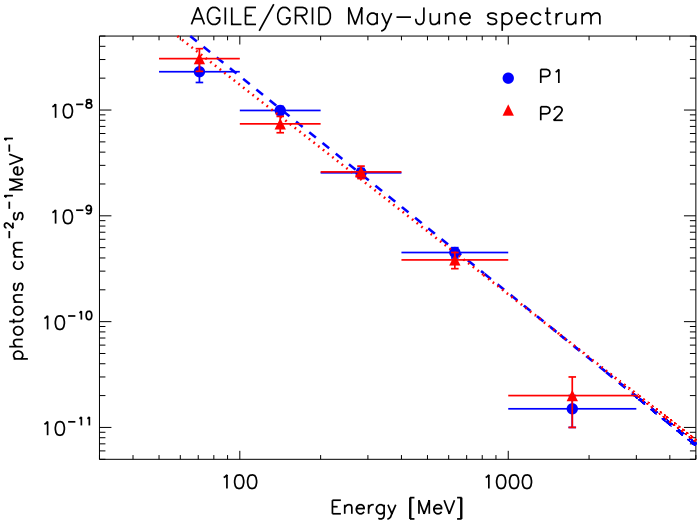


**Figure 7.2:** AGILE-GRID average $\gamma$-ray spectrum for periods P1 (May 10–June 9) and P2 (June 15–30) during May–June 2008. Only three energy bins were considered for the spectral fitting: 100–200 MeV, 200–400 MeV, 400–1000 MeV. The blue-dashed and the red-dotted lines represent the best–fit power law models for P1 and P2, respectively [adapted from Vercellone et al. 2009b].

The correlation between the flux level and the spectral slope in the $\gamma$-ray energy band was extensively studied by means of the analysis of the EGRET data, but a decisive general result for the blazars is not found (Nandikotkur et al. 2007). Figure 7.5 shows the AGILE-GRID photon index as a function of the $\gamma$-ray flux at different epochs. A 'harder-when-brighter' trend seems to be present in the long timescale AGILE observation. A similar trend was observed only for 3C 279 in the EGRET *era* (Hartman et al. 2001), but this could be due to the fact that 3C 279 was the only object for which a long-term monitoring in $\gamma$-rays is performed by EGRET. At the present, with AGILE and *Fermi* satellites we are able to follow a large number of blazars on very long timescales, and 3C 454.3

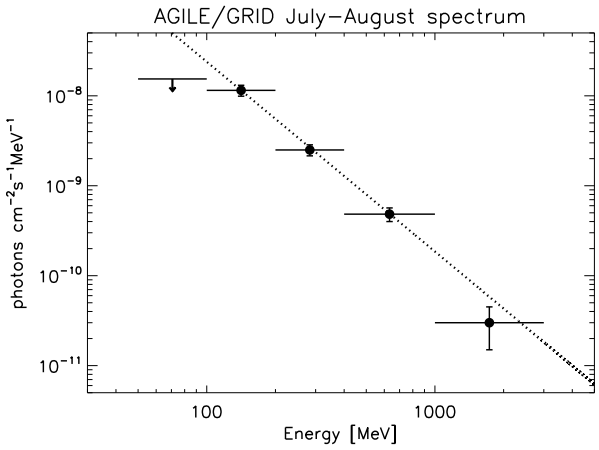


**Figure 7.3:** AGILE-GRID average $\gamma$-ray spectrum over the entire period July–August 2008. Only three energy bins were considered for the spectral fitting: 100–200 MeV, 200–400 MeV, 400–1000 MeV. The dashed line represents the best–fit power law model [adapted from Vercellone et al. 2009b].

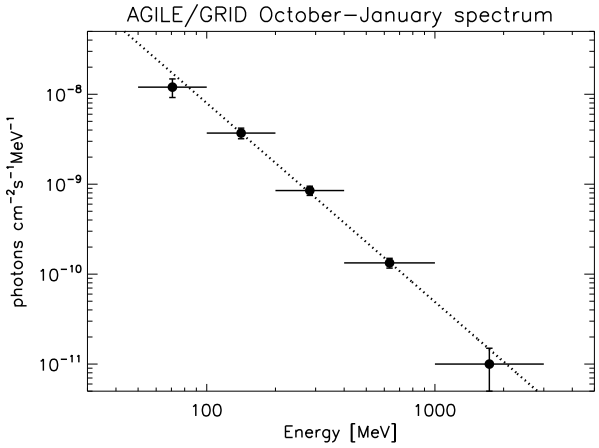


**Figure 7.4:** AGILE-GRID average $\gamma$-ray spectrum over the entire period October 2008 – January 2009. Only three energy bins were considered for the spectral fitting: 100–200 MeV, 200–400 MeV, 400–1000 MeV. The dashed line represents the best–fit power law model [adapted from Vercellone et al. 2009b].

is the best example of it.

During the various AGILE pointings, 3C 454.3 was located substantially off-axis in the SuperAGILE field of view. For this reason, only 3-$\sigma$ upper limits can be derived in the 20–60 keV energy band during the AGILE-GRID observations. Table 7.3 summarizes the SuperAGILE observations and their results.

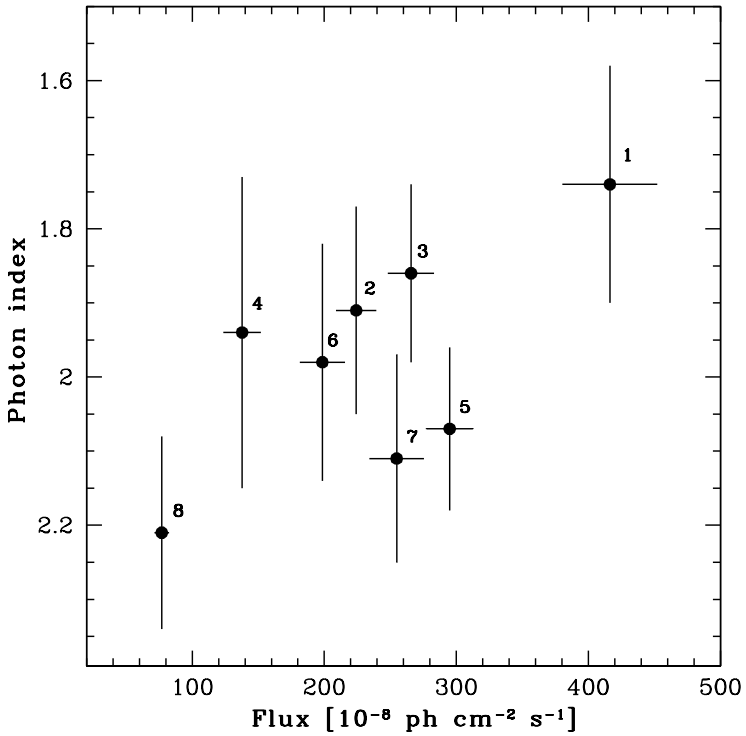


**Figure 7.5:** AGILE-GRID photon index as a function of the $\gamma$-ray flux above 100 MeV. Number beside each points represents the epochs listed in Table 7.1 [Vercellone et al. 2009b].

**Table 7.3:** SuperAGILE observation log and analysis results. Upper limits are reported at 3-$\sigma$ confidence level.

| Start Time (UTC) | End Time (UTC) | $\theta_X$ (Deg.) | $\theta_Z$ (Deg.) | Exposure (ks) | $F_{20-60\,keV}$ (mCrab) |
|---|---|---|---|---|---|
| 2008-05-31 10:18 | 2008-06-09 13:38 | −23.0 | +06.0 | 380 | < 16 |
| 2008-06-15 14:11 | 2008-06-21 12:59 | −36.0 | +08.0 | 270 | < 18 |
| 2008-07-25 21:39 | 2008-08-02 23:29 | +03.4 | −42.0 | 345 | < 18 |
| 2008-10-17 18:47 | 2008-10-29 23:12 | −00.8 | −45.0 | 460 | < 21 |

## 7.3 Multifrequency data

During this long-term $\gamma$-ray monitoring of 3C 454.3, the source was also intensively monitored from radio-to-optical by means of the GLAST AGILE Support Program (GASP) project of the Whole Earth Blazar Telescope (WEBT) and the Monitoring of Jets in AGN with VLBA Experiment (MOJAVE) project. Moreover, several multifrequency campaigns on 3C 454.3 were organized by AGILE in order to obtain simultaneous observation over the whole electromagnetic spectrum, allowing us to study truly simultaneous SEDs from radio to $\gamma$-rays. Therefore, data in mid-infrared, optical/UV and X-rays are collected by *Spitzer*, *Swift*, RXTE, INTEGRAL, and *Suzaku* observatories by means of Target of Opportunity (ToO), Discrete's Discretionary Time (DDT) requests and approved Guest Investigation Programs. In the following Sections, we will present the multifrequency data collected from radio to hard X-rays during the different AGILE observation epochs of 3C 454.3.

### 7.3.1 GASP-WEBT data

3C 454.3 has been monitoring by the WEBT since the exceptional 2004–2005 outburst (Villata et al. 2006) throughout the whole period of the AGILE observation. Figure 7.6 shows the GASP-WEBT light curve in the *R* optical band, displaying several intense flares with a dynamic range of $\sim 2.4$ mag in about 14 days, while Figure 7.7 shows the GASP-WEBT light curves in the near-IR (*J*, *H*, *K*), radio (5, 8, and 14.5 GHz), and mm (37, 230, and 345 GHz), respectively.

At the beginning of the 2007–2008 observing season, a renewed optical activity was observed prompted the WEBT to go on with the monitoring. Indeed, a multipeak optical outburst was observed in July–August 2007, triggering the first AGILE observation of the source. During November–December 2007, simultaneously to the $\gamma$-ray observation by AGILE, the optical flux appears extremely variable, with a brightening of several tenths of magnitude in few hours. The brightest level $R = 12.58$ mag observed on 2007 December 1 is only 0.6 mag fainter than the maximum brightness ever observed from this source ($R = 12.00$ mag, on 2005 May 9). Many episodes of fast (i.e. intranight) variability were observed, most notably on 2007 December 12, when a flux increase of about 1.1 mag in 1.5 hours was detected, followed by a steep decrease of about 1.2 mag in 1 hour (Fig. 7.8). This is one of the fastest variations ever observed in blazars, even if the inferred brightness temperature is still well below the limit of brightness temperature for inverse Compton catastrophe ($T_b \sim 10^{12}$ K). In fact, by assuming $H_0 = 71\ \mathrm{km\ s^{-1}\ Mpc^{-1}}$, the 1.2 mag dimming in 1 hour in the *R* band yields $T_b \sim 5 \times 10^9$ K. This very fast optical flare is most likely a real variation in the jet. An alternative mechanism that could produces a similar optical flare

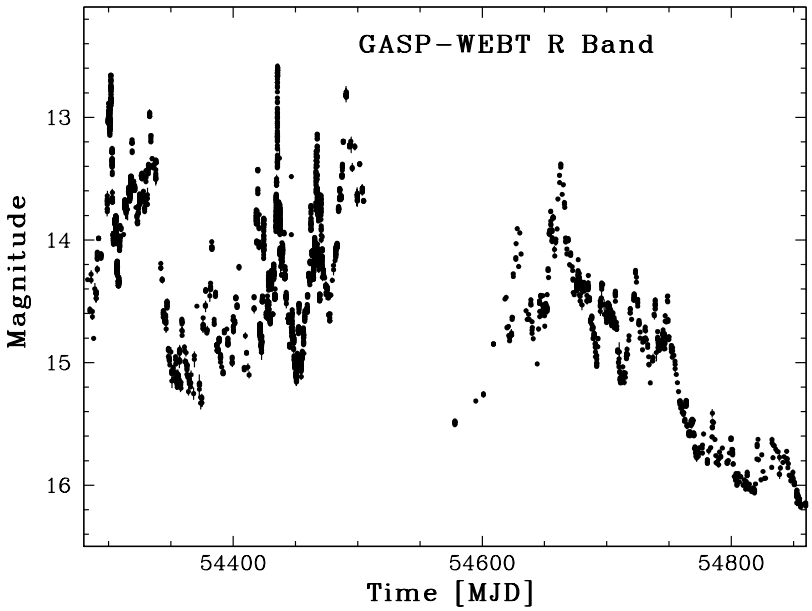


**Figure 7.6:** GASP-WEBT light curve in the *R* optical band in the 2007–2008 and 2008–2009 observing seasons [Vercellone et al. 2009b].

is a dramatic event in the host galaxy, like a Gamma-Ray Burst (GRB). However, most GRBs are associated to the death of young massive stars common in star-forming galaxies, while blazars are usually hosted in elliptical galaxies. A microlensing effect (e.g. a MACHO in our Galaxy) is possible, but unlikely because they are events observed with much longer time scales (Wood & Mao 2005).

During 2008, the optical flux started to increase in mid-May and a first noticeable flare peaked in mid-June, at the end of the first AGILE observation period of the year. A further bright flare was observed to double-peak on July 7–10 (JD $\sim$ 2454655–57) followed by the brightest phase of the outburst, peaking around July 16.1 (JD $\sim$ 2454663.6). Then, the optical flux started to drop with a decreasing trend with several flares superposed.

The comparison between the $\gamma$-ray and optical data, especially during periods of high variability, can give an important contribution to the knowledge of blazar emission mechanisms. Therefore, we study and discuss the $\gamma$-optical correlation through the AGILE and WEBT dataset in the Section 7.4.

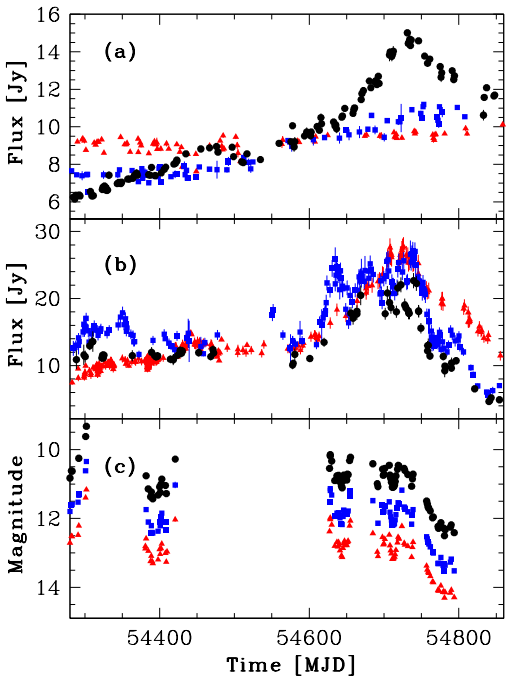


**Figure 7.7:** *Panel (a)*: Red triangles, blue squares and black circles represent the radio flux at 5, 8, and 14.5 GHz, respectively. *Panel(b)*: Red triangles, blue squares, and black circles represent the radio flux at 37, 230, and 345 GHz, respectively. *Panel(c)*: Red triangles, blue squares, and black circles, represent the *J*, *H*, *K* bands, respectively [Vercellone et al. 2009b].

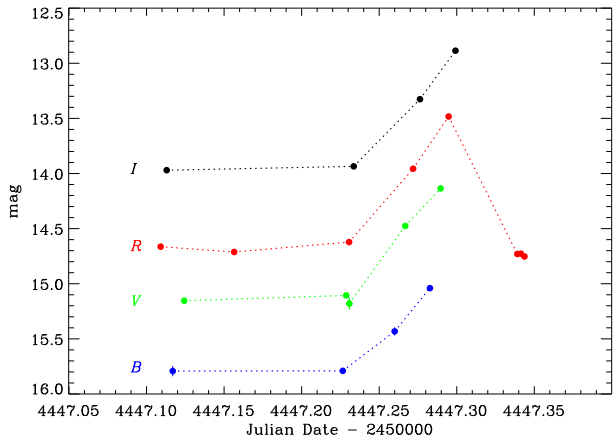


**Figure 7.8:** The extraordinary episode of optical fast variability observed on 2007 December 12 by GASP-WEBT in *B*, *V*, *R* and *I* bands [Raiteri et al. 2008b].

### 7.3.2 *Swift* data

The *Swift* satellite (Gehrels et al. 2004) performed several observations of 3C 454.3 between 2007-07-26 and 2009-01-01, with all three on board experiments: the X-ray Telescope (XRT; Burrows et al. 2005), the UltraViolet and Optical Telescope (UVOT; Roming et al. 2005) and the coded-mask Burst Alert Telescope (BAT; Barthelmy et al. 2005). These observations were obtained both by means of several dedicated ToOs and by activating *Swift* Cycle-3 and Cycle-4 Proposals. Finally, a long-lasting monitoring program driven by AGILE and *Fermi* covers the period July–October 2008.

#### 7.3.2.1 *Swift*/XRT

The XRT data were processed with standard procedures (`xrtpipeline` v0.12.1), adopting the standard filtering and screening criteria, and using FTOOLS in the `Heasoft` package (v.6.6.1). The source count rate was variable during the different observing periods, ranging from 0.26 to 1.8 counts $s^{-1}$ . For this reason, the data were collected both in photon counting (PC) and windowed timing (WT) mode, and in the analysis selected XRT event grades 0–12 and 0–2 for the PC and WT events, respectively (see Burrows et al. 2005). Several *Swift*/XRT observations in PC data showed an average count rate higher than 0.5 counts $s^{-1}$, therefore in these cases pile-up correction was required. We extracted the source events from an annulus extraction region with an inner radius of 3 pixels (estimated by means of the PSF fitting technique) and an outer radius of 30 pixels (1 pixel $\sim$ 37 arcsec). When the average count rate was lower than 0.5 counts $s^{-1}$, we used the full 30 pixels radius region. To account for the background we extracted events within an annular region centered on the source with radii of 110 and 116 pixels. WT data instead are not affected by pile-up at the observed count rate ($CR < 3$ counts $s^{-1}$).
Ancillary response files were generated with the task `xrtmkarf`, and account for different extraction regions, vignetting and PSF corrections. We used the spectral redistribution matrices (RMF, v011) in the Calibration Database maintained by HEASARC. *Swift*/XRT uncertainties are given at 90% confidence level for one interesting parameter, unless otherwise stated.

The *Swift*/XRT spectra were rebinned in order to have at least 20 counts per energy bin and use the $\chi^2$ statistics. Spectral analysis was performed using the `XSPEC 11.3.2` fitting package and we fit the spectra in the 0.3–10 keV energy range with an absorbed power law model. The Galactic absorption was fixed to the value of $N_{\rm H}^{\rm Gal} = 1.34 \times 10^{21}\,{\rm cm}^{-2}$, as obtained by Villata et al. (2006) by means of a deep *Chandra* observation in spectroscopic mode. There is a good agreement among various authors about the existence of an excess absorp-

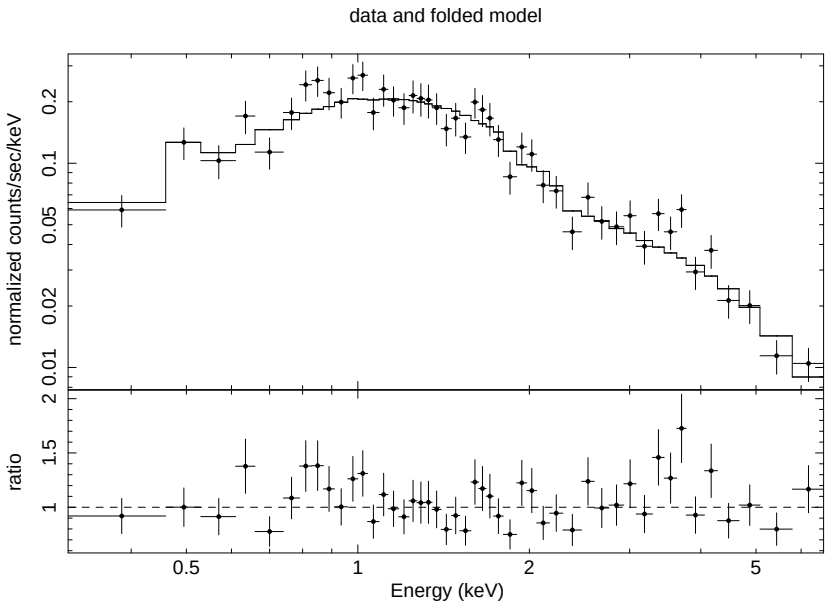


**Figure 7.9:** *Swift*/XRT data and model of 3C 454.3 for the observation carried out in 2007 December 15 [Donnarumma et al. 2009b].

**Table 7.4:** Fitting results of *Swift*/XRT observations of 3C 454.3 on December 2007. A power law model with $N_{\rm H}$ free to vary is used.

| Observation date | $N_{\rm H}$ $10^{22}$ cm$^{-2}$ | Flux (2-10 keV) erg cm$^{-2}$ s$^{-1}$ | Spectral slope $\Gamma$ | $\chi^2_{\rm red}$/d.o.f. |
|---|---|---|---|---|
| 13 Dec 2007 | $0.13 \pm 0.03$ | $(3.04 \pm 0.24) \times 10^{-11}$ | $1.74 \pm 0.10$ | 1.28/54 |
| 15 Dec 2007 | $0.14 \pm 0.03$ | $(2.49 \pm 0.22) \times 10^{-11}$ | $1.76 \pm 0.12$ | 1.14/44 |

tion in X-rays for 3C 454.3. In particular, this value is in agreement with that found by Raiteri et al. (2007, 2008b) fitting the spectra of 3C 454.3 acquired by XMM-*Newton*. Moreover, fitting the *Swift*/XRT spectra with free absorption the distribution of $N_{\rm H}$ ranging from the Galactic value $7.24 \times 10^{20}$ cm$^{-2}$ (Kalberla et al. 2005) to values well above the Chandra value, with a peak around the *Chandra* value. As example, we report the analysis of the two XRT ToO observations performed on 2007 December 13 and 15 (see Table 7.4 and Fig. 7.9) during the multifrequency campaign of December 2007. Leaving the value of $N_{\rm H}$ free to vary we obtained a value well consistent with that found by Villata et al. (2006).

Figure 7.10 shows the *Swift*/XRT photon index as a function of the X-ray flux in the 2–10 keV energy band. Black circles and red squares represent data acquired in PC and WT mode, respectively. We investigated the possible presence

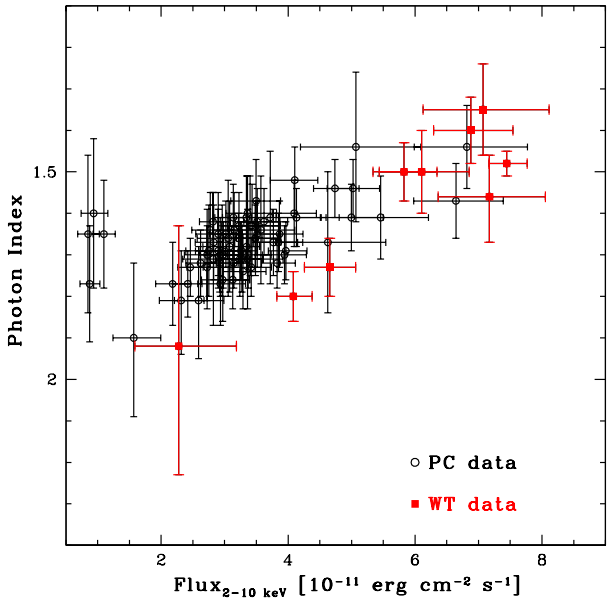


**Figure 7.10:** *Swift*/XRT photon index as a function of the 2–10 keV flux. Red squares and black circles mark the *Swift*/XRT windowed timing (WT) and photon counting (PC) data, respectively [Vercellone et al. 2009b].

of a spectral trend in the X-ray data. If we consider WT data only, a 'harder-when-brighter' trend seems to be present. Fitting the data with a constant model, we can exclude this model at the 99.9993% level. When analyzing the PC data only (as well as the sum of the PC and WT data), this spectral trend vanishes, and a fit with a constant model still holds. Nevertheless, if we exclude the points at fluxes $F_{2-10\,\mathrm{keV}} < 2 \times 10^{-11}$ erg cm$^{-2}$ s$^{-1}$ a trend still holds. This is an indication that the meaurements at low fluxes could correspond to physically different state of the source than the high fluxes one, but considering that only four observations (performed in December 2008) are at low and intermediate X-ray states a more prolonged monitoring of 3C 454.3 also when the source was at fluxes $F_{2-10\,\mathrm{keV}}$ $< 10^{-11}$ erg cm$^{-2}$ s$^{-1}$ will be crucial to test in detail the possible presence of a spectral trend.

#### 7.3.2.2 *Swift*/UVOT

The UVOT data analysis was performed using the `uvotimsum` and `uvotsource` tasks included in the `FTOOLS` software package (HEASOFT v6.6.1). The latter task calculates the magnitudes through aperture photometry within a circular re-

gion and applies specific corrections due to the detector characteristics. Source counts were extracted from a circular region with a 5 arcsec radius. The background was extracted from source-free circular regions in the source surroundings. The reported magnitudes are on the UVOT photometric system described in Poole et al. (2008), and are not corrected for Galactic extinction.

Figure 7.11 shows the UVOT observed magnitudes (in the $V$, $B$, $U$, $UW1$, $UM2$, and $UW2$ bands) as a function of time for the whole observing period. In order to diminish the statistical uncertainties, we selected observations with a number of degrees of freedom (d.o.f.) $> 10$. We note that a common dimming trend is present both in the optical/UV and in the X-ray energy bands, a behaviour is in agreement with the $\gamma$-ray activity observed by AGILE.

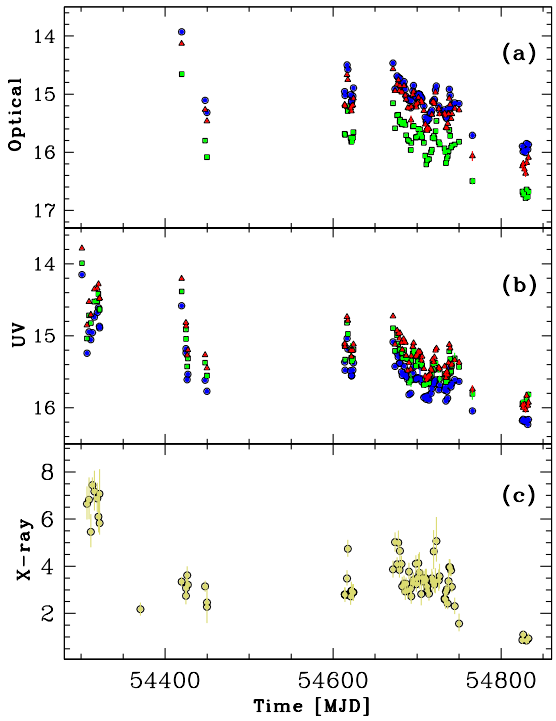


**Figure 7.11:** Panel (a): *Swift*/UVOT light curves (observed magnitudes) in the $V$ (red triangles), $B$ (green quares), and $U$ (blue circles). Panel (b): *Swift*/UVOT light curves (observed magnitudes) in the $W1$ (red triangles), $M2$ (green quares), and $W2$ (blue circles). Panel (c): *Swift*/XRT light curve (observed fluxes) in the 2–10 keV energy band in units of $10^{-11}$ erg cm$^{-2}$ s$^{-1}$ [Vercellone et al. 2009b].

#### 7.3.2.3 *Swift*/BAT

We analyzed *Swift*/BAT Survey data in order to study the hard X-ray emission of 3C 454.3 and to investigate its evolution as a function of time. We produced a light curve for the source at a 16-days binning using the procedures described in Krimm et al. (2006; 2008, and references therein; also see [1]). Figure 7.12 shows the long-term *Swift*/BAT light curve in the 15–150 keV energy range in units of mCrab. The source has not been always detectable throughout the considered period, and in several time interval only 3-$\sigma$ upper limits can be derived. No clear trend or high activity states of 3C 454.3 are detected by *Swift*/BAT in the same period monitored by AGILE (July 2007–January 2009).

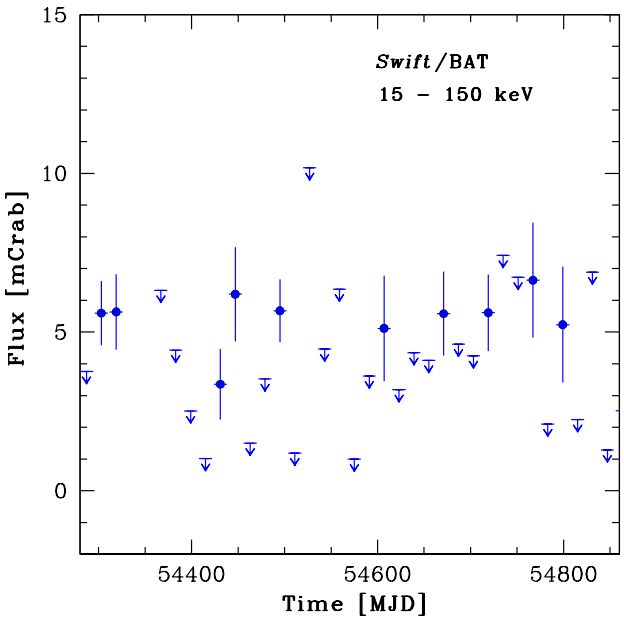


**Figure 7.12:** *Swift*/BAT light curve in units of mCrab between July 2007 and January 2009. Downward arrows show 3-$\sigma$ upper limits.

### 7.3.3 INTEGRAL and *Suzaku* data

During the multiwavelength campaigns organized by AGILE in November and December 2007, we have triggered ToO observations by the INTEGRAL and *Suzaku* satellites, respectively. INTEGRAL data were collected on revolutions

[1] http://swift.gsfc.nasa.gov/docs/swift/results/transients/Transient_synopsis.html

**Table 7.5:** INTEGRAL/IBIS spectral fit results. [a]Flux in the 20–200 keV band in units of $10^{-3}$ ph cm$^{-2}$ s$^{-1}$ obtained from the spectral fits.

| Rev | $\Gamma$ | $\chi^2_{\rm red}$ (d.o.f.) | Flux[a] |
|---|---|---|---|
| 623 | $1.78^{+0.33}_{-0.30}$ | 1.21 (11) | 1.52 |
| 624 | $1.71^{+0.41}_{-0.36}$ | 0.54 (11) | 1.42 |
| 623+624 | $1.75^{+0.25}_{-0.23}$ | 0.89 (11) | 1.49 |

623 (2007 November 20 03:35 UT – November 22 20:45 UT), and 624 (2007 November 22 20:45 UT – November 24 15:50 UT), for a total of about 300 ks, whereas *Suzaku* data were collected on December 5. In the following Sections we briefly describe the INTEGRAL and *Suzaku* data analysis and results.

#### 7.3.3.1 INTEGRAL observation

The ESA INTEGRAL $\gamma$-ray Observatory, launched in 2002 October, carries three co-aligned coded mask telescopes. INTEGRAL data were collected during 2007 November 20–24. We analyzed the data from the IBIS instrument (Ubertini et al. 2003), sensitive in the energy range 15 keV–10 MeV and with a FoV of $29^\circ \times 29^\circ$ , and in particular to the ISGRI lower energy detector layer. All the observations are organized into un-interrupted 2000–3600 s long science windows (SCW): light curves and spectra were extracted for each individual SCW.

Wide-band spectra (17–150 keV) of the source were obtained using data from IBIS instrument. All the data were processed using the Off-line Scientific Analysis (OSA) version 7.0 software released by the INTEGRAL Scientific Data Centre. INTEGRAL data were analyzed using FTOOLS and XSPEC 11.3.2 in the `Heasoft` package (v.6.4). We assumed a single power law model to fit the IBIS data. Table 7.5 summarizes the INTEGRAL/IBIS spectral fit results.

#### 7.3.3.2 *Suzaku* observation

Following the AGILE detection of the flaring state in early December, 3C 454.3 was observed with *Suzaku* (Mitsuda et al. 2007) on 2007 December 5 as a ToO, with a total duration of 40 ks. *Suzaku* carries four sets of X-ray telescopes (Serlemitsos et al. 2007), each one equipped with a focal-plane X-ray CCD camera (XIS: X-ray Imaging Spectrometer; Koyama et al. 2007) that is sensitive in the energy range of 0.3–12 keV, together with a non-imaging Hard X-ray Detector (HXD; Takahashi et al. 2007; Kokubun et al. 2007), which covers the 10–600 keV energy band with Si PIN photo-diodes and GSO scintillation detectors. 3C 454.3 was focused on the nominal center position of the XIS detectors.

*Suzaku* satellite carries 4 XIS detectors, 3 Front Illuminated CCD (XIS 0, XIS 2 and XIS 3) and one Back Illuminated CCD (XIS 1). On 2006 November 9 a large amount of leaked charge suddenly appeared in the sensor XIS 2 and this dectector became unusable for scientific observations.
For the XIS, we analyzed the screened data, reduced via *Suzaku* software version 2.1. The reduction followed the prescriptions described in the '*Suzaku* Data Reduction Guide' provided by the *Suzaku* guest observer facility at the NASA/GSFC[2]. The screening was based on the following criteria: (1) only ASCA-grade 0, 2, 3, 4, 6 events are accumulated, while hot and flickering pixels were removed from the XIS image using the script, (2) the time interval after the passage through the South Atlantic Anomaly (T_SAA_HXD) is greater than 500 s, (3) the object is at least 5° and 20° above the rim of the Earth (ELV) during night and day, respectively. In addition, we also selected the data with a cut-off rigidity (COR) larger than 6 GV. After this screening, the net exposure for good time intervals is 35.1 ks. The XIS events were extracted from a circular region with a radius of 4.3′ centred on the source peak, whereas the background was accumulated in an annulus with inner and outer radii of 5.0′ and 7.0′ pixels, respectively. The response (RMF) and auxiliary (ARF) files are produced using the analysis tools and , which are included in the software package HEAsoft version 6.4.1.

The HXD/PIN event data (version 2.1) are processed with basically the same screening criteria as those for the XIS, except that ELV $\geq 5°$ through night and day, and COR $\geq 8$ GV. The HXD/PIN instrumental background spectra were generated from a time dependent model provided by the HXD instrument team for each observation (see Kokubun et al. 2007). Both the source and background spectra were made with identical good time intervals (GTIs) and the exposure was corrected for a detector deadtime of 6.9%. We used the response files version _ _ _20070914. , provided by the HXD instrumental team. Similarly, the HXD/GSO event data (version 2.1) were processed with a standard analysis technique described in the '*Suzaku* Data Reduction Guide'. Despite the relatively high instrumental background of the HXD/GSO, the source was marginally detected at 5.5-$\sigma$ level between 80 and 120 keV. We used the response files version _ _ _20080129. . Spectral analysis was performed using the XSPEC fitting package 12.3.1. and we fitted both the soft and hard X-ray spectra with a power law with Galactic absorption free to vary. The XIS spectra are well fitted with a power law with $\Gamma = 1.63$, absorbed with $N_H = 1.1 \times 10^{21}$ cm$^{-2}$, which infers the absorbed fluxes of $4.51^{+0.07}_{-0.03} \times 10^{-11}$ erg cm$^{-2}$ s$^{-1}$ and $3.20^{+0.04}_{-0.01} \times 10^{-11}$ erg cm$^{-2}$ s$^{-1}$ in the energy bands 0.3–10 keV and

[2]http://suzaku.gsfc.nasa.gov/docs/suzaku/analysis/abc. See also seven steps to the *Suzaku* data analysis at http://www.astro.isas.jaxa.jp/suzaku/analysis

2–10 keV, respectively. The differece between XIS 0 and XIS 3 spectra with respect to the XIS 1 spectrum below 2 keV is due to the different sensitivity of the CCD in the soft X-ray band.

The hard X-ray spectrum determined by HXD/PIN and GSO seems to be a bit flatter than those determined by the XIS only below 10 keV, as it is shown in the residuals reported in Fig. 7.13, where a model with a single power law is assumed. We found that it is better fitted by a power law photon index $\Gamma = 1.35 \pm 0.14$, which gives $F_{10-100\,\mathrm{keV}} = 1.37^{+0.10}_{-0.08} \times 10^{-10}$ erg cm$^{-2}$ s$^{-1}$. The uncertainties reported above are at 90% confidence level.

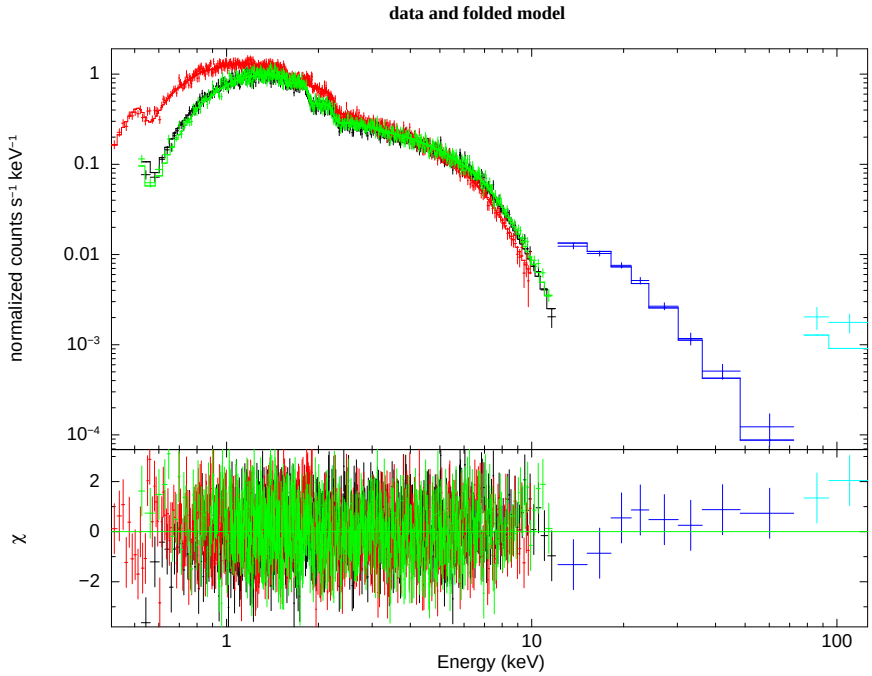


**Figure 7.13:** *Suzaku* broad-band spectrum of 3C 454.3 for the observation carried out in 2007 December 5: black, red and green points for XIS 0, XIS 1, XIS 3, respectively; blue points for PIN; cyan points for GSO. A single power law over the whole energy range is assumed [Donnarumma et al. 2009b].

### 7.3.4 RXTE data

The *Rossi* X-ray Timing Explorer (RXTE) satellite observed 3C 454.3 in two epochs: from 2007-07-28 to 2007-08-04 and from 2008-05-30 to 2008-06-19. We analyze the data obtained with the *Proportional Counter Array* (PCA; Jahoda et al. 1996), sensitive in the 2–60 keV energy range.

The PCA is composed of 5 identical units (*Proportional Counter Units*, PCUs), but since PCU2 was the only unit always operative during our observations and it is the one which is best calibrated, we report the results obtained from the PCU2 data only. The data were processed using the FTOOLS v6.4.1 and screened using standard filtering criteria. The net exposure times for the whole data-set in the first and second epoch were 36.6 ks and 17.4 ks, respectively.

The background light curves and spectra for each observation were produced using the model appropriate to faint sources. We restricted our analysis to the 3–20 keV energy range, in order to minimize the systematic errors due to background subtraction and calibration of the *PCA* instrument.

The average count rate during the second epoch is reduced. In order to investigate possible changes in the spectral shape with time we extracted light curves in two energy ranges (3–7 keV and 7–20 keV). Their hardness ratio did not show any significant variation.

A cumulative spectrum for the first and the second epoch was extracted and simultaneously fitted with a power law model corrected for Galactic absorption, allowing only the power law normalization to assume a different value in the two spectra. A good fit was obtained ($\chi^2_{\rm red} = 0.90$, for 76 d.o.f.) with a photon index $\Gamma = 1.65 \pm 0.02$, and a flux in the 3–20 keV energy band $F_{3-20\,\rm keV} = 9.5 \times 10^{-3}$ photons cm$^{-2}$ s$^{-1}$ and $F_{3-20\,\rm keV} = 5.1 \times 10^{-3}$ photons cm$^{-2}$ s$^{-1}$ for the first and second epoch spectrum, respectively. Extrapolating this power law fit to the 18–60 keV energy range, we obtain fluxes of $2.3 \times 10^{-3}$ photons cm$^{-2}$ s$^{-1}$ and $1.2 \times 10^{-3}$ photons cm$^{-2}$ s$^{-1}$. These flux values (approximately 10 and 5 mCrab, respectively) are consistent with the upper limits obtained by SuperAGILE in the same time periods.

The average RXTE flux during the $\gamma$-ray flare detected in July 2007 was about a factor of two higher than the flux detected in May–June 2008, even if during both the July 2007 and the May–June 2008 campaigns the hard X-ray flux varied significantly, by about 50%, on a time scale of about one week.

### 7.3.5 *Spitzer* data

During the AGILE November 2007 campaign, given the high $\gamma$-ray activity detected from 3C 454.3, we obtained a DDT for a mid-Infrared follow-up by *Spitzer* (Werner et al. 2004). The DDT was approved for 2 epochs for a total duration of 0.8 hours of the Infrared Spectrograph (IRS, Houck et al. 2004) providing short-low and long-low observations of 3C 454.3 scheduled for December 13 and 15. Both observations provided us with a low resolution spectrum ($\Delta\lambda/\lambda \sim 80$) in the energy range $\sim$ 5–38 $\mu$m.

Data were acquired in the IRS standard staring mode: observations were obtained at two positions along the slit to enable sky subtraction. Each ramp duration was set to 14.68 s with a number of cycles equal to 5. Each set of data was processed with the IRS Standard Pipeline *SMART* developed at the Spitzer Science Center to produce calibrated data frames (Basic Calibrated Data, BCD files). Moreover, the BCD files covering the same spectral range were coadded and then sky-subtracted spectra were obtained. The absolute flux calibration was estimated by using the electron-to-Jy conversion polynomial given in the appropriate *Spitzer* calibration file. In Fig. 7.14 we present the two spectra obtained on December 13 and 15. We performed a linear fit of the two spectra, obtaining a flux equal to $(1.59 \pm 0.02) \times 10^{-10}$ and $(1.38 \pm 0.02) \times 10^{-10}$ erg cm$^{-2}$ s$^{-1}$ for December 13 and 15, respectively, and therefore a slightly decrease is observed, in agreement with what observed in $\gamma$-rays (see Fig. 7.18).

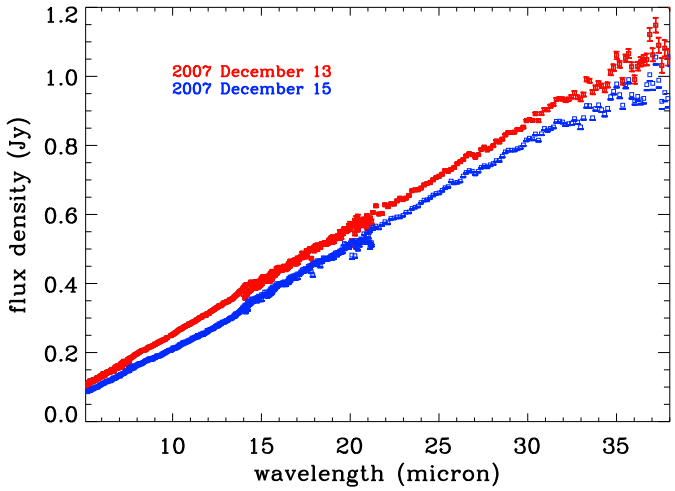


**Figure 7.14:** *Spitzer* spectra of 3C 454.3 for the observation carried out in 2007 December 13 (red points) and 15 (blue points) [Donnarumma et al. 2009b].

### 7.3.6 VLBI data

High resolution radio VLBI data were obtained from the MOJAVE[3] project, a long-term program to monitor with the full VLBA at 15 GHz the radio brightness and polarization variations in jets associated with active galaxies visible in the northern sky (Lister et al. 2009). We obtained the calibrated $I$ images and

[3]Monitoring Of Jets in Active galactic nuclei with VLBA Experiments

used the AIPS package to derive the position and flux density of the core and of a few substructures in the jets using the task JMFIT (Gaussian fit) (see Fig. 7.15). Moreover, this source was additionally observed by VLBA at four epochs during the period of the maximum brightness within the BK150 VLBA experiment to measure parsec-scale spectra of $\gamma$-ray bright blazars (Sokolovsky et al., in preparation). We use 15 and 43 GHz results from this program to provide better radio coverage of the high activity period. These data are in agreement with MOJAVE results and give a better statistics in the high active period. The core is always unresolved by our Gaussian fit and uncertainties on the flux density are dominated by calibration uncertainties (a few percent).

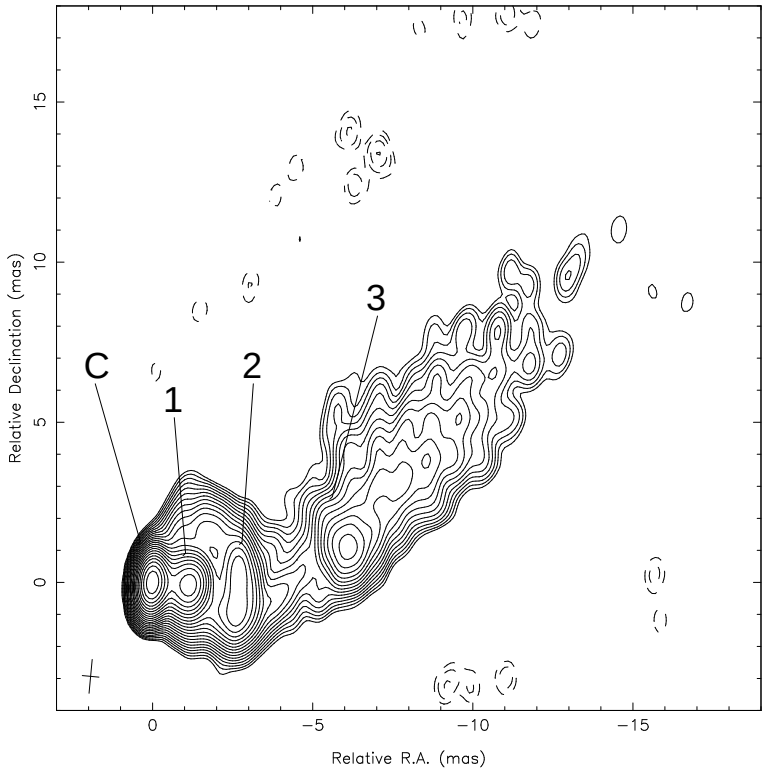


**Figure 7.15:** VLBI image of 3C 454.3 at 15 GHz on 2007 August 9 (MJD 54231). The peak flux density is 2.8 Jy beam$^{-1}$. The cross in the bottom left corner shows the beam FWHM, which is 1.07 × 0.52 mas at -5.4 deg [Vercellone et al. 2009b].

In Figure 7.16 we show the 3C 454.3 VLBI radio core flux at 15 and 43 GHz (panel (a)), the radio components flux density at 15 GHz (panel (b)), and the distance of radio components from the core (panel (c)) as a function of time. The flux shows a constant increase from 2006 June 15 (MJD 53901) until 2008

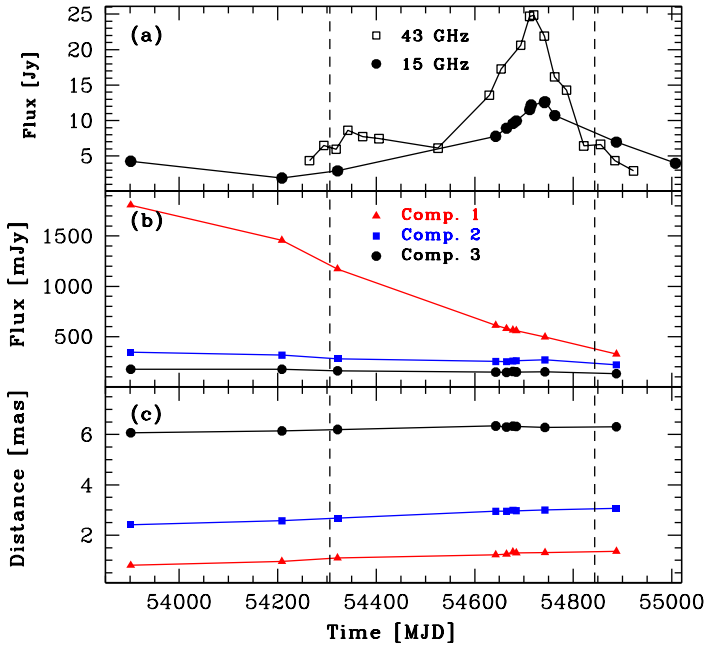


**Figure 7.16:** Panel (a): radio core flux density at 15 GHz (filled circles) and at 43 GHz (open squares), respectively. Panel (b): radio components flux density at 15 GHz. Panel (c): radio components motion at 15 GHz. The vertical dashed lines represent the start (2007 July 24) and the stop (2009 January 12) of all the AGILE observations, respectively [Vercellone et al. 2009b].

October 3 (MJD 54742), followed by a fast decrease towards the last epoch presented here, 2009 June 25 (MJD 55007). Jet components show a well defined flux density decrease (component 1) or a slower flux density decrease which becomes almost constant in the last epochs. Proper motion is evident, but slowing in time for components 1 and 2; it is almost absent for component 3.

All data are in agreement with a strong core flux density variability possibly connected to the $\gamma$-ray activity, while jet components are moving away and slowly decreasing in flux density, and are not affected by the recent core activity. Recently Kovalev et al. (2009), correlating the *Fermi*-LAT three month data with the MOJAVE ones find a connection between the radio and the $\gamma$-ray emission and arguing that the central region of the blazars being the source of $\gamma$-ray flares.

Figure 7.17 clearly shows a strong enhancement of the radio core flux starting about on MJD 54500. The radio variability is not well correlated with the variability at higher frequencies. Moreover, the radio flux density increase is

smooth and longer in time, while $\gamma$-ray and optical flares are evolving faster.

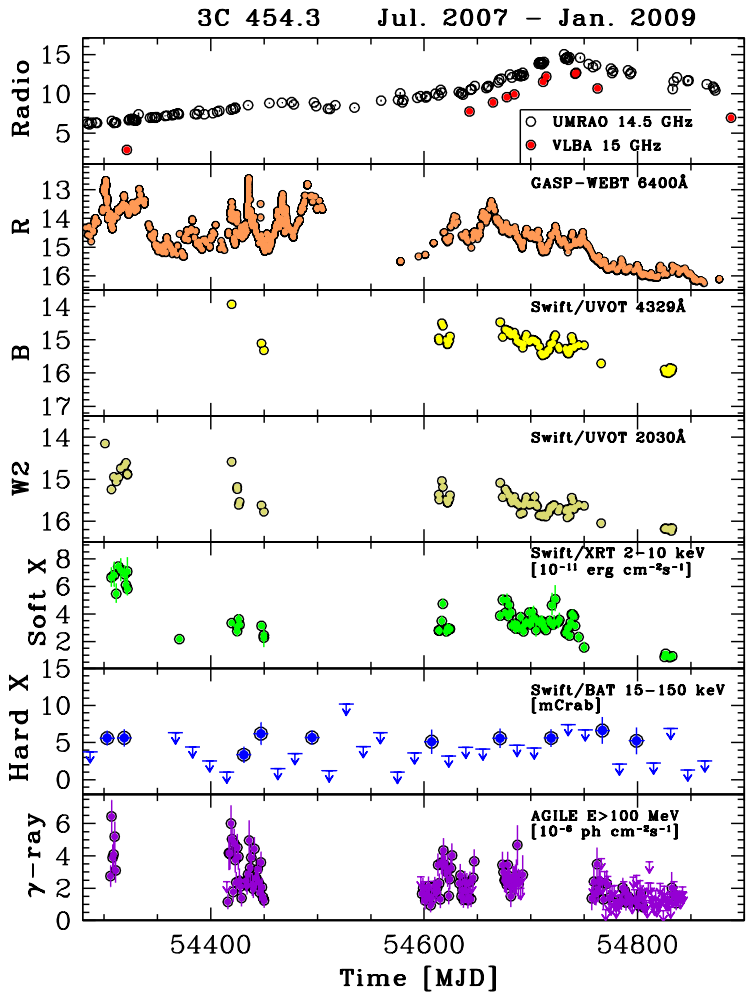


**Figure 7.17:** 3C 454.3 light curves between July 2007 and January 2009 at decreasing energies from bottom to top. Data were collected by AGILE-GRID, *Swift*/BAT, *Swift*/XRT, *Swift*/UVOT, GASP-WEBT, VLBA and UMRAO [Vercellone et al. 2009b].

At 230 GHz the flux density variability mimics the VLBI radio core properties to MJD 54600, when a large flux density increase is visible, with a peak at about MJD 54630. At this frequency the source remains in an active phase up to MJD 54700. This poses an interesting question as to the nature of such an increase of the core radio flux. As reported in Ghisellini et al. (2007) it is likely

that the emitting region is more compact and has a smaller bulk Lorentz factor closer to the black hole. We assume that in the region active at 43 GHz, in the quiescent state, the jet Lorentz factor is $\Gamma \sim 10$ (Giovannini et al. 2001). To obtain the flux density increase of the core at 43 GHz (from $\sim 5$ Jy up to 25 Jy) the Doppler factor has to increase up to $\delta \sim 30$. Such an increase requires that the source is oriented at a small angle $\theta$ with respect to the line of sight, since a large change in the jet velocity will produce a small increase in the Doppler factor. A Doppler factor $\delta = 30$ can be obtained if $\theta = 1.5^\circ$ and $\Gamma = 20$, corresponding to a bulk velocity increase from 0.9950 to 0.9987. A larger orientation angle (e.g. $\theta = 3^\circ$) with the same increase in the jet velocity, will produce only a small change in the Doppler factor $\delta$, from 16 to 19.

The presence of one or more new jet components is not revealed in the high resolution VLBA images, even if the most recent VLBA images at 43 GHz suggest a jet expansion near to the radio core starting from MJD $\sim$ 54600. Because of the presence of multiple bursts at $\gamma$-ray band and a single peak in the radio band it is not possible to correlate the radio peak with a single $\gamma$-ray or optical burst. We can speculate that a multiple source activity in the optical and $\gamma$-ray bands is integrated in the radio emitting region in a single event, with a clear flux density peak on MJD $\sim$ 54720 and we can assume that 43 GHz is the self-absorption frequency at that epoch.

The different behaviour observed in the radio, optical and $\gamma$-ray bands from the end of 2007 could be alternatively interpreted in the framework of a jet helical model (see Villata et al. 2009), in which the change of orientation of a curved jet yields different alignment configurations within the jet and therefore a different angle of view with respect to the line of sight of the observer. During 2007, a more pronunced fluxes and variability in optical and $\gamma$-ray seems to favor the inner portion of the jet as the more beamed one. On the other hand, the dimming trend in these energy bands, whereas the mm flux emission and its enhanced variability during 2008, seem to indicate that the more extended region of the jet became more aligned with respect to the observer line of sight.

## 7.4 Optical/$\gamma$-ray correlation

Considering the long-term monitoring of 3C 454.3 provided by GASP-WEBT and AGILE in optical as well as in $\gamma$-ray energy bands, we investigated the correlation between the $\gamma$-ray flux and the optical flux density in the *R*-band by means of the discrete correlation function (DCF; Edelson et al. 1988). This method was developed to study unevenly sampled data sets. The upper limits on the $\gamma$-ray fluxes were considered as detections, with fluxes equal to one half of the limit.

We investigated four distinct periods: July 2007, November–December 2007, May–August 2008, and October 2007–January 2009.

During July 2007, AGILE observed 3C 454.3 for only 5 days, therefore the low statistics prevents us to obtain reliable results with the DCF for this period. In contrast, the period November–December 2007 offers a good opportunity to test the correlation, since the period of common monitoring lasted for more than a month (see Fig. 7.18). The corresponding DCF (Figure 7.19) shows a maximum DCF $\sim 0.38$ for a null time lag. However, the shape of the peak is asymmetric, and if we calculate the centroid (Peterson 1998), we find that the time lag between $\gamma$-ray and optical emission is $-0.42$ days, i.e. about 10 hours. We estimated the uncertainty on the time lag by means of the statistical method known as 'flux randomization/random subset selection' (FR/RSS; Peterson et al. 1998; Raiteri et al. 2003). We run 2000 FR/RSS realizations and for each of them calculated the centroid corresponding to the maximum. The resulting centroid distribution, shown in Figure 7.19, allows us to conclude that the $\gamma$-optical correlation occurs with a time lag of $\tau = -0.4^{+0.6}_{-0.8}$, the uncertainty corresponding to a 1-$\sigma$ error for a normal distribution. This result is in agreement with what was found by analyzing the 2007 December dataset only, with a DCF maximum at a time lag of –1 day and a centroid of $\tau = -0.56$ days. The analysis of the November dataset only instead showed a DCF peak occurred at $\tau = 0$, but with a value of DCF $\sim 0.5$, that indicates a moderate correlation.

Moreover, considering the interesting rapid optical flare observed by GASP-WEBT on 2007 December 12 (Raiteri et al. 2008b), with an exceptional variability, we analyzed the $\gamma$-ray data between 5 and 16 December 2007 with a data binning of 12 hours (Fig. 7.20). The analysis showed an enhancement of a factor $\sim 2$ of the $\gamma$-ray flux during the second half of December 12, that remarkbly includes the time of the optical event, with an increase comparable with the 1.1 mag optical brightening. constraining the possible delay between $\gamma$-ray and optical emission within 12 hours. This support the evidence of a change in the jet emission in the EC scenario.

Unfortunately, during the period May–August 2008 the optical peaks occurred when AGILE was not observing the source. Finally, we computed the DCF corresponding to October 2007 – January 2009. We obtain a broad maximum, indicating a fair correlation ($\mathrm{DCF}_{\mathrm{max}} \sim 0.66$) but with large errors, peaking at –2 day time lag, and a centroid around 0 day. This result is consistent with that obtained in November–December 2007 and with the one obtained by Bonning et al. (2009a), analyzing the public $\gamma$-ray data from *Fermi*-LAT and the optical SMARTS data.

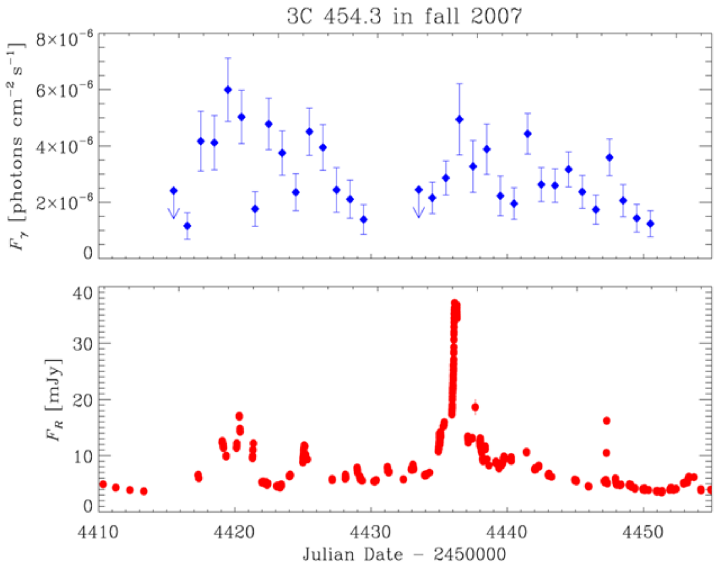


**Figure 7.18:** Light curves of 3C 454.3 in $\gamma$-ray (upper panel) and optical band (lower panel) acquired during November–December 2007 by AGILE and GASP-WEBT, respectively [D'Ammando et al. 2009d].

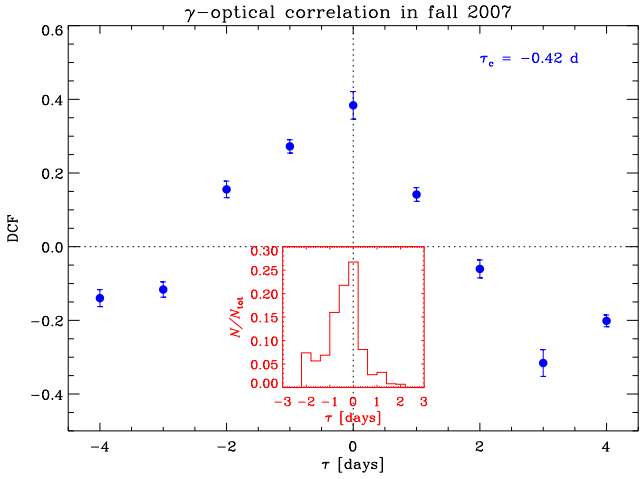


**Figure 7.19:** Discrete correlation function between the $\gamma$-ray and optical fluxes during November–December 2007. The uncertainty in the time-lag can be computed according to the FR/FSS method. The inset shows the resulting centroid distribution [Vercellone et al. 2009b].

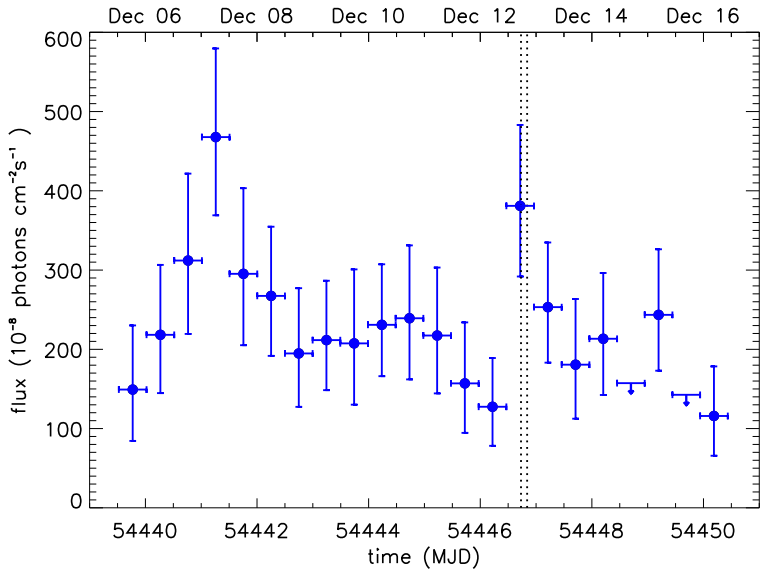


**Figure 7.20:** AGILE $\gamma$-ray light curve with a binning of 12 hr during the period 2007 December 5 and 16, E > 100 MeV. The vertical lines mark the time (< 3 hr) of the exceptional optical event of 2007 December 12 [Donnarumma et al. 2009b].

## 7.5 Modeling the spectral energy distributions

Considering the wide coverage obtained over the entire electromagnetic spectrum of 3C 454.3 between July 2007 and January 2009, we have the opportunity to build the SED of the source in different epochs and study in detail the emission mechanisms at work in this blazar.

In fact, different emission mechanisms can be invoked to explain the $\gamma$-ray emission in the blazars. In the leptonic scenario, the low–frequency peak in the SED is interpreted as synchrotron radiation from high–energy electrons in the relativistic jet, while the high–energy peak can be produced by IC on different flavours of seed photons. In the synchrotron self Compton model (SSC; e.g. Ghisellini et al. 1985) the seed photons come from the jet itself. Alternatively, the seed photons can be those of the accretion disk (ECD: external Compton scattering of direct disk radiation; Dermer et al. 1992), or those of the BLR clouds (ECC, external Compton scattering from clouds; Sikora et al. 1994). The target seed photons can also be those produced by the dust torus surrounding the central engine (ERC(IR), external Compton scattering from IR-emitting dust; Sikora et al. 2002).

We fit the SED of 3C 454.3 in the different epochs by means of a one-zone leptonic model, considering the contributions from SSC, ECD and ECC components. The emission along the jet is assumed to be produced in a spherical blob with comoving radius $R$ by accelerated electrons characterized by a comoving broken power law energy density distribution of the form

$$n_{\rm e}(\gamma) = \frac{K\gamma_{\rm b}^{-1}}{(\gamma/\gamma_{\rm b})^{\alpha_{\rm l}} + (\gamma/\gamma_{\rm b})^{\alpha_{\rm h}}}\,, \tag{7.1}$$

where $\gamma$ is the electron Lorentz factor assumed to vary between $10 < \gamma < 1.5 \times 10^4$, $\alpha_{\rm l}$ and $\alpha_{\rm h}$ are the pre– and post–break electron distribution spectral indexes, respectively, and $\gamma_{\rm b}$ is the break energy Lorentz factor. We assume that the blob contains a random average magnetic field $B$ and that it moves with a bulk Lorentz factor $\Gamma$ at an angle $\theta_0$ with respect to the line of sight. The relativistic Doppler factor is then $\delta = [\Gamma\,(1 - \beta\,\cos\theta_0)]^{-1}$, where $\beta$ is the usual blob bulk speed in units of the speed of light.

Our modelling of the source high-energy emission is based on an IC model with two main sources of external target photons: (1) an accretion disk characterized by a blackbody spectrum peaking in the UV with a bolometric luminosity $L_{\rm d}$ for a IC scattering blob at a distance $d = 4.6 \times 10^{16}$ cm from the central part of the disk; (2) a BLR with a spectrum peaking in the $V$ band, placed at a distance from the blob of $r_{\rm BLR} = 4 \times 10^{18}$ cm, and assumed to reprocess 10% of the irradiating continuum (Tavecchio et al. 2008; Raiteri et al. 2007; Raiteri et al. 2008a).

These two regions contribute to the ECD and the ECC, respectively, and it is interesting to test the relative importance of the two components that can be emitted by the relativistic jet of 3C 454.3 and the possible presence of other emission components in the different observation epochs.

We first consider the SED of November 2007, including AGILE-GRID, INTEGRAL/IBIS, *Swift* (UVOT and XRT) and GASP-WEBT data of the period November 19–22 (MJD 54423.5–54426.5). The SED is shown in Fig. 7.21, where the dotted, dashed, and dot–dashed lines represent the contributions of the accretion disk blackbody, the external Compton on the disk radiation and the external Compton on the BLR radiation, respectively. The ECD contribution can account for the soft and hard X-ray portion of the spectrum, which show a moderate, if any, time variability in the *Swift*/XRT and INTEGRAL/IBIS data (see Section 7.6.1). However, the ECD component alone cannot account for the hardness of the $\gamma$-ray spectrum observed by AGILE and a dominant contribution from ECC seems to provide a better fit of the data in the $\gamma$-ray energy band. The best fit parameters values are: $\alpha_{\rm l} = 2.2$, $\alpha_{\rm h} = 5.0$, $\gamma_{\rm b} = 500$, $K = 12$ cm$^{-3}$, $B \sim 8$ G, $\Gamma = 8.4$, $\theta_0 = 2.6^\circ$, $R = 3.5 \times 10^{16}$ cm, $L_{\rm d} = 5 \times 10^{46}$ erg s$^{-1}$, and $r = 0.05$ pc (where $r$ is the distance between the accretion disk and the emitting region).

The energetics of 3C 454.3 can be computed by estimating the isotropic luminosity in the $\gamma$-ray band, $L_\gamma^{\rm iso}$, and comparing it with the Eddington, the bolometric, and the particle injection luminosities. For a given source with redshift $z$, the isotropic emitted luminosity in the energy band $\epsilon$ is defined as

$$L(z)_\epsilon = \frac{4\pi F d_{\rm l}^2(z)}{(1+z)^{(1-\alpha)}}\,, \tag{7.2}$$

where, in our case, $\epsilon$ is the $\gamma$-ray energy band with $E_{\rm min} = 100$ MeV and $E_{\rm max} = 10$ GeV, $\alpha$ is the $\gamma$-ray energy spectral index, $\mathrm{F}(\nu) \propto \nu^{-\alpha}$ is the energy differential flux, $F = \int_{E_{\rm min}/{\rm h}}^{E_{\rm max}/{\rm h}} F(\nu)\,d\nu$ is the flux in the $\gamma$-ray band, and the luminosity distance is given by

$$d_{\rm l}(z_1, z_2) = (1+z_2)^2 \times \frac{c/H_0}{1+z_2} \int_{z_1}^{z_2} [E(z)]^{-1} dz\,, \tag{7.3}$$

where $\mathrm{z}_1 = 0$, $\mathrm{z}_2 = \mathrm{z}_{\rm src}$ and

$$E(z) = \sqrt{\Omega_{\rm M}(1+z)^3 + (1-\Omega_{\rm M}-\Omega_\Lambda)(1+z)^2 + \Omega_\Lambda}\,, \tag{7.4}$$

where $H_0$ is the Hubble constant, $\Omega_{\rm M}$ and $\Omega_\Lambda$ are the contribution of the matter and of the cosmological constant, respectively, to the density parameter. We assume $H_0 = 70$ km s$^{-1}$ Mpc$^{-1}$, $\Omega_{\rm M} = 0.3$, and $\Omega_\Lambda = 0.7$. Using the observed average $\gamma$-ray flux, we obtain $L_\gamma^{\rm iso} = 3.9 \times 10^{48}$ erg s$^{-1}$.

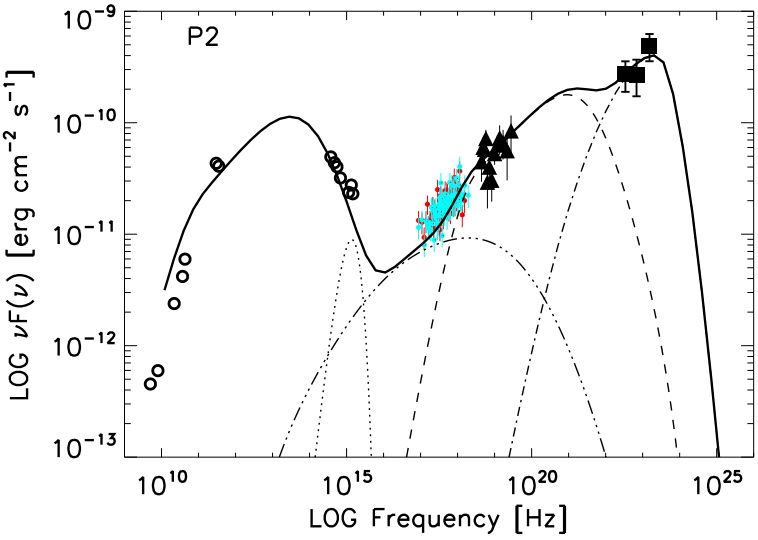


**Figure 7.21:** SED for the period MJD 54423.5–54426.5. Filled squares represent the AGILE-GRID data in the energy range 100 MeV–1 GeV; filled triangles represent INTEGRAL/IBIS data in the energy range 20–200 keV (orbits 623+624); small filled circles represent *Swift*/XRT data in the energy range 0.3–10 keV; open symbols represent radio to UV data taken from Raiteri et al. (2008b), corresponding to MJD 54425. The dotted, dashed, dot–dashed, and the triple–dot dashed lines represent the accretion disk, the ECD, ECC, and the SSC contributions, respectively [Vercellone et al. 2009a].

Moreover, from the values used for fitting the SED and from Equation 7.1 we can compute the particle injection luminosity, $L_{\rm inj}$ , obtaining:

$$L_{\rm inj} = \pi R^2 \Gamma^2 c \int [d\gamma\ m_{\rm e} c^2 \gamma\, n(\gamma)] = 3 \times 10^{44}\,{\rm erg\,s^{-1}}. \qquad (7.5)$$

Assuming for 3C 454.3 a black hole mass $M_{\rm BH} = 4.4 \times 10^9\,{\rm M_\odot}$ (Gu 2001), we obtain an Eddington luminosity of the order of $L_{\rm Edd} = 5.7 \times 10^{47}$ erg s$^{-1}$ to be compared with the bolometric luminosity $L_{\rm bol} = 1.9 \times 10^{47}$ erg s$^{-1}$ reported in Woo & Urry (2002). We obtain, therefore, that the source energetic is comparable to the value obtained by Tavecchio et al. (2007) for the power of the inner portion of jet, few $\times 10^{47}$ erg s$^{-1}$.

The wide multifrequency coverage obtained during December 2007, thanks to AGILE, *Spitzer*, *Swift*, *Suzaku*, GASP-WEBT and REM observations, allowed us to build the SED for three different epochs: December 5, 13, and 15. In these periods, the X-ray part of the SED shows a softening towards lower frequencies that can be due to two causes: a contribution from bulk Comptonization by cold

electrons in the jet (Celotti, Ghisellini & Fabian 2007), or the emergence of the SSC contribution in soft X-rays from the more energetic EC component due to the disk and the BLR.

The mid-Infrared *Spitzer* data and GASP-WEBT optical data available in December 13 and 15 well define the synchrotron peak, and combined with the resolved *Swift* X-ray spectrum and the AGILE $\gamma$-ray data constrain the model parameters, arguing for the latter cause, even if some contribution from bulk Comptonization cannot be ruled out.

In December 13 and 15, 3C 454.3 was in a different state with respect to the one analyzed in November: optical and UV fluxes appeared lower by a factor 2–3, suggesting that the synchrotron emission peaks at a frequency 5–10 times lower than the one observed in November, as confirmed also from the mid-Infrared data. On the other hand, the soft X-ray data were only a little bit lower than in November. Despite the softer synchrotron peak, $\gamma$-ray data showed in the SED the persistence of a hard peak at $\simeq$ 1 GeV, similar to the higher states observed by AGILE in July 2007 and November 2007 (see Anderhub et al. 2009a). We attempted to fit the SEDs of December with a one-zone SSC model plus the contribution of external seed photons coming from an accretion disk and a BLR, similar to that of November 2007. With this model, we succeeded to fit the synchrotron bump as well as the X-ray data assuming parameters similar to the November ones, but a lower break Lorentz factor ($\gamma_{\rm b} \simeq 350$) was required to account for the softness of the synchrotron bump. With this $\gamma_{\rm b}$ the EC from a standard BLR peaks at $h\nu \simeq h\nu_{\rm soft}\,\Gamma\gamma_{\rm b}^2\delta/(1+z) \sim 10^8$ eV. This is in contrast with the observed hardness of the $\gamma$-ray spectrum up to 1 GeV. We note that the ECD can account for the rising hard X-ray portion of the SED, which did not show clear variability, but both the disk and BLR components cannot account for the hardness of the $\gamma$-ray spectrum.

Thus, we consider a further external source of seed photons. A possibile candidate is the hot extended corona that must be consistently produced in steady accretion/ejection flows as shown by MHD numerical simulations (Tzeferacos et al. 2009). Hence, we added to the model the contribution by external seed photons coming from the hot corona. In Table 7.6 are reported the best fit parameters of the modeling of the SEDs. Remarkably, the lower $\gamma_{\rm b}$ required in these epochs, makes the BLR a too soft contributor at GeV energies, while the contribution of the hot corona succeeded to account for the persistence of the hard $\gamma$-ray spectra measured by AGILE.

On December 5, the low energy peak of the SED is less constrained with respect to the December 13 and 15 ones due to the lack of the mid-Infrared data, but the *Suzaku* X-ray data (green points in Fig. 7.22) better constrain the rise of the IC emission. We fitted this SED with almost the same model assumed for the other two epochs, but the higher optical flux and the lower $\gamma$-ray flux detected

with respect to December 13 required a higher magnetic field and a lower $\gamma_b$ (see Table 7.6).

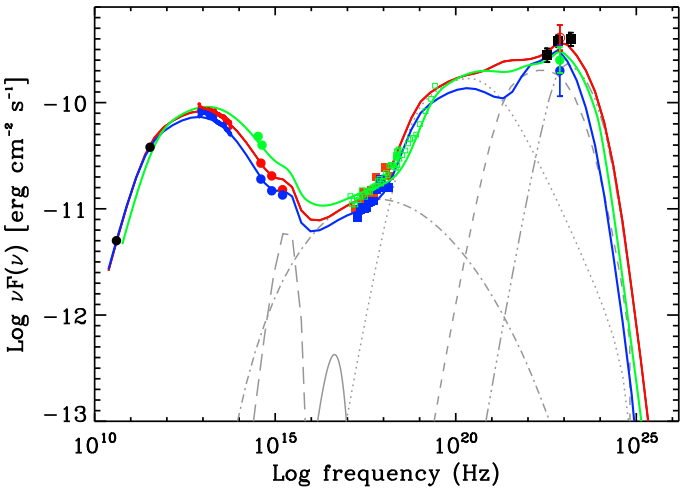


**Figure 7.22:** SEDs of 3C 454.3 for 2007 December 5, 13 and 15 (green, red and blue solid lines, respectively). The $\gamma$-ray spectrum for $E > 100$ MeV (black squares), exctracted from data acquired between December 5–16 and the radio points (black circles) from Raiteri et al. (2008a) are also reported. The gray lines represent the contribution of the disk (long dashes), corona (solid), SSC (dot-dashed), EC disk (dotted), EC BLR (dashed), EC corona (dash dot dot) to the model [Donnarumma et al. 2009b].

Given the different $\gamma$-ray states of the source analyzed in the November and December campaigns, we compared the particle injection luminosity, $L_{\rm inj}$ (see eq. (7.5)) measured during the two multiwavelength campaigns. We found the particle injection luminosity of December to be $6 \times 10^{43}$erg s$^{-1}$, a factor of 5 lower than the November one. This difference is due to both the lower $\gamma_b$ and $\gamma_{\rm min}$ values needed to reproduce the SED in the states of December.

**Table 7.6:** Model parameters for the December 5, 13 and 15 observations of 3C 454.3.

| Observation date | $\Gamma$ | B Gauss | R cm | K cm$^{-3}$ | $\gamma_b$ | $\gamma_{\rm min}$ | $\alpha_l$ | $\alpha_h$ |
|---|---|---|---|---|---|---|---|---|
| 5-Dec-2007 | 18 | 2.5 | $2.2 \times 10^{16}$ | 50 | $3 \times 10^2$ | 30 | 2.3 | 4.2 |
| 13-Dec-2007 | 18 | 2 | $2.2 \times 10^{16}$ | 52 | $3.5 \times 10^2$ | 38 | 2.3 | 4.2 |
| 15-Dec-2007 | 18 | 2 | $2.2 \times 10^{16}$ | 52 | $3.2 \times 10^2$ | 35 | 2.3 | 4.2 |

Finally, we fit the SEDs of the period 2008 May 31 – June 1 (MJD 54617–54618), when 3C 454.3 entered a phase of high $\gamma$-ray activity, 2008 July 26 – August 15 (MJD 54673–54693), when the $\gamma$-ray flux was almost constant, and 2008 November 30 – 2009 January 14 (MJD 54800–54845), when the source reached the minimum $\gamma$-ray flux, in order to investigate the possible differences in the jet parameters during different activity states. For the fit we use a one-zone leptonic model, considering the contributions from the SSC, ECD and ECC components plus the emission from the accretion disk, clearly detected during faint states of the source (Raiteri et al. 2007). Table 7.7 shows the best-fit parameters of the modeling of SEDs corresponding to the three periods, shown in Figures 7.23, 7.24, and 7.25. The thin solid, dotted, dashed, dot-dashed, and the triple-dot-dashed, represent the accretion disk blackbody, the synchrotron, the SSC, the external Compton on the disk, and the external Compton on the BLR radiation, respectively, while the thick solid line represents the sum of all the individual components. The insert of Figure 7.25 shows the portion of the SED dominated by the contribution of the disk blackbody radiation, which clearly emerges since the source is a relative low state. This observation confirm the presence of an important contribution of the accretion disk emission during the low activity states of 3C 454.3, as already detected by Raiteri et al. (2008a) with a simultaneous GASP and XMM-*Newton* observation.
We find that the three SEDs can be reproduced well by very similar parameters, the main difference being the shape of the electron distribution and the break energy Lorentz factor.

Finally, we computed for the three different SEDs the total power carried in the jet, $P_{\rm jet}$, defined as

$$P_{\rm jet} = L_{\rm B} + L_{\rm p} + L_{\rm e} + L_{\rm rad} \ \ {\rm erg\,s^{-1}} \tag{7.6}$$

where $L_{\rm B}$, $L_{\rm p}$, $L_{\rm e}$, and $L_{\rm rad}$ are the power carried by the magnetic field, the cold protons, the relativistic electrons, and the produced radiation, respectively. We obtain a value of $P_{\rm jet}$ of $3.2\times10^{46}$ erg s$^{-1}$, $3.7\times10^{46}$ erg s$^{-1}$, and $2.5\times10^{46}$ erg s$^{-1}$ for the three periods, respectively. The total power of the jet is lower at the end of the AGILE observing period, following the general trend of decrease of the emission observed over the entire electromagnetic spectrum (except for the radio emission).

**Table 7.7:** Input parameters for the model of SED 1, SED 2, and SED 3.

| Parameter | SED1 | SED2 | SED3 | Units |
|---|---|---|---|---|
| $\alpha_{\rm l}$ | 2.3 | 2.5 | 2.0 | |
| $\alpha_{\rm h}$ | 4.0 | 4.0 | 4.2 | |
| $\gamma_{\rm min}$ | 30 | 30 | 18 | |
| $\gamma_{\rm b}$ | 300 | 280 | 180 | |
| $K$ | 80 | 80 | 100 | $\rm cm^{-3}$ |
| $R$ | 21.5 | 21.5 | 21.5 | $10^{15}$ cm |
| $B$ | 2 | 2 | 2 | G |
| $\delta$ | 34 | 34 | 34 | |
| $L_{\rm d}$ | 5 | 5 | 5 | $10^{46}\,\rm erg\,s^{-1}$ |
| $r_{\rm d}$ | 0.015 | 0.015 | 0.015 | pc |
| $\Theta_0$ | 1.15 | 1.15 | 1.15 | degrees |
| $\Gamma$ | 20 | 20 | 20 | |
| $P_{\rm jet}$ | 3.2 | 3.7 | 2.5 | $10^{46}\,\rm erg\,s^{-1}$ |

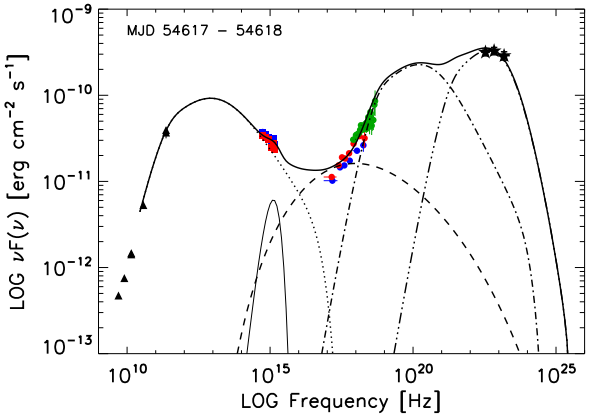


**Figure 7.23:** SED of 3C 454.3 centered on MJD 54617–54618. Black triangles, red (blue) squares, red (blue) circles, green circles, and black stars represent radio, MJD 54617 (54618) *Swift*/UVOT, MJD 54617 (54618) *Swift*/XRT, RXTE, and AGILE-GRID data, respectively. UV and X-ray data are de-reddened and corrected for Galactic extintion. The thin solid, dotted, dashed, dot-dashed, and the triple-dot-dashed, represent the accretion disk blackbody, the synchrotron, the SSC, the external Compton on the disk, and the external Compton on the BLR radiation, respectively. The thick solid line represent the sum of all the individual components [Vercellone et al. 2009b].

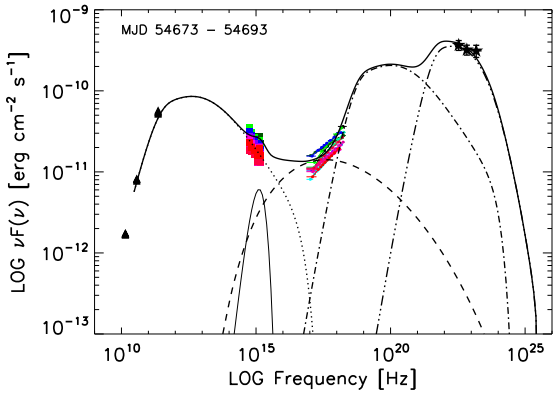


**Figure 7.24:** SED of 3C 454.3 during the period MJD 54673–54693. Black triangles, multicolor squares, circles, and black stars represent radio, *Swift*/UVOT, *Swift*/XRT, and AGILE-GRID data, respectively. UV and X-ray data are de-reddened and corrected for Galactic extintion. The thin solid, dotted, dashed, dot-dashed, and the triple-dot-dashed, represent the accretion disk blackbody, the synchrotron, the SSC, the external Compton on the disk, and the external Compton on the BLR radiation, respectively. The thick solid line represent the sum of all the individual components [Vercellone et al. 2009b].

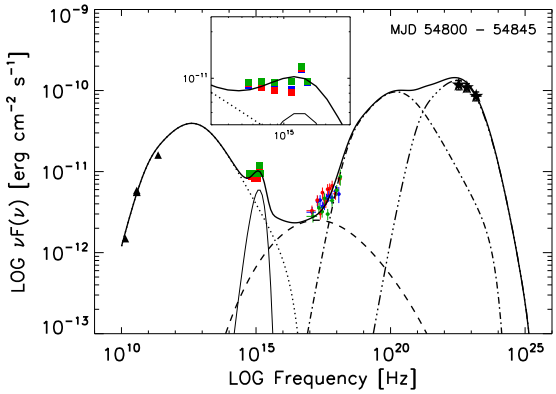


**Figure 7.25:** SED of 3C 454.3 during the period MJD 54800–54845. Black triangles, multicolor squares, circles, and black stars represent radio, *Swift*/UVOT, *Swift*/XRT, and AGILE-GRID data, respectively. UV and X-ray data are de-reddened and corrected for Galactic extintion. The thin solid, dotted, dashed, dot-dashed, and the triple-dot-dashed, represent the accretion disk blackbody, the synchrotron, the SSC, the external Compton on the disk, and the external Compton on the BLR radiation, respectively. The thick solid line represent the sum of all the individual components. The insert shows the portion of the SED dominated by the contribution of the disk blackbody radiation [Vercellone et al. 2009b].

3C 454.3 was observed during the active phases of July–August 2007 and November–December 2007 also with the MAGIC telescope and these data were analyzed with the MAGIC standard analysis tools, deriving only upper limits for the emission at TeV energies. For the periods around the ends of July and November, characterized by the most complete multifrequency coverage, including AGILE $\gamma$-ray data, we constructed the spectral energy distributions with nearly simultaneous observations from optical to TeV energy bands (Figure 7.26).

For July (left panel) we show the nearly simultaneous data in the optical (KVA), optical/UV (*Swift*/UVOT), X-ray (*Swift*/XRT) and $\gamma$-ray (AGILE-GRID) band. For November (right panel) the data in the optical, X-ray (*Swift*/XRT and INTEGRAL) and $\gamma$-ray (AGILE/GRID) data, averaged over the entire period of the AGILE observations (2007 November 11 – December 1) are shown. For comparison is also shown (open circles) historical data. Upper limits from MAGIC observations (18–21 July and 27, 28, 30 November) are shown as triangles (observed: empty; EBL-deabsorbed: filled). For the EBL deabsorption is used the LowSFR model of Kneiske et al. (2004) which predicts a low level of the EBL close to what is presently inferred from observations, both directly (e.g. Franceschini et al. 2008) and indirectly (Aharonian et al. 2006; Mazin & Raue 2007; Albert et al. 2008a). We modeled the SED with a one-zone leptonic model including SSC components plus the scattering of the external photons originating in the disk and/or in the BLR.

The upper limits in the VHE band for the 3C 454.3 obtained by MAGIC are consistent with the expectations of the leptonic models for FSRQs, predicting a sharp decrease of the flux above few tens of GeV, due to the internal absorption of $\gamma$-rays and the decreased efficiency of the inverse Compton emission at high energy.

Moreover, these observations indicate that even upper limits at VHE energies if accompanied by simultaneous observations in the MeV-GeV band by AGILE and *Fermi*, can be useful to test current emission models for FSRQs.

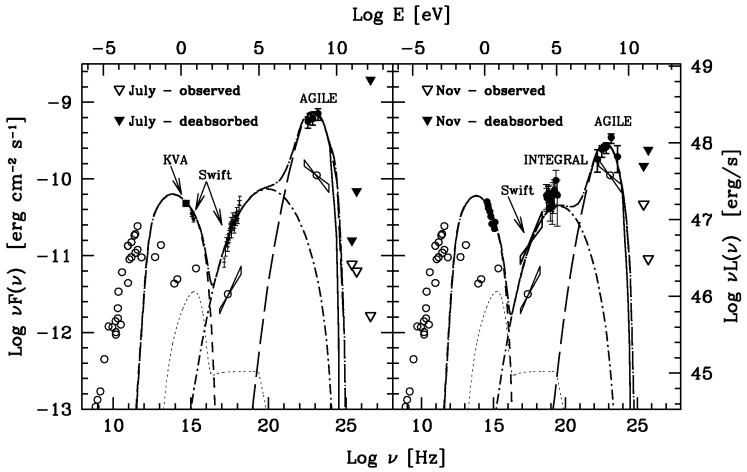


**Figure 7.26:** SED of 3C 454.3 build with multifrequency data available for the period close to the MAGIC observation at the end of July 2007 (left panel; optical: KVA, optical-UV: *Swift*/UVOT, X-ray: *Swift*/XRT, GeV band: AGILE-GRID) and November 2007 (right panel: optical-UV: *Swift*/UVOT, X-ray: *Swift*/XRT and INTEGRAL, GeV band: AGILE-GRID). Triangles report the observed (empty) and the deabsorbed (filled) upper limits of MAGIC in three different bands. For comparison we also report (open circles) historical data (Kühr et al. 1981, NED, Gear et al. 1994, Stevens et al. 1994, Impey & Neugebauer 1988, Smith et al. 1988 for radio and optical; Tavecchio et al. 2007b for X-rays from *Chandra*). The open circle and the bow-tie in the MeV-GeV region indicate the average EGRET spectrum (Hartman et al. 1999). Solid line reports the results of the overall model. We also report the single emission components: synchrotron (dashed), SSC (dotted-dashed) and EC (long dashed).The dotted line shows the emission of the accretion disk [Anderhub et al. 2009a].

## 7.6 The extraordinary $\gamma$-ray flare of December 2009

At the end of November 2009, the AGILE satellite started to detect a prolonged flaring $\gamma$-ray activity from 3C 454.3, with a peak on December 1–2 of the order of $1000 \times 10^{-8}$ ph cm$^{-2}$ s$^{-1}$ (Striani et al. 2009a), a flux level similar to that observed by *Fermi*-LAT on 2008 July 10 (Abdo et al. 2009e). In optical band, after a mild activity in August–October 2009 ($R \sim 14.5$–15 mag), and a decrease in November ($R \sim 15$–15.2 mag), a very fast flux increase was observed by GASP-WEBT, leading to a brightening of more than 1 mag between November 21 and December 1–2, when reached $R \sim 14.1$ mag (Villata et al. 2009).

Surprisingly, the $\gamma$-ray flux continues to increase and between 2009-12-02 06:30 UT and 2009-12-03 08:30 UT a quick-look maximum likelihood analysis of the AGILE data yields a flux of about $(1800 \pm 400) \times 10^{-8}$ ph cm$^{-2}$ s$^{-1}$, showing a dramatic increase of the $\gamma$-ray flux in 24 hours (Striani et al. 2009b), confirmed also by *Fermi*-LAT (Escande et al. 2009). This flux is more than twice the flux of the Vela pulsar, the brightest persistent source in the $\gamma$-ray sky. Figure 7.28 shows in the bottom panel the historical light curve of the AGILE observation of 3C 454.3, from July 2007 until the exceptional flaring state detected in December 2009, and in the top panel the $\gamma$-ray light curve in detail between 7 November and 17 December 2009. These observations are carried out with the AGILE satellite in spinning mode.

Considering the activity of this blazar, an intense monitoring observations by *Swift* started from December 1. The quicklook analysis of the *Swift*/XRT data revealed that the X-ray flux of 3C 454.3 has reached on 4 December the same level of the giant X-ray flare observed by the same source in May 2005 (Giommi et al. 2006). We fit the spectrum of the *Swift*/XRT data in the 0.3–10 keV energy band with an absorbed power law model with column density $N_H = 1.34 \times 10^{21}$ cm$^{-2}$, the value found by previous *Chandra* observation (Villata et al. 2006). The preliminary results of XRT analysis from Sakamoto et al. (2009) are reported in Table 7.8.

Also *Swift*/BAT detects flaring activity of 3C 454.3 in the same period, with a flux of 20 mCrab on 1 December 2009 and rising up to 50 mCrab on 3 December 2009 (Krimm et al. 2009b), and the optical activity increased again, with a peak on 3 December of $R = 13.83$ and a simultaneous flaring behaviour also in IR (Bonning et al. 2009b).

Following the AGILE and *Fermi* detections of this huge $\gamma$-ray flare, the INTEGRAL satellite performed a ToO observations of 3C 454.3. Integrating the data from 2009-12-06 16:41 UT to 2009-12-09 07:46 UT for a net exposure of about 205 ks we obtain a detection of the blazar with IBIS at a flux F(20–40

keV) = 13 mCrab and F(40–100 keV) = 16 mCrab [$9.8 \times 10^{-11}$ erg cm$^{-2}$ s$^{-1}$ and $1.5 \times 10^{-10}$ erg cm$^{-2}$ s$^{-1}$, respectively] (Vercellone et al. 2009c). The 20–40 flux level observed by INTEGRAL/IBIS shows a clear decaying trend of the hard X-ray emission with respect to the the flux observed by *Swift*/BAT.

The $\gamma$-ray flux observed by 3C 454.3 on 2–3 December 2009 is the highest flux ever observed by a blazar, and even more amazing is the persistent state of very high $\gamma$-ray activity of the source on timescales of 2-3 weeks. Moreover, it is interesting to note that analyzing the AGILE $\gamma$-ray data separately in the energy range 100–400 MeV and for E > 400 MeV, it seems evident that during the exceptional flaring event of 2–3 December a great increase of the flux measured for photons with energy higher than 400 MeV with respect to the behaviour observed in the energy band 100–400 MeV is observed (see Fig. 7.29). This could be an indication of an episode of acceleration in which the accelerated electron population increases, saturating at high energy first with respect to those producing for IC the $\gamma$-ray emission below 400 MeV. Detailed study of the light curves and the spectral energy distribution related to this exceptional flaring event is under investigation.

**Table 7.8:** Results of *Swift*/XRT observations of 3C 454.3. Power law model with $N_{\rm H}$ fixed to the Galactic value of $1.34 \times 10^{21}$ cm$^{-2}$ (Villata et al. 2006).

| Observation date | Flux (2–10 keV) erg cm$^{-2}$ s$^{-1}$ | Photon Index $\Gamma$ | $\chi^2_{\rm red}$ (d.o.f.) |
|---|---|---|---|
| 01-Dec-2009 | $1.14 \times 10^{-10}$ | $1.58 \pm 0.05$ | 1.14 (134) |
| 02-Dec-2009 | $1.32 \times 10^{-10}$ | $1.56 \pm 0.05$ | 1.05 (160) |
| 03-Dec-2009 | $1.22 \times 10^{-10}$ | $1.60 \pm 0.06$ | 1.10 (136) |
| 04-Dec-2009 | $1.58 \times 10^{-10}$ | $1.52 \pm 0.03$ | 1.13 (317) |

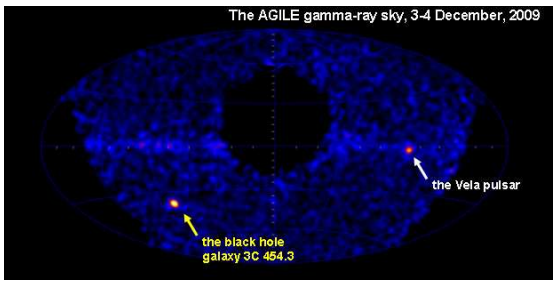


**Figure 7.27:** Intensity map of the $\gamma$-ray sky observed by AGILE on 3–4 December with E > 100 MeV, where it is clearly visible that at that time the $\gamma$-ray sky was dominated by the exceptional flare of 3C 454.3.

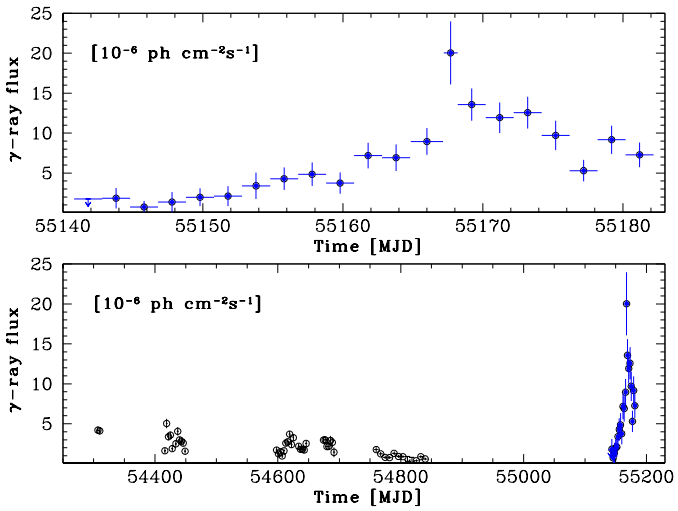


**Figure 7.28:** *: Top panel*: the AGILE $\gamma$-ray light curve of 3C 454.3 between 7 November and 17 December 2009 with a 2-day resolution for photons with E > 100 MeV (except for 3 December 2009, where a 1-day timebin is used). It is clearly visible the exceptional $\gamma$-ray flare of the source occurred on 2-3 December 2009. *Bottom panel*: AGILE historical $\gamma$-ray light curve of 3C 454.3 between July 2007 and December 2009 for E > 100 MeV.

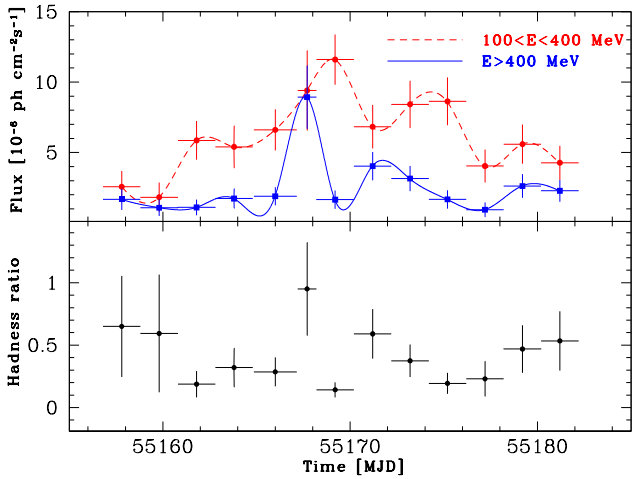


**Figure 7.29:** *: Top panel*: the AGILE light curve of 3C 454.3 between 7 November and 17 December 2009 in the energy range 100–400 MeV (red) and for photons with energies higher than 400 MeV (blue). *Bottom panel*: Hardness ratio between the flux (E > 400 MeV) and the flux (100–400 MeV).

## 7.7 Summary and remarks

1. 3C 454.3 is the blazar that exhibited the most high activity in $\gamma$-ray band in the last two years from July 2007 until the exceptional flaring activity of December 2009, when the source became for at least one week the brightest source in the $\gamma$-ray sky.

2. The $\gamma$-ray emission observed by AGILE during the long-term monitoring for E > 100 MeV is clearly highly variable, on timescales of the order of one day or even shorter, with prominent flares reaching on daily timescale the magnitude of the Vela pulsar and in exceptional cases also higher than it.

3. A dimishing trend of the $\gamma$-ray flux from July 2007 to January 2009 is observed by AGILE, with a hint of 'harder-when-brighter' behaviour in $\gamma$-rays, previously observed only for 3C 279 by EGRET.

4. Emission in optical range appears to be weakly correlated with that at $\gamma$-rays, with a lag of the $\gamma$-ray flux with respect to the optical one less than one day during bright states. The weak correlation could be due to the fact that overimposed to the overall long-term trend some sub-structures on shorter timescale with different variability could be present in optical and $\gamma$-rays.

5. While at almost all frequencies the flux shows a diminishing trend with time between July 2007 to January 2009, the 15 GHz radio core flux increases, although no new jet component seems to be detected.

6. The different behaviour of the light curves at different frequencies could be interpreted by a changing of the jet geometry between 2007 and 2008.

7. The dominant emission mechanism in $\gamma$-rays is the inverse Compton scattering of external photons from the BLR clouds scattering off the relativistic electrons in the jet, even if in some particular states (e.g. when a hardness of the $\gamma$-ray spectrum together with the softness of the synchrotron emission is observed, as in November 2007) the contribution of the seed photons from a hot corona could be important for the IC mechanism.

Chapter 8

# The Virgo region

## 8.1 Virgo region

The Virgo region is one of the best studied region of the sky by the *Compton Gamma-Ray Observatory* (*CGRO*), especially with EGRET, but also with OSSE and Comptel instruments. During the CGRO observation of the Virgo region it was revealed the presence of two bright and variable $\gamma$-ray blazars, 3C 273 and 3C 279, making Virgo a promising sky region for further $\gamma$-ray observations. Therefore, the AGILE satellite performed a dedicated pointing of the Virgo region for 3 times during the first two years of operation: July 2007, December 2007 – January 2008 and June 2009, for a total of $\sim$ 6 weeks. In particular, in July 2007 a $\gamma$-ray flare of 3C 279 was detected by AGILE, whereas during December 2007 – January 2008 a multifrequency campaign on 3C 273 was organized.

In this Chapter we present the AGILE and multiwavelength data collected on 3C 279 and 3C 273, respectively, during these two epochs and discuss the theoretical implications of the results of the data analysis for the emission mechanisms of these two objects. The analysis and results shown are published in Giuliani et al. (2009) and Pacciani et al. (2009a).

## 8.2 3C 279

### 8.2.1 Introduction

3C 279 (z = 0.536) is an optically violent variable (OVV) quasar, the first and one of the brightest blazar discovered to emit in $\gamma$-ray band by EGRET (Hartman et al. 1992c, 2001). The Spectral Energy Distribution (SED) of this source shows

two broad bumps with the first peak occurring at far-IR ($\sim 10^{13}$ Hz) and the second one extending in the MeV–GeV energy range, typical of the Flat Spectrum Radio Quasars (FSRQs). This blazar is highly variable at all frequencies of the spectrum, particularly in the high frequency part of the two bumps, showing a variability on time scales ranging from days to months. Dramatic variability on short timescales is a well-known characteristic of this object, with an amplitude that seems to increase with frequency.

3C 279 is the first quasar that exhibited apparent superluminal motion (Whitney et al. 1971) and high-resolution VLBI radio maps show correlations between flare activity and components ejected from the core (Wehrle et al. 2001). The observation of radio blobs emitted by 3C 279 (Lindfords et al. 2006) strongly supports the presence of a jet. It has been argued that the misalignment between the jet and the line of sight is only two degrees (Lindfords et al. 2005).

Despite its relatively large distance, this FSRQ is probably the most intensively studied blazar in every band of the electromagnetic spectrum, due also to the fact that this source has been bright and variable throughout the EGRET *era*. Therefore, 3C 279 has received a remarkable coverage at all frequencies in addition to the $\gamma$-ray range. In the $\gamma$-ray energy band 3C 279 has been detected several times by EGRET. Each time it was observed, even in low quiescent states (Hartman et al. 2001), it showed integrated flux changes up to a factor of 100 (Maraschi et al. 1994; Wehrle et al. 1998). The $\gamma$-ray emission exhibited the largest amplitude variability on both long (months) and short (days) time scales. The photon indexes of the $\gamma$-ray energy spectra during the different levels of activity of the source ranging from 1.7 to 2.4 and a correlation between average fluxes and spectral indices is still debated (Nandikotkur et al. 2007; Hartman et al. 2001).

Moreover, 3C 279 was also detected by OSSE (50 keV – 1 MeV) at the transition region from hard X-rays and $\gamma$-rays, and COMPTEL at low energy (1–30 MeV) $\gamma$-rays (McNaron-Brown et al. 1995). Although flux variations were found in the OSSE and EGRET energy bands, only marginal flux variations were observed in the COMPTEL energy band. Hartman et al. (2001) argued that this behaviour could be explained by considering the Comptonization of direct accretion disc photons at COMPTEL energies and the Comptonization of accretion disc photons scattered into the jet region by the Broad Line Region (BLR) clouds at EGRET energies.

Analyzing the data of 3C 279 collected by the *International Ultraviolet Explorer* in very low activity state, during 1992 December–1993 January, evidence for a thermal component in UV due to the emission from the accretion disk were noted by Pian et al. (1999). This Seyfert-like component, present in other blazars such as 3C 273 (Grandi and Palumbo et al. 2004; Türler et al. 2006), 3C 454.3 (Raiteri et al. 2007) and AO 0235+164 (Raiteri et al. 2006), seems to be de-

tected only in low/quiescent activity state of the sources, when the contribution of the beamed synchrotron radiation is less important. In the optical band 3C 279 varies dramatically on different time scales ranging from intense outbursts that last about one year to microvariability on the scale of hours (see e.g. Kartaltepe and Balonek 2007). Historically the source has a *R*-band magnitude ranging between 12.5 and 17.5 (e.g. Chatterjee et al. 2008). The variability profile of the flares observed seems to be consistent with the optical emission of 3C 279 being dominated by synchrotron emission produced in the strong magnetic field of the relativistic jet.

Recently, the MAGIC telescope has detected very high energy (VHE) $\gamma$-rays from 3C 279 (Albert et al. 2008a). This detection has come as a surprise. In fact, the detection of the VHE $\gamma$-ray emission from a source at such a distance could constrain the current theories about the density of the extragalactic background light (EBL), providing an indication that the Universe appears more transparent at cosmological distance than previously believed.

### 8.2.2 AGILE observations

At the beginning of the Science Performance Verification Phase, AGILE repointed the Virgo region, in the context of a multiwavelength campaign organized by Ann Wehrle, and observed the blazar 3C 279 for a total of 44 hours of effective time. The source was close ($\sim 2^\circ$) to the center of the field of view of the Gamma-Ray Imaging Detector (GRID) onboard AGILE for the whole observing time. SuperAGILE observed 3C 279 for a total on-source net exposure time of about 100 ks.

Level-1 AGILE-GRID data were analyzed using the AGILE Standard Analysis Pipeline (see 4.3.6). Counts, exposure, and Galactic background $\gamma$-ray maps, were created with a bin-size of $0.25^\circ \times 0.25^\circ$ for photons with energy greater than 100 MeV. We selected only events flagged as confirmed $\gamma$-ray events, and all events collected during the South Atlantic Anomaly and whose reconstructed directions form angles with the satellite-Earth vector smaller than $80^\circ$ are rejected.

During the period between 9 and 13 July 2007, AGILE-GRID detected a $\gamma$-ray source with position consistent with 3C 279 at a significance level of 11.1-$\sigma$ (see Fig. 8.1) with an average flux of $(210 \pm 38) \times 10^{-8}$ photons cm$^{-2}$ s$^{-1}$ for E > 100 MeV, as derived from a maximum likelihood analysis using the radio position of the source (l = 305.10° b = 57.06°). AGILE detected the source at a flux level comparable to that measured by EGRET when the source was in a flaring state. Fitting the $\gamma$-ray fluxes with a constant model (the weighted mean of the 1-day average flux values) and following McLaughlin et al. (1996) we obtain a variability coefficient of V = 0.32. Considering that a value of V >

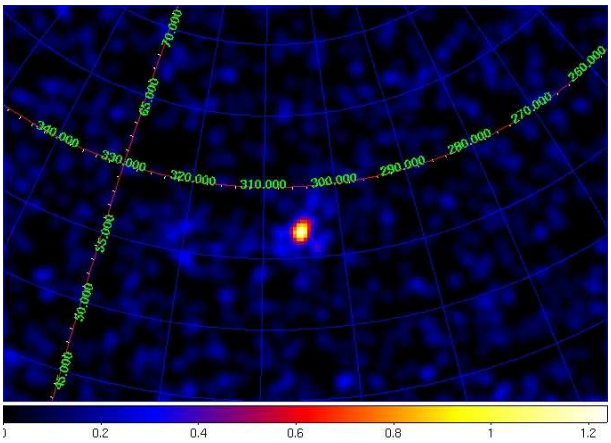


**Figure 8.1:** Gaussian-smoothed counts map in Galactic coordinates for the 3C 279 region over the observing period 9–13 July 2007. Only photons with an energy greater than 100 MeV have been selected [Giuliani et al. 2009].

1 indicates that the source is variable, this analysis shows that 3C 279 is not variable in $\gamma$-ray band during the short AGILE observation.

Fitting the AGILE-GRID data with a simple power law model we obtain for the average $\gamma$-ray spectrum of 3C 279 a photon index of $\Gamma = 2.22 \pm 0.23$. The photon index is calculated with the weighted least squares method, considering only three energy bins for the fit: 100–200 MeV, 200–400 MeV and 400–1000 MeV. The source instead was not detected (above 5-$\sigma$) by the SuperAGILE Iterative Removal of Sources (IROS) applied to the image, in the 20–60 keV energy range. A 3-$\sigma$ upper limit of 10 mCrab was obtained from the observed count rate by a study of the background fluctuations at the position of the source and a simulation of the source and background contributions with IROS.

### 8.2.3 *Swift*/XRT observations

During the AGILE observation, the source was monitored simultaneously in X-ray band by *Swift*/XRT through 4 Target of Opportunity (ToO) observations. The *Swift* X-ray Telescope (XRT; Burrows et al. 2004, 0.2–10 keV) data were processed with standard procedures (`xrtpipeline` v0.11.6) adopting the standard filtering and screening criteria. All the observations were carried in photon counting (PC) mode and photons were selected with grades in the range 0–12.

Spectral analysis was performed using the XSPEC fitting package 12.3.1, with the results shown in Table 8.1. We fit the spectra with an absorbed power law with Galactic absorption fixed at the value $N_{\rm H} = 2.05 \times 10^{20}$ cm$^{-2}$ (Kalberla

et al. 2005). *Swift*/XRT uncertainties are given at 90% confidence level for one interesting parameter, unless otherwise stated. Data were rebinned in order to have at least 20 counts per energy bin and to use the $\chi^2$ statistics.
*Swift*/XRT detected the source between 10 and 13 July 2007 with a 2–10 keV flux nearly constant of about $10^{-11}$ erg cm$^{-2}$ s$^{-1}$ (see Table 8.1).

**Table 8.1:** Results of *Swift*/XRT observations of 3C 279. Power law model with $N_{\rm H}$ fixed to the Galactic value of $2.05 \times 10^{20}$ cm$^{-2}$ (Kalberla et al. 2005) is used.

| Observation date | Flux (2–10 keV) erg cm$^{-2}$ s$^{-1}$ | Photon Index $\Gamma$ | $\chi^2_{\rm red}$ (d.o.f.) |
|---|---|---|---|
| 10-Jul-2007 | $1.20 \times 10^{-11}$ | $1.42 \pm 0.05$ | 1.21 (73) |
| 11-Jul-2007 | $1.17 \times 10^{-11}$ | $1.47 \pm 0.07$ | 0.86 (52) |
| 12-Jul-2007 | $1.05 \times 10^{-11}$ | $1.47 \pm 0.06$ | 1.07 (57) |
| 13-Jul-2007 | $1.13 \times 10^{-11}$ | $1.48 \pm 0.06$ | 0.96 (50) |

### 8.2.4 REM observations

The photometric optical observations were carried out with the Rapid Eye Mount (REM; Zerbi et al. 2004), a robotic telescope located at the ESO Cerro La Silla observatory (Chile). The REM telescope has a Ritchey-Chretien configuration with a 60 cm f/2.2 primary and an overall f/8 focal ratio in a fast moving alt-azimuth mount providing two stable Nasmyth focal stations. At one of the two foci the telescope simultaneously feeds, by means of a dichroic, two cameras: REMIR for the NIR (Conconi et al. 2004) and ROSS for the optical (Tosti et al. 2004), used in order to obtain nearly simultaneous data. A detailed description of the procedure of data reduction and analysis is reported e.g. in Dolcini et al. 2005. The REM telescope has continuously observed 3C 279 for about 1 year between December 2006 and December 2007, including the AGILE observation period. The light curve produced by REM in the *R*-band is shown in Fig. 8.2. It confirms the high varibility of the source already observed in optical band on timescales of months in the past.

### 8.2.5 Discussion

The multiwavelength studies performed in the past on 3C 279 showed that during $\gamma$-ray flares most of the power emitted by the source lies in the high-energy $\gamma$-ray band. In accordance with leptonic models for blazars, the high-energy peak in the SED is due to inverse Compton emission from the relativistic electrons

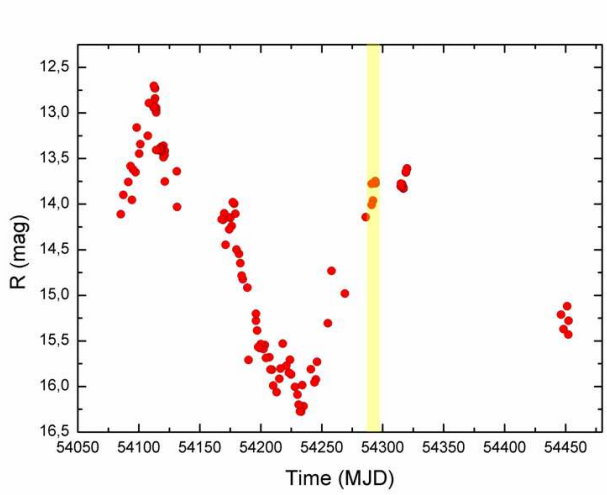


**Figure 8.2:** Long-term *R*-band light curve as observed by REM between December 2006 and December 2007. The yellow shaded region indicates the period covered by the AGILE-GRID observation [Giuliani et al. 2009].

accelerated by the jet. In the case of 3C 279, the external Compton scattering of direct disk radiation (EDC) and external Compton scattering of radiation from clouds (ECC) components dominate the $\gamma$-ray band yielding a total spectrum which varies as a function of the relative contribution of these two components. A possible correlation between $\gamma$-ray flux value and spectral index has been investigated using the EGRET data, without obtaining conclusive results (Nandikotkur et al. 2007). A continuity in the observed spectral properties of BL Lac objects and FSRQs has been postuled by Fossati et al. (1998), with the $\gamma$-ray spectral index getting progressively harder from FSRQs to High-energy peaked BL Lacs (HBLs). However, this trend is expected for the average spectral properties of these sources, whereas studies of individual objects have suggested a hardening of the $\gamma$-ray spectral index in FSRQs with an increase in flux (see Mukherjee et al. 1996; Sreekumar et al. 1996; Bloom et al. 1997).

EGRET observations of 3C 279 hinted at a gradual hardening during the flaring states, that can be interpreted as the ECC component dominate during the flaring states. Only one flare (during EGRET observation P9) showed a soft spectrum EDC dominated. Our AGILE observation seems to be similar to the P9 flare, supporting the idea that a soft spectrum during flaring episodes is not a extremely rare event. Hartman et al. (2001) suggest that softening spectra can be due to a low state of the accretion disk occurred before of the EGRET observation P9, which led to a reducted accretion disk radiation as source for the ECC

component.

From the *R*-band light curve (see Fig. 8.2) emerges that a strong minimum occurred at MJD $\sim$ 54230, about 2 months before the period covered by the GRID observations (indicated by the yellow shaded region in figure). This optical minimum might be correlated with a low accretion state of the disk. Infact, even if the relation between highly relativistic jets and accretion processes in AGN is one of the fundamental open problems in astrophysics, the current theoretical models of the formation of jet suggest that the power could be generated by means of accretion, extracted from the disk rotational energy and converted into kinetic power of the jets (Blandford & Payne 1982). As also underlined in the new blazar sequence proposed by Ghisellini and Tavecchio (2008) the accretion rate of the disk seems to be strictly related to the jet power of the blazars and hence to the synchrotron emission, observed in the optical band for 3C 279. Therefore, this reduction of activity of the disk should reflect in the decrease of the photon seed population produced by the disk and then in a ECC component deficit. This effect was delayed of two months, roughly the light travel time required to the photons to go from the inner disk to the BRL, then the decrease of the ECC emission should be visible in the period approximately coincident with the AGILE observation.

To test this hypothesis we fit the optical, X-rays and $\gamma$-rays data with a SCC+ECC+ECD model similar to the model used to fit the P9 EGRET observation in Hartman et al. (2001), but with different parameters values, finding a good agreement with the data. We use a double power law distribution for the electron energy density with spectral index $p_1 = 2.0$ from $\gamma_{\rm min} = 100$ to $\gamma_{\rm break} = 600$ and $p_2 = 4.0$ for $\gamma$ over 600, with a density at break $n_{\rm e} = 30$ cm$^{-3}$ and $\gamma_{\rm max} = 6 \times 10^3$. The blob have radius $R = 2.5 \times 10^{16}$ cm, magnetic field $B = 1.8$ G and it moves with a bulk Lorentz factor $\Gamma = 13$ at an angle $\theta = 2^\circ$ with respect to the line of sight. The relativistic Doppler factor is then $\delta = 21.5$. The accretion disk luminosity assumed is $L_{\rm d} = 5 \times 10^{45}$ erg s$^{-1}$ with a BRL reprocessing a 10% of the illuminating continuum. Figure 8.3 shows the SED for the GRID observing period of July 2007, including simultaneous optical (REM) and X-ray (*Swift*/XRT) data and indicating the individual model components: accretion disk emission, SSC, ECC and ECD.

### 8.2.6 Summary and remarks

During the period 2007 June 9–13, AGILE detected the FSRQ 3C 279 during a bright $\gamma$-ray state, with an average flux of $(210 \pm 38) \times 10^{-8}$ photons cm$^{-2}$ s$^{-1}$ for E > 100 MeV. $\gamma$-ray flux variations on 1-day timescale seem not to be present in our data, while longer timescales cannot be investigated due to the short AGILE observing time. The spectrum measured by AGILE is consistent with a

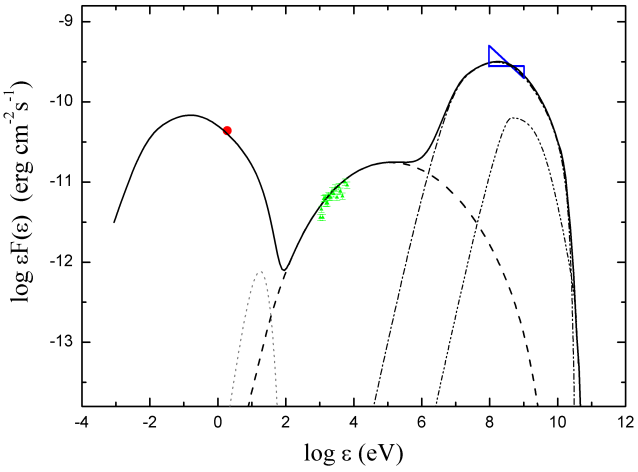


**Figure 8.3:** Spectral Energy Distribution of 3C 279 for the AGILE-GRID observation (blue bow-tie), including simultaneous optical (red dot) and X-ray (green triangles) data, collected by REM and *Swift*/XRT, respectively. The dotted, dashed, dot-dashed and double-dot dashed lines represent the contributions of the accretion disk blackbody, the SSC, the external Compton on the disk radiation and the external Compton on the BRL radiation, respectively [Giuliani et al. 2009].

power law with photon index $\Gamma = 2.22 \pm 0.23$ in the energy range 100 MeV – 1 GeV. This soft spectrum observed during a flaring episode, a behaviour already observed during EGRET P9 observation, could be an indication of a dominant contribution of the EDC emission compared to ECC emission. These EGRET and AGILE observations indicate that, although the inverse Compton scattering of relativistic electrons of synchrotron or ambient photons is responsible for the emission at hard X-rays and $\gamma$-ray energies for FSRQs such as 3C 279, not in all cases the accretion disk radiation reprocessed by the BLR is the main source of seed photons for the IC. Therefore the ECC emission is the dominant mechanism in $\gamma$-rays.

An alternative source of seed photons for the IC mechanism is the infrared dust in the surrounding torus (Sikora et al. 2002). Recently, Sikora et al. (2009) proposed that external Compton of infrared dust [ERC(IR)] could provide an important contribution in the broad band spectrum of FSRQs. In that case the emission zone extends up to millimiter photosphere and thus mm-band variations accompanying $\gamma$-ray flares were expected. However, simultaneous long-term mm/sub-mm and $\gamma$-rays observations are necessary to test this hypothesis. A long-term monitoring is also necessary to study the timescale in which the

source activity varies in order to discriminate the dominant contribution to the high energy emission. In fact, the ERC(IR) could play an important role during the soft $\gamma$-ray regime, but considering that the IR emitting region is very large and far away the energy density of this radiation field remains approximatively constant over a much longer length scale than the seed photons from the accretion disk radiation reprocessed in the BLR (Blazejowski et al. 2000). However, the energy density from the dust torus would suppress most of the radiation approaching 1 TeV, unless assuming extreme values of the bulk motion, and therefore a dominant contribution of ERC(IR) seems to be ruled out for the VHE flare observed by MAGIC.

Claryfing the exact nature of the seed photons for the IC scattering would explain the origin of the emission exhibited by 3C 279 at the highest energies and more in general provide us a new level of insight on the jet structure and the emission mechanisms in blazars.

## 8.3 3C 273

### 8.3.1 Introduction

3C 273 is a bright and nearby (z = 0.158) radio quasar. This is a very peculiar AGN because it shows the properties characteristic of a blazar, like the strong radio emission, a jet with apparent superluminal motion, large flux variations and a spectral energy distribution with the two humps typical of blazars (see Couvoisier 1998 for a review), but also other features typical of Seyfert galaxies appear as well as the broad emission lines, the soft X-ray excess and the big blue bump. For this reason this source has been extensively studied in the past at all frequencies (see e.g. Soldi et al. 2008).

3C 273 was detected in 1962 as a very bright double radio source (Schmidt 1963). One component was identified with the optical quasar, the other with the jet seen in optical. It was later detected at X-rays (Bowyer et al. 1970) and in July 1976 a source coinciding with the position of 3C 273 was discovered to emit in $\gamma$-rays by COS-B (Swanenburg et al. 1978), and confirmed by another COS-B observation in June 1978 (Bignami et al. 1981). The average flux detected by COS-B was $\sim 60 \times 10^{-8}$ photons cm$^{-2}$ s$^{-1}$ for E > 100 MeV.

EGRET pointed this FSRQ several times, not always detecting it, with an average flux over all the EGRET observations of $(15.4 \pm 1.8) \times 10^{-8}$ photons cm$^{-2}$ s$^{-1}$ for E > 100 MeV. 3C 273 was detected in high $\gamma$-ray activity in June 1991 (Lichti et al. 1995) with a flux of $(56 \pm 8) \times 10^{-8}$ photons cm$^{-2}$ s$^{-1}$ for E > 70 MeV. von Montigni et al. (1997) reported a flux variation during the campaign in October–November 1993 from $(22 \pm 5) \times 10^{-8}$ to $(56 \pm 12) \times 10^{-8}$ photons

$cm^{-2}$ $s^{-1}$ for E > 100 MeV. The source showed large $\gamma$-ray variability during a 7-weeks long EGRET campaign performed between December 1996 and January 1997, with a flux variation from $(25 \pm 9) \times 10^{-8}$ to $(76 \pm 13) \times 10^{-8}$ photons $cm^{-2}$ $s^{-1}$ for E > 100 MeV (Collmar et al. 2000), but no outstanding variation was detected with COMPTEL in the energy range 0.75–30 MeV. During that campaign, a double synchrotron flare episode was detected by the UKIRT telescope observing in the near-IR (*K* band), and by RXTE/PCA in the 3–10 keV band (Lawson et al. 1998), showing correlated variability and a < 1 day lag of X-rays with respect to near-IR emission. The flux variations (30–40%) and the durations were similar in the two energy bands. In a joint X-ray and near-IR campaign in 1999, another flare was observed with a lag of 1 day of X-rays with respect to near-IR. The flare lasted 2 days in the *K*-band and 4 days in X-rays (Sokolov et al. 2004).

A multiwavelength campaign with INTEGRAL, XMM-*Newton* and RXTE has been performed in June 2004 (Türler et al. 2006), triggered by the sub-millimeter monitoring, observing a sub-mm flux almost half the lowest jet activity ever observed in a similar campaign in March 1986 (Robson et al. 1986). This campaign showed spectral features of the source usually overwhelmed by the dominant jet activity. In particular, three further weak humps due to dust emission components are identified in the infrared band.

Even if the SED of this source roughly shows the typical humps of blazars, there is no general agreement on their origin. Not only the nature of the hard X to $\gamma$-ray emission is controversial, but also the big blue bump and the origin of the millimeter to near-IR emission is in doubt. In the June 1991 campaign, the low energy part of the spectrum showed a peak at $6.7 \times 10^{11}$ Hz, and another not measured peak must be present in $10^{13}$–$10^{14}$ Hz. With all these features, the theoretical modelling of the SED is challenging. Sometimes models for the SED of blazars are loosely constrained or different models can fit the same data. Studying the emission evolution of the source, especially before, during and after flaring episodes in $\gamma$-rays, can help to constrain the models.

In the case of 3C 273, the SED was studied in very different theoretical scenarios (see e.g. von Montigni et al. 1997). The MeV peak has been fitted in the context of pure synchrotron self Compton (SSC), or in the context of the external Compton (EC) model, considering the photons of the big blue bump, assumed to be emitted by the accretion disk, as the seed photons for the inverse Compton emission. Also proton-induced cascade models have been proposed, fitting the broad band energy spectrum collected in November–December 1993 over more than 17 decades of energy.

After 8 years from the last observations in $\gamma$-rays, the AGILE satellite, with its Gamma-Ray Imager Detector, has opened new access to the observational window 30 MeV – 30 GeV. We organized a 3-week multifrequency campaign on

this bright source involving REM, RXTE, INTEGRAL, *Swift* and AGILE, with the aim of studying the correlated variability in the different energy ranges and building a time-resolved energy density distribution for each of the 3-weeks from near-IR to $\gamma$-rays for testing the emission mechanisms working in this blazar.

### 8.3.2 The multiwavelength campaign

We coordinated a multiwavelength campaign on 3C 273 over 3 weeks, between 2007 December 16 and 2008 January 8. The AGILE satellite pointed at the Virgo region for the entire period with its $\gamma$-ray and hard X-ray instruments. INTEGRAL pointed at the source for one complete revolution ($\sim$2.5 days) for each of the 3 weeks. Optical and near-infrared data were provided by the REM telescope that monitored the source every 2-3 days. We requested two further ToO observations with the *Swift* satellite in the last week of the campaign. The first *Swift* observation started 1.5 days after the end of the last INTEGRAL pointing. Table 8.2 summarizes the observations of the different observatories involved in the campaign. A detailed description of the analysis and results of the AGILE, INTEGRAL, *Swift* and REM observations is given in the next subsections.

**Table 8.2:** Schedule of the observations during the MW campaign on 3C 273.

| Observatory | start time (UT) | stop time (UT) |
|---|---|---|
| AGILE | 2007-12-16 17:14 | 2007-12-23 02:18 |
| | 2007-12-24 07:12 | 2007-12-30 23:03 |
| | 2008-01-04 13:35 | 2008-01-08 11:06 |
| INTEGRAL | 2007-12-19 18:08 | 2007-12-22 06:44 |
| | 2007-12-25 17:39 | 2007-12-28 06:27 |
| | 2007-12-31 17:13 | 2008-01-03 04:00 |
| *Swift* | 2008-01-04 16:11 | 2008-01-04 17:47 |
| | 2008-01-06 11:57 | 2008-01-06 15:24 |
| REM | 2007-12-11 8.20 | 2008-01-14 7.26 |

#### 8.3.2.1 AGILE observations

AGILE monitored the source continuously from 2007-12-16 17:14 UT to 2008-01-08 11:06 UT, with two gaps of 1 and 4.5 days, respectively, due to technical maintenance of the satellite (see Table 8.2 for details). The resulting net exposure of 3C 273 for both the GRID and SA instruments on board AGILE is 742 ks.

Level-1 AGILE-GRID data were analyzed using the AGILE Standard Analysis Pipeline (see Section 4.3.6). Counts, exposure, and Galactic background

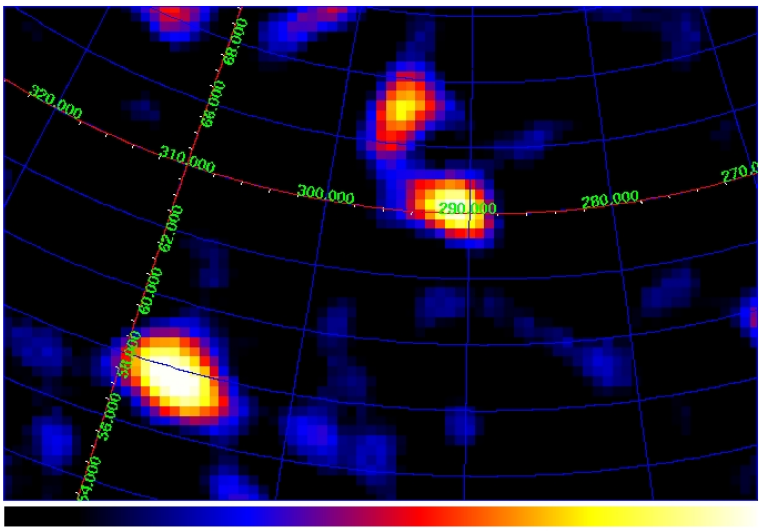


**Figure 8.4:** Gaussian-smoothed counts map of Virgo region in $\gamma$-rays obtained from GRID instrument on board AGILE, from 2007-12-24 07:11 to 2007-12-30 23:03 UT , for E > 100 MeV. 3C 273 is the source at the center of the image. The spot north-west of 3C 273 is the unidentified source 3EG J1236+0457, while the source at sud-west of 3C 273 is the blazar 3C 279.

$\gamma$-ray maps were created with a bin-size of $0.3^\circ \times 0.3^\circ$ for photons with energy greater than 100 MeV. We selected only events flagged as confirmed $\gamma$-ray events, and all events collected during the South Atlantic Anomaly and whose reconstructed directions form angles with the satellite-Earth vector smaller than $80^\circ$ are rejected in order to reject the Earth-albedo background. We divided the total GRID observing time in 3 blocks each approximately one week long (see Table 8.2).

In the first and third week of our campaign 3C 273 was not detected in $\gamma$-rays by GRID, while in the second week it was detected at a rather high $\gamma$-ray activity, with a flux comparable to the EGRET detection of the June 1991. The sky image in the energy range 100 MeV – 30 GeV, exposed for the second week of the campaign, is shown in Figure 8.4. Near 3C 273 an unidentified source is clearly visible in the image. Also the other famous blazar present in the Virgo region, 3C 279, is detected at a significance level of 4.8-$\sigma$ over the entire campaign, with a flux of $(25 \pm 7) \times 10^{-8}$ ph cm$^{-2}$ s$^{-1}$. The results of the analysis of the GRID data of 3C 273 is reported in Table 8.3 for the three individual blocks and for the whole period. Considering that for the first and third week the source was not detected by GRID at a significance level > 3-$\sigma$, upper limits with 95%

**Table 8.3:** Flux measurements and significance of detection of 3C 273 with AGILE-GRID in the different weeks. [a]Flux in units of $10^{-8}$ photons cm$^{-2}$ s$^{-1}$. [b]Upper limit with 95% confidence level.

| | 1st week | 2nd week | 3rd week | Total |
|---|---|---|---|---|
| Significance [$\sigma$] | 1.4 | 4.4 | 1.5 | 4.6 |
| Flux (E > 100 MeV)[a] | < 20[b] | 33 ± 11 | < 50[b] | 22 ± 6 |

confidence level are provided (see Mattox et al. 1996). The same data are also shown in the top panel of Fig. 8.5.

In the second half of the observation of the Virgo region, an unidentified source associable to 3EG J1236+0457 appeared at $\sim 5^\circ$ from 3C 273, rather bright in the second and third week of observation, with a flux of the order of 60 $\times 10^{-8}$ photons cm$^{-2}$ s$^{-1}$ in the third week (see Pacciani et al. 2009b). During December 2008, *Fermi*-LAT detected high $\gamma$-ray activity from a source coincident with 3EG J1236+0457, with a flux reaching 150 $\times 10^{-8}$ photons cm$^{-2}$ s$^{-1}$ (Tramacere et al. 2008). Thanks to the *Swift* ToO observation of the field in X-rays and optical/UV bands (Tramacere et al. 2008) and subsequently the KANATA optical observations (Ikejiri et al. 2009), this source has been associated with an AGN at redshift z = 1.76 of the Sloan Digital Sky Survey: SDSS J123932.75+044305. A tentative assocation between the EGRET source and the SDSS source had been suggested also by Mattox et al. (2001).

Due to the presence of this bright source within a distance comparable to the GRID PSF and the brief exposure (only 4 days) the statistical uncertainties in the estimation of the upper limit with the likelihood procedure is higher for the third observing block with respect to the first observing block.

The SuperAGILE (SA) instrument (Feroci et al. 2007) is a one-dimensional coded-mask imager, producing two orthogonal one-dimensional sky images of the observed sky, starting from photon-by-photon data on user-defined time intervals. SA provided images of 3C 273 in the energy range 18–60 keV simultaneously with the GRID observation. Based on the available statistics, we divided the complete 3-week observation in 5 bins of 3-4 days each. The first two SA bins are simultaneous to the first GRID observing block, the next two bins are simultaneous to the second GRID observing block, while the last SA bin is simultaneous to the third GRID observing block, due to the shorter exposure in the third week.

SuperAGILE data analysis was performed using the *TDS source* package of the standard *SASOA* pipeline (Lazzarotto et al. 2008), which extracts high level products from the photon-by-photon SA data. For each AGILE orbit the source count rate was automatically extracted in the energy range 20–60 keV, excluding the events taken during the satellite passage through the South Atlantic Anomaly

and when the Earth occulted the line of sight of the source. The detector images accumulated from the event list are corrected using pointing information from the star tracker. Since SA is a coded mask, the attitude correction depends on the source position in the field of view of each detector. During the AGILE observation, 3C 273 scanned the central part of the field of view, ranging from 7.7 to -2.4 deg in the X instrumental coordinate and from 11.0 to -12.4 deg in the Z instrumental coordinate. Normalized count rates (in units of counts $cm^{-2}$ $s^{-1}$) were then obtained by considering the effective area of the exposed portion of the detectors and assuming a Crab-like spectrum (e.g. Frontera et al. 2007). Fluxes in units of the Crab flux were calculated by applying a normalization factor of 0.15 to the normalized count rates. The average 20–60 keV flux measured by SA over the complete 3-week observation is (23.9 ± 1.2) mCrab, with a source detection significance of 14-$\sigma$ and 16-$\sigma$ in the X and Z coordinate, respectively. The results of a time-resolved analysis are reported in 5 time-bins in the specific panel of Fig. 8.5 for the 20–60 keV energy range.

#### 8.3.2.2 INTEGRAL observations

The INTEGRAL mission (Winkler et al. 2003) observed 3C 273 with all the instruments from 19 December 2007 to 3 January 2008 in the revolutions 633, 635, and 637, with the rectangular dithering pointing strategy, for a total observing time of 7.5 days. It corresponds to a net source exposure of 122 ks for JEM-X, 580 ks for ISGRI, and 494 ks for SPI. The INTEGRAL observations are divided into uninterrupted 2000-s intervals, the so-called science windows (SCWs).

The X-ray and soft $\gamma$-ray observations were carried out with JEM-X unit 1 in the range 3–35 keV (Lund et al. 2003), ISGRI (Ubertini et al. 2003) in the range 18–400 keV, and SPI (Vedrenne et al. 2003) in the 20 keV – 8 MeV band. The effective energy ranges used in the analysis are 5–20 keV for JEM-X, 18–200 keV for ISGRI, and 100–500 keV for SPI, excluding the energy regions with too low effective area and the lowest energies, affected by electronic noise. For SPI we reported the energy range where its effective area is comparable to or higher than the ISGRI one.
Data were processed using the Off-line Scientific Analysis (OSA) 7.0 software released by the Integral Scientific Data Centre. ISGRI light curves and spectra were extracted for each individual SCW. The spectrum from JEM-X was extracted from a mosaic image at the position of the source. Due to the dithering pointing strategy, the source is not always in the JEM-X field of view. The SPI data were integrated for the three INTEGRAL revolutions together to achieve an acceptable sensitivity up to 500 keV. The average measured flux was: (13.81 ± 0.25) mCrab in 5–20 keV (JEM-X, 56-$\sigma$ detection significance), and (22.30 ±

**Table 8.4:** Spectral fitting parameters of INTEGRAL data in the 18–120 keV energy range. [a]Flux in units of $10^{-10}$ erg cm$^{-2}$ s$^{-1}$.

| | 1st week (rev 633) | 2nd week (rev 635) | 3rd week (rev 637) |
|---|---|---|---|
| Photon index | 1.77 ± 0.07 | 1.87 ± 0.09 | 1.80 ± 0.07 |
| Flux (20-40 keV)[a] | 1.73 ± 0.05 | 1.44 ± 0.05 | 1.69 ± 0.05 |

0.32) mCrab in 20–60 keV (ISGRI, 70-$\sigma$ detection significance). SPI provides a marginal detection of the source (4.4-$\sigma$ detection significance) with an average flux of (41 ± 9) mCrab in 100–500 keV.
The light curves in the energy ranges 5–20, 20–60, 60–100, 100–200 keV from the above instruments are shown in Figure 8.5 with a bin size of 200 ks (one INTEGRAL revolution), except for the 20–60 keV energy range, where the counting statistics allowed for a 25 ks bin size. The simultaneous 20–60 keV flux measurements by SuperAGILE and ISGRI appear in good agreement.

The spectra taken during the three individual INTEGRAL revolutions, can be fitted with a simple power law model in the 18–120 keV energy range. No significant spectral evolution is detected, except for a marginal evidence of softening in the spectrum from revolution 635. The best-fit parameters are reported in Table 8.4.

#### 8.3.2.3 *Swift* observations

To continue the monitoring of the source in X-rays until the end of the AGILE observation pointing, after the INTEGRAL observation, we requested two *Swift* ToO observations on 3C 273.

The observations of the X-Ray Telescope (XRT; Burrows et al. 2005) were taken in two epochs: on 2008 January 4, starting at 16:10:44 UT for a total exposure of 454 s in Windowed Timing (WT) mode and 2.5 ks in Photon Counting (PC) mode and on 2008 January 6, starting at 11:56:44 UT, for a total exposure of 448 s in WT mode and 2.8 ks in Photon Counting (PC) mode. For the following analysis we used the dedicated XRT pipeline (`xrtpipeline` v 0.11.6). Grade filtering was applied by selecting the 0–2 and 0–12 ranges for the WT mode and PC mode data, respectively. To account for the presence of the bad column, in the spectra extraction we used the exposure maps computed for each epoch and from them we generated the ancillay response files. The latter are very sensitive to the source centroid. In fact for the presence of the bad column we could not estimate accurately the XRT source centroid and therefore we run the pipeline fixing the source position at the coordinates given from optical

and radio observations in the SIMBAD archive, that is R.A. (J2000) = $12^h\ 29^m\ 06.70^s$ and Dec. (J2000) = $02^\circ\ 03'\ 08.6''$. We then computed the effective area over four different positions centered at a distance of 3.1″ (90% error radius) from the SIMBAD one, in order to evaluate the effects due to the uncertainty on the source centroid. These resulted to be less than 10%.

Moreover, the data acquired in PC mode are affected by pile-up in both the observational epochs (average count rate ∼8 counts/s), but for the presence of a bad column crossing the source region, we could not apply standard methods based on Point Spread Function fitting to evaluate the dimension of the saturated region to be excluded. We therefore selected a historical XRT observation of 3C 273 that shows similar source count rate but with no bad column crossing the source region. For the comparison of the source count rates we selected an extraction region that does not contain the bad column (e.g. a semi-annulus region). XRT observations of 3C 273 taken on 2005 November 15 satisfy these requirements. We found that an annular source extraction region with inner radius of 6 pixels and outer radius of 20 pixels enables to avoid pile-up effects and we applied this region to our analysis, centering it on the SIMBAD position. Varying the inner region of 1 pixel, we found that the final results vary of less than 5%. Assuming an absorbed simple power law spectral model, with absorption fixed at $N_{\rm H} = 1.79 \times 10^{20}$ cm$^{-2}$ (Kalberla et al. 2005), we then computed the 2–10 keV integrated fluxes using the corresponding ancillary file for each position. We assumed the flux estimated at the SIMBAD position as the correct one and we used the four different values obtained at the four positions at 3.1" to estimate the flux uncertainty. We found a flux of $F_{2-10\,\rm keV} = 1.8^{+0.3}_{-0.1} \times 10^{-10}$ erg cm$^{-2}$ s$^{-1}$ for the first epoch and $F_{2-10\,\rm keV} = 1.9^{+0.3}_{-0.1} \times 10^{-10}$ erg cm$^{-2}$ s$^{-1}$ for the second epoch. However, considering that contemporaneous presence of pile-up effect and a bad column crossing the center of the source extraction region in both observational epochs, we use the data in PC mode only for comparison for the results obtained with the data in WT mode, not affecting by pile-up.

For the data collected in WT mode the signal was extracted from a rectangular region (40 pixels wide and 20 pixels in height), assuming as nominal the position centered on the SIMBAD coordinates of 3C 273. The *Swift* star sensors precision introduces a systematic uncertainty in the evaluation of the satellite pointing, providing a mismatch between the source centroid on the CCD evaluated with the star sensors data and the effective one. In order to evaluate the effects of this systematics on the flux and spectral index estimation, we computed the effective area also over two other positions shifted of 3.1" (a region that encloses 90% of the PSF from the SIMBAD source position). The difference between the results obtained at the SIMBAD position and the shifted ones is then taken as a systematic uncertainty, denoted below as '(syst)'.

Assuming also in this case an absorbed simple power law spectral model,

with absorption fixed at $N_{\rm H} = 1.79 \times 10^{20}$ cm$^{-2}$, we found a photon index $\Gamma = 1.61 \pm 0.05$, with an observed 2–10 keV flux of $1.85 \times 10^{-10} \pm 0.04$ (stat) $\pm$ 0.03 (syst) erg cm$^{-2}$ s$^{-1}$ during the first epoch ($\chi^2_{\rm red} = 0.9$, 92 d.o.f.). No significant variations were observed during the second epoch, where the photon index is $\Gamma = 1.57 \pm 0.06$ and the observed 2–10 keV flux is $1.75 \times 10^{-10} \pm 0.04$ (stat) $\pm$ 0.08 (syst) erg cm$^{-2}$ s$^{-1}$ ($\chi^2_{\rm red} = 1.0$, 71 d.o.f.). The worst quality of the image in the second observation with respect to the first observation caused the systematics to be higher. The star sensor systematics do not affect the photon index estimation in WT mode. The results obtained with the data collected in PC mode are in well agreement. XRT data are shown in Figure 8.5.

The UltraViolet/Optical Telescope (UVOT; Roming et al. 2005) observed the source with all lenticular filters except for the White one (U, V, B, UVW1, UVM2 and UVW2), with exposures of 213 s for each optical filters and 810, 610, and 850 s for the UV ones in the first observation; 268 s for the optical filters and 537, 729, 358 s in the UV for the second observation. Data were reduced with the `uvotmaghist` task distributed within the `HEAsoft` 6.3.2 package and the calibrations included in the release of 2007-07-11 of the 'Calibration Database' (CALDB). Source counts were extracted for all filters from circular aperture of 5″ radius, the background from source-free circular aperture of 12″ radius and count-rates converted to fluxes using the standard zero points. The count-rate of the source is near the limit of acceptability for the 'coincidence loss' correction factor included in the CALDB ($\sim$90 cts s$^{-1}$) in filters U, B, UVW1 and UVW2 for both observations. Therefore we considered in our analysis only the V and UVM2 filters for both observations, and also the B for the second observation. The fluxes were then de-reddened using a value for E($B - V$) of 0.021 mag (Schlegel et al. 1998) with $A_\lambda/E(B-V)$ ratios calculated for UVOT filters using the mean Galactic interstellar extinction curve from Fitzpatrick (1999). No significant variability was detected within each single exposure for both observations. UVOT data are shown in Figure 8.5.

#### 8.3.2.4 RXTE/ASM and *Swift*/BAT data

With the aim to add to the INTEGRAL, *Swift* and SuperAGILE observations a long-term monitoring in the 2–10 keV and 15–50 keV energy band, we used the public light curve from the All Sky Monitor[1] (ASM; Levine et al. 1996) on board *Rossi*XTE and the Burst Alert Telescope[2] (BAT; Krimm et al. 2006) on board *Swift*. Due to their observing strategy, both instruments provided sparse observations of different durations. The typical exposure times are 90s for ASM

[1] http://xte.mit.edu/asmlc/ASM.html

[2] http://swift.gsfc.nasa.gov/docs/swift/results/transients/

and 840s for BAT, and the typical observation rate is 20 and 9 times per day, respectively.

The flux measurements by BAT are sparse and with different exposure, depending on the specific satellite pointing strategy, therefore we grouped the available data with a bin size of 3 days. To account for the huge spread in the signal to noise ratio between data, a weighting factor inversely proportional to the flux error was applied during the rebinning operation. The BAT light curve in the range 15–50 keV is shown in Figure 8.5 and shows the same trend as the Super-AGILE and ISGRI instruments but a slightly lower flux, likely due to the slightly different bandpasses.

#### 8.3.2.5 REM observations

The Rapid Eye Mount (REM) telescope (Zerbi et al. 2004) has monitored 3C 273 in near-IR and optical bands for a period of 34 days, from 2007 December 11 to 2008 January 14. REM is a fully robotic, 60 cm telescope, that allows to execute simultaneously optical and near-infrared photometry and low-resolution spectroscopy. It hosts two parallel cameras: ROSS for optical observations covering the range 0.45–0.95 $\mu$m (V, R, I filters), and REMIR for near-IR observations covering 0.95–2.3 $\mu$m range with 4 filters (z, J, H and K). For this campaign we used the two instruments with all their filters, except for the z on REMIR, to obtain nearly simultaneous data in order to study the almost instantaneous spectrum of 3C 273 from near-IR to optical bands. The J, H, K images were exposed for 30 s, while the V, R, I images for 300 s. The sets of 6 bands observations were obtained every 2–3 days during this 3-week campaign.

Data reduction and photometry of the near-IR and optical frames from the REM observations has been carried out through the GAIA[3] software using images corrected by bias, dark and flat-field (see Stetson 1987). The instrumental magnitudes have been calibrated using the comparison star sequences reported in Gonzales et al. (2001) for the optical and the near-IR bands. Three bright isolated stars in the field of view were used as reference to calculate the instrumental magnitude shift.
The light curves over the 34 days monitoring for the J, H, K, V, R, I bands of REM are shown in Figure 8.5. The large errors for some data point are due to the presence of the moon, causing errors in the photometry of 3C 273 and/or of the reference stars. Small differences in the simultaneous measurements in V band by REM and UVOT are most likely to be due to the slightly different bandpasses.

[3] http://docs.jach.hawaii.edu/star/sun214.htx/sun214.html

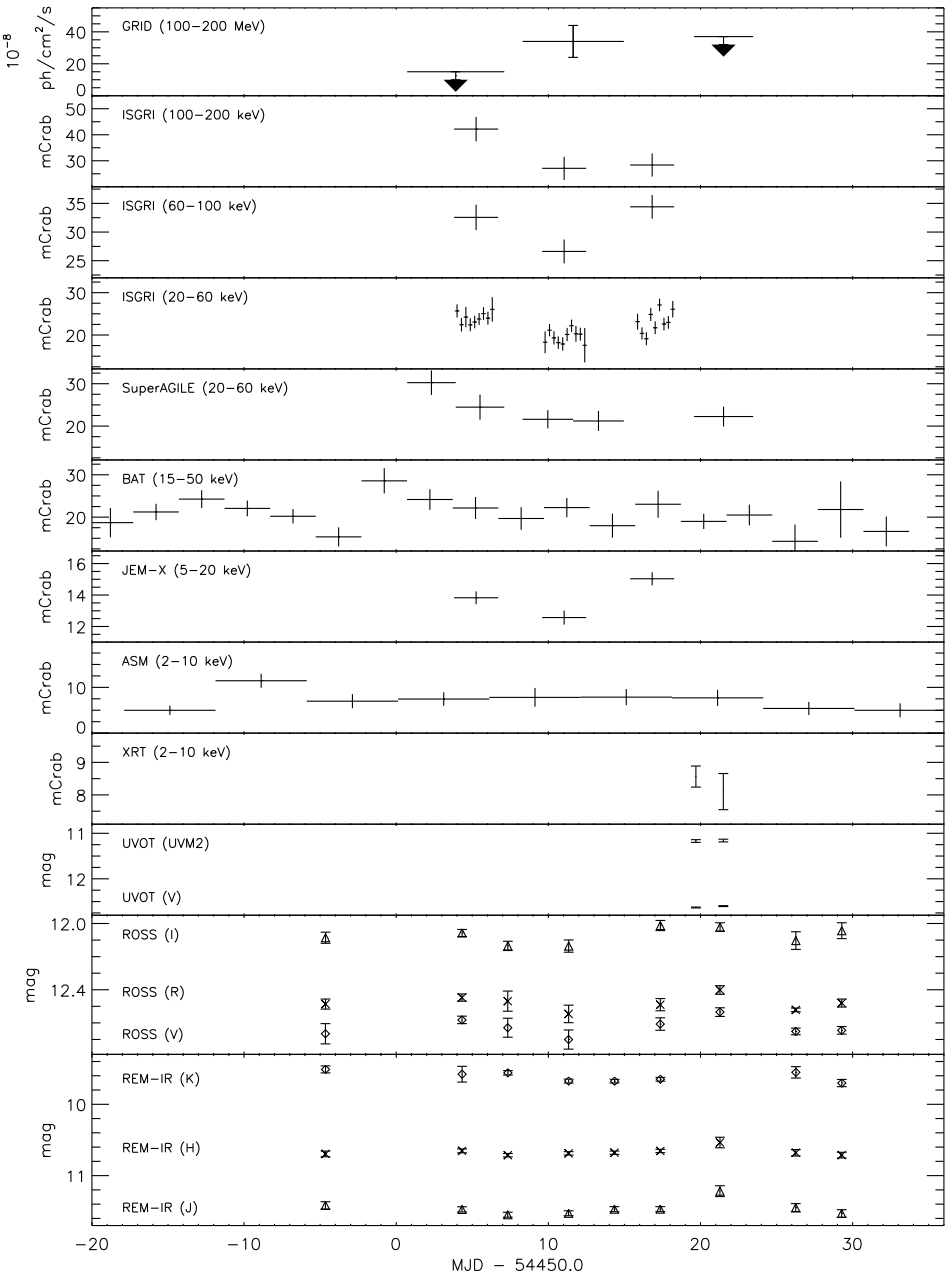


**Figure 8.5:** Complete set of light curves collected during the multifrequency observations of 3C 273. From top to bottom: GRID data in the energy range 100–200 MeV, the ISGRI data in 100–200 keV, 60–100 keV, 20–60 keV, SuperAGILE in 20–60 keV range, BAT in 15–50 keV, JEM-X in 5–20 keV, ASM in 2–10 keV, XRT in 2–10 keV, UVOT fluxes with UVM2 and V filters, and REM fluxes with V (diamonds), R (crosses), I (triangles) filters from ROSS, and J (triangles), H (crosses), K (diamonds) filters from REMIR. The time is referred to MJD 54450.0, corresponding to 2007–12–16 00:00 UT, the starting day of the campaign [Pacciani et al. 2009a].

### 8.3.3 Discussion

The complete set of light curves from the multiwavelength campaign is shown in Figure 8.5, ordered by wavelengths (except for REMIR data). From the comparison of the light curves, the source exhibited $\gamma$-ray activity only in the second week of the AGILE observation. At the same time, a reduction of $\sim$ 20% in the soft and hard X-ray flux was detected by all the involved instruments. Instead, the near-IR, optical and UV fluxes remained constant within $\sim$ 10% variability. From the analysis of the light curves no strong evidence for correlations can then be derived between the $\gamma$-ray activity and the source emission in other bands.

In order to study the spectral variability, we divided the campaigns in 3 weeks, according with the GRID observing blocks and build the complete SEDs for the first two epochs, in order to understand the origin of the $\gamma$-ray activity. We also try to briefly evaluate the possible contribution of a Seyfert-like reflection component in the X-ray/soft $\gamma$-ray energy spectrum.

#### 8.3.3.1 Limits on Seyfert-like spectral features

The broad band spectra of 3C 273 taken by *Beppo*SAX between 1997 and 2000 allowed to disentangle the contribution of the jet and Seyfert-like features (Grandi and Palumbo 2004). In case of our campaign, the possible XRT calibration uncertainties between 0.4 and 0.6 keV (see Cusumano et al. 2007) does not allow us to study in detail the soft excess, whereas the Iron line studies (Yaqoob & Serlemitsos 2000 and references therein) prevented to us by the counting statistics. Instead, the INTEGRAL data allow us to study the reflection hump contribution to the spectra, emerging at 20–60 keV.

Unfortunately, results in this spectral region are very sensitive to possible uncertainties in the cross-calibrations between JEM-X and ISGRI instruments. In the following we use the cross calibration factors for the instruments onboard INTEGRAL fixed to the value $C_{ISGRI} = 0.99$ and $C_{JEM-X} = 1.02$, and keep free the XRT normalization factor (also to account for the systematics in XRT data relative to our specific observation). SPI data were not used in this analysis. It is also important to note that the declared INTEGRAL cross-calibration factors are reported for Crab-like spectra, while the energy spectrum of 3C 273 is harder, and this could introduce a systematic error.

We built three energy spectra, each spectrum contains the ISGRI data for that revolution. The first XRT observation was performed 1.5 days after the end of the last INTEGRAL pointing, thence we used XRT data for the third spectrum only. In order to reach enough significance, all the JEM-X data of the campaign were merged together in the spectrum of the third week. We corrected the JEM-

X multiplicative factor to account for the true normalization factor for the third week (during the third week the JEM-X flux was 1.08 times the mean flux of the campaign).

The energy spectra of the three epochs were fitted simultaneously. We first attempted a fit with an absorbed ($N_{\rm H} = 1.79 \times 10^{20}$ cm$^{-2}$) simple power law plus a Compton reflection hump (the PEXRAV model in XSPEC), with parameters set proposed in Grandi and Palumbo (2004) and only the PEXRAV normalization allowed to vary in the fitting, but linked for the three epochs. The power law parameters also were linked for the three epochs, except for their normalization, left completely free to vary. With this approach, we tested the hypothesis that the hard X-ray variability among the three epochs was entirely due to the jet-component. The best-fit result is acceptable ($\chi^2_{\rm red} = 1.15$, 47 d.o.f., null hypothesis probability = 0.24).

We then try to introduce a break in the description of the jet component, substituting the simple power law with a broken power law, and adopted the same fitting strategy, again under the hypothesis of a variability entirely due to the jet-component. An acceptable fit was achieved ($\chi^2_{\rm red} = 0.84$, 45 d.o.f., null hypothesis probability = 0.76) with photon indexes $\Gamma_1 = 1.46 \pm 0.12$ and $\Gamma_2 = 1.71 \pm 0.05$ and break energy $E_{\rm b} = 4 \pm 2$ keV. The normalization factor for the reflection component is $(13.3 \pm 5.0) \times 10^{-3}$ ph cm$^{-2}$ s$^{-1}$ keV$^{-1}$, instead for the broken power law is $(27.1 \pm 9.3)/(19.5 \pm 7.9)/(25.4 \pm 8.6) \times 10^{-3}$ ph cm$^{-2}$ s$^{-1}$ keV$^{-1}$ for the revolution 633, 635, and 637, respectively. The cross-calibration obtained for XRT is $C_{\rm XRT} = 1.01 \pm 0.11$. We note that using only a broken power law without a reflection component provides a slightly worse best-fit result, with a $\chi^2_{\rm red} = 1.20$ (46 d.o.f., null hypothesis probability = 0.17).

We note that the uncertainties on the normalization factor for the PEXRAV and broken power law seem to be correlated. Therefore, in order to compare the contribution of the jet in the three epochs, in terms of the value of the normalization of the broken power law, we performed another fit by fixing the PEXRAV parameters to their best fit value. The uncertainty on the normalization of the broken power law under this assumption shows that the jet-component variation between the first and the second week is indeed statistically significant, while the difference between the values in the second and third is marginally consistent with the combined 90% uncertainties on the individual parameters.

Thus, from our analysis of the time-resolved X-to-soft-$\gamma$-ray energy spectrum, we can derive that the variability observed from the light curves in this energy range is most likely due to the jet-component, described as a broken power law in our emission model, although a non-variable reflection component seems also to be required by the spectral data presented here.

#### 8.3.3.2 Spectral energy distribution

With the aim of understanding the origin of the $\gamma$-ray emission, we build the SED of 3C 273 for the first and second week. Due to the uncertainty in the evaluation of the $\gamma$-ray flux of 3C 273 for the third week, we do not consider the SED relative to that observation. For both the SEDs, we used the spectrum extracted from all three JEM-X observations together, applying a correction factor to the spectra to obtain the observed count rate in the 5–20 keV band from each revolution. Due to the statistics, the SPI data are obtained from the integration of the three INTEGRAL revolutions together.

We modeled the SED including synchrotron emission, synchrotron self Compton and external Compton components (see Maraschi et al. 1992; Marscher et al. 1992; Sikora et al. 1994). The possible reflection hump is not taken into account in the SED model. The resulting SEDs for the first and second week are shown in Fig. 8.6.

The observed variability of the SED between the first and second week cannot be associated with a synchrotron flare. In that case an enhancement of the emission at all the observed wavelengths is expected. The variability behaviour can be reproduced as a shift toward higher energies of the electron density, thence related not to the injection of a new blob, but to electron acceleration. According to this hypothesis, we modelled the variability keeping the bulk Doppler factor, the blob radius and the disk luminosity unchanged. Instead, we varied the parameters related to the accelerated electrons: the electrons energy distribution ($n_e$, $\gamma^*$ and $p_2$) and, slightly, the tangled magnetic field. But the choice of the SED parameters allowing for a change from the first to the second week is not unique. The chosen parameters of the SED model for the two epochs are reported in Table 8.5.

The flux at frequencies higher than $3 \times 10^{14}$ Hz, consistently with the large viewing angle (6°), appears dominated by thermal emission from the disk and/or from the BLR. Thus, we expect that the emission in the range of frequencies observed by REM does not vary on daily timescales, and to hide variations of the synchrotron emission except in the near-IR bands. The REM observations, show variations lower than $\sim$ 10-15% in the near-IR and optical bands. Our model, showed in Fig. 8.6, produces no variations of the synchrotron emission in the near-IR and optical energy regions. A moderate shift of the direct synchrotron spectrum towards higher frequencies is detectable in the far-IR and in the soft X-rays, if not hidden by other thermal components (e.g. the components suggested in Türler et al. (2006), and the soft excess reported in Grandi and Palumbo (2004)), but we do not have coverage of that energy regions for all the campaign.

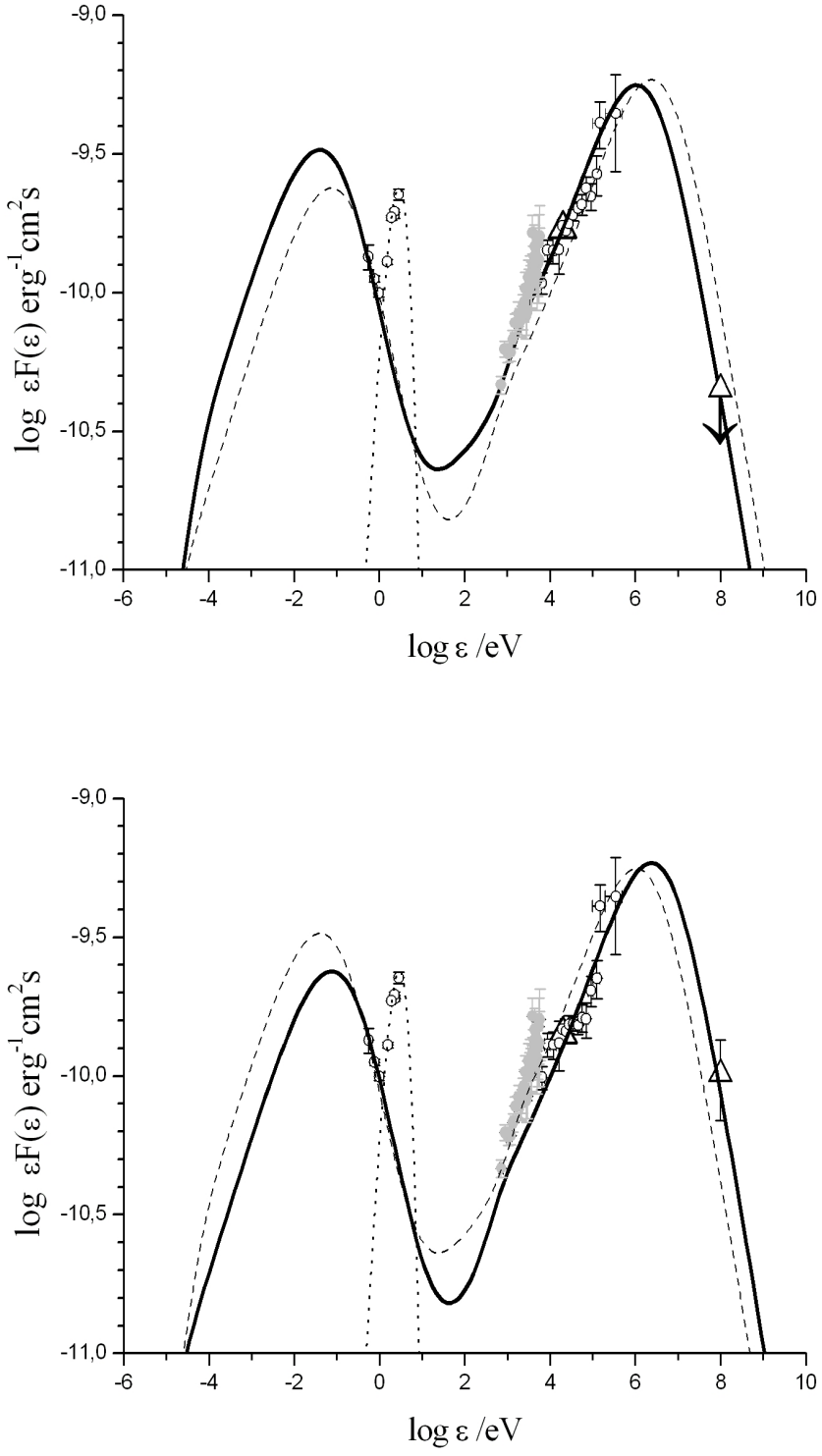


**Figure 8.6:** Spectral Energy Distribution of 3C 273 for the first (top panel) and the second week (bottom panel). Triangles are for AGILE data. The grey data refers to the XRT observations, performed in the third week. The solid line is the model for the simultaneous data of the week, whereas the model for the other week is reported for comparison as dashed line [Pacciani et al. 2009a].

**Table 8.5:** Parameters for the SED for the first and second week of the campaign. $p_1$ and $p_2$ are the pre- and post-break spectral index for the electron population, $\gamma^*$ is the break energy Lorentz factor, $\gamma_{\rm min}$ is the cut-off energy of the electron population, B the tangled magnetic field, $r$ the radius of the spherical blob in the comoving frame, $\delta$ the Doppler factor, $n_{\rm e}$ the electron density.

| $p_1$ | $p_2$ | $\gamma^*$ | $\gamma_{\rm min}$ | B (Gauss) | $r$ ($10^{16}$ cm) | $\delta$ | $L_{\rm d}$ (erg cm$^{-2}$ s$^{-1}$) | $n_{\rm e}$ (e$^-$/cm$^3$) |
|---|---|---|---|---|---|---|---|---|
| 2 | 5 | 200 | 3 | 12 | 2 | 9 | $6 \times 10^{45}$ | 150 |
| 2 | 4.7 | 300 | 3 | 10 | 2 | 9 | $6 \times 10^{45}$ | 70 |

Variations are instead revealed in the inverse Compton reprocessing in the X-ray and $\gamma$-ray domain. The relative variations detected, $\sim$ 20–30% and a factor $\sim$ 2–3, respectively, together with the fact that the $\gamma$-ray flux appears anti-correlated to the X-ray flux, indicates that a shift toward higher energy in the electron density is very likely responsible for the observed variability.

Sikora et al. (2001) proposed a scenario in which, during the acceleration phase, the accelerated electrons population increases, saturating first at high energy. When the phase of electrons acceleration stops, the energy break $\gamma^*$ of the electrons population moves to lower energies, reaching the critical energy $\gamma_{\rm C}$ (balancing the radiative cooling time with the duration of the acceleration period) or even lower values. In that model, the $\gamma$-ray light curve reaches its maximum before the hard X-ray, then decay faster than hard X-ray light curve. This scenario might be able to fit the data of our multiwavelength campaign, provided that the second week is related to an electrons acceleration phase, and the first week to the late phase of a previous episode. Thence the $\gamma$-ray activity and the high value of $\gamma^*$ during the second week of observation seems to be the signature of the acceleration phase.

### 8.3.4 Summary and remarks

1. We presented the data collected during a pre-scheduled 3-week multiwavelength campaign on 3C 273 carried out between mid-December 2007 and January 2008, covering from the near-IR to the $\gamma$-ray energy bands.

2. The source was detected in a high state in X-rays, with a 5–100 keV flux a factor of $\sim$ 3 higher than the typical value in historical observations (Courvoisier et al. 2003). Instead, the AGILE $\gamma$-ray data showed a flux lower than or equal to the EGRET measurements.

3. The simultaneous light curves from $\gamma$-ray to near-IR do not show any strong correlation, except for an indication of an anti-correlated variability between X-rays and $\gamma$-rays: all the soft and hard X-ray measurements show a decreasing trend at the time of the AGILE detection in the $\gamma$-rays in the second week of observation, preceded and followed by no $\gamma$-ray detections in the first and third week of our campaign.

4. Using a one-zone homogeneous SSC plus EC from an accretion disk, we find that the spectral variability between the first and the second week is consistent with an acceleration episode of the electron population responsible for the synchrotron emission. Even if the possible synchrotron variations in far-IR and soft X-rays are not detectable because we do not have adequate coverage in these parts of the spectrum, the signature of the acceleration is revealed by the inverse Compton peak in the X-ray and $\gamma$-ray energy ranges.

5. A possible shift of the IC peak were proposed comparing the June 1991 multiwavelength campaign with the OSSE observation in September 1994 (McNaron-Brown et al. 1997). Our multifrequency observation and modeling suggest that this behaviour could be a more general feature of this source, happening on shorter timescales.

6. Considering the weak X-ray flux in the second week, we study the Seyfert-like disk reflection hump in this source. The wide band spectral data from all the INTEGRAL instruments show that the jet emission alone does not describe perfectly the energy spectrum. A reflection hump improves slightly the X-ray spectral modeling. We then found that in the second week the jet contribution to the X-ray emission gets dimmer, due to the shift to higher energy of the electron population, making the likely constant disk contribution emerge.

Chapter 9

# TeV blazars

## 9.1 Introduction

With the advent of the latest generation of Imaging Atmospheric Cherenkov Telescopes (IACTs) the number of sources detected in the TeV energy regime has significantly increased. The majority of TeV sources are galactic, however 30 extragalactic sources are detected until now, of which 28 are AGNs, the most distant reported being 3C 279 (Albert et al. 2008a). Only eight of the 28 AGN TeV-emitters were detected by EGRET (Hartman et al. 1999) and most of these sources were discovered at TeV energies only by the new generation of IACTs, therefore the number of TeV blazars detected contemporaneous at MeV–GeV and TeV energy bands is very low.

Therefore, until recently multiwavelength campaings have been large unable to probe information on the part of the electromagnetic spectrum between $\sim$ 150 keV and $\sim$ 100 GeV as no instrument operating at those energies has existed. With the launch of two new $\gamma$-ray satellites, AGILE and *Fermi*, a large part of this gap in coverage have been closed giving the possibility to remove the degenerecies in the modelling the spectral energy distribution (SED) of these objects. In fact, simultaneous observations from MeV to TeV, where most of the energy of blazars is emitted, could provide important informations on the physics underlying the emission from these objects.

In this Chapter, we present the result of the multiwavelength campaigns involving $\gamma$-ray AGILE observations, together with MAGIC and VERITAS TeV observations of Mrk 421, W Comae and PG 1553+113. The analysis and results presented are published in Donnarumma et al. (2009a), Acciari et al. (2009b) and Aleksic et al. (2009).

## 9.2 Mrk 421

Mrk 421 is a nearby blazar (z = 0.031), one of the brightest and best studied BL Lac objects detected in $\gamma$-rays by EGRET (Lin et al. 1992). It was the first extragalactic source detected in the TeV energy range using Imaging Atmospheric Cherenkov telescopes (Punch et al. 1992). Mrk 421 was also the source with the fastest observed flux variations among the TeV blazars, before the very fast variability recently observed by Mrk 501 (Albert et al. 2007c) and PKS 2155−304 (Aharonian et al. 2007).

Mrk 421 was detected and studied at all accessible wavelengths of the electromagnetic spectrum from radio to very high evergy (VHE) $\gamma$-rays, extending over $\sim$ 19 decades in energy. It belongs to the class of High-energy peaked BL Lac objects (HBLs), showing a double-humped spectral energy distribution with a first peak usually in the soft to medium X-ray range, and a second one at GeV–TeV energies (Sambruna et al. 1996; Fossati et al. 1998). The first hump is interpreted as due to synchrotron radiation from high-energy electrons in a relativistic jet, while the origin of the second peak is still uncertain. In the leptonic scenario it is interpreted as inverse Compton (IC) scattering of the synchrotron (synchrotron self Compton: SSC) or external photons (external Compton: EC) by the same population of relativistic electrons. The observed correlated variability between X-rays and TeV energy bands (Maraschi et al. 1999; Fossati et al. 2008; Wagner 2008) seems to be well explained in the SSC framework, whereas the EC scenario is unlikely to apply in HBLs, due to the low density of ambient photons. However, a recent multifrequency campaign on the HBL PKS 2155−304 during a low activity state with H.E.S.S., *Fermi*, *Swift*, RXTE and ATOM observations (Aharonian et al. 2009) showed different spectral and variability properties with respect to what usually observed for HBLs in flaring states, challenging the SSC model. Alternatively, hadronic models invoke proton-initiated cascades and/or proton-synchrotron emission cannot be excluded (Aharonian 2000; Mücke et al. 2003).

Leptonic and hadronic scenarios for HBLs predict different properties of the $\gamma$-ray emission in relation to the emission in other energy bands. Specifically, the hadronic models, as opposed to the leptonic SSC ones, predict a flatter slope of the IC emission at $\sim$ 100 MeV than that of the synchrotron emission in the optical/UV energy bands. Therefore, a way to distinguish between the different emission models is to close the gaps in the SED, as well as to determine the position of the second peak in the SED and to obtain simultaneous, time-resolved data in a broad energy range. High Energy (HE) and VHE $\gamma$-ray observations of flaring BL Lacs and simultaneous multiwavelength data are thus the keys to investigate these two scenarios.

During the AGILE ToO observation towards W Comae in June 2008 (see

next Section), a hard X-ray flare of Mrk 421 was detected by SuperAGILE on 2008 June 10 (Costa et al. 2008). This observation was later followed by a detection in HE $\gamma$-rays by the Gamma-Ray Imaging Detector (Pittori et al. 2008). A prompt *Swift* ToO observation, complemented the ongoing multifrequency campaign of Mrk 421 with also GASP-WEBT observation in optical, MAGIC and VERITAS observation at TeV energies.

### 9.2.1 AGILE observations

The AGILE satellite observed Mrk 421 with its two detectors GRID and SuperAGILE, in the energy ranges 30 MeV–30 GeV and 20–60 keV respectively, between 2008-06-09 17:02 UT and 2008-06-15 02:17 UT for a total net exposure on the source of $\sim$ 260 ks.

The GRID data were analyzed using the AGILE standard pipeline (see Section 4.3.6). Counts, exposure, and Galactic background $\gamma$-ray maps were created with a bin-size of $0.25^\circ \times 0.25^\circ$. Only events flagged as $\gamma$-rays and not recorded while the satellite crosses the South Atlantic Anomaly were accepted. We also rejected all events with reconstructed direction within $10^\circ$ from the Earth limb, thus reducing the contamination from Earth's $\gamma$-ray albedo.

Mrk 421, observed at $\sim 20^\circ$ off-axis with respect to the boresight, was not regularly detected at a significance level higher than 3-$\sigma$ on daily time scales[1]. Instead, a 4.5-$\sigma$ significance level over the whole 5-day period resulted from a maximum likelihood analysis in the energy range 100 MeV–10 GeV. The average $\gamma$-ray flux is $(42 \pm 13) \times 10^{-8}$ photons cm$^{-2}$ s$^{-1}$ for E > 100 MeV, about $\sim 3$ times higher than the average flux detected by EGRET ($\sim 13 \times 10^{-8}$ photons cm$^{-2}$ s$^{-1}$; Hartman et al. 1999) and $\sim 1.5$ times higher, but still consistent, with the highest flux observed by EGRET during May 1994, $(27 \pm 7) \times 10^{-8}$ photons cm$^{-2}$ s$^{-1}$. Due to the relative faintness of the source and the short exposure, the GRID data do not allow us to extract a reliable energy spectrum.

On 2008 June 10, SuperAGILE detected enhanced hard X-ray emission from Mrk 421. The measured daily flux in 20–60 keV was found to be above 30 mCrab, almost an order of magnitude larger than its typical flux in quiescence. In the following days, the flux increased up to reach about 55 mCrab on 2008 June 13. The 20–60 keV SuperAGILE light curve between 9 and 13 June 2008 is shown in Fig 9.1c. The flux increased by a factor of $\sim 2$ over 4 days, starting to decrease the last day of the observation.

We use the publicly available light curves for this source from the *Swift*/BAT experiment[2] in the 15–50 keV energy range (a bandpass similar to the Super-

[1]The peak of the $\gamma$-ray activity, considering time-bins of 2 days, is detected by AGILE between 2008-06-10 23:00 UT and 2008-06-12 23:00 UT.

[2]http://swift.gsfc.nasa.gov/docs/swift/results/transients/weak/Mrk421/

AGILE one), in order to obtain good coverage also before and after the AGILE observation (black squares in Fig. 9.1c), revealing that SuperAGILE indeed observed the maximum brightness of this hard X-ray flare. Both SuperAGILE and BAT count rates were converted to physical units by assuming a Crab-like spectrum (see e.g. Frontera et al. 2007), thus allowing a comparison of the two data set despite the slightly different bandpasses.

SuperAGILE photon-by-photon data allows extraction of a time-averaged energy spectrum from the mask-convolved data. Given the lack of substantial spectral variability in the SuperAGILE/ASM hardness ratio (Fig. 9.1e) we accumulated the average energy spectrum from the data of the last 4 days of the observations, when the source flux varied between 35 and 55 mCrab, for a total net source exposure of $\sim$ 140 ks. Despite poor statistics, this 4-point energy spectrum is able to reasonably constrain the photon index of a simple power law, $\Gamma = 2.43^{+0.69}_{-0.64}$ ($\chi^2_{\rm red} = 0.8$, 2 d.o.f.). The average flux obtained over the 4 days is F (20-60 keV) = $(4.90 \pm 0.54) \times 10^{-10}$ erg cm$^{-2}$ s$^{-1}$.

### 9.2.2 *Swift*/XRT observation

Following the SuperAGILE detection, on 2008 June 12 we triggered a ToO observation with the *Swift* X-Ray Telescope (XRT) that promptly observed the source for $\sim$ 5 ks between 2008 June 12 19:33:20 UT and June 13 at 01:57:37 UT (MJD 54629.8–54630.1).

The XRT data were processed using the standard procedure (`xrtpipeline` v0.12.0), with filtering and screening criteria by using FTOOLS in the `Heasoft` 6.4 package. Observations were taken in Windowed Timing (WT) mode at a count rate of 120–150 cts s$^{-1}$. We selected XRT grades 0–2 (Burrows et al. 2005) and extracted the WT data in a rectangular region of 40×20 pixels centered on the source. The background was also extracted within a similar rectangular region of 40×20 pixels, far from possible background sources. Due to calibration uncertainties of XRT, we restricted our spectral fit to the energy range 0.7–9.0 keV and added a 3% systematics to the model (Cusumano et al. 2007). The XRT spectral data are well described by an absorbed log-parabolic model. We performed a joint fit of the XRT data and the SuperAGILE 4-day average spectrum using a log-parabolic model, defined as:

$$F(E) = KE^{-a-b\log(E)} \text{ photons cm}^{-2}\text{ s}^{-1}$$

where $a$ is the photon index at 1 keV and $b$ is the curvature parameter (Massaro et al. 2004; Massaro et al. 2008). The log-parabolic model corrected for Galactic absorption ($N_{\rm H}^{\rm Gal} = 1.61\times10^{20}$ cm$^{-2}$; Lockman & Savage 1995) usually describes adequately the featureless and curved spectrum in HBLs (see e.g. Tramacere et al. 2007). The log-parabolic distribution give an interpretation of this feature

in the framework of energy dipendent acceleration that naturally leads to log-parabolic spectral distributions, with a possible power law tail at lower energies. The joint fit provides $a = 1.65^{+0.01}_{-0.02}$, $b = 0.37^{+0.01}_{-0.01}$ ($\chi^2_{\rm red} = 1.4$, 763 d.o.f.), which implies a peak energy of $2.97^{+0.22}_{-0.18}$ keV, and predicts fluxes $F_{2-10\,\rm keV} = 2.56 \times 10^{-9}$ erg cm$^{-2}$ s$^{-1}$ and $F_{20-60\,\rm keV} = (5.7 \pm 0.6) \times 10^{-10}$ erg cm$^{-2}$ s$^{-1}$, comparable to the stand-alone SuperAGILE best fit.

Interestingly, the 2–10 keV flux measured by XRT on June 12–13, $\sim 2.6 \times 10^{-9}$ erg cm$^{-2}$ s$^{-1}$, is higher than the flux observed during previous multifrequency campaign on Mrk 421 ($< 2 \times 10^{-9}$ erg cm$^{-2}$ s$^{-1}$: Fossati et al. 2008; Lichti et al. 2008). A joint analysis of the XRT and SuperAGILE data, covering the range from 0.7 to 60 keV, provides a best-fit spectral model consistent with a log-parabolic shape, with parameters implying a peak energy $\sim$3 keV, in good agreement with the steeper positive correlation between the peak energy and the maximum of the SED found by Tramacere et al. 2007 (see their Fig. 3), although our value of the peak energy shows a significant shift with respect to typical values of 0.5–1 keV usually obtained for this source. We note that during a *Swift* observation on July 2006, the source reached a 2–10 keV flux of the order of $\sim 4 \times 10^{-9}$ erg cm$^{-2}$ s$^{-1}$, with a peak energy larger than 10 keV (Tramacere et al. 2009).

### 9.2.3 RXTE/ASM

Given the high flux observed by *Swift*/XRT, we retrieved the public light curves provided by the All Sky Monitor (ASM)[3] to trace the evolution of the soft X-rays during the entire AGILE observation. Figure 9.1b shows the daily light curve of Mrk 421 in the energy range 2–12 keV, obtained by properly averaging the dwell-by-dwell data. The emission at soft X-rays is well correlated with the hard X-ray emission.

The ASM data show that the XRT observation took place when the source was at its maximum emission in soft X-rays (MJD $\sim$ 54630). Comparing the relative intensity of the two flares in Fig. 9.1, it appears that the second peak is significantly harder than the first one. This is also shown in Fig. 9.1e, where we computed the daily-averaged hardness ratio between hard (15–60 keV) and soft (2–12 keV) X-rays. The source appears to have undergone the hardest part of this double-humped flare just during the AGILE detection in $\gamma$-rays.

[3] http://xte.mit.edu/asmlc/ASM.html

### 9.2.4 Observations in the VHE $\gamma$-rays

The 4-telescope array VERITAS (Acciari et al. 2008a) at the Fred Lawrence Whipple Observatory (Arizona) and the single-dish instrument MAGIC (Baixeras et al. 2004; Tescaro et al. 2007) at La Palma are IACTs covering an energy range from $\sim$ 100 GeV to some tens of TeV. The instruments have a typical energy resolution of $< 20\%$ (VERITAS) and 20–30% (MAGIC), and event-by-event angular resolution of $< 0.14^\circ$. Wobble-mode observations (Daum et al. 1997) at an $0.4^\circ$ offset from the camera center were taken on five nights (2008 June 3–8) with MAGIC at zenith angles (ZA) between $28^\circ$ and $48^\circ$ and on four nights (2008 May 27, June 1, 5, 6) with VERITAS (wobble offset: $0.5^\circ$) at ZA between $32^\circ$ and $40^\circ$ during partial moon light conditions. The total live-time after applying quality selection is 2.95 hours and 1.17 hours with MAGIC and VERITAS, respectively. The data were analyzed using the MAGIC (Albert et al. 2008c) and VERITAS (Daniel et al. 2007; Acciari et al. 2008) standard calibration and analyses and image parameters (Hillas 1985). For VERITAS, the $\gamma$-ray direction and air shower impact parameter on the ground are reconstructed using the stereoscopic techniques in Hofmann et al. (1999) and Krawczynski et al. (2006). Any $\gamma$-ray excess is derived from the $\theta^2$ distribution, where $\theta$ represents the angular distance between the source position in the sky and the reconstructed arrival position of the air shower. For MAGIC, $\theta$ is estimated using the DISP method (Fomin et al. 1994). For VERITAS, 99.9% of the background of cosmic-rays is rejected by using selection cuts on $\theta^2$, mean scaled width and length, and by using quality cuts of each event. The MAGIC analysis utilizes a random forest method (Albert et al. 2008b) to discriminate the dominating background of hadronic cosmic-ray events and for the energy estimation of the $\gamma$-ray events. The energy and effective area of each event is reconstructed from Monte Carlo simulations. The integral flux and energy spectrum of the source is then derived from the effective areas for nights with a significant detection.

Two independent analysis of both the MAGIC and VERITAS data sets yielded consistent results. In total, a signal corresponding to a significance level of 44-$\sigma$ (VERITAS) and 66-$\sigma$ (MAGIC) is obtained by following eq. 17 of Li & Ma (1983). Taking advantage of the overlapping MAGIC and VERITAS observations, we present a combined VHE light curve. The combined MAGIC-VERITAS data (Fig. 9.1d) show a transient flare peaking near MJD 54622. The VERITAS energy spectrum for June 6 is provided. A power law fit over the energy range 0.3–5 TeV resulted in a $\chi^2_{\rm red} = 0.7$, with a photon index $\Gamma = 2.78 \pm 0.09$. The intrinsic $\gamma$-ray spectrum of the source reconstructed by removing attenuation effects by the extragalactic background light (Hauser & Dwek 2001) following the procedure of Raue & Mazin (2008)[4] yields a photon index $\Gamma =$

[4] http://www.desy.de/~mraue/ebl/

$2.59 \pm 0.08$, which is not significantly harder than the measured spectrum due to the relatively low redshift of the source (z = 0.031).

### 9.2.5 Optical and UV observations

Mrk 421 is one of the 28 $\gamma$-ray-loud blazars that are regularly monitored by the GLAST-AGILE Support Program (GASP) of the Whole Earth Blazar Telescope (WEBT). The GASP observations of Mrk 421 started in early 2007 November. The *R*-band data were calibrated according to the photometric sequence by Villata et al. (1998). A careful data analysis is warranted because the source flux is contaminated by the emission of the host galaxy and nearby objects. The flux contribution of these objects was subtracted according to Nilsson et al. (2007). Moreover, we corrected for a Galactic extinction of $A_{\mathrm{R}} = 0.042$ mag. The resulting *R*-band light curve during the period considered is shown in Fig. 9.1a.

During the *Swift* pointing on 2008 June 12–13, the UVOT (Poole et al. 2008) instrument observed Mrk 421 in the UV*W*1 and UV*W*2 photometric bands. The `uvotsource` tool is used to extract counts, correct for coincidence losses, apply background subtraction, and calculate the source flux. We applied a standard 5 arcsec radius source aperture, and a 20 arcsec background region. The source fluxes are dereddened using the interstellar extinction curve in Fitzpatrick (1999).

### 9.2.6 Discussion

Mrk 421 showed a very interesting broad-band activity over 12 decades in energy during the first half of 2008 June as derived from GASP-WEBT, *Swift*, AGILE, MAGIC and VERITAS observations. Using the multifrequency data collected, we were able to derive time-resolved SEDs. We distinguish two periods: *period* 1 (2008 June 6), with the inclusion of optical, X-ray (RXTE and BAT) and TeV data (VERITAS); and *period* 2 (2008 June 9–15), including optical, UV, X-rays (XRT and SuperAGILE) and $\gamma$-ray data (AGILE).

The source shows a very interesting time-variable broad band emission that appears to be in overall agreement with a SSC model (see Fig. 9.2). The optical, soft and hard X-ray bands strongly constrain the SED around the synchrotron peak, and its daily variability reveals the physical processes of Mrk 421. Possible correlated variability is shown in Fig. 9.1 between the optical (with an overall decreasing trend with superimposed spikes of emission), the X-rays (with several emission peaks lasting few days), and the high-energy parts of the spectrum. Based on the physical constraints obtained for the synchrotron peak, we can model both the HE and VHE $\gamma$-ray emission.

We first model the synchrotron peak of emission using optical, soft X-ray and hard X-ray data collected during the *period* 1. The short time-variability observed (Fig. 9.1) constrains the size of the emitting region to $R < cT\delta \sim 5 \times 10^{16}(\delta/20)$ cm. Hence, we consider a one-zone SSC model based on a blob of comoving size $R = 4 \times 10^{16}$ cm, with a relativistic Doppler factor $\delta = 20$ and characterized by non-thermal comoving electron energy distribution function described by a double power law:

$$n_e(\gamma) = \frac{K\gamma_b^{-1}}{(\gamma/\gamma_b)^{p_1} + (\gamma/\gamma_b)^{p_2}} \tag{9.1}$$

where the comoving Lorentz factor ($\gamma$) varies in the range $\gamma_{min} = 4 \times 10^3 < \gamma < \gamma_{max} = 1.3 \times 10^6$, the normalization density constant is $K = 4 \times 10^{-4}$ cm$^{-3}$, the break energy is $\gamma_b = 3.6 \times 10^5$, with low-energy and high-energy photon indexes $p_1 = 2.22$ and $p_2 = 4.5$, respectively (see Table 9.1). With these parameters we found that the data for *period* 1 are best fitted with a comoving magnetic field $B = 0.1$ G.

The variability observed between the two periods may be caused mainly by two effects: (A) hardening/softening of the electron energy distribution function caused by particle acceleration processes; (B) increase/decrease of the comoving particle density, as a consequence of additional particle injection/loss by shock processes. For case (A) we expect TeV variability to be comparable with the X-ray one, because the emission is in the Klein-Nishina regime. Alternately, for case (B) we expect the TeV relative variability ($\Delta F/F$) to be a factor of 2 greater than that of the X-ray flux variability.

The AGILE, MAGIC and VERITAS data seem to support the case (A). We compare the SEDs for *period* 1 and *period* 2, to better assess the spectral evolution. In Fig. 9.2 we show our optimized modelling of the time-resolved synchrotron peak and consequent SSC high-energy emission for the *period* 1 as well as for 2008 June 12–13 sub-interval of the *period* 2. In the last case, the adopted model parameters are $p_1 = 2.1$, $p_2 = 5$, $\gamma_b = 4.2 \times 10^5$, and $K = 6 \times 10^{-4}$ cm$^{-3}$. Our theoretical model predicts for *period* 2 a VHE flux at about 7 Crab units, a factor of 2 larger with respect to that detected in *period* 1, with an IC peak slightly shifted towards higher energies. Unfortunately, the moonlight hampered measurements by MAGIC and VERITAS in this second period.

However, the ARGO-YBJ experiment since 2007 November is performing a continuous monitoring of Mrk 421 and detected a VHE flux at a significance level of 4.2-$\sigma$, with a suitable events selection (see Vernetto 2009), during the period 2008 June 11–13 (Di Sciascio 2009). The ARGO measurements appear in fair agreement with the expected emission from the theoretical model previously proposed, as shown in Fig 9.3, in which the ARGO measurements are

overimposed to the SED reported in Fig 9.2. The soft X-ray data seems to be well correlated with the TeV observations, confirming that the flare observed in *period* 2 is a factor 2 larger with respect to that observed in *period* 1.

From a more detailed investigation of the light curves in Fig. 9.1 a complex optical vs. X-ray variability of Mrk 421 is observed. The optical light curve shows variations of the order of 10% on a time scale of $\sim$ few days, superimposed on a long decay during the entire period. Instead, individual soft and hard X-ray peaks result in increased fluxes by a factor of $\sim 2.5$ and $\sim 5$, respectively, and no long term decay appears. This different behaviour of the X-ray radiation and the bulk of the optical emission may interestingly suggest a more complex scenarios than A) and B) ones previously proposed: optical and X-ray emission comes from two different jet regions, each one characterized by its own variability. A possible scenarios is that the inner jet region would produce the X-rays and it would be at least partially transparent to the optical radiation. On the other hand, the outer region can only produce lower-frequency emission. The signature of the X-ray events visible in the optical light curve would come from the inner region and would be diluted by the optical radiation emitted from the outer region.

This behaviour could be explained by a geometrical model in which the emitting plasma flows along a rotating helical path (see Villata & Raiteri 1999). The mechanism producing the flux enhancement propagates downstream, crossing region with different opacity and triggering X-ray and optical outburst as it crosses the corresponding emitting region. The different parts of the jet have a different viewing angle and therefore the Doppler enhancement of the optical and X-ray emitting region is different. This model has already provided an interpretation for the long-term behaviour of other BL Lac objects such as Mrk 501 (Villata & Raiteri 1999), S5 0716+714 (Ostorero et al. 2001), AO 0235+16 (Ostorero et al. 2004) and BL Lacertae (Villata et al. 2009c). However, to test this model also for Mrk 421 observations over a longer period is necessary in order to investigate the possible orientation variation of helical inhomogeneous emitting jet.

### 9.2.7 Summary and remarks

1. A multiwavelength campaign was organized on Mrk 421 between 2008 May 24 and June 23, involving GASP-WEBT, *Swift*, AGILE, MAGIC and VERITAS observations.

2. The source was observed in high activity state between 6 and 15 June 2009 in soft X-ray, hard X-ray, HE and VHE $\gamma$-ray bands.

3. SuperAGILE, RXTE/ASM and *Swift*/BAT show a clear correlated flaring structure between soft and hard X-rays with a high flux/amplitude variability in hard X-rays. Hints of the same flaring behaviour is also detected in optical band by GASP-WEBT.

4. *Swift*/XRT observed the source at one of the highest 2–10 keV flux ever observed, with a peak of the synchrotron at $\sim 3$ keV, showing a shift with respect to the typical values of 0.5–1 keV.

5. VERITAS and MAGIC observed the source on 2008 June 6–8 in a bright state well correlated with the simultaneous peak in X-rays.

6. The $\gamma$-ray flare observed by AGILE can be interpreted within the framework of the SSC model in terms of a rapid acceleration of leptons in the jet.

7. The VHE flare observed by ARGO during 11–13 June 2008 confirm the level of flux predicted by our theoretical model for the period of the AGILE observation.

8. The optical and X-ray behaviour suggests a possible more complex scenario, in which optical and X-ray radiation comes from two different regions of the jet, with different variability and could be explained in the context of a helical jet model.

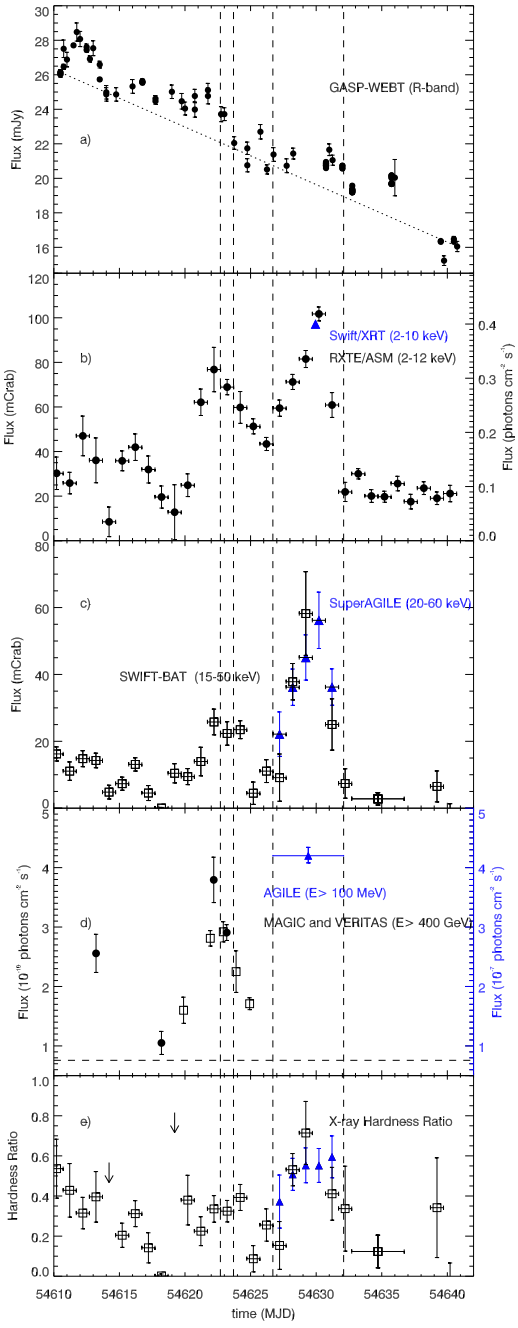


**Figure 9.1: a)** *R*-band optical light curve from GASP-WEBT (May 24–June 23); **b)** ASM (2–12 keV) light curve and XRT (2–10 keV) flux (blue triangle); **c)** SuperAGILE (20–60 keV, blue triangles; 1 Crab = 0.20 ph cm$^{-2}$ s$^{-1}$) and BAT (15–50 keV, empty black squares; 1 Crab = 0.29 ph cm$^{-2}$ s$^{-1}$); **d)** MAGIC and VERITAS (E > 400 GeV, empty black squares and black circles, respectively), the Crab flux at E > 400 GeV (horizontal dashed line), AGILE (E > 100 MeV, blue triangle); **e)** the hardness ratio computed by using the SuperAGILE and ASM data for each day. The dashed vertical lines mark *period* 1 and *period* 2 [Donnarumma et al. 2009a].

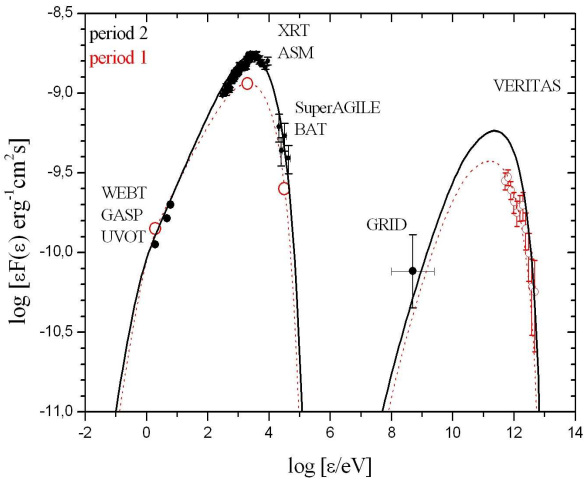


**Figure 9.2:** SEDs of Mrk 421 obtained by combining the GASP-WEBT, *Swift*/UVOT, RXTE/ASM, *Swift*/XRT, SuperAGILE, *Swift*/BAT, GRID and VERITAS data in *period* 1 and *period* 2 (red empty cirles and black filled circles, respectively). Both are one-zone SSC models (red dashed line for *period* 1 and black solid line for *period* 2) [Donnarumma et al. 2009a].

**Table 9.1:** SSC model parameters for the SED of Mrk 421 on 6 June 2008 (*period* 1) and 9–15 June 2008 (*period* 2).

| parameter | period 1 | period 2 |
|---|---|---|
| $\gamma_b$ | $3.6 \times 10^5$ | $4.2 \times 10^5$ |
| $\gamma_{max}$ | $1.3 \times 10^6$ | $1.3 \times 10^6$ |
| $p_1$ | 2.22 | 2.1 |
| $p_2$ | 4.5 | 5 |
| $B$ [G] | 0.1 | 0.1 |
| $K$ [cm$^{-3}$] | $4 \times 10^{-4}$ | $6 \times 10^{-4}$ |
| $\delta$ | 20 | 20 |
| $\theta$[°] | 2 | 2 |

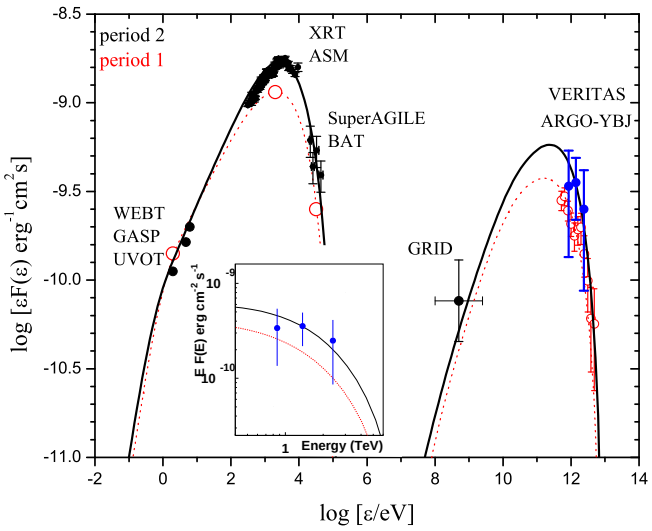


**Figure 9.3:** SEDs of Mrk 421 with the ARGO-YBJ data collected on June 11–13 together with the data presented in Donnarumma et al. (2009a). The inset shows a zoom on the ARGO-YBJ data [Di Sciascio 2009].

## 9.3 W Comae

W Com (ON 231; z = 0.102) is a $\gamma$-ray blazar classified as an intermediate-frequency peaked BL Lac (IBL) object (see e.g. Nieppola et al. 2006), based on the locations of the low-energy synchrotron peak in its spectral energy distribution.

The source has discovered at radio frequencies (Biraud 1971) and later detected at X-ray energies by *Einstein* in June 1980 (Worrall & Wilkes 1990). Observations with *Beppo*SAX in 1999 clearly showed that the transition between the low and the high-energy peaks in the SED occurs around $\sim 4$ keV (Tagliaferri et al. 2000). In April–May 1998, an exceptional optical outburst was detected by W Comae showing rapid variability on timescales of hours (Massaro et al. 1999). At $\gamma$-ray energies W Comae was detected by EGRET in the 100 MeV – 10 GeV band (Hartman et al. 1999) and in a re-analysis of the data up to 25 GeV (Dingus & Bertsch 2001). Due to its rather hard spectrum detected by EGRET ($\Gamma = 1.73 \pm 0.18$) with no sign of cut-off the source become even more interesting for very high-energy energy (VHE; E > 100 GeV) observations. However, the source was not detected by Whipple above 300 GeV (Kerrick et al. 1995; Horan et al. 2004) nor by STACEE (Scalzo et al. 2004).

Due to the improved sensitivity of current-generation IACTs such as VERITAS, MAGIC and H.E.S.S., IBLs are became attractive targets of observations at VHE $\gamma$-rays, particularly because they offer the possibility of extension of the VHE blazars catalog to include non-HBL objects. VHE observations of different blazar classes, will help us in the understanding of the relationship of the different blazar populations and the mechanism for particle acceleration and emission in the highly-relativistic jets.

W Com was the first IBL to be detected at very high energies (Acciari et al. 2008b). It was discovered at TeV energies by VERITAS during observations carried out over January–April 2008. In particular, during this period a strong VHE $\gamma$-ray flare was measured over a 4-day interval in the middle of March. VERITAS reported a steep photon spectrum ($\Gamma = 3.81 \pm 0.35_{\rm stat} \pm 0.34_{\rm sys}$)[5] and an integral flux of 9% of the Crab Nebula flux during the flare nights. The VERITAS detection triggered *Swift* observations, and the multiwavelength data obtained were adequately explained by an external Compton (EC) model (Acciari et al. 2008b).

In 2008 June, VERITAS detected a second VHE flare of W Comae, when the source was approximately three times brighter than during the 2008 March observation. Considering the VHE flare observed by VERITAS a multiwavelength campaign was triggered, including observations with the AGILE $\gamma$-ray

[5]The subscripts *stat* and *sys* denote the statistical and systematic error.

telescope and the *Swift* and XMM-*Newton* X-ray telescopes. Observations in radio, near-IR, and optical bands have been assured by GASP-WEBT.
We describe the multiwavelength data collected by GASP-WEBT, *Swift*, XMM-*Newton*, AGILE and VERITAS throughout the flare and derive the SED of the source, discussing its theoretical implication for the emission mechanisms.

### 9.3.1 VHE $\gamma$-ray observations: VERITAS

VERITAS is an array of four imaging Cherenkov telescopes located at the Fred Lawrence Whipple Observatory in southern Arizona. It combines a large effective area (up to $10^5$ m$^2$) over a wide energy range (100 GeV to 30 TeV) with good energy resolution (15-20%) and angular resolution ($\approx 0.1^o$) and a field of view of $3.5^o$.

VERITAS observed W Com for 230 minutes on 2008 June 7–9. All observations pass quality-selection criteria, which remove data taken during bad weather or affected by hardware-related problems. Data were taken in wobble mode, wherein the source was positioned at a fixed offset of $0.5^o$ from the camera center. This allows the simultaneous estimate of the background (Fomin et al. 1994). The regions around the VHE $\gamma$-ray blazar 1ES 1218+304 (Acciari et al. 2008c), located about $2^\circ$ north of W Com, and around bright stars (*B*-band magnitude brighter than 6) are excluded from the background estimation (see Fig. 9.4). All observations were undertaken in moonlight conditions, where the elevated background light levels lead to a lower sensitivity for the detection of $\gamma$-rays at the threshold. The different elevations combined with the continuity changing background light conditions due to the Moon results in a wide range of energy threshold from 200 to 420 GeV for these observations.

The VERITAS analysis data steps consist of image calibration and cleaning, second-moment parameterization of the telescope images (Hillas 1985), stereoscopic reconstruction of the event impact position and direction, $\gamma$-hadron separation (see e.g. Krawczynski et al. 2006), and the generation of photon sky maps. Most of the far more numerous background events are rejected by comparing the parameterized shape of the event images in each telescope with the expected shapes of $\gamma$-ray showers modeled by Monte Carlo simulations. *Mean-reduced-scaled width* and *mean-reduced-scaled length* cuts (see definition in Acciari et al. 2008a), and an additional cut on the arrival direction of the incoming $\gamma$-ray ($\Theta^2$, defined as the square of the angular distance to the position of W Com to the reconstructed shower direction), reject more than 99.9% of successfully reconstructed cosmic-ray background events, while keeping 45% of the $\gamma$-rays. The cuts applied here are: integrated charge per image >75 photoelectrons, mean-reduced-scaled width and length between -1.2 and 0.5, and $\Theta^2 < 0.015$ deg$^2$. The number of background events in the source region are estimated from the

same field of view using the 'reflected-region' model with 10 background regions (Aharonian et al. 2001).

**Table 9.2:** Details of VERITAS observations of W Com on 2008 June 7–9. The energy threshold for fluxes and upper flux limits (99% confidence level; assuming a photon index of $\Gamma = 3.68$) is 200 GeV. Errors are given at the 1-$\sigma$ level.

| MJD | Observation Time min | Significance $\sigma$ (pre-trials) | Flux $cm^{-2}\ s^{-1}$ |
|---|---|---|---|
| 54624.16 - 54624.23 | 100.2 | 8.9 | $(5.0 \pm 0.8) \times 10^{-11}$ |
| 54625.17 - 54625.24 | 100.2 | 7.9 | $(6.2 \pm 1.2) \times 10^{-11}$ |
| 54626.18 - 54626.20 | 32.0 | -1.0 | $< 3.21 \times 10^{-11}$ |

Figure 9.4 shows the sky around W Com as seen by VERITAS in VHE $\gamma$-rays. A significant flux from W Com is detected by VERITAS at VHE for the entire data set taken on 2008 June 7–9. A total of 117 excess events (195 *on-source* events and 78 normalized *off-source* events, normalization factor of 0.10) are measured. This corresponds to a significance of 10.3 standard deviations, calculated following Equation 17 in Li et al. 1983. Table 9.2 lists the significances and fluxes above 200 GeV in the different periods, assuming a power law spectral shape with a photon index of 3.68. Figure 9.5 shows the light curve for these observations. W Com is not detected on 2008 June 9 (MJD 54626), but observations were restricted to only 32 min due to very high background light levels caused by the Moon. The average flux on 2008 June 7–8 is 2.5-3 times higher than during the $\gamma$-ray flare from W Com in March 2008 (Acciari et al. 2008b).

The shape of the differential photon spectrum between 180 GeV and 3 TeV with the measurements from 2008 June 7–8 is consistent with a power law $dN/dE = C \times (E/400\ \mathrm{GeV})^{-\Gamma}$ with a photon index $\Gamma = 3.68 \pm 0.22_{stat} \pm 0.3_{sys}$ and a flux normalization constant $C = (6.5 \pm 0.9_{stat} \pm 1.3_{sys}) \times 10^{-11}\ \mathrm{cm^{-2}s^{-1}TeV^{-1}}$. The $\chi^2$ of the fit is 3.27 for 5 d.o.f. For comparison, the flare in VHE $\gamma$-rays from W Com in 2008 March (Acciari et al. 2008b) is well fit by a power law with a consistent photon index $\Gamma = 3.81 \pm 0.35_{stat} \pm 0.34_{sys}$, but smaller flux constant $C = (2.00 \pm 0.31_{stat} \pm 0.5_{sys}) \times 10^{-11}\ \mathrm{cm^{-2}s^{-1}TeV^{-1}}$.

### 9.3.2 HE $\gamma$-ray observations: AGILE

The Gamma-Ray Imaging Detector (GRID) onboard AGILE pointed towards W Com continuously from 2008 June 9 18:00 UT to June 15 12:00 UT. Preliminary and partial results of this observation are reported in Verrecchia et al. 2008. The

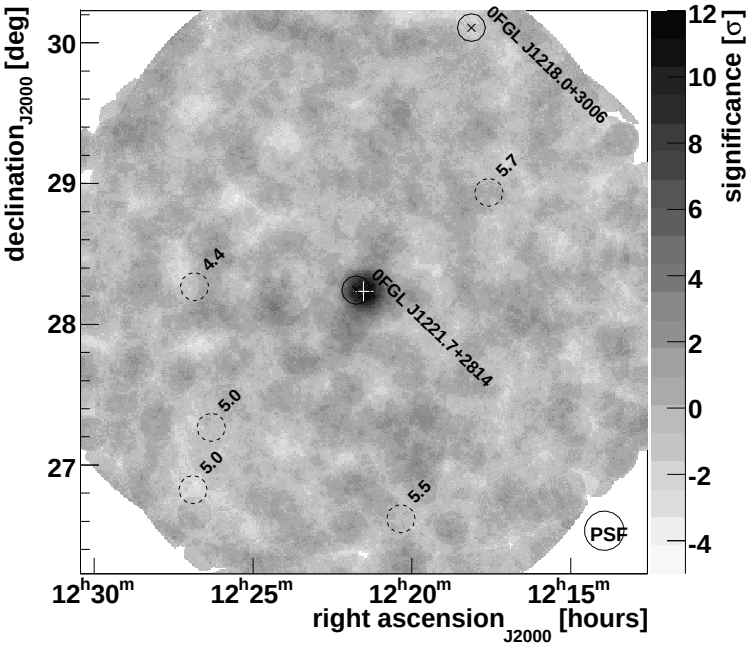


**Figure 9.4:** Sky map of significance in $\gamma$-ray around W Comae. The position of W Com derived from radio data (Fey et al. 2004) is indicated by a white cross. The dashed circles indicate positions of bright stars and their *B*-band magnitudes in the field of view; regions around these stars are excluded from the background estimation. Two sources reported in the *Fermi* bright $\gamma$-ray source list and firmly associated with the blazars W Com and B2 1215 (Abdo et al. 2009d) are shown with their 95% confidence area as circles with 'x' in their center. The circle at the bottom right indicates the angular resolution of VERITAS [Acciari et al. 2009b].

GRID data is analyzed using the AGILE standard pipeline with a bin size of $0.25^\circ \times 0.25^\circ$ (see Section 4.3.6). Only events flagged as $\gamma$-rays and not recorded while the satellite crossed the South Atlantic Anomaly are accepted. Events with reconstructed direction less than $10^\circ$ of the Earth limb are rejected, thus reducing contamination from Earth's $\gamma$-ray albedo.

W Com, observed about 3 degrees off-axis with respect to the boresight, was detected at a significance level of 3.7-$\sigma$ (pre-trials) for E > 100 MeV from 12 (03:00 UT) to 13 (03:00) June 2008, with a flux of $(90 \pm 32) \times 10^{-8}$ ph cm$^{-2}$ s$^{-1}$. This flux is roughly a factor of 1.5 higher than the highest flux detected by EGRET (Hartman et al. 2001) and significantly higher than the weekly averaged peak flux of $(17.2 \pm 3.5) \times 10^{-8}$ ph cm$^{-2}$ s$^{-1}$ reported by *Fermi*-LAT during its

first three months of all-sky monitoring (Abdo et al. 2009d). No excess at a significance level > 3-$\sigma$ is found in the rest of the observing period and upper limits at 2-$\sigma$ are obtained; results can be found in Table 9.3 and Figure 9.5. The paucity of photons prevents us from extracting a spectrum.

**Table 9.3:** Details and results of the AGILE-GRID observations of W Com on 2008 June 9–15 for E > 100 MeV. Upper limits are estimated at 99% confidence level. Errors are given at the 1-$\sigma$ level.

| MJD | Significance $\sigma$ | Flux (E > 100 MeV) ph cm$^{-2}$ s$^{-1}$ |
|---|---|---|
| 54626.75 - 54629.12 | <3 | $< 60 \times 10^{-8}$ |
| 54629.12 - 54630.12 | 3.7 | $(90 \pm 34) \times 10^{-8}$ |
| 54630.12 - 54632.50 | <3 | $< 55.5 \times 10^{-8}$ |

SuperAGILE, the hard X-ray imager onboard AGILE (18–60 keV), observed the source for a net exposure time of 253 ks. The source position in the orthogonal SuperAGILE reference system is ~ (3,0) deg, which means that the exposed area is close to the full on-axis effective area (see Feroci et al. 2007). W Com was not been detected with SuperAGILE, and we estimate a 3-$\sigma$ upper limit in the 20–60 keV energy of 6 mCrab $\simeq 6.9 \times 10^{-11}$ erg cm$^{-2}$ s$^{-1}$ (assuming a photon index Crab-like of $\Gamma = 2.1$).

### 9.3.3 X-ray observations: *Swift* and XMM-*Newton*

Observations of W Com with the *Swift* satellite were taken on 2008 June 7–9 and were partly contemporaneous with VERITAS and AGILE observations. The XRT data are reduced using the `HEAsoft` 6.5 package. Event files are calibrated and cleaned following the standard filtering criteria using the `xrtpipeline` task and applying the most recent XRT calibration files (v11). All data were taken in Photon Counting (PC) mode, with grades 0–12 selected over the energy range 0.3–10 keV. Due to the rates larger than 0.5 counts s$^{-1}$ pile-up in the core of the point spread function (PSF) is present, therefore the source events are extracted from an annular region with an inner radius of 3 pixels and an outer radius of 30 pixels. Background counts are extracted from a 40 pixel radius circle in a source-free region. Ancillary response files are generated using the `xrtmkarf` task, with corrections applied for the PSF losses and CCD defects. To ensure valid $\chi^2$ minimization statistics during spectral fitting, the spectra are re-binned to contain a minimum of 20 counts in each bin. The spectra can be described by a single power law convolved with Galactic and local absorption. Table 9.4 summarizes the XRT observations with the best fit model parameters.

**Table 9.4:** Details and results of the *Swift*/XRT observations of W Com on 2008 June 7–9. The galactic $N_H$ has been fixed to a value of $1.88 \times 10^{20}$ cm$^{-2}$ (Dickney and Lockman 1990). The redshift of the source was assumed to be z = 0.102. Errors are given at the 1-$\sigma$ level.

| MJD | Exposure ksec | Photon index $\Gamma$ | Flux (2–10 keV) $10^{-12}$ erg cm$^{-2}$ s$^{-1}$ |
|---|---|---|---|
| 54624.97 - 54624.98 | 0.52 | 2.49 ± 0.19 | 3.90 ± 0.97 |
| 54625.04 - 54625.05 | 0.84 | 2.71 ± 0.15 | 3.70 ± 0.76 |
| 54625.11 - 54625.12 | 1.38 | 2.55 ± 0.09 | 4.75 ± 0.55 |
| 54625.17 - 54625.20 | 2.51 | 2.36 ± 0.05 | 9.33 ± 0.74 |
| 54625.24 - 54625.27 | 2.47 | 2.59 ± 0.07 | 4.62 ± 0.37 |
| 54626.11 - 54626.21 | 5.07 | 2.69 ± 0.10 | 1.00 ± 0.18 |

W Com was also observed by the XMM-*Newton* Observatory (Jansen et al. 2001) between 2008 June 14 and June 18 over three consecutive orbits. The three observations comprise data from the EPIC detectors (0.2–10 keV) in Small Window mode. The data have been analysed using SASv7.1 (Gabriel et al. 2004). Several filtering criteria have been applied to the EPIC data, including filtering for time periods of high background activity following the standard procedure, and filtering only for single- and double-pattern events for EPIC-pn and single to quadruple for EPIC-MOS, as well as including only events with good quality (quality FLAG=0). For the spectral analysis, circular source and annular background extraction regions centered on the source are selected by maximizing the signal-to-noise ratio.

The spectra are re-binned in order to oversample the intrinsic energy resolution of the EPIC cameras by a factor not more than 3 and to have number of counts in each spectral channel larger than 25. This ensure the applicability of the $\chi^2$ quality-of-fit estimator to find the best fit model. Fits are performed in the 0.2–10 keV energy range simultaneously for the three EPIC cameras, where the systematic difference between the EPIC cameras is below ~5% in normalization. For the spectral analysis and fitting procedure XSPEC v12.4 is used. The data can be best described similar to the XRT data by a single power law convolved with galactic and local absorption. Table 9.5 summarizes the XMM observations with the best fit model parameters.

The measurements reveal strong variability in X-rays on time scales of much less than one day. Figure 9.5 (panel C) show that the X-ray flux changed by a factor of two during the VHE high state on MJD 54625. This is comparable to observations of W Com with *Beppo*SAX in 1998 by Tagliaferri et al. (2000), where flux variations of a factor of three in less than 5 hours is reported. The

**Table 9.5:** Details and results of the XMM-*Newton* observations of W Com on 2008 June 14–18. The galactic $N_H$ has been fixed to a value of $1.88 \times 10^{20}$ cm$^{-2}$ (Dickney and Lockman 1990). The redshift of the source was assumed to be z = 0.102. Errors are given at the 1-$\sigma$ level.

| MJD | Exposure ksec | $N_H$ $10^{20}$ cm$^{-2}$ | Ph. Index $\Gamma$ | Flux(2–10 keV) erg cm$^{-2}$ s$^{-1}$ |
|---|---|---|---|---|
| 54631.50 - 54631.55 | 28.0 | $2.20^{+0.09}_{-0.09}$ | $2.79^{+0.01}_{-0.01}$ | $2.69^{+0.02}_{-0.02} \times 10^{-12}$ |
| 54633.15 - 54633.17 | 16.0 | $1.39^{+0.14}_{-0.13}$ | $2.88^{+0.02}_{-0.02}$ | $1.53^{+0.03}_{-0.02} \times 10^{-12}$ |
| 54635.14 - 54635.16 | 11.0 | $1.05^{+0.16}_{-0.15}$ | $2.77^{+0.02}_{-0.02}$ | $1.89^{+0.03}_{-0.03} \times 10^{-12}$ |

X-ray flux during the VHE low state of June 2008 is very similar to the X-ray activity measured during the detection of W Com in March 2008.

### 9.3.4 Radio-to-UV observations

Optical observations of W Com were carried out at the following observatories (the majority part of the GASP-WEBT): Abastumani, Crimean, Roque de los Muchachos (KVA), Talmassons, Torino, San Pedro Martir, Northern Optical Telescope (NOT) and Sapienza University. Magnitude calibration is obtained with respect to the photometric sequence by Fiorucci et al. (1996). Near-infrared (*JHK*) data were acquired at the Campo Imperatore Observatory.

*Swift*/UVOT (Roming et al. 2005) observations were taken in the photometric bands of UV*W1*, UV*M2*, and UV*W2*. The `uvotsource` tool is used to extract counts from the UVOT data, correct for coincidence losses, apply background subtraction, and calculate the source flux. The standard 5 arcsec radius source aperture is used, with a 20 arcsec background region.

At radio frequencies, data at 43 GHz were taken with the 32 m antenna at Noto (Bach et al. 2007), at 14.5 GHz with the 26 m telescope of the UMRAO (Aller et al. 2003), and at 36.8 GHz with the 13.7 m Metsähovi radio telescope (Teräsranta et al. 1998). Data reduction of the optical and radio data followed standard methods and procedures, and we refer to the above papers for details. The near infrared, optical and UV data are corrected for absorption in our Galaxy using the dust maps of Schlegel et al. (1998) and the extinction curve of Cardelli et al. (1989). Since the blazar is observed in a bright state, a host galaxy contribution has not been subtracted.

### 9.3.5 Modeling the SED

The spectral energy distribution of two different time-interval is modelled using the equilibrium version of the leptonic one-zone jet model described in Böttcher et al. (2002b). This model assumes a population of ultrarelativistic electrons and positrons into a spherical emission region of co-moving radius $R_B$, which is moving with a relativistic speed $\beta$c, corresponding to the bulk Lorentz factor $\Gamma$. Lacking more detailed constraints on the viewing angle $\theta$ between the jet direction and the line of sight, we fix $\theta$ to be the superluminal angle, for which the bulk Lorentz factor $\Gamma$ equals the Doppler factor $\delta = [\Gamma\ (1 - \beta\ \cos\ \theta)]^{-1}$ , which determines the Doppler shift of photon energies and relativistic boosting of intensities. We note that our results mainly depend on $\delta$ so that alternative combinations of $\Gamma$ and $\theta$ yielding the same Doppler factor as the one used in our model calculations.

The spectrum of the injected pair population is specified through the injection power $L_{\rm e}$ and a power law with low- and high-energy cut-offs, $\gamma_{\rm min}$ and $\gamma_{\rm max}$ respectively, and a specified index q. The particle escape is parameterized through an escape time scale parameter $\eta > 1$ as $t_{\rm esc} = \eta R/c$. The balance between escape and radiative cooling will lead to a break in the equilibrium particle distribution at a break Lorentz factor $\gamma_{\rm b}$, where $t_{\rm esc} = t_{\rm cool}(\gamma)$. The cooling time scale is evaluated self-consistently taking into account synchrotron, SSC, EC cooling. Depending on whether $\gamma_{\rm b}$ is greater than or less than $\gamma_1$, the system will be in the slow cooling or fast cooling regime. In the fast cooling regime ($\gamma_{\rm b} < \gamma_1$), the equilibrium distribution will be a broken power law with $n(\gamma) \propto \gamma^{-2}$ for $\gamma_{\rm b} < \gamma < \gamma_1$ and $n(\gamma) \propto \gamma^{-(q+1)}$ for $\gamma_1 < \gamma < \gamma_2$. In the slow cooling regime ($\gamma_{\rm b} > \gamma_1$), the equilibrium distribution will be $n(\gamma) \propto \gamma^{-q}$ for $\gamma_1 < \gamma < \gamma_{\rm b}$ and $n(\gamma) \propto \gamma^{-(q+1)}$ for $\gamma_{\rm b} < \gamma < \gamma_2$. The number density of injected particles is normalized to the resulting power in ultrarelativistic electrons propagating along the jet

$$L_e = \pi R_e^2\, \Gamma^2 \beta_\Gamma\, c\, m_e c^2 \int_1^\infty \gamma n(\gamma) d\gamma \tag{9.2}$$

The magnetic field $B$ in the emission region is a free parameter. The corresponding Poynting flux along the jet is $L_B = \pi R_e^2\, \Gamma^2 \beta_\Gamma\, c\, u_B$, with the magnetic energy density $u_B = B^2/(8\pi)$. For each model calculation, the resulting equipartition parameter, $e_B = L_B/L_e$, is evaluated. Modeling results of a large number of blazars, in particular FSRQs, have shown that leptonic models can achieve reasonable fits with the emission region being close to equipartition, typically $0.1 \lesssim e_B \lesssim 1$. However, there is no physical justification for the source components being close to equipartition. It might be that the particle and the mag-

netic fields energies in the source components tend towards equipartition, but there is no proof that this must be so. It has been conjectured that the magnetic field in the source components may be stretched and tangled by motions in the plasma, so there might be rough equipartition between the magnetic energy density and the energy density in turbulent motions. The turbulent motions might also be responsible for accelerating the high energy particles, and these particles might come into equipartition with the turbulent energy density if the acceleration mechanism was very efficient. In this way, it is possible that there might be a physical justification for the source components being close to the equipartition, but there is really no more than a conjecture. Moreover, the equipartition value correspond to the minimum total energy requirements and an increase of the energy requirements can pose problems for some of the most luminous sources. Therefore, while we disfavor possible fit results with $e_B$ far from unity, we can not strictly rule out such scenarios.

Once the quasi-equilibrium particle distribution in the emission region is calculated, the code evaluates the radiative output from synchrotron emission, SSC, and EC emission self-consistently with the radiative cooling rates. For the EC component, we assume an external radiation field which is isotropic in the stationary rest frame and can be approximated by a thermal blackbody with peak frequency $\nu_{\rm ext}$ and radiation energy density $u_{\rm ext}$. The latter two quantities are free model parameters. The direct emission from this external radiation field is added to the SED. Absorption of high-energy $\gamma$-rays by the extragalactic background light is taken into account using the model of Franceschini et al. (2008).

We try to fit the VERITAS flare detection and high X-ray state (MJD 54624.0 – 54626.0) with two different models: a pure SSC model and a model that comprises also an EC component. A Doppler factor of 20 (i.e. $\delta = \Gamma = 20$) consistent with all observational constraints, and well in the range of Doppler factors commonly adopted in other blazar modeling works, allowed acceptable fits to the SEDs. We therefore fixed $\delta = \Gamma = 20$ for the rest of the fitting procedure.

The injection spectral index is tightly constrained by the observed X-ray energy spectral index $\alpha = q/2$, since electrons emitting synchrotron radiation in the X-ray regime are always above the critical Lorentz factor $\gamma_{\rm b}$. In our calculations, the size of the emission region is constrained by the shortest observed variability time scale $\delta t_{\rm var,min}$ through $R_B \leq c\,\delta t_{\rm var,min}\,D/(1+z)$. Together with the value of the magnetic field, the low-energy cut-off ($\gamma_1$) determines the location of the synchrotron and $\gamma$-ray peaks in the SED, while the high-energy cut-off ($\gamma_2$) influences the location of the high-energy cut-offs of the SED, in particular the synchrotron component. The cut-off of the SSC component is, in addition, strongly influenced by Klein-Nishina effects. Parameters of the SSC fit are listed in Table 9.6.

No SSC model fit was possible with the emission region being close to

equipartition. Since there is virtually no observational constraint on the high-energy emission in the low (MJD 54626) and intermediate X-ray state (MJD 54631), we could choose a low injection power and relatively high magnetic field to achieve a synchrotron peak flux comparable to the flaring state, but at a much lower SSC flux. In the SSC interpretation, the most significant difference between the various states consists of a change in the electron injection spectral index $q$ from 2.55 in the flaring state to 3.50 and 3.40 in the low and intermediate state.

Also for a model with an EC component, the electron spectral index $q$ is tightly constrained through the X-ray spectral index, while the variability time scale constrains the radius of the emission region. In order to avoid the problem of required large injection powers (to obtain a high SSC flux) and accordingly small magnetic fields (not to overpredict the synchrotron flux), the VHE $\gamma$-ray emission can be interpreted as EC emission. In order for Comptonization of an external radiation field to be efficient out to $\gamma$-ray energies of $E \gtrsim E_{\rm VHE} = 300$ GeV, the external radiation field has to peak at energies $E_{\rm ext} \lesssim (m_e c^2)^2/E_{\rm VHE} \sim 0.9$ eV, i.e. in the near-infrared. Therefore, line emission from a putative BLR, for which there is no evidence in W Comae, would have a too high photon energy characteristic to serve efficiently as a source photon field for EC scattering to produce an IC spectrum with peak energy near the VHE $\gamma$-ray band. It is therefore more likely that infrared emission from a dusty torus dominates the external radiation field responsible for EC emission at VHE $\gamma$-rays. We find that an external radiation field peaking at $\nu_{\rm ext} = 1.5 \times 10^{14}$ Hz can, at the same time, serve as an efficient source for EC emission and explains the slight near-IR bump in the SED of W Comae. This bump could also be due to the host galaxy, and future observations of variability of the IR component or very high-resolution imaging are required to break this degeneracy. The parameters of our SSC+EC fit are listed in Table 9.6. With the assumption of such an external radiation field, acceptable fits to each of the states of W Comae can be achieved within a factor of $\sim 3$ of equipartition.

### 9.3.6 Summary

1. The IBL object W Comae was discovered by VERITAS during a strong outburst on 2008 June 7–8, with a three times flux higher than that observed in March 2008.

2. The VERITAS observations triggered a multiwavelength campaign including AGILE $\gamma$-ray, *Swift* and XMM-*Newton* X-ray, UV, GASP optical and radio observations.

3. The SED of W Comae during the VHE $\gamma$-ray flare (MJD 54624–54626) can be modelled by a simple leptonic SSC model, but the wide separation of the two peaks in the SED requires low ratio of the magnetic field to electron energy density ($\epsilon_B = 2.3 \times 10^{-3}$), far from the equipartition.

4. In the SSC scenario, the most important difference between the high, intermediate and low states observed in the campaign is due to the change of the electron injected spectral indexes.

5. The SSC+EC model returns magnetic field parameters closer to equipartition, providing a satisfactory description of the broadband SED. A similar result is obtained for the VHE flare observed in March 2008 (Acciari et al. 2008b).

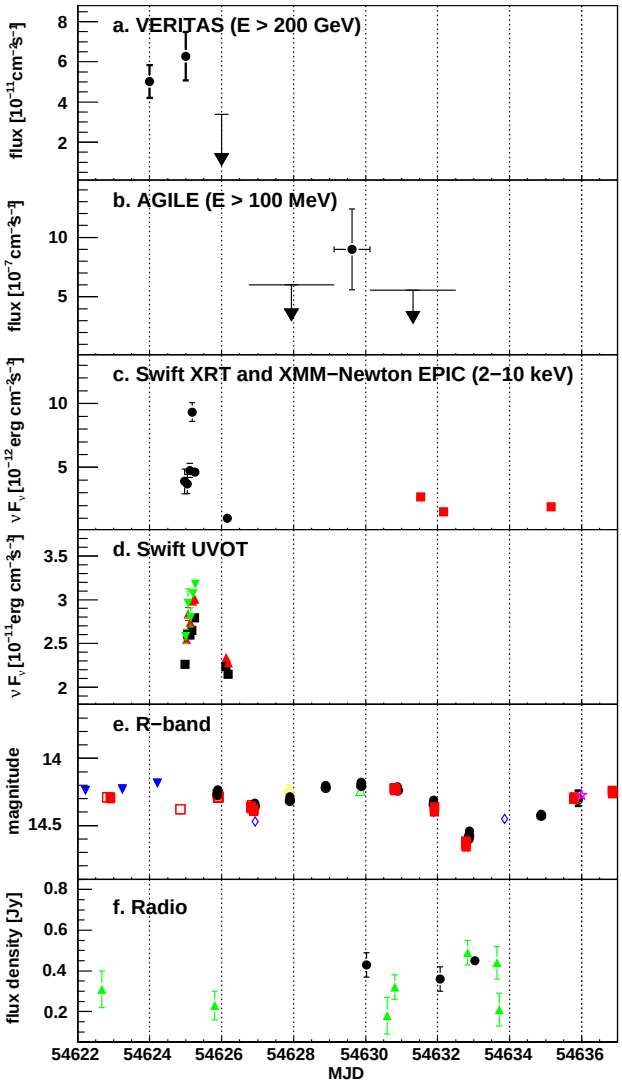


**Figure 9.5:** Multiwavelength light curves of W Comae from MJD 54622 to MJD 54636. Panel a: VHE $\gamma$-rays light curve (E > 200 GeV) as measured by VERITAS. Panel b: HE $\gamma$-ray light curve (E > 100 MeV) as measured by AGILE. Panel c: 2–10 keV *Swift*/XRT (circles) and XMM-*Newton* EPIC (squares) X-ray light curves. Panel d: *Swift*/UVOT (UVW1: squares; UVM2: downward-pointing triangles; UVW2: upward-pointing triangles) light curves. Panel e: optical *R*-band light curve (filled circles: Tuorla; filled squares: Abastumani; filled triangles: San Pedro Martir; diamonds: Sapienza University; open circles: KVA; open squares: Crimean; open stars: NOT; open triangles: Torino; open crosses: Talmassons). Panel f: Radio light curves (circles: UMRAO at 14.5 GHz; triangles: Metsähovi at 37 GHz). Downward pointing arrows indicate upper limits at 99% confidence level [Acciari et al. 2009b].

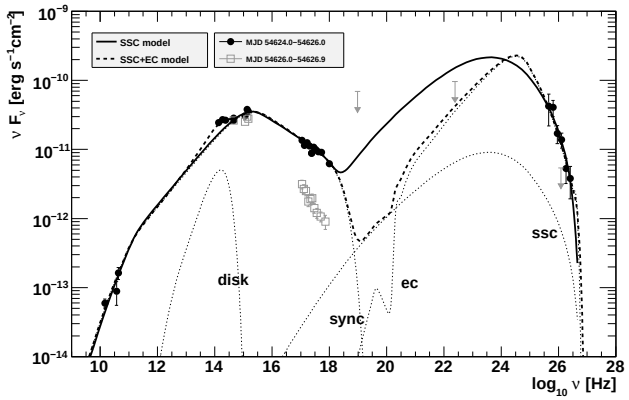


**Figure 9.6:** SED of W Comae for the period MJD 54624–54626, including VERITAS, *Swift* (XRT and UVOT), optical and radio data (filled circular markers). The averages of the optical, NIR, and radio fluxes calculated in the period MJD 54610 to 54645 are shown. Downward arrows indicate upper limit at 99% confidence level. For comparison, the VERITAS, AGILE, and *Swift* (UVOT and XRT) data for MJD 54626–54626.9 are shown as grey open squares and grey downward arrows. Results from SSC and SSC+EC models are shown as continuous and dashed lines, respectively. The single emission components are indicated by dotted lines [Acciari et al. 2009b].

**Table 9.6:** Parameters of the SSC and SSC+EC models for the SED of W Com on MJD 54624.0 – 54626.0.

| Parameter | Symbol | SSC | SSC+EC |
|---|---|---|---|
| Doppler factor | $\delta$ | 20 | 20 |
| Electron power [erg s$^{-1}$] | $L_{\rm e}$ | $3.4\times10^{44}$ | $5.7\times10^{43}$ |
| Blob radius [cm] | $R_{\rm b}$ | $3\times10^{15}$ | $10^{16}$ |
| Low-energy cut-off | $\gamma_1$ | $9\times10^{3}$ | $8\times10^{3}$ |
| High-energy cut-off | $\gamma_2$ | $2.5\times10^{5}$ | $3\times10^{5}$ |
| Electron injection index | $q$ | 2.55 | 2.55 |
| Magnetic field [G] | $B$ | 0.24 | 0.35 |
| B-field equipartition parameter | $e_{\rm B}$ | $2.3\times10^{-3}$ | 0.32 |
| Electron escape time scale parameter | $\eta$ | 300 | 300 |
| Minimum variability time scale [hr] | $\delta t_{\rm var,min}$ | 1.5 | 5.1 |
| External radiation peak frequency [Hz] | $\nu_{\rm ext}$ | – | $1.5\times10^{14}$ |
| External radiation energy density [erg cm$^{-3}$] | $u_{\rm ext}$ | – | $2.4\times10^{-4}$ |

## 9.4 PG 1553+113

PG 1553+113 was discovered in the Palomar-Green survey of UV-excess stellar objects (Green et al. 1986). It is classified as a BL Lac object based on its featureless spectrum (Miller & Green 1983; Falomo & Treves 1990) and its significant optical variability (Miller et al. 1988). PG 1553+113 is well studied from radio to X-rays and has been the subject of several multifrequency campaigns. In X-rays it has been detected by different observatories, with energy spectra measured by both *Beppo*SAX (Donato et al. 2005) and XMM-*Newton* (Perlman et al. 2005). Based on its spectral energy distribution, PG 1553+113 is classified as a High-frequency peaked BL Lac (Giommi et al. 1995).

PG 1553+113 was firmly detected at very high energy $\gamma$-rays (VHE; E > 100 GeV) by MAGIC at a significance level of 8.8-$\sigma$ above 200 GeV, based on data from April–May 2005 and January–April 2006 (Albert et al. 2007d). Observations with the H.E.S.S. telescope array in 2005 yielded a tentative detection in VHE band, at the level of 4-$\sigma$ (5.3-$\sigma$ using a low energy threshold analysis; Aharonian et al. 2006), which was confirmed later with the combination of the 2005 and 2006 datasets (Aharonian et al. 2008b). Both H.E.S.S. and MAGIC Collaborations reported a soft spectrum with a differential photon index of $\Gamma = 4.0 \pm 0.6$ and $\Gamma = 4.2 \pm 0.3$, respectively. These VHE data were used indipendently to derive an upper limit on the redshift of the source of z < 0.74.

In fact, the redshift of PG 1553+113 is essentially unknown. It was intially determined to be z = 0.36 (Miller & Green 1983), but later this claim was withdrawn (Falomo & Treves 1990). Up to now no emission or absorption lines have been measured despite several observation campaigns with optical instrument. The host galaxies was not resolved in *Hubble Space Telescope* (*HST*) images of PG 1553+113 (Scarpa et al. 2000). However, an ESO-VLT spectroscopic survey of unknown-redshift BL Lac objects suggests for this source a redshift of $z > 0.09$ (Sbarufatti et al. 2006), while the absence of host galaxy detection in further HST images raises this lower limit to z > 0.25 (Treves et al. 2007). On the other hand, the absence of a break in the VHE spectrum can be interpreted as suggesting z < 0.42 (Mazin & Goebel 2007). The possibility of a large redshift is of critical importance to VHE observations due to the absorption of VHE by pair production on the extragalactic background light (EBL).

The logarithmic ratio of its 5 GHz radio flux to its 2 keV X-ray flux has been found to vary from $\log(F_{2\,\mathrm{keV}}/F_{5\,\mathrm{GHz}}) = -4.99$ to –3.88 (Osterman et al. 2006; Rector et al. 2003). Considering that a BL Lac is classified as extreme when it has $\log(F_{2\,\mathrm{keV}}/F_{5\,\mathrm{GHz}}) \geq -4.5$, this high value of this ratio places PG 1553+113 among the most extreme HBLs, together with 1ES 0229+200, H 1426+428 and 1ES 1959+650 (Rector et al. 2003). PG 1553+113 seems to show an optical/UV emission higher than X-ray emission (Tramacere et al. 2007b), a behaviour in

agreement with that expected by an extreme HBL objects.

After the first detection of PG 1553+113 with MAGIC, a multifrequency campaign on this source was conducted in July 2006 (Albert et al. 2009). We performed an extensive campaign on PG 1553+113 between March and April 2008, with optical, X-ray, high-energy (HE) $\gamma$-ray, and very-high-energy (VHE) $\gamma$-ray observations with the KVA, Abastumani, REM, *Rossi*XTE/ASM, AGILE and MAGIC telescopes, respectively. This is the first simultaneous broad-band (i.e., HE+VHE) $\gamma$-ray observation, although the AGILE data allow to estimate only an upper limit of the flux of the source. We present the multiwavelength data collected during this campaign, determine the spectral energy distribution in order to study the emission processes at work in PG 1553+113.

### 9.4.1 Optical and near-IR observations

The KVA (Kungliga Vetenskaps Akademien) telescope is located at the Roque de los Muchachos, in the Canary Islands of La Palma and is operated by the Tuorla Observatory. The telescope is composed of a 0.6m f/15 Cassegrain devoted to polarimetry, and a 0.35m f/11 SCT auxiliary telescope for multicolour photometry. This telescope has been successfully operated remotely since autumn 2003. The KVA is used for optical (*R*-band) support observations during MAGIC observations. Typically, one measurement per night and per source is conducted. Photometric measurements are made in differential mode, i.e. by obtaining CCD images of the target and calibrated comparison stars in the same field of view (Fiorucci & Tosti 1996; Fiorucci et al. 1998; Villata et al. 1998).

Observations at the Abastumani Observatory (Georgia) were performed with the 70 cm meniscus telescope (f/3). The frames were acquired in the Cousins' *R* band and were reduced with the DAOPHOT II package[6]. The source magnitude was derived from differential photometry with respect to a reference star in the same field, which lies $\sim$ 46 arcsec east and $\sim$ 5 arcsec south of PG 1553+113. According to the USNO 2.0 Catalogue (Monet et al. 1998), its magnitude is $R = 13.2$.

REM (Rapid Eye Mount; Zerbi et al. 2004; Covino et al. 2004) is a 60 cm robotic telescope located at the ESO La Silla observatory (Chile). The telescope simultaneously feeds two cameras, one for the near-infrared and one for the optical, by a dichroic. The cameras have imaging capabilities with the NIR ($J, H, K$) and visual large bands ($V, R, I$) filters. REM acquired photometry of PG 1553+113 on 2008 April 18, 25 and May 2 with all available filters. The data reduction followed standard procedures (see e.g. Dolcini et al. 2005). The mean flux of observation is reported in Table 9.9. The NIR magnitudes were calibrated

[6] `http://www.star.bris.ac.uk/ mbt/daophot/`

against the 2MASS catalog. For the SED reconstruction, all magnitudes have been dereddened with the dust IR maps (Schlegel et al. 1998).

### 9.4.2 X-rays observations: RXTE/ASM

The All Sky Monitor (ASM) on board the *Rossi* X-ray Timing Explorer satellite (Levine et al. 1996) consists of three wide angle scanning shadow cameras. The cameras, mounted on a rotating drive assembly can cover almost 70% of the sky every 1.5 hours. The measurements were done between 2008 March 1 and May 31. The mean measured flux of PG 1553+113 is shown in Table 9.9 .

### 9.4.3 HE observations: AGILE

The Gamma-ray Imaging Detector (GRID) on board the AGILE satellite observed PG 1553+113 in three different time intervals: 2008 March 16–21, March 25–30 and April 10–30. The GRID data were analyzed using the AGILE standard pipeline (see Section 4.3.6), with a bin size of $0.25^\circ \times 0.25^\circ$ for E > 100 MeV. Only events flagged as confirmed $\gamma$-rays and not recorded while the satellite crossed the South Atlantic Anomaly were accepted. We also rejected all events with a reconstructed direction within $10^\circ$ from the Earth limb, thus reducing contamination from Earth's $\gamma$-ray albedo.

PG 1553+113, observed at about 50 degrees off-axis with respect to the boresight, was not detected by the GRID at a significance level > 3-$\sigma$ and therefore the 95% confidence level upper limit was calculated. Considering that AGILE has a higher particle background at very high off-axis angles, we calculated also the upper limit selecting only photons with energies greater than 200 MeV in order to minimize the possible contamination at low energies. The log of the AGILE observations and the results of the analysis are reported in Table 9.9. During March–April 2008, the source was substantially off-axis in the field of view of SuperAGILE, the hard X-ray (20–60 keV) imager onboard AGILE.

The HE data reduction results from AGILE are summarized in Table 9.7. The 2-$\sigma$ upper limits obtained by AGILE are consistent with the average flux observed by the *Fermi*-LAT for this source during August–October 2008 (Abdo et al. 2009d). The upper limit obtained in the third time interval has been used for modeling the SED.

### 9.4.4 VHE observations: MAGIC

The MAGIC Telescope (Baixeras et al. 2004; Cortina et al. 2005) is the most recent generation IACT at La Palma, Canary Islands, Spain. Thanks to its low trigger threshold of 50 GeV (25 GeV with a special trigger set up; Albert et

**Table 9.7:** Upper limit at 2-$\sigma$ calculated from AGILE data in three different time intervals.

| Time interval | Energy | U.L. [ph cm$^{-2}$s$^{-1}$] |
|---|---|---|
| March 16-21 | $> 100$ MeV | $56 \times 10^{-8}$ |
| | $> 200$ MeV | $36 \times 10^{-8}$ |
| March 25-30 | $> 100$ MeV | $55 \times 10^{-8}$ |
| | $> 200$ MeV | $28 \times 10^{-8}$ |
| April 10-30 | $> 100$ MeV | $34 \times 10^{-8}$ |
| | $> 200$ MeV | $21 \times 10^{-8}$ |

al. 2008c), MAGIC is well suited for multifrequency observations, together with the satellites operating in the GeV range.

The MAGIC observations for this campaign were carried out on 2008 March 16–18 and April 13, 28–30. The zenith angle of the data set ranges from 18 degree to 36 degree. Observations were performed in wobble mode (Fomin et al. 1994), where the object was observed at 0.4 degree offset from the camera center in opposite directions every 20 minutes. After data rejection based on the standard quality cuts and the trigger rate, 7.18 hours of total effective observation time data was selected.

An automatic analysis pipeline (Dorner at al. 2005; Bretz & Dorner 2008) was used to process the data, which includes the muon calibration (Goebel et al. 2005), and an absolute mispointing correction (Riegel et al. 2005). The charge distribution and arrival time information of the pulses of neighboring pixels was used to suppress the contribution from the night sky background in the shower images (Aliu et al. 2009). Three OFF regions were used to determine the background, providing a scaling factor of 1/3 for the background calculation. The shape and orientation of the shower images were used to discriminate $\gamma$-like events from the overwhelming background. To select the $\gamma$-like events a dynamical cut in Area (Area=$\pi$·WIDTH·LENGTH) versus SIZE (total charge contained in an image) and a cut in $\vartheta$ (angular distance between real source position and reconstructed source position) were applied. More details on the cuts can be found in Riegel & Bretz (2005), and the above mentioned image parameters are described by Hillas (1985).

The reconstructed $\gamma$-ray spectrum is shown in Fig. 9.7. For the spectral reconstruction, looser cuts were applied to ensure that more than 90% of the simulated $\gamma$ photons survived. Varying cut efficiencies between 50% and 95% over the entire energy range were applied to the data in order to check systematic effects of the cut efficiency on the spectral shape (shown as grey area in

Fig. 9.7). Data which has been affected by calima[7] has been corrected following the method described in Dorner et al. (2009).

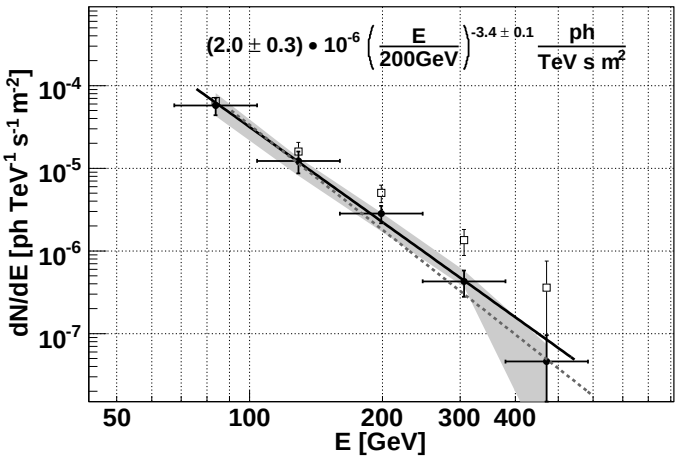


**Figure 9.7:** The MAGIC measured spectrum of PG 1553+113 (filled circles). The $\chi^2_{\rm red}$/d.o.f. of the fit is 1.36/3. The EBL-corrected points are shown as empty squares. The spectrum obtained during the first MAGIC observation is shown in dashed line [Aleksic et al. 2009].

Analyzing the MAGIC data, an excess of 415 $\gamma$-like events, over 1835 normalized background events was found, yielding a significance of 8.0-$\sigma$. The resulting differential VHE spectrum of PG 1553+113, averaged over all observing intervals, is plotted in Fig. 9.7 (filled circles). It can be well described by a power law $\frac{dN}{dE} = F_0\left(\frac{E}{200GeV}\right)^{-\Gamma}$ m$^{-2}$ s$^{-1}$ TeV$^{-1}$, where $F_0$ is the normalization flux at 200 GeV and $\Gamma$ is the photon index, which are given in Table 9.8 . The values obtained during our previous observations (Albert et al. 2007d) are also given.

**Table 9.8:** The $F_0$ and $\Gamma$ of the MAGIC observations during March–April 2008, considering single epochs and the entire period. As a reference also the values obtained during previous MAGIC observations are reported.

| Observation period | $F_0$ [ph TeV$^{-1}$s$^{-1}$m$^{-2}$] | $\Gamma$ |
|---|---|---|
| March–April 2008 | $2.0 \pm 0.3 \times 10^{-6}$ | $3.4 \pm 0.1$ |
| March 2008 | $1.9 \pm 0.4 \times 10^{-6}$ | $3.5 \pm 0.2$ |
| April 2008 | $2.1 \pm 0.4 \times 10^{-6}$ | $3.3 \pm 0.2$ |
| April–May 2005 + January–April 2006 | $1.8 \pm 0.3 \times 10^{-6}$ | $4.2 \pm 0.3$ |

[7]Calima is the sand dust from the Sahara in an air layer between 1.5 km and 5.5 km a.s.l. causing absorption of the Cherenkov light.

The interaction of VHE $\gamma$-rays with the extragalactic background light (EBL; a recent review can be found in Mazin & Raue 2007), leads to attenuation of the VHE $\gamma$-ray flux via $e^+/e^-$ pair production. We computed the deabsorbed (i.e., intrinsic) fluxes using a specific 'low star formation model'of the EBL (Kneiske et al. 2004), assuming a source redshift of z = 0.3. The resulting deabsorbed points are represented as empty squares in Fig. 9.7 .

### 9.4.5 Discussion and summary

The SED of PG 1553+113 during March–April 2008 is shown in Fig. 9.8. The VHE and HE $\gamma$-ray fluxes from MAGIC and AGILE, respectively, are reported. The fluxes and corresponding effective observation frequencies of the other telescopes which contribute to this multifrequency campaign are reported in Table 9.9. The X-ray point, provided by RXTE/ASM, represents the average flux between 2008 March 1 and May 31. The optical *R*-band point, provided by the KVA telescope, is the average flux obtained on March 18 and 19. The flux provided by Abastumani is the average flux of April 1 – May 17 observations. In addition to these data, we also used the NIR flux measured from REM. To assess the soundness of this addition, we checked the optical variability of the source during this period using Abastumani data, and found that the source was essentially stable, with a minimum and maximum values of $\log(\nu F_\nu)$ are $-10.14$ and $-10.02$, respectively. For comparison of the HE flux, we included the average flux detected by *Fermi*-LAT, Flux (E > 100 MeV) = $(8 \pm 1) \times 10^{-8}$ ph cm$^{-2}$ s$^{-1}$ and photon index $\Gamma = 1.7 \pm 0.6$ (Abdo et al. 2009d). Moreover, the average flux in the 14–30 keV energy band obtained from *Swift*/BAT during 39 months of observation (December 2004 – February 2008) is also included, F(14–30 keV) = $(0.97 \pm 0.22) \times 10^{-11}$ erg cm$^{-2}$ s$^{-1}$ (Cusumano et al. 2009).

**Table 9.9:** Effective frequencies, and corresponding fluxes of PG 1553+113 from KVA, Abastumani, REM and RXTE instruments obtained during this campaign.

| Instrument | $\log(\nu$ [Hz]) | $\log(\nu$F($\nu$)) [erg cm$^{-2}$ s$^{-1}$] |
|---|---|---|
| KVA | 14.63 | -10.17 |
| Abastumani | 14.63 | -10.08 |
| REM | 14.38 | -10.33 |
| | 14.27 | -10.34 |
| | 14.13 | -10.38 |
| XTE | 18.03 | -10.3 |

We fit the resulting simultaneous SED with a homogeneous one-zone SSC model. The model assumes that the source is a spherical region of plasma of

radius $R$, moving with a Doppler factor $\delta$ towards the observer at an angle $\theta$ with respect to the line of sight threaded with a uniforming distributed tangled magnetic field of strength $B$. The injected relativistic particle population is described as a broken power law spectrum with normalization $K$, extending from $\gamma_{\rm min}$ to $\gamma_{\rm max}$ with indices $n_1$ and $n_2$ below and above the break Lorentz factor $\gamma_{\rm b}$. By fitting the observed flux with the model, we obtain the following parameters: $\gamma_{\rm min} = 1$, $\gamma_{\rm b} = 3 \times 10^4$, $\gamma_{\rm max} = 2 \times 10^5$, $K = 0.5 \times 10^4$ cm$^{-3}$, $p_1 = 2$, $p_2 = 4.7$, $B = 0.7$ G, $R = 1.3 \times 10^{16}$ cm, and $\delta = 23$. The optical and X-ray flux constrain on the slope of electron energy distribution (EED), while X-ray and VHE spectrum fix the Lorentz factors.

The difference between the 2008 March–April observation and the previous one published in Albert et al. (2007d) is due to flux variation in the X-ray and small variation of the slope of VHE spectrum. Comparing the SED of 2005–2006 with that relative of March–April 2008, Doppler factor (21 and 23, respectively) and the size of emission region ($1.3 \times 10^{16}$ and $1.16 \times 10^{16}$, respectively) are comparable, while the magnetic field is 0.7 G in both cases. The major difference in SED is arising from the difference in EED.

During this campaign, no significant variability of VHE flux is found. The integral flux (E > 200 GeV) during these observations is $(1.3 \pm 0.3) \times 10^{-7}$ cm$^{-2}$ s$^{-1}$, while during the first MAGIC observations the flux was $(1.0 \pm 0.4) \times 10^{-7}$ cm$^{-2}$ s$^{-1}$. The X-ray flux increases by about a factor of two, while the averaged X-ray flux during 39 months of *Swift*/BAT observation agrees with our SED. Optical flux during first MAGIC observation and current observation does not show any significant variability. The *Fermi* bowtie and lowest-energy MAGIC data points together with the model fit indicate a variability at HE or VHE $\gamma$-rays.

Our results suggest that the variability of PG 1553+113 at different frequencies is time dependent: hence, only a simultaneous multifrequency monitoring campaign over a large time span will give more information on the source. Relative to this fact, it is worth mentioning that the AGILE and MAGIC data presented here constitute the first simultaneous broad-band $\gamma$-ray observation (and ensuing SED) of any blazar, though the first simultaneous detection accomplished during the multifrequency campaign of Mkn 421 (Donnarumma et al. 2009a), and the first broad-band $\gamma$-ray spectrum was obtained from PKS 2155-304 (Aharonian et al. 2009) by H.E.S.S. and *Fermi*.

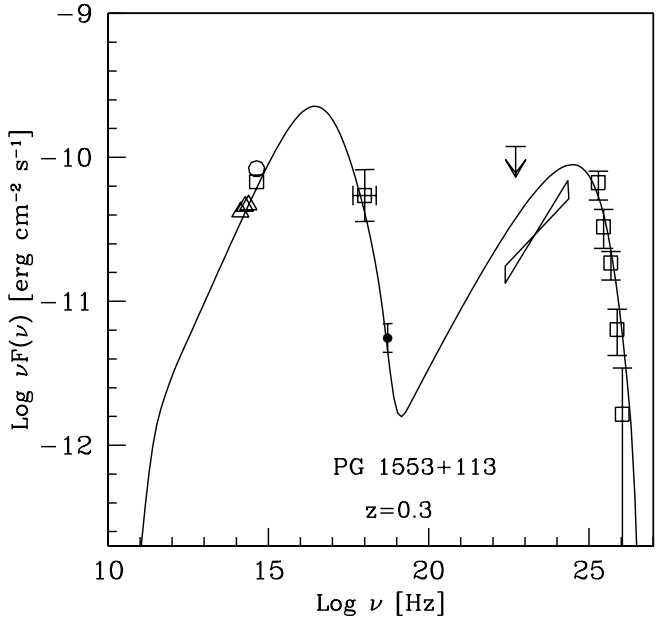


**Figure 9.8:** The average SED of PG 1553+113 measured in March–April 2008. The empty triangles denote the REM data, the open square represents the KVA data, the open circle denotes the Abastumani data, and the open square denotes RXTE/ASM data. The arrow at HE denotes the AGILE upper limit. The empty squares in VHE range are the deabsorbed MAGIC data. We also show the non-simultaneous average flux from *Fermi*-LAT (bowtie) and *Swift*/BAT (small filled circle) [Aleksic et al. 2009].

Chapter 10

# Concluding remarks

Blazars are the most extreme subclass of Active Galactic Nuclei (AGNs), characterized by the emission of strong non-thermal radiation across the entire electromagnetic spectrum, from radio to very high $\gamma$-ray energies. This emission is interpreted as the result of the electromagnetic radiation from a relativistic jet that is viewed closely aligned to the line of sight of the observer, thus causing strong relativistic amplification (Blandford & Rees 1978).

Considering that the large fraction of the total power of blazars is emitted in the $\gamma$-rays, information in this energy band is crucial to study the different radiation models. More than ten years after the EGRET *era*, the AGILE satellite (and subsequently also the *Fermi* satellite) filled the gap in the MeV–GeV band giving further impulse to the study of the high-energy astrophysics phenomena in blazars. However, notwithstanding the importance of the information provided by the $\gamma$-ray observations, correlated multiwavelength studies are the key to achieve a better understanding of the structure of the inner jet, the origin of the seed photons for the inverse Compton process and the emission mechanisms at work in blazars.

In this Thesis I presented the results on multiwavelength studies of the brightest blazars detected by AGILE in $\gamma$-rays (PKS 1510−089, S5 0716+714, 3C 454.3, 3C 279, 3C 273, Mrk 421, W Comae, and PG 1553+113), together with the data simultaneously collected from other observatories such as *Spitzer*, *Swift*, RXTE, *Suzaku*, INTEGRAL, MAGIC, VERITAS, as well as radio-to-optical coverage by means of the GASP project of the WEBT and the REM telescope. This wide multiwavelength coverage gave me the opportunity to study the correlated variability among the emission at different frequencies and build time-resolved spectral energy distribution from radio to $\gamma$-rays, in order to investigate in detail the emission mechanisms of the blazars, uncovering in some cases a

more complex behaviour with respect to the standard emission models. In this last Chapter, I briefly focus on the most interesting results obtained during my studies.

The first general remark is that, because of the wide field of view of its Gamma-Ray Imaging Detector, in 2.5 years of operation AGILE has simultaneously monitored a large number of known and candidate $\gamma$-ray blazars and the number of intense $\gamma$-ray emitting blazars detected is low, and no new $\gamma$-ray blazars in flare were observed. During the EGRET *era* 9 blazars were observed with a flux higher than $100 \times 10^{-8}$ photons cm$^{-2}$ s$^{-1}$ and only 3C 279 (Hartman et al. 2001), PKS 0528+134 (Mukherjee et al. 1996) and PKS 1622−297 (Mattox et al. 1997) showed really high $\gamma$-ray fluxes. The AGILE results confirm the idea that only a special class of blazars show significant $\gamma$-ray activity on timescales of year/decade. Also the preliminary results from the first months of *Fermi* operation seem to show not only that the number of significative $\gamma$-ray emitters is low, but also that, as noted by AGILE, at a distance of years almost always the same objects seem to show intense $\gamma$-ray flares. What are the peculiar properties of these objects, if any, is still not completely clear. Recent studies in radio of a subsample of the blazars detected by *Fermi*-LAT in the first three months showed that the $\gamma$-ray emitter blazars have faster apparent jet speeds (Lister et al. 2009), wider apparent opening angles (Pushkarev et al. 2009), and higher VLBI brightness temperatures (Kovalev et al. 2009). Future investigations of a larger sample detected in $\gamma$-rays by *Fermi* and AGILE could give firm conclusion on it.

Among the intense $\gamma$-ray flares of blazars detected by AGILE, the two bright flares observed by the Intermediate BL Lac S5 0716+714 during September and October 2007 ($\sim 200 \times 10^{-8}$ photons cm$^{-2}$ s$^{-1}$) represent not only one of the highest $\gamma$-ray flux observed by a BL Lac object but offered us the possibility to test the maximum power extractable from a roting supermassive black hole (SMBH) via the *pure* Blandford-Znajek (BZ) mechanism (Blandford & Znajek 1977). In fact, because of the high power of the source and lack of signs for ongoing accretion or surrounding gas, detecting $\gamma$-ray emission from such sources provides a direct probe of the emission mechanisms and the underlying powerhouse. The BZ mechanism for electrodynamical energy extraction from a Kerr black hole spun up to maximal rotation by past accretion episodes constitutes a natural benchmark for the power of the jet. The recent estimation of the redshift of S5 0716+714 and the simultaneous observations in optical, X-rays and $\gamma$-rays allowed us to modeling the SED of these two flaring episodes and estimate the energetics of the source. Recently, Nilsson et al. (2008) pinpointed the host galaxy of S5 0716+714 and derived a redshift of $z = 0.31 \pm 0.08$. For this host galaxy a $M_{BH} \sim 5 \times 10^8$ should accord with the fundamental plane of BL Lacs (Falomo et al. 2003). The total jet power calculated for the two flares of the source observed by AGILE, $P_{tot,\,flare} = (3.5 \pm 1.0) \times 10^{45}$ erg s$^{-1}$, slightly

exceed the jet power provided by the BZ mechanism for the black hole mass previously estimated, assuming a conservative value of $B$ ($10^{-4}$ G): $P_{BZ} \simeq 2 \times 10^{45}\ M_9$ erg s$^{-1}$. This result confirms the extreme energetics of S5 0716+714 during these flares and challenges the mechanism of energy extraction from a rotating SMBH.

Moreover, a one-zone synchrotron self Compton (SSC) model fails to reproduce the SED of the two flares occurred on 11 September and 23 October 2007, built with AGILE, *Swift*, and GASP-WEBT simultaneous observations. The quadratic dependence observed between the synchrotron and IC fluxes ruled out an external Compton contribution, whereas two SSC components reproduces the complex variability observed, suggesting the presence of a fast variable component responsible for the optical, soft X-ray and $\gamma$-ray emission and a slow variable component responsible for the radio and hard X-ray emission. This is in agreement also with the different variability observed during the *Swift* monitoring of the source in October–November 2007, during which strong variability was observed in soft X-rays, moderate variability at optical/UV frequencies and a constant behaviour in hard X-rays.

The modeling of the SEDs of S5 0716+714 indicated as, even if the broad band emission appears in agreement with the SSC paradigm, a more complex model with two SSC components is needed to interpret our data. The case of S5 0716+714 is not unique among the BL Lacs, also for the multifrequency observation of Mrk 421 and W Comae in June 2008 a one-zone SSC model seems to be a good representation of the broad band spectrum, but the observations collected during the multiwavelength campaigns seem to open to more complex interpretations of the data. In particular, the optical and X-ray light curves of Mrk 421 during June 2008 show different variability: a decreasing trend of the optical emission with superimposed spikes of emission, whereas several emission peaks lasting few days without a general trend is observed in X-rays. Although the X-rays/very high energy (VHE) $\gamma$-rays correlation seems to confirm the interpretation within the framework of the SSC model, the different behaviour at optical and X-rays suggests a more complex scenario, in which the optical and X-ray radiation are produced in different regions of a helical jet, with the inner jet region that produces the X-rays and it is partially transparent to the optical radiation, whereas the outer region produces only the low-frequency emission. This implies not only a different variability, due to the different opacity of the two regions, but also a different flux enhancement, due to the fact that the different viewing angle of the two regions with respect to the observer leads to a different Doppler boosting.

For W Comae instead a simple SSC interpretation is challenged by the request in the modeling of the SED of a equipartition parameter far from unity. Even if there is not a physical justification for a source component being close to the

equipartition, considering that the equipartition corresponds to the minimum total energy requirements, a value far to the equipartition could involve an increase of the energy requirements and therefore it is disadvantageous, in favour of the addition of an external Compton component with seed photons originated from the dusty torus that could explains also the slightly near-IR bump observed in the SED of the source.

The possibility to build time-resolved SEDs from radio to $\gamma$-rays gave us the opportunity to challenge the emission mechanism models also for FSRQs, and in particular the long term monitoring of 3C 454.3 over 18 months has been the best case for test the emission models in FSRQs in different epochs (and therefore different activity states). The modeling of the SEDs collected during the several multiwavelength campaigns organized by AGILE on 3C 454.3 confirmed the previous findings that the dominant emission mechanism in $\gamma$-rays, for this object as well as for the FSRQs in general, is the inverse Compton scattering of external photons from Broad Line Region (BLR) scattering off the relativistic electrons in the jet, but even if true for most of the activity states it is not an assumption valid for all the states observed by AGILE. In fact, 3C 454.3 during the December 2007 campaign was observed in a different state with respect to the other observations performed by AGILE. In particular, with respect to the observation of November 2007 optical and UV fluxes appeared lower of a factor 2, with the synchrotron radiation, well defined by the mid-Infrared *Spitzer* data and the GASP-WEBT optical data, peaked at frequency 5–10 times lower than in November. Despite the softer synchrotron peak, $\gamma$-ray data showed the persistence of a hard peak at $\sim$ 1 GeV, similar to the state observed by AGILE in July 2007 and November 2007. We attempted to fit the SEDs with a one-zone SSC model, adding the contribution of external seed photons coming from an accretion disk and a BLR. In order fit the synchrotron peak as well as the *Swift* soft X-ray data a low break Lorentz factor ($\gamma_{\rm break} \sim 350$) is required, implying a peak of the contribution of the external Compton from the BLR at $h\nu \simeq h\nu_{\rm soft}\Gamma\gamma_{\rm b}^2\delta/(1+z) \sim 10^8$ eV. This is in contrast with the hardness of the $\gamma$-ray spectrum up to 1 GeV observed by AGILE. Therefore, a further contribution is needed to model the $\gamma$-ray data in the SEDs of 3C 454.3 of December 2007 and the best candidate is a hot corona with temperature T = $10^6$ K and luminosity $L_{\rm cor} = 10^{45}$ erg s$^{-1}$, distant 0.5 pc from the blob.

Another example of the fact that not in all the activity states of FSRQs the main source of seed photons for IC is the accretion disk emission reprocessed by the BLR is provided by the AGILE detection of an intense $\gamma$-ray flare by 3C 279 during July 2007. In that case, the soft $\gamma$-ray spectrum observed by AGILE during a high $\gamma$-ray state could be an indication of the low accretion state of the disk some months before the AGILE observations, suggesting a dominant contribution in $\gamma$-rays of the external Compton scattering of direct disk radiation

compared to the external Compton scattering of the BLR. As a matter of fact, a strong minimum in the optical band was detected by REM two months before the AGILE observations and the reduction of the activity of the disk causes the decrease of the photon seed population produced by the disk and then a deficit of the external Compton of the photons reprocessed by the BLR, an effect delayed by the light travel time required to the photons to go from the inner disk to the BLR.
Therefore, from the modeling of the different SEDs of BL Lacs and FSRQs observed by AGILE seems to emerge that the SSC and the EC frameworks, respectively, are good approximation for describing on average the high activity states of the two flavours of blazars, but going into details of the single observation more complex scenarios sometimes are requested. Furthermore, most of the previous multifrequency observations of blazars, especially those that involve $\gamma$-ray observations were triggered by a high state of the source, the study of low/quiescient states of these sources is still an unexplored area. The investigation of the $\gamma$-ray emission from blazars, together with simultaneous observations from radio to TeV energy bands, during low/quiescient activity states could open a new window to further correlated investigations of the blazars over the whole electromagnetic spectrum, comparing the behaviour and the physical parameters of those observations with those obtained during flaring states in order to reach a deeper insight on the jet structure and the emission mechanisms at work in blazars.

Moreover, long-term monitoring of blazars give us the possibility to look into the time scale along which the activity state of blazars varies in the different parts of the spectrum and to observe these blazars during different emission states: not only the most intense activity state of the source, during which the jet emission is dominant but also during the faint states in which is likely to observe also features usually overwhelmed by the non-thermal emission.

3C 454.3 and PKS 1510−089 have been the sources monitored over the longer timescales by AGILE. These blazars showed high variability in $\gamma$-rays with several flaring episodes, even if the overall behaviour of the two blazars seems to be different. A diminishing trend in $\gamma$-ray flux intensity between July 2007 and January 2009 was observed for 3C 454.3, with a decreasing of the total power of the jet. A diminishing trend of the flux with time is observed from near-IR to $\gamma$-rays, the flux at 15 GHz instead increases, although no new jet component in radio seems to be detected. This different behaviour of the light curves at different frequencies could be interpreted by a changing of the jet geometry between 2007 and 2008. Considering this regular diminishing trend of the $\gamma$-ray activity observed over almost two years it is even more surprising the extraordinary flare of 3C 454.3 observed by AGILE in early December 2009, when the source became the brightest source in the $\gamma$-ray sky for at least one week, reach-

ing the highest flux ever observed by a blazar in $\gamma$-rays ($\sim 2000 \times 10^{-8}$ photons $cm^{-2}$ $s^{-1}$).

PKS 1510−089 instead in the last two years exhibited rapid flares at different time detected by AGILE and *Fermi*, and also during the extraordinary activity of March 2009 different flaring events seems to be due to the overlapping of subsequent episodes, suggesting a complex structure of the flaring episodes in this source. Moreover, after the $\gamma$-ray flares of March 2008 and March 2009 a significant increase of the flux density was observed also at high radio frequencies, suggesting that a common mechanism produces the flaring episode at radio and $\gamma$-rays. Notwithstanding the possible difference in the long-term behaviour, a hint of spectral evolution in $\gamma$-rays is present in both the source, with a harder-when-brighter behaviour during the most intense flaring episodes, a feature already observed by EGRET in 3C 279 and PKS 0528+134, but not confirmed as general behaviour of the blazars.

Even if the study of the correlation between optical and $\gamma$-ray emission in blazars has always been very difficult, because a common long-term monitoring is necessary in order to obtain firm results, the long-term monitoring of 3C 454.3 provided by GASP-WEBT and AGILE in optical as well in $\gamma$-ray energy bands offered the opportunity to investigate this correlation by means of the Discrete Correlation Function (DCF; Edelson et al. 1998). In particular during the longer continuos observation period, November–December 2007, the corresponding DCF shows a maximum of $\sim 0.38$ for a null time lag. However, calculating the centroid we obtained a time lag of –0.42 days between $\gamma$-ray and optical band, i.e. a delay of the $\gamma$-ray emission of about 10 hours with respect to the optical emission. This result is in agreement with what found if the November or December 2007 dataset is analyzed separately; moreover, the time lag estimated is in agreement with what found for 3C 454.3 by Bonning et al. (2009a) analyzing the public $\gamma$-ray data of *Fermi*-LAT and the optical SMARTS data. However, it is interesting to note that the correlation between the emission in the two energy bands is not strong, suggesting that, even if during the high activity state the signs of the jet activity is visible in both the energy domains and at a bright synchrotron state usually correspondes a bright $\gamma$-ray state with an overall correlation, some differences can be observed in detailed comparison on long timescale.

On the other hand, the comparison of the $\gamma$-ray and optical light curves of PKS 1510−089 during March 2009 seems to show a possible time lag of 1–2 days between the optical and $\gamma$-rays, suggesting one more time a more complex behaviour for the optical/$\gamma$-ray correlation, especially for FSRQs, where not only the synchrotron emission but also the thermal disk emission contribute to the optical emission observed. The almost continuos and contemporaneous observation of all the $\gamma$-ray sky with the AGILE and *Fermi* satellites is assur-

ing a formidable opportunity to monitor several blazars at the same time and together with the radio-to-optical observations from ground-based telescopes (such as GASP-WEBT, SMARTS, REM, the F-GAMMA projects, etc.) will allow a long and deep monitoring of a large number of sources and finally a detailed study of correlated variability at different frequency, up to now limited to only few objects.

The broad band coverage provided by the multifrequency campaigns organized by AGILE gave me also the opportunity to investigate the presence of Seyfert-like features in some blazars. In particular, optical/UV observations of PKS 1510−089 in March 2008 and March 2009 showed the presence in the broad band spectrum of the source of two thermal features: the little blue bump, due to the Fe II, Mg II and Balmer continuum produced by the BLR, and the big blue bump, due to the accretion disk emission. The fact that the synchrotron component of PKS 1510−089 usually peaks around $10^{13}$ Hz (see Bach et al. 2007; Nieppola et al. 2008) allow us to observe these thermal features in this source. However, during the huge $\gamma$-ray flare of PKS 1510−089 of 25–26 March 2009 the radio-to-UV SED seems to show a flat spectrum in the optical/UV, suggesting the presence of the synchrotron emission in this part of the spectrum and therefore a shift of the synchrotron peak. In that case, the increase of the synchrotron emission leads to the decrease of the evidence of the little and big blue bumps in the spectrum of PKS 1510−089. A significative shift of the synchrotron peak seems to be a behaviour more common in HBLs with respect to FSRQs such as PKS 1510−089. Interestingly this is not the only behaviour typical of HBLs observed in PKS 1510−089. In fact, during the observations of March 2008 (and partially also in March 2009) a harder-when-brighter behaviour was observed in its X-ray spectrum. Usually in FSRQs as PKS 1510−089 only little variability is observed on short time scales from hours to days, and also on longer timescales the X-ray spectral shape is almost constant with only small variations. We interpreted the spectral evolution observed during the *Swift* observations of March 2008 in just two days, soon after the rapid $\gamma$-ray flaring episode, as another hint of the rapid change in activity by this source likely due to the change in contribution of one of the two components that contributes to the X-ray spectrum, the SSC and EC components, and therefore to an indication of different variability of this two components.

To conclude, as described in my Thesis, the blazars are a very intruiguing class of objects that shows a variety of peculiar behaviour that immediately attracted the attention of astrophysics around the world. However, the studies of blazars were always made difficult by the impossibility to obtain detailed observation of these objects over the entire electromagnetic spectrum. In particular, the $\gamma$-ray domain remained inaccessible for over 10 years after the end of the EGRET experiment, depriving us of important information for understanding

the emission mechanisms at work in the blazars. Finally, with two $\gamma$-ray satellites in orbit a new window on these sources is now opened, not only for the observations in $\gamma$-rays but also for further coordinated investigations of blazars over the whole electromagnetic spectrum. As some results of this Thesis show, the behaviour of blazars could be more complex of that expected in the canonical SSC and EC frameworks, but the key to substantially improve the understanding on location, size, structure and dynamics of the emitting regions and on particle acceleration mechanisms in blazars are the simultaneous and broad band multi-frequency studies on the largest possible number of objects. Actually we have the opportunity to involve together a great number of ground-based and space-born observatories. It will allow us to expand the number of sources studied and the amount of information on them, finally shedding light on most of the mysteries of this exciting class of objects. What you have read here, probably, is just the beginning.

# List of Figures

# List of Tables

Appendix A

# List of my publications concerning the Ph.D. Thesis

## A.1 Peer reviewed publications

- **F. D'Ammando**, G. Pucella, C. M. Raiteri, et al., *AGILE detection of a rapid gamma-ray flare from the blazar PKS 1510-089 during the GASP-WEBT monitoring*, A&A, 508, 181 (2009)

- S. Vercellone, **F. D'Ammando**, V. Vittorini, et al., *Multiwavelength Observations of 3C 454.3. III. Eighteen Months of Monitoring of the "Crazy Diamonds"*, submitted to ApJ (2009)

- A. Giuliani, **F. D'Ammando**, S. Vercellone, et al., *AGILE observation of a gamma-ray flare from the blazar 3C 279*, A&A, 494, 509 (2009)

- A. W. Chen, **F. D'Ammando**, M. Villata, et al., *AGILE detection of variable $\gamma$-ray activity from the blazar S5 0716+714 in September-October 2007*, A&A, 489, L37 (2008)

- G. Pucella, V. Vittorini, **F. D'Ammando**, et al., *AGILE detection of intense gamma-ray emission from the blazar PKS 1510-089*, A&A, 491, L21 (2008)

- I. Donnarumma, G. Pucella, V. Vittorini, **F. D'Ammando**, et al., *Multiwavelength observations of 3C 454.3. II. The AGILE 2007 December campaign*, ApJ, 707, 1115 (2009)

## Appendix A. List of my publications concerning the Ph.D. Thesis

- L. Pacciani, I. Donnarumma, V. Vittorini, **F. D'Ammando**, et al., *High energy variability of 3C 273 during the AGILE multiwavelength campaign of December 2007 - January 2008*, A&A, 494, 49 (2009)

- A. Paggi, F. Massaro, V. Vittorini, A. Cavaliere, **F. D'Ammando**, F. Vagnetti, M. Tavani, *SSC radiation in BL Lac sources, the end of the tether*, A&A, 504, 821 (2009)

- S. Vercellone, A. W. Chen, V. Vittorini, A. Giuliani, **F. D'Ammando**, et al., *Multiwavelength observations of 3C 454.3. I. The AGILE 2007 November campaign on the Crazy Diamond*, ApJ, 690, 1018 (2009)

- I. Donnarumma, V. Vittorini, S. Vercellone, E. Del Monte, M. Feroci, **F. D'Ammando**, et al., *The June 2008 flare of Markarian 421 from optical to TeV energies*, ApJ, 691, L13 (2009)

- V. Vittorini, M. Tavani, A. Paggi, ..., **F. D'Ammando**, et al., *Powerful high energy emission of the remarkable BL Lac object S5 0716+714*, ApJ, 706, 1433 (2009)

- V. Acciari, the VERITAS Collaboration, ..., **F. D'Ammando**, et al., *Multiwavelength observations of a TeV-Flare from W Comae*, ApJ, 707, 612 (2009)

- H. Anderhub, the MAGIC Collaboration, S. Vercellone, I. Donnarumma, **F. D'Ammando**, M. Tavani, *MAGIC upper limits to the VHE gamma-ray flux of 3C454.3 in high emission state*, A&A, 498, 83 (2009)

- P. Giommi, S. Colafrancesco, S. Cutini, ..., **F. D'Ammando**, et al., *AGILE and Swift simultaneous observations of the blazar S5 0716+714 during the bright flare of October 2007*, A&A, 487, L49 (2008)

- C. M. Raiteri, M. Villata, W. P. Chen, ..., **F. D'Ammando**, et al., *The high activity of 3C 454.3 in autumn 2007. Monitoring by the WEBT during the AGILE detection*, A&A, 485, L17 (2008)

- S. Vercellone, A. W. Chen, A. Giuliani, ..., **F. D'Ammando**, et al., *AGILE detection of a strong gamma-ray flare of the blazar 3C 454.3*, ApJ, 676, L13 (2008)

- J. Aleksic, the MAGIC Collaboration, ..., **F. D'Ammando**, et al., *Simultaneous multi-frequency observations of the unknown redshift blazar PG 1553 +113 in March–April 2008*, submitted to A&A (2009)

## A.2 Proceedings

- **F. D'Ammando**, S. Vercellone, I. Donnarumma, et al., *Multiwavelength observations of the gamma-ray blazars detected by AGILE*, Proceedings of the 1st Roman Young Researchers Meeting, 2009 July 21, Roma, Italy [arXiv:0912.2558]

- **F. D'Ammando**, C. M. Raiteri, M. Villata, et al., *Not only once: the amazing gamma-ray activity of the blazar PKS 1510−089*, to be published in ASP Conference Series, Proceedings of the conference "Accretion and Ejection in AGN: a Global View", 2009 June 22-26, Como, Italy [arXiv:0910.0966]

- **F. D'Ammando**, S. Vercellone, I. Donnarumma, et al., *Blazars: the gamma-ray view of AGILE*, Proceedings of the "Recontres de Moriond: Very High Energy Phenomena in the Universe", 2009 February 1-8, La Thuile, Italy [arXiv:0905.0253]

- **F. D'Ammando**, A. W. Chen, S. Vercellone, et al., *AGILE detection of variable gamma-ray activity from the intermediate BL Lac S5 0716+714*, Proceedings of the "8th National Conference on AGN", 2008 May 19-22, Torino, Italy

- **F. D'Ammando**, A. W. Chen, M. Villata, et al., *AGILE detection of variable gamma-ray activity from the blazar S5 0716+714 during September-October 2007*, Proceedings of Science, Proceedings of "Workshop on Blazar Variability across the Electromagnetic Spectrum", 2008 April 22-25, Palaiseau, France

- M. Marisaldi, **F. D'Ammando**, S. Vercellone, et al., *AGILE and blazar studies*, Proceedings of the "31th International Cosmic Ray Conference", 2009 July 7-15, Lodz, Poland [arXiv:0906.1451]

- L. Pacciani, **F. D'Ammando**, I. Donnarumma, et al., *AGILE detection of 3C 273 and 3C 279*, Proceedings of the "8th National Conference on AGN", 2008 May 19-22, Torino, Italy

- I. Donnarumma, L. Pacciani, V. Vittorini, **F. D'Ammando**, et al., *Joint INTEGRAL and AGILE observations of FSRQs*, Proceedings of Science, Proceedings of the "7th INTEGRAL Workshop", 2008 September 8-11, Copenaghen, Denmark

- S. Vercellone, I. Donnarumma, G. Pucella, **F. D'Ammando**, *AGILE results on gamma-ray loud Flat Spectrum Radio Quasars observations*, Proceedings of the "8th National Conference on AGN", 2008 May 19-22, Torino, Italy

- L. Pacciani, I. Donnarumma, V. Vittorini, **F. D'Ammando**, et al., *AGILE observation of gamma ray variability of the bright blazar 3C 273 during the MWL campaign of Dec 2007 - Gen 2008*, Proceedings of Science, Proceedings of "Workshop on Blazar Variability across the Electromagnetic Spectrum", 2008 April 22-25, Palaiseau, France

- S. Vercellone, I. Donnarumma, A. Bulgarelli, A. W. Chen, **F. D'Ammando**, et al., *The "Crazy Diamond" (and other blazars)*, Proceedings of the "Science with the new generation of high energy gamma-ray experiments: Bridging the Gap Between GeV and TeV", AIP Conference Proceedings, Vol. 1112, 121 (2008)

- S. Vercellone, I. Donnarumma, A. Bulgarelli, A. W. Chen, **F. D'Ammando**, et al., *AGILE and gamma-ray blazars: the Crazy Diamonds and other gems*, Proceedings of the "4th International Meeting on High Energy Gamma-Ray Astronomy", AIP Conference Proceedings, Vol. 1085, 443 (2008)

- N. Mankuzhyil, D. Dorner, E. Prandin, M. Persic, E. Pian, **F. D'Ammando**, S. Vercellone, *Simultaneous multi-frequency observation of PG 1553+113*, Proceedings of the "31th International Cosmic Ray Conference", 2009 July 7-15, Lodz, Poland [arXiv:0907.0740]

## A.3 Astronomer's Telegrams

- **F. D'Ammando**, M. Perri, A. Tramacere, N. Gehrels, E. Hoversten, H. Krimm, *Swift/XRT follow-up confirms the flaring activity of Mrk 421*, ATel 2295

- **F. D'Ammando**, N. Gehrels, E. Hoversten, P. Romano, S. Vercellone, *Swift detection of a bright X-ray flare from OJ 287*, ATel 2267

- **F. D'Ammando**, H. Krimm, P. Romano, S. Vercellone, *Swift follow-up observations of the blazar PKS 1510-089 after a high optical flare*, ATel 2047

- **F. D'Ammando**, S. Vercellone, M. Tavani, et al., *AGILE detection of the flaring gamma-ray blazar PKS 1510-089*, ATel 1957

- **F. D'Ammando**, A. Bulgarelli, S. Vercellone, et al., *AGILE detection of a gamma-ray source coincident with Blazar PKS 1510-08*, ATel 1436
- T. Sakamoto, **F. D'Ammando**, N. Gehrels, et al., *Swift/XRT observations of a huge flare from 3C 454.3*, ATel 2329
- S. Vercellone, **F. D'Ammando**, E. Striani, et al., *Swift detection of an X-ray transient possibly associated with IGR J17354-3255*, ATel 2019
- S. Vercellone, **F. D'Ammando**, G. Pucella, et al., *AGILE detection of a gamma-ray re-brightening of the blazar PKS 1510-089*, ATel 1976
- G. Pucella, **F. D'Ammando**, M. Tavani, et al., *AGILE detection of a persistent and very intense gamma-ray flaring state of the blazar PKS 1510-089*, ATel 1968
- I. Donnarumma, **F. D'Ammando**, L. Pacciani, et al., *Renewed gamma ray activity of 3C 454.3 detected by AGILE*, ATel 1545
- V. Vittorini, I. Donnarumma, **F. D'Ammando**, et al., *Blazar 3C 454.3 in gamma-ray high state: new AGILE detection*, ATel 1581
- G. Pucella, M. Tavani, **F. D'Ammando**, et al., *AGILE detection of day-to-day gamma-ray variability from Blazar 3C 454.3*, ATel 1300
- C. Pittori, F. Verrecchia, S. Vercellone, **F. D'Ammando**, et al., *AGILE detection of continued gamma-ray activity of the blazar 3C 454.3*, ATel 1634
- E. Striani, F. Verrecchia, C. Pittori, M. Tavani, **F. D'Ammando**, et al., *AGILE detection of the gamma-ray blazar PKS 1830−211*, ATel 2242
- S. Vercellone, M. Fiocchi, E. Pian, ..., **F. D'Ammando**, et al., *INTEGRAL/IBIS observation of the blazar 3C 454.3 during the decaying phase of the gamma-ray super-flare*, ATel 2344
- E. Striani, S. Vercellone, F. Verrecchia, ..., **F. D'Ammando**, et al., *AGILE detects an extraordinary gamma-ray activity from the FSRQs 3C 454.3*, ATel 2326
- E. Striani, S. Vercellone, F. Verrecchia, ..., **F. D'Ammando**, et al., *AGILE detects intense and prolonged gamma-ray activity from the FSRQs 3C 454.3*, ATel 2322

## Appendix A. List of my publications concerning the Ph.D. Thesis

- A. Bulgarelli, F. Gianotti, M. Trifoglio, ..., **F. D'Ammando**, et al., *AGILE confirms high gamma-ray state of GB6 B1310+4844*, ATel 2310
- D. Gasparrini, F. Verrecchia, C. Pittori, ..., **F. D'Ammando**, et al., *AGILE detection of new flaring activity from blazar 3C 454.3*, ATel 1592
- C. Pittori, S. Cutini, D. Gasparrini, ..., **F. D'Ammando**, et al., *AGILE detection of the blazar Mrk 421*, ATel 1583
- F. Verrecchia, D. Gasparrini, S. Cutini, ..., **F. D'Ammando**, et al., *AGILE detection of the blazar W Comae in the gamma-ray energy band*, ATel 1582
- E. Costa, E. Del Monte, I. Donnarumma, ..., **F. D'Ammando**, et al., *Super-AGILE detects enhanced hard X-ray emission from Mkn 421*, ATel 1574
- A. W. Chen, S. Vercellone, A. Giuliani, ..., **F. D'Ammando**, et al., *AGILE detection of a gamma-ray source coincident with Blazar 3C 454.3*, ATel 1278
- A. Bulgarelli, S. Vercellone, A. Chen, ..., **F. D'Ammando**, et al., *AGILE detection of a gamma-ray source off the Galactic Plane*, ATel 1199
- A. Bulgarelli, A. Chen, S. Vercellone, ..., **F. D'Ammando**, et al., *AGILE pointing at 3C 454.3: end of observations and preliminary results*, ATel 1167
- S. Vercellone, A. Chen, A. Giuliani, ..., **F. D'Ammando**, et al., *AGILE gamma-ray detection of the Blazar 3C 454.3*, ATel 1160

# Bibliography

[1] Abdo, A. A., et al. 2009a, ApJ, 707, 55

[2] Abdo, A. A., et al. 2009b, ApJS, 183, 46

[3] Abdo, A. A., et al. 2009c, ApJ, 699, 31

[4] Abdo, A. A., et al. 2009d, ApJ, 700, 597

[5] Abdo, A. A., et al. 2009e, ApJ, 699, 817

[6] Abramowicz, M. A., Igumenshchev, I., Quataert, E., et al. 2002, ApJ, 565, 1101

[7] Acciari, V. A., et al. 2008a, ApJ, 679, 1427

[8] Acciari, V. A., et al. 2008b, ApJ, 684, L73

[9] Acciari, V. A., et al. 2008c, ApJ, 695, 1370

[10] Acciari, V. A., et al. 2009a, ApJ, 693, L104

[11] Acciari, V. A., et al. 2009b, ApJ, 707, 612

[12] Agudo, I., Krichbaum, T. P., Ungerechts, H., et al. 2006, A&A, 456, 117

[13] Aharonian, F. 2000, NewA, 5, 377

[14] Aharonian, F., et al. 2001, A&A, 370, 112

[15] Aharonian, F., et al. 2006, Nature, 440, 1018

[16] Aharonian, F., et al. 2007, ApJ, 664, L71

[17] Aharonian, F., Buckley, J., Kifune, T., and Sinnis, G. 2008a, Rep. Prog. Physics, 71, 1

[18] Aharonian, F., et al. 2008b, A&A, 477, 481

[19] Aharonian, F., et al. 2009, ApJ, 696, L150

[20] Albert, J., et al. 2006, ApJ, 648, L105

[21] Albert, J., et al. 2007a, ApJ, 667, L21

[22] Albert, J., et al. 2007b, ApJ, 666, L17

[23] Albert, J., et al. 2007c, ApJ, 669, 862

[24] Albert, J., et al. 2007d, A&A, 654, 119

[25] Albert, J., et al. 2008a, Science, 320, 1752

[26] Albert, J., et al. 2008b, NIMPA, 588, 424

[27] Albert, J., et al. 2008c, ApJ, 674, 1037

[28] Albert, J., et al. 2009, A&A, 493, 467

[29] Aleksic, J., et al. 2009, submitted to A&A [arXiv:0911.1088]

[30] Aliu, E., et al. 2009, Astropart. Phys., 30, 293

[31] Aller, M. F., Aller, H. D., & Hughes, P. A. 1996, ASP Conf. Ser. 110, Proc. of Blazar Continuum variability, ed. Miller, Webb, & Noble, 193

[32] Aller, M. F., et al. 1997, in American Institute of Physics Conference Series, Vol. 410, Proceedings of the Fourth Compton Symposium, ed. C. D. Dermer, M. S. Strickman, & J. D. Kurfess, 1423

[33] Aller, M. F., et al. 2003, ApJ, 586, 33

[34] Anderhub, H., et al. 2009a, A&A, 498, 83

[35] Anderhub, H., et al. 2009b, ApJ, 704, L129

[36] Antonucci, R. R. J., & Miller, J. S. 1985, ApJ, 297, 621

[37] Antonucci, R. 1993, Annual Review A&A, 31, 473

[38] Arnaud, K. A. 1996, 'Astronomical Data Analysis Software and Systems V', eds. Jacoby G. and Barnes J., ASP Conf. Series, 101, 17

[39] Atwood, B., et al. 2009, ApJ, 697, 1071

[40] Axford, W. I., Leer, E., & Skadron, G. 1977, Proc. 15 ICRC (Budapest), 11, 132

[41] Bach, U., Krichbaum, T. P., Ros, E., et al. 2005, A&A, 433, 815

[42] Bach, U., Raiteri, C. M., Villata, M., et al. 2007, A&A, 464, 175

[43] Baixeras, C., et al. 2004, Nucl. Instrum. Meth. A, 518, 188

[44] Balbus, S. A., and Hawley, J. F. 2002, ApJ 573, 749

[45] Balonek, T. 2005, vsnet -alert 8383 and 8405

[46] Barbiellini, G., et al. 2001, Amer. Inst. Phys. Conf. Series, Vol. 587, Gamma 2001: Gamma-Ray Astrophysics, ed. S. Ritz, N. Gehrels, & C. R. Shrader, 754

[47] Barthelmy, S. D., Barbier, L. M., Cummings, J. R., et al. 2005, Space Science Reviews, 120, 143

[48] Bassani, L., Landi, R., Malizia, A., et al. 2007, ApJ, 669, L1

[49] Bednarek, W. 1993, ApJ, 402, 29

[50] Begelman, M. C. 1979, MNRAS, 187, 237

[51] Begelman, M. C, Blandford, R. D., & Rees, M. 1984, RvMP, 56, 255

[52] Begelman, M. C., & Sikora, M. 1987, ApJ, 322, 650

[53] Bell, A. R., 1978, MNRAS, 182, 147

[54] Beloborodov, A. M. 1999, in ASP Conf. Ser. 161: High Energy Processes in Accreting Black Holes, 295

[55] Bessell, M. S., Castelli, F., & Plez, B. 1998, A&A, 333, 231

[56] Biermann, P. L., Duerbeck, H., Eckart, A., et al. 1981, ApJ, 247, L53

[57] Biermann, P. L., Chirvasa, M., Falcke, H., et al. 2002, Proceedings of the 7eme Colloquium Cosmologie, Eds. Sanchez and de Vega [arXiv:0211503]

[58] Bignami, G. F., et al. 1975, Space Sci. Instrum., 1, 245

[59] Bignami, G. F., Bennett, K., Buccheri, R., et al. 1981, A&A, 93, 71

[60] Bignami, G. F., Caraveo, P. A., and Lamb, R. C. 1983, ApJ, 272, L9

[61] Biraud, F. 1971, Nature, 232, 178

[62] Blandford, R. D., & Znajek, R. L. 1977, MNRAS 179, 433

[63] Blandford, R. D., & Rees, M. J. 1978, in BL Lac Objects ed A. M. Wolfe (Univ. Pittsburgh Press), 328

[64] Blandford, R. D., and Ostriker, J. P. 1978, ApJ, 221, L29

[65] Blandford, R. D., & Königl, A. 1979, ApJ, 232, 34

[66] Blandford, R. D., & Payne, D. G. 1982, MNRAS, 199, 883

[67] Blandford, R. D., and McKee, C. F. 1982, ApJ, 255, 419

[68] Blandford, R. D., & Eicher, D. 1987, PhR, 154, 1

[69] Blandford, R. D. 1990, Advanced Course of the Swiss Society for Astrophysics and Astronomy: Active Galactic Nuclei

[70] Blandford, R. D., and Begelman, M. C. 1999, MNRAS, 303, 1

[71] Blandford, R. D. 2002, in Lighthouse of the Universe, eds. Gilfanov, Sunyaev, Chuzarov, 381

[72] Blazejowski, M., Sikora M., Moderski, R., Madejski, G. M. 2000, ApJ, 545, 107

[73] Bloom, S. D., & Marscher, A. P. 1996, ApJ, 461, 657

[74] Bloom, S. D., et al. 1997, ApJ, 490, L145

[75] Blumenthal, G. R., Gould, R. J. 1970, Reviews of Modern Physics, vol. 42, issue 2, 237

[76] Bolton, J. G., & Ekers, J. 1966, Aust. J Phys., 19, 559

[77] Bonning, E. W., et al. 2009a, ApJ, 697, L81

[78] Bonning, E., Bailyn, M., Buxton, M., et al. 2009b, Astronomer's Telegram, 2322

[79] Böttcher, M., Mukherjee, R., & Reimer, A. 2002a, ApJ, 581, 143

[80] Böttcher, M., & Chiang, J. 2002b, ApJ, 581, 127

[81] Böttcher, M. 2007, Ap&SS, 309, 95

[82] Bowyer, C. S., Lampton, M., Mack, J., et al. 1970, ApJ, 161, L1

[83] Bretz, T., & Dorner, D. 2008, AIP Conf. Proc., 1085, 664

[84] Browning, R., Ramsden, D., and Wright, P. J. 1971, Nature, 232, 99

[85] Burbidge, E. M., & Kinnan, T. D. 1966, ApJ, 145, 654

[86] Burrows, D. N., Hill, J. E., Nousek, J. A., et al. 2005, Space Science Reviews, 120, 165

[87] Canizares, C. R., and White, J. L. 1989, ApJ, 339, 27

[88] Caraveo, P. A., et al. 1980, A&A, 91, L3

[89] Cardelli, J. A., Clayton, G. C., & Mathis, J. S. 1989, ApJ, 345, 245

[90] Carosati, D., Larionov, V. M., Larionova, L., et al. 2007, Astronomer's Telegram, 1223, 1

[91] Cash, W., 1979, ApJ, 228, 939

[92] Cassaro, P., Stanghellini, C., Bondi, M., et al. 1999, A&AS, 139, 601

[93] Cattaneo, P. W., et al. 2009, Nucl. Instr. Meth. Phys. Res. A, in press

[94] Cavaliere, A., Morrison, P. 1980, ApJ, 238, L63

[95] Cavaliere, A., & D'Elia, V. 2002, ApJ, 571, 226

[96] Celotti, A., Ghisellini, G., Fabian, A. C. 2007, MNRAS, 375, 417

[97] Celotti, A., & Ghisellini, G. 2008, MNRAS, 385, 283

[98] Chadwick, P. M., Latham, I. J., and Nolan, S. J. 2008, J. Phys. G, 35, 1

[99] Charles, M., et al. 2009, ApJ, 702, 791

[100] Chatterjee, R., Jorstad, S. G., Marscher, A. P., et al. 2008, ApJ, 689, 79

[101] Chen, A. W., D'Ammando, F., Villata, M., et al. 2008, 489, L37

[102] Chi, X., Wolfendale, A. W. 1991, J. Phys. G, 17, 987

[103] Ciprini, S., and Corbel, F. 2009, Astronomer's Telegram, 1897

[104] Clark, G. W., Garmire, G. P., Kraushaar, W. L. 1968, AJ 153, L203

[105] Clavel, J., Wamsteker, W., & Glass, I. S. 1989, ApJ, 337, 236

[106] Clemens, D. P. 1985, ApJ, 295, 422

[107] Collin, S., & Huré, J. M. 2001, A&A, 372, 50

[108] Collmar, W., Reimer, O., Bennett, K., et al. 2000, A&A, 354, 513

[109] Conconi, P., Cunniffe, R., D'Alessio, F., et al. 2004, SPIE, 5492, 1602

[110] Cortina, J., et al. 2005, Proc. 29th ICRC, 5, 359

[111] Costa, E., et al. 2001, X-ray Astronomy: Stellar Endpoints, AGN, and the Diffuse X-ray Background, ed. N. E. White et al. (New York: AIP) 599, 582

[112] Costa, E., Del Monte, E., Donnarumma, I., et al. 2008, Astronomer's Telegram, 1574

[113] Courvoisier, T. J. L. 1998, A&AR, 9, 1

[114] Courvoisier, T. J. L., Beckmann, V., Bourban, G., et al. 2003, A&A, 411, L343

[115] Covino, S., Stefanon, M., Fernandez-Soto, A., et al. 2004, SPIE, 5492, 1613

[116] Crummy, J., Fabian, A. C., Gallo, L., et al. 2006, MNRAS, 365, 1067

[117] Cusumano, G., et al. 2007, submitted to Il Nuovo Cimento [arXiv:0701813v1]

[118] Cusumano, G. et al. 2009, A&A, in press [arXiv:0906.4788]

[119] Cutini, S., and Hays, E. 2009, Astronomer's Telegram, 2033

[120] D'Ammando, F., Bianchi, S., Jiménez-Bailón, E., et al. 2008a, A&A, 482, 499

[121] D'Ammando, F., Chen, A. W., Villata, M., et al. 2008b, Proceedings of the Workshop on Blazar Variability across the Elecotromagnetic spectrum, PoS, 33

[122] D'Ammando, F., Pucella, G., Raiteri, C. M., et al. 2009a, A&A, 508, 181

[123] D'Ammando, F., Raiteri, C. M., Villata, M. 2009b, ASP Conference, Proc. Conference 'Accretion and Ejection in AGN: a Global View', ed. Maraschi, Ghisellini, Della Ceca, Tavecchio [arXiv:0910.0966]

[124] D'Ammando, F., et al. 2009c, in preparation

[125] D'Ammando, F., et al. 2009d, Proc. 1st RYRM 2009 [arXiv:0912.2558]

[126] Dame, T. M., Hartmann, D., Thaddeus, P. 2001 ApJ, 547, 792

[127] Daniel, M. K., et al. 2007, Proc. 30th ICRC, Merida, Mexico, 283

[128] Dar, A., and Laor, A. 1997, ApJ, 478, 5

[129] Daum, A., et al. 1997, Astropart. Phys., 8, 1

[130] Del Monte, E., et al. 2007, NIM A, 572, 708

[131] Dermer, C. D., Schlickeiser, R., Mastichiadis, A. 1992, A&A, 256, L27

[132] Dermer, C. D., & Schlickeiser, R. 1993, ApJ, 416, 458

[133] Dermer, C. D., & Schlickeiser, R. 2002, ApJ, 576, 667

[134] Dickney, J. M., & Lockman, F. J. 1990, ARA&A, 28, 215

[135] Dingus, B., & Bertsch, D. L. 2001, in AIP Conf. Proc. 587, Gamma 2001, ed. Ritz, Gehrels, Shrader, 251

[136] Di Sciascio, G. 2009, to appear in Mem. S.A.It. [arXiv:0907.2526]

[137] Dolcini, A., et al. 2005, A&A, 443, 33

[138] Donato, D., Sambruna, R., Gliozzi, M., A&A, 433, 1163

[139] Donato, D., Ghisellini, G., Tagliaferri, G., Fossati, G. 2001, A&A, 375, 739

[140] Donnarumma, I., Pucella, G., Vittorini, V., et al. 2009a, ApJ, 707, 612

[141] Donnarumma, I., Vittorini, V., Vercellone, S., et al. 2009b, ApJ, 691, L13

[142] Dorner, D., et al. 2005, Proc. 29th ICRC, 5, 175

[143] Dorner, D., Nilsson, K., Bretz, T. 2009, A&A, 493, 721

[144] Drury, L. O'C. 1983, Rep. Prog. Phys., 46, 963

[145] Edelson, R. A., & Krolik, J. H. 1988, ApJ, 333, 646

[146] Elvis, M., Plummer, D., Schachter, J., Fabbiano, G. 1992, ApJS, 80, 257

[147] Escande, L., Tanaka, Y. T. 2009, Astronomer's Telegram 2328

[148] Fabian, A. C. 1999, MNRAS, 308, L39

[149] Falomo, R., & Treves, A. 1990, PASP, 102, 1120

[150] Falomo, R, Carangelo, N., Kotilainen, J. K., Treves, A. 2003, ApJ, 595, 624

[151] Fanaroff, B. L., Riley, J. M. 1974, MNRAS, 167, 31

[152] Fernini, I., Burns, J. O., and Perley, R. A. 1997, AJ, 114, 2292

[153] Feroci, M., et al. 2007, Nucl. Instr. Meth. Phys. Res. A, 581, 728

[154] Feroci, M., Costa, E., Del Monte, E., et al. 2009, A&A, in press [arXiv:0910.4895]

[155] Ferrarese, L., Merritt, D. 2000, ApJ, 539, L9

[156] Ferrero, E., Wagner, S. J., Emmanoulopolous, D., et al. 2007, A&A, 457, 133

[157] Fey, A. L., et al. 2004, AJ, 127, 3587

[158] Fichtel, C. E., Hartman, R. C., Kniffen, et al. 1975, ApJ, 198, 163

[159] Fichtel, C. E., Bertsch, D. L., Hartman, R. C., et al. 1983, ICRC, 18th, Bangalore, India, 8, 19

[160] Fichtel, C. E., & Trombka, J. I., 1997, Gamma-Ray Astrophysics, NASA Reference Publication n. 1386, September 1997

[161] Fiore, F., Giommi, P., Vignali, C., et al. 2001, MNRAS, 327, 771

[162] Fiore, F., Matt, G., La Franca, F., et al. 2002, in ASP Conf. Ser. 258: Issues in Unification of Active Galactic Nuclei, 205

[163] Fiorucci, M., & Tosti, G. 1996, A&AS, 116, 403

[164] Fiorucci, M., et al. 1998, PASP, 110, 105

[165] Fishman, G. J. 1995, in Seventeenth Texas Symposium on Relativistic Astrophysics and Cosmology, ed. Böhringer, Morfill and Trümper. Annals of the New York Academy of Sciences, Vol. 759 (New York, NY: The New York Academy of Sciences), 232

[166] Fitzpatrick, E., 1999, PASP, 111, 63

[167] Fomin, V. P., et al. 1994, Astroparticle Physics, 2, 137

[168] Foschini, L., Tagliaferri, G., Pian, E., et al. 2006, A&A, 455, 871

[169] Fossati, G., Maraschi, L., Celotti, A., et al. 1998, MNRAS, 299, 433

[170] Fossati, G., Buckley, J. H., Bond, I. H., et al. 2008, ApJ, 677, 906

[171] Franceschini, A., Rodighiero, G., Vaccari, M. 2008, A&A, 487, 837

[172] Frontera, F., Orlandini, M., Landi, R., et al. 2007, ApJ, 666, 86

[173] Früwirth, R. 1987, Nuclear Instrument and Method in Physics Research A, 262, 444

[174] Fürmann, L., Krichbaum, T. P., Witzel, A., et al. 2008, A&A, 490, 1019

[175] Gabriel, C., Denby, M., Fyfe, D. J., et al. 2004, in ASP Conf. Ser. 314: Astronomical Data Analysis Software and Systems (ADASS) XIII, 759

[176] Galeev, A. A., Rosner, R., & Vaiana, G. S. 1979, ApJ, 229, 318

[177] Gambill, J. K., Sambruna, R. M., Chartas, G., et al. 2003, A&A, 401, 505

[178] Gear, W. K., Stevens, J. A., Hughes, D. H., et al. 1994, MNRAS, 267, 167

[179] Gebhardt, K., Bender, R., Bower, G., et al. 2000, ApJ, 539, L13

[180] Gehrels, N., Chincarini, G., Giommi, P., et al. 2004, ApJ, 611, 1005

[181] Georganopoulos, M., Kazanas, D. 2003, ApJ, 594, L27

[182] George, I. M., & Fabian, A. C. 1991, MNRAS, 249, 352

[183] Ghez, A. M., Klein, B. L., Morris, M., & Becklin, E. E. 1998, ApJ, 509, 678

[184] Ghisellini, G., Maraschi, L., & Treves, A. 1985, A&A, 146, 204

[185] Ghisellini, G., & Madau, P. 1996, MNRAS, 280, 67

[186] Ghisellini, G., Celotti, A., Fossati, G., et al. 1998, MNRAS 301, 451

[187] Ghisellini, G. 1999, AN, 320, 232

[188] Ghisellini, G., & Celotti, A. 2001, A&A, 379, L1

[189] Ghisellini, G., Celotti, A., & Costamante, L. 2002, A&A, 386, 833

[190] Ghisellini, G., Haardt, F., & Matt, G. 2004, A&A, 413, 535

[191] Ghisellini, G., Tavecchio, F., Chiaberge, M. 2005, A&A, 432, 401

[192] Ghisellini, G., Foschini, L., Tavecchio, F., & Pian, E. 2007, MNRAS, 382, L82

[193] Ghisellini, G., and Tavecchio, F. 2008, MNRAS, 386, L28

[194] Ghisellini, G., Maraschi, L., & Tavecchio, F. 2009a, MNRAS, 396, L105

[195] Ghisellini, G., Tavecchio, F., Foschini, L., et al. 2009b, MNRAS, in press [arXiv:0909.0932]

[196] Ghosh, H., Pogge, R. W., Mathur, S., et al. 2007, ApJ, 650, 105

[197] Giannios, D., Uzdensky, D., Begelman, M. 2009, MNRAS, 395, L29

[198] Gierlinski, M., & Done, C. 2004, MNRAS, 349, L7

[199] Ginzburg, V. L., Syrovatskii, S. L. 1964, The Origin of Cosmic Rays, New York: Macmillan 1964

[200] Giommi, P, Ansari, S. G., Micol, A. 1995, A&AS, 109, 267

[201] Giommi, P., Massaro, E., Chiapetti, L., et al. 1999, A&A, 351, 59

[202] Giommi, P. et al. 2006, A&A, 456, 911

[203] Giommi, P., Massaro, E., Padovani, P., et al. 2007, A&A, 468, 97

[204] Giommi, P., Colafrancesco, S., Cutini, S., et al. 2008a, A&A, 487, L49

[205] Giommi, P., Perri, M., Verrecchia, F., et al. 2008b, Astronomer's Telegram, 1495

[206] Giovannini, G., Cotton, W. D., Feretti, L., Lara, L., & Venturi, T. 2001, ApJ, 552, 508

[207] Giroletti, M., Giovannini, G., Ferretti, L., et al. 2004, ApJ, 600, 127

[208] Giuliani, A., et al. 2004, Mem. Soc. Astron. Italiana Suppl., 5, 135

[209] Giuliani, A., et al. 2006, Nucl. Instr. Meth. Phys. Res. A, 568, 692

[210] Giuliani, A., Mereghetti, S., Fornari, F., et al. 2008, A&A, 491, L25

[211] Giuliani, A., D'Ammando, F., Vercellone, S., et al. 2009, A&A, 494, 509

[212] Giuliani, A., Fuschino, F., Vianello, G., et al. 2010, ApJ, 708, L84

[213] Goebel, F., et al. 2005, Proc. 29th ICRC, 5, 179

[214] Goebel, F., et al. 2007, Proc. 30th ICRC, 3, 1481

[215] Gonzàlez-Pèrez, J. N., Kidger, M. R., and Martìn-Luis, F. 2001, AJ, 122, 2055

[216] Grandi, P., and Palumbo, G. 2004, Science, 306, 998

[217] Green, R. F., Schmidt, M., Liebert, J. 1986, ApJS, 61, 305

[218] Grupe, D., & Mathur, S. 2004, ApJ, 606, L41

[219] Gu, M., Cao, X., & Jiang, D. R. 2001, MNRAS, 327, 1111

[220] Guetta, D., Ghisellini, G., Lazzati, D., Celotti, A. 2004, A&A, 421, 877

[221] Haardt, F., & Maraschi, L. 1991, ApJ, 380, L51

[222] Haardt, F., Maraschi, L., & Ghisellini, G. 1994, ApJ, 432, L95

[223] Hartman, R. C., Kniffen, D. A., Thompson, D. J., et al. 1979, AJ, 230, 597

[224] Hartman, R. C., Bertsch, D. L., Fichtel, C. E., et al. 1992a, NASCP, 3137, 116

[225] Hartman, R. C., et al. 1992b, IAU circ, 5477, 2

[226] Hartman, R. C., et al. 1992c, ApJ, 385, 1

[227] Hartman, R. C., et al. 1993, ApJ, 407, L41

[228] Hartman, R. C., Bertsch, D. L., Bloom, S. D., et al. 1999, ApJS, 123, 79

[229] Hartman, R. C., et al. 2001, ApJ, 553, 683

[230] Hartman, R. C., Kadler, M., & Tueller, J. 2008, ApJ, 688, 852

[231] Hauser, M. G., & Dwek, E. 2001, ARA&A, 39, 249

[232] Hermsen, W., et al. 1977, Nature, 269, 494

[233] Hill, G. J., and Lilly, S. J. 1991, ApJ, 367, 1

[234] Hillas, M. 1985, Proc. of the 19th ICRC (La Jolla, USA), 3, 445

[235] Hofmann, W., et al. 1999, Astropart. Phys., 25, 380

[236] Homan, D. C., Ojha, R., Wardle, J. F. C., et al 2001, ApJ, 549, 840

[237] Horan, D., Badran, H. M., Bond, I. H., et al. 2004, ApJ 304, 51

[238] Hoyle, F., Fowler, W. A. 1963, MNRAS, 125, 169

[239] Hufnagel, B. R., & Bregman, J. N. 1992, ApJ, 386, 473

[240] Hughes, E. B., Hofstadter, R., Rolfe, J., et al. 1980, IEEE Transactions on Nuclear Science, NS-27, 364

[241] Hunter, S. D., Bertsch, D. L., Catelli, J. R., et al. 1997, ApJ, 481, 205

[242] Ichimaru, S. 1977, ApJ, 214, 840

[243] Ikejiri, Y., Yamanaka, M., Takahashi, H., et al. 2009, Astronomer's Telegram 1892

[244] Impey, C. D., Neugebauer, G. 1988, AJ, 95, 307

[245] Jahoda, K., Swank, J. H., Giles, A. B., Stark, M. J., et al. 1996, in SPIE Conference Series, vol. 2808, ed. O. H. Siegmund & M. A. Gummin, 59

[246] Jansen, F., et al. 2001, A&A, 365, L1.

[247] Jones, F. C. 1968, Phys. Rev, 167, 1159

[248] Jones, F. C. 1994, ApJ, 90, 561

[249] Jorstad, S. G., Marscher, A. P., Lister, M. L., et al. 2005, AJ, 130, 1418

[250] Kalberla, P. M. W., Button, W. B., Hartmann, D., et al. 2005, A&A, 440, 775

[251] Kardashev, N. S., 1962, Soviet Astronomy, vol. 6, 317

[252] Kartaltepe, J. S., and Balonek, T. J. 2007, AJ, 133, 2866

[253] Kaspi, S., Smith, P. S., Netzer, H., et al. 2000, ApJ, 533, 631

[254] Kaspi, S., Maoz, D., Netzer, H., et al. 2005, 629, 61

[255] Kataoka, J., Mattox, J. R., Quinn, J., et al. 1999, ApJ, 514, 138

[256] Kataoka, J., Stawarz, L., Aharonian, F., et al. 2006, ApJ, 641, 158

[257] Kataoka, J., Madejski, G., Sikora, M., et al. 2008, ApJ, 672, 787

[258] Kellermann, K. I., Sramek, R. A., Schmidt, M., et al. 1989, AJ, 198, 1195

[259] Kellermann, K. I., Sramek, R. A., Schmidt, M., et al. 1994, AJ, 108, 1163

[260] Kerrick, A. D., Akerlof, C. W., Biller, S., et al. 1995, ApJ, 452, 588

[261] Khachikian, E. Y., & Weedman, D. W. 1971, Astrofizika, 7, 389

[262] Kirk, J. G., Mastichiadis, A. 1999, APh, 11, 45

[263] Klebesadel, R. W., Strong, I. B., and Olson, R. A. 1973, ApJ, 182, L85

[264] Kneiske, T. M., Bretz, T., Mannheim, K., Hartmann, D. H. 2004, A&A, 413, 807

[265] Kniffen, D. A., Fichtel, C. E., Hartman, R. C. , et al. 1975, Proc. 14th Internat. Cosmic Ray Conf. (Munich), 1, 100

[266] Kokubun, M., et al. 2007, Publications of the ASJ, 59, 53

[267] Kollgaard, R. I., Wardle, J. F. C., Roberts, D. H., Gabudza, D. C. 1992, AJ, 104, 1687

[268] Kovalev, Y. Y., et al. 2009, ApJ, 696, L17

[269] Koyama, K., et al. 2007, Pulications of the ASJ, 59, 23

[270] Krawczynski, H., et al. 2006, Astropart Phys., 25, 380

[271] Krimm, H., et al. 2006, Astronomer's Telegram, 904

[272] Krimm, H. A., Barthelmy, S. D., Cummings, J. R., Markwardt, C. B., Skinner, G., Tueller, J., & Swift/BAT Team 2008, in AAS/High Energy Astrophysics Division, Vol. 10, AAS/High Energy Astrophysics Division, #07.01

[273] Krimm, H. A., Barthelmy, S. D., Baumgartner, W., et al. 2009a, Astronomer's Telegram, 1963

[274] Krimm, H. A., Barthelmy, S. D., Baumgartner, W., et al. 2009b, Astronomer's Telegram, 2330

[275] Krimsky, G. E. 1977, Dokladay Acad. Nauk, SSR, 242, 1306

[276] Kudoh, T., Matsumoto, R., Shibata, K. 1998, ApJ, 508, 186

[277] Kühr, H., et al. 1981a, A&A, 45, 367

[278] Kühr, H., Pauliny-Toth, I. I. K., Witzel, A., Schmidt, J. 1981b, AJ, 86, 854

[279] Kurfess, J. D. 1996, A&A Supp., 120, 5

[280] Labanti, C., et al. 2006, proc SPIE, 6266, 62663

[281] Labanti, C., Marisaldi, M., Fuschino, F., et al. 2009, Nucl. Instr. Meth. Phys. Res. A, 598, 470

[282] Laing, R. A., Jenkins, C. R., Wall, J. V., and Unger, S. W. 1994, ASP, San Francisco, The First Stromlo Symposium: The Physics of Active Galaxies, 201

[283] Laor, A. 1990, MNRAS, 246, 369

[284] Larionov, V., Konstantinova, T., Kopatskaya, E., et al. 2008, Astronomer's Telegram, 1502

[285] Lawson, A. J., & Turner, M. J. L. 1997, MNRAS, 288, 920

[286] Lawson, A. J., McHardy, I. M., and Newsam, A. M. 1998, Nucl. Phys. B, 69, 439-444

[287] Lazzarotto, F., Costa, E., Del Monte, E., et al. 2008, ASPC, 394, 593

[288] Leventhal, M., MacCallum, C. J., and Stang, P. D. 1978, ApJ, 225, L1

[289] Levine, A. M., Bradt, H., Cui, W., et al. 1996, ApJ, 469, L33

[290] Liang, E. P. T., & Price, R. H. 1977, ApJ, 218, 247

[291] Liang, E. P. T. 1979, ApJ, 231, L111

[292] Lichti, G. G., Balonek, T., Courvoisier, T. J. -L., et al. 1995, A&A 298, 711

[293] Lichti, G. G., Bottacini, E., Ajello, M., et al. 2008, A&A, 486, 721

[294] Lin, Y. C., Bertsch, D. L., Chiang, J., et al. 1992, ApJ, 401, 61

[295] Lin, Y. C., Bertsch D. L., Dingus B. L., et al. 1995, ApJ, 442, 96

[296] Lindfors, E. J., Valtoja, E., and Türler, M. 2005, A&A, 440, 845

[297] Lindfors, E. J., Türler, M., and Valtoja, E. 2006, A&A, 456, 895

[298] Lister, M. L., Homan, D. C., Kadler, M., et al. 2009, ApJ, 696, L22

[299] Lobanov, A. P., Krichbaum, T. P., Graham, D. A., et al. 2000, A&A, 364, 391

[300] Lockmann, F. J., & Savage, B. D. 1995, ApJS, 97, 1

[301] Longair, M. S. 2000, High energy astrophysics, vol. 1 & 2, Cambridge U Press

[302] Lund, N., Budtz-Jorgensen, C., Westergaard, N. J., et al. 2003, A&A 411, 231

[303] Lynden-Bell, D. 1969, Nature, 223, 690

[304] Mahoney, W. A., Ling, J. C., Jacobson, A. S., and Tapphorn, R. M. 1980, Nucl. Instrum. Methods, 178, 363

[305] Maiolino, R., Marconi, A., Salvati, M., et al. 2001, A&A, 365, 28

[306] Malkan, M. A., & Moore, R. L. 1986, ApJ, 300, 216

[307] Mannheim, K. 1993, A&A, 269, 67

[308] Maraschi, L., Ghisellini, G., Celotti, A. 1992, ApJ, 397, L5

[309] Maraschi, L., Grandi, P., Urry, C. M., et al. 1994, ApJ 1994, 435, L91

[310] Maraschi, L., Fossati, G., Tavecchio, F., et al. 1999, ApJ, 526, L81

[311] Maraschi, L., Ghisellini, G., Tavecchio, F., et al. 2008, IJMPD, 17, 1457

[312] Marisaldi, M., Fuschino, F., Labanti, C., et al. 2009, Journal of Geophysical Research - Space Physics, in press

[313] Marscher, A. P., Gear, W. K. 1985, ApJ, 298, 114

[314] Marscher, A. P., and Bloom, S. D., 1992, Proceedings of The Compton Observatory Science Workshop, 346

[315] Marscher, A. P., Jorstad, S. G., Gomez, J. -L., et al. 2002, Nature, 417, 625

[316] Marscher, A. P., Jorstad, S. G., D'Arcangelo, F. D., et al. 2008, Nature, 452, 966

[317] Marshall, H. L., Schwartz, D. A., Lovell, J. E. J., et al. 2005, ApJS, 156, 13

[318] Massaro, E., Maesano, M., Montagni, F., et al. 1999, A&A, 342, L49

[319] Massaro, E., Perri, M., Giommi, P., et al. 2004, A&A, 422, 103

[320] Massaro, F., Tramacere, A., Cavaliere, A., et al. 2008, A&A, 478, 395

[321] Matt, G., Perola, G. C., & Piro, L. 1991, A&A, 247, 25

[322] Mattox, J. R. 1993, ApJ, 410, 609

[323] Mattox, J. R., Bertsch, D. L., Chiang, J., et al. 1996, ApJ, 461, 396

[324] Mattox, J. R., Wagner, S. J., Malkan, M., et al. 1997, ApJ, 476, 692

[325] Mattox, J. R., Hartman, R. C., & Reiner, O. 2001, ApJS, 135, 155

[326] Mazin, D., & Raue, M. 2007, A&A, 471, 439

[327] Mazin, D., & Goebel, F. 2007, ApJ, 655, L13

[328] McLaughlin, M. A., Mattox, J. R., Cordes, J. M., et al. 1996, ApJ, 473, 763

[329] McLure, R. J., Kukula, J. S., Dunlop, J. S., et al. 1999, MNRAS, 308, 377

[330] McLure, R. J., and Dunlop, J. S. 2001, MNRAS, 321, 515

[331] McNaron-Brown, K., Johnson, W. N., Jung, G. V., et al. 1995, ApJ, 451, 575

[332] McNaron-Brown, K., Johnson, W. N., Dermer, C. D., and Kurfess, J. D., 1997, ApJ, 474, L85

[333] Meier, D. L., Koide, S., Uchida, Y. 2001, Science, 291, 84

[334] Meier, D. L. 2002, NewAR, 46, 247

[335] Miller, H. R., & Green, R. F. 1983, Bull. AAS, 15, 957

[336] Miller, H. R., et al. 1988, in proc. IUE Symposium, Grenbelt, ESA SP-281, 303

[337] Mitsuda, K., et al. 2007, Publication of the ASJ, 59, 1

[338] Montagni, F., Maselli, A., Massaro, E., et al. 2006, A&A, 451, 435

[339] Monet, D., et al. 1998, The PMM USNO-A2.0 Catalog

[340] Moore, R. L., Stockman, H. S. 1981, ApJ 243, 404

[341] Morrison, P. 1958, Nuovo Cimento, 7, 858

[342] Mücke, A., Protheroe, R. J., Engel, R., et al. 2003, APh, 18, 593

[343] Mukherjee, R., Dingus, B. L., Gear, W. K., et al. 1996, ApJ, 470, 831

[344] Mukherjee, R., Halpern, J., Mirabal, N., & Gotthelf, E. V. 2002, ApJ, 574, 693

[345] Murphy, D. W., Browne, I. W. A., and Perly, R. A. 1993, MNRAS, 264, 298

[346] Nandikotkur, J., Jahoda, K. M., Hartman, R. C., et al. 2007, ApJ, 657, 706

[347] Narayan, R., Yi, I. 1994, ApJ, 428, L13

[348] Narayan, R., Yi, I., and Mahadevan, R. 1995, Nature, 374, 623

[349] Narayan, R., Mahadevan, R., Grindlay, J. E., et al. 1998, ApJ, 492, 554

[350] Netzer, H., Peterson, B. M. 1997, ASSL, 218, 85

[351] Neugebauer, G., Oke, J. B., Becklin, E. E., et al. 1979, ApJ, 230, 79

[352] Nieppola, E., Tornikoski, M., & Valtaoja, E. 2006, A&A, 445, 441

[353] Nieppola, E., Valtoja, E., Tornikoski, M., et al. 2008, A&A, 488, 867

[354] Nilsson, K., Pasanen, M., Takalo, L. O., et al. 2007, A&A, 475, 199

[355] Nilsson, K., et al. 2008, A&A, 487, L29

[356] Oke, J. B., Gunn, J. E. 1974, ApJ, 189, L5

[357] Osterman, M. A., Miller, H. R., Campbell, A. M., et al. 2006, AJ, 132, 873

[358] Ostorero, L., Raiteri, C. M., Villata, M., et al. 2001, Mem. SAI, 72, 147

[359] Ostorero, L., Villata, M., Raiteri, C. M. 2004, A&A, 419, 913

[360] Ostorero, L., Wagner S. J., Gracia, J., et al. 2006, A&A, 451, 797

[361] Owen, F. N., and Ledlow, M. J. 1994, ASP, San Francisco, the First Stromlo Symposoium: The Physics of Active Galaxies, 319

[362] Pacciani, L., Donnarumma, I., Vittorini, V., et al. 2009a, A&A, 494, 49

[363] Pacciani, L. 2009b, ASP Conf, Proceedings Conf. 'Accretion and Ejection in AGN: a Global View', in press

[364] Pacholczyk, A. G. 1970, Radio Astrophysics: Nonthermal Processes in Galactic and Extragalactic Sources (San Francisco: W. H. Freeman & Co)

[365] Padovani, P., Urry, C. M. 1990, ApJ, 356, 75

[366] Padovani, P., Urry, C. M. 1991, ApJ, 368, 373

[367] Padovani, P., Giommi, P. 1995, ApJ, 444, 567

[368] Padovani, P., Costamante, L., Ghisellini, G., et al. 2002, ApJ, 581, 895

[369] Padovani, P., Perlman, E. S., Landt, H., et al. 2003, ApJ, 588, 128

[370] Padovani, P. 2007, Ap&SS, 309, 63

[371] Panessa, F., & Bassani, L. 2002, A&A, 394, 435

[372] Papaloizou, J. C. B., & Lin, D. N. C. 1995, Annual Review A&A Supp., 33, 505

[373] Pellizzoni, A., Pilia, M., Possenti, A., et al. 2009a, ApJ, 695, L115

[374] Pellizzoni, A., Pilia, M., Possenti, A., et al. 2009b, ApJ, 691, 1618

[375] Pellizzoni, A., Trois, A., Tavani, M., et al. 2009c, Science, in press

[376] Perlman, E. S., Padovani, P., Landt, H., et al. 2001, ASPC, 227, 200

[377] Perlman, E. S., Madejski, G., Georganopoulos, M., et al. 2005, ApJ, 625, 727

[378] Perola, G. C., Piro, L., Altamore, A., et al. 1986, ApJ, 306, 508

[379] Perola, G. C., Matt, G., Cappi, M., et al. 2002, A&A, 389, 802

[380] Perotti, F., Fiorini, M., Incorvaia, S., et al. 2006, Nucl. Instr. Meth. Phys. Res. A, 556, 228

[381] Peterson, B. M. 1993, PASP, 105, 247

[382] Peterson, B. M., Wandel, A. 1999, AAS, 194, 4912

[383] Peterson, B. P. 2001, in Advanced Lectures on the Starburst-AGN Connection, Proc. Conf. Tonantzintla, Puebla, Mexico, 26-30 June 2000

[384] Peterson, B. P., Ferrarese, L., Gilbert, K. M., et al. 2004, ApJ, 613, 682

[385] Petrucci, P. O., Haardt, F., Maraschi, L., et al. 2000, ApJ, 540, 131

[386] Pian, E., & Treves, A. 1993, ApJ, 416, 130

[387] Pian, E., et al. 1999, ApJ, 521, 112

[388] Pian, E., et al. 2006, A&A, 449, L21

[389] Pittori, C., Cutini, S., Gasparrini, D., et al. 2008, Astronomer's Telegram, 1583

[390] Pittori, C., Verrecchia, F., Chen, A. W., et al. 2009, A&A, 506, 1563

[391] Poole, T. S., Breeveld, A. A., Page, M. J., et al. 2008, MNRAS, 383, 627

[392] Prest, M., Barbiellini, G., Bordignon, G., et al. 2003, Nucl. Instr. Meth. Phys. Res. A, 501, 280

[393] Prestage, R. M., Peacock, J. A. 1988, MNRAS, 230, 131

[394] Prieto, M. A., Pérez García, A. M., & Rodríguez Espinosa, J. M. 2001, A&A, 377, 60

[395] Pringle, J. E. 1981, Annual Review A&A, 19, 137

[396] Pucella, G., Vittorini, V., D'Ammando, F., et al. 2008, A&A, 491, L21

[397] Pucella, G., D'Ammando, F., Tavani, M., et al. 2009, Astronomer's Telegram, 1968

[398] Punch, M., Akerlof, C. W., Cawley, M. F., et al. 1992, Nature, 358, 477

[399] Pushkarev, A. B., Kovalev, Y. Y., Lister, M. L., Savolainen, T. 2009, A&A, 507, L33

[400] Quataert, E., Narayan, R., and Reid, M. J. 1999, ApJ, 517, 101

[401] Quataert, E., and Gruzinov, A. 2000, ApJ, 539

[402] Quirrenbach, A., Witzel, A., Wagner, S., et al. 1991, ApJ, 372, 71

[403] Raiteri, C. M., Villata, M., Lanteri, L., et al. 1998, A&AS, 130, 495

[404] Raiteri, C. M., Villata, M., Tosti, G., et al. 2003, A&A, 402, 151

[405] Raiteri, C. M., Villata, M., Kadler, M., et al. 2006, A&A, 459, 713

[406] Raiteri, C. M., Villata, M., Larionov, V. M., et al. 2007, A&A, 473, 819

[407] Raiteri, C. M., Villata, M., Larionov, V. M., et al. 2008a, A&A, 491, 755

[408] Raiteri, C. M., et al. 2008b, A&A, 485, L17

[409] Rastorgueva, E. A., et al. 2009, A&A, 494, L5

[410] Raue, M., & Mazin, D. 2008, Int. J. Mod. Phys. D, 17, 1515

[411] Ravasio, M., Tagliaferri, G., Ghisellini, G., et al. 2002, A&A, 383, 763

[412] Rector, T. A., and Stocke, J. T. 2001, AJ, 122, 565

[413] Rector, T. A., Gabuzda, D. C., & Stocke, J. T. 2003, AJ, 125, 1060

[414] Rees, M. J. 1966, Nature, 211, 468

[415] Rees, M. J., Phinney, E. S., Begelman, M. C., Blandford, R. D. 1982, Nature, 295, 17

[416] Remillard, R. 2005, Astronomer's Telegram, 484

[417] Riegel, B., et al. 2005, Proc. 29th ICRC, 5, 219

[418] Riegel, B., & Bretz, T. 2005, Proc. 29th ICRC, 5, 215

[419] Riegler, G. R., Ling, J. C., Mahoney, W. A., et al. 1981, ApJ, 248, L13

[420] Roming, P. W. A., Kennedy, T. E., Mason, K. O., et al. 2005, Space Science Reviews, 120, 95

[421] Rybicki, G. B., Lightman, A. P. 1979, Wiley Interscience

[422] Sakamoto, T., D'Ammando, F., Gehrels, N., et al. 2009, Astronomer's Telegram, 2329

[423] Sambruna, R. M., Barr, P., Giommi, P., et al. 1994, ApJS, 95, 371

[424] Sambruna, R. M., Maraschi, L, Urry, C. M. 1996, ApJ, 463, 444

[425] Sambruna, R. M., Tavecchio, F., Ghisellini, G., et al. 2007, ApJS, 669, 884

[426] Sanders, D. B., Phinney, E. S., Neugebauer, G., Soifer, B. T., & Matthews, K. 1989, ApJ, 347, 29

[427] Sbarufatti, B., et al. 2006, ApJ, 132, 1

[428] Scalzo, R. C., Boone, L. M., Bramel, D., et al. 2004, ApJ, 607, 778

[429] Scarpa, R., Urry, C. M., Falomo, R., et al. 2000, ApJ, 532, 740

[430] Schlegel, D. J., Finkbeiner, D. P., Davis, M. 1998, ApJ, 500, 525

[431] Schlikeiser, R., Campeanu, A., et al. 1993, ICRC, 2 , 211

[432] Schmidt, M. 1963, Nature, 197, 1040

[433] Schmidt, M. 1968, ApJ, 151, 393

[434] Schönfelder, V., Bennett, K., Bloemen, H., et al. 1996, A&A Supp., 120, 13

[435] Serlemitsos, P. J., et al. 2007, Publication of the ASJ, 59, 9

[436] Seyfert, C. K. 1943, ApJ, 97, 28

[437] Sguera, V., Bassani, L., Malizia, A., et al. 2005, A&A, 430, 107

[438] Shakura, N. I., & Sunyaev, R. A. 1973, A&A, 24, 337

[439] Siebert, J., Brinkmann, W., Drinkwater, M. J., et al. 1998, MNRAS, 301, 261

[440] Sikora, M., Begelman, M. C., Rees, M. J. 1994, ApJ, 421, 153

[441] Sikora, M., Madejski, G., Moderski, R., Poutanen, J. 1997, ApJ, 484, 108

[442] Sikora, M., Blazejowski, M., Begelman, M. C., Modersky, R. 2001, ApJ, 554, 1; erratum: 2001, ApJ, 561, 1154

[443] Sikora, M., Blazejowski, M., Moderski, R., Madjeski, G. M. 2002, ApJ 577, 78

[444] Sikora, M., Begelman, M. C., Madjeski, G. M., Lasota, J. -P. 2005, ApJ, 625, 72

[445] Sikora, M., Stawarz, L., Moderski, R., et al. 2009, ApJ 704, 38

[446] Singh, K. P., Rao, A. R., & Vahia, M. N. 1990, ApJ, 365, 455

[447] Singh, K. P., Shrader, C. R., & George, I. M. 1997, ApJ, 491, 515

[448] Smith, P. S., Elston, R., Berriman, R. G. 1988, ApJ, 326, L39

[449] Sokolov, A., Marscher, A. P., and McHardy, I. M. 2004, ApJ, 613, 725

[450] Soldi, S, Türler, M., Paltani, S., et al. 2008, A&A, 486, 411

[451] Spada, M., Ghisellini, G., Lazzati, D., Celotti, A. 2001, MNRAS, 325, 1559

[452] Sreekumar, P., Bertsch, D. L., Dingus, B. L., et al. 1996, ApJ, 464, 628

[453] Stetson, P. B. 1987, PASP, 99, 191

[454] Stevens, A. J., Litchfield, S. J., Robson, E. I., et al. 1994, ApJ, 437, 91

[455] Stickel, M., Fred, J. W., & Kühr, H. 1993, A&AS, 98, 393

[456] Striani, E., Vercellone S., Verrecchia, F., et al. 2009a, Astronomer's Telegram, 2326

[457] Striani, E., Vercellone S., Verrecchia, F., et al. 2009b, Astronomer's Telegram, 2322

[458] Strittmatter, P. A., Serkowski, K., Caswell, R., et al. 1972, 175, L7

[459] Strong, A. W., Moskalenko, I. V., Reimer, O. 2004, ApJ, 613, 956

[460] Strong, A. W. 2007, Ap&SS, 309, 35

[461] Swanenburg, B. N., Hermsen, W., and Bennett, K. 1978, Nature, 275, 298

[462] Swanenburg, B. N., et al. 1981, ApJ, 243, L69

[463] Tadhunter, C. N., Morganti, R., Robinson, A., et al. 1998, MNRAS, 298, 1035

[464] Tagliaferri, G., et al. 2000, A&A, 354, 431

[465] Tagliaferri, G., Ravasio, M., Ghisellini, G., et al. 2003, A&A, 400, 477

[466] Takahashi, T., et al. 2007, Publications of the ASJ, 59, 35

[467] Tanner, A. M., Bechtold, J., Walker, C. E., et al. 1996, AJ, 112, 62

[468] Tavani, M., Barbiellini, G., et al. 2008a, Nucl. Instr. Meth. Phys. Res. A, 588, 52

[469] Tavani, M., Barbiellini, G., et al. 2009a, A&A, 502, 995

[470] Tavani, M., Sabatini, S., Pian, E., et al. 2009b, ApJ, 698, L142

[471] Tavani, M., Bulgarelli, A., Piano, G., et al. 2009c, Nature, 462, 620

[472] Tavecchio, F., Maraschi, L., & Ghisellini, G. 1998, ApJ 509, 608

[473] Tavecchio, F., Maraschi, L., Ghisellini, G., et al. 2000, ApJ, 543, 535

[474] Tavecchio, F., Maraschi, L., Ghisellini, G., et al. 2002, ApJ, 573, 137

[475] Tavecchio, F., Maraschi, L., Ghisellini, G., et al. 2007a, ApJ, 665, 980

[476] Tavecchio, F., Maraschi, L., Wolter, A., et al. 2007b, ApJ, 662, 900

[477] Tavecchio, F., Ghisellini, G. 2008, MNRAS, 386, 945 980

[478] Teräsranta, H., et al. 1998, A&AS, 132, 305

[479] Tescaro, D., Bartko, H., Galante, N., et al. 2007, in Proc. 30th ICRC, Merida, Mexico [arXiv:0709.1410]

[480] Thompson, D. J., Fichtel, C. E., Kniffen D. A., and Ögelman, H. B. 1975, ApJ, 200, L79

[481] Thompson, D. J. 2008, Rep. Prog. Phys., 71

[482] Torricelli-Ciamponi, G., & Pietrini, P. 2002, A&A, 394, 415

[483] Tosti, G., Bagaglia, M., Campeggi, C., et al. 2004, SPIE, 5492, 689

[484] Tosti, G., Chiang, J., Lott, B., Do Couto E Silva, E., Grove, J. E., & Thayer, J. G. 2008, Astronomer's Telegram, 1628

[485] Tramacere, A., Massaro, F., Cavaliere, A. 2007a, A&A, 463, 521

[486] Tramacere, A., Giommi, P., Massaro, E., et al. 2007b, A&A, 467, 501

[487] Tramacere, A. 2008, Astronomer's Telegram, 1743

[488] Tramacere, A., Rea, N. 2008, Astronomer's Telegram, 1888

[489] Tramacere, A., Giommi, P., Perri, M., et al. 2009, A&A, 501, 879

[490] Tran, H. D. 2001, ApJ, 554, L19

[491] Tran, H. D. 2003, ApJ, 583, 632

[492] Tremaine, S., Gebhardt, K., Bender, R., et al. 2002, ApJ, 574, 740

[493] Treves, A., et al. 2007, A&A, 473, 17

[494] Türler, M., et al. 2006, A&A , 451, L1

[495] Tzeferacos, P., Ferrari, A., Mignone, A., Bodo, G., & Massaglia, S. P. 2009, accepted for publication in MNRAS

[496] Ubertini, P., et al. 2003, A&A, 411, L131

[497] Uchiyama, Y., Urry, C. M., Cheung, C. C., et al. 2006, ApJ, 648, 910

[498] Ulrich, M., Maraschi, L., Megan, C. M. 1997, ARA&A, 35, 445

[499] Urry, C. M., Padovani, P., Stickel, M. 1991, ApJ, 382, 501

[500] Urry, C. M., & Padovani, P. 1995, Publication of the Astronomical Society of the Pacific. J Phys., 107, 803

[501] Urry, C. M., Scarpa, R., O'Dowd, M., et al. 2000, ApJ, 532, 816

[502] Vedrenne, G., Roques, J. -P., Schonfelder, V., et al. 2003, A&A, 411, 63

[503] Vercellone, S., Chen, A. W., Giuliani, A., et al. 2008, ApJ, 676, L13

[504] Vercellone, S., Chen, A. W., Vittorini, V., et al. 2009, ApJ, 690, 1018

[505] Vercellone, S., D'Ammando, F., Vittorini, V., et al. 2009b, submitted to ApJ

[506] Vercellone, S., Fiocchi, M., Pian, E., et al. 2009c, Astronomer's Telegram, 2344

[507] Vermulen, R. C., Cohen, M. H. 1994, ApJ, 430, 467

[508] Vernetto, S. 2009, in Proc. 31th Int. Cosmic Ray Conf., in press

[509] Verrecchia, F., et al. 2008, Astronomer's Telegram, 1582

[510] Villata, M., et al. 1998, A&AS , 130, 305

[511] Villata, M., Raiteri, C. M. 1999, ASPC, 159, 489

[512] Villata, M., Raiteri, C. M., Balonek, et al. 2006, A&A, 453, 817

[513] Villata, M., Raiteri, C. M., Aller, M. F., et al. 2007, A&A, 464, L5

[514] Villata, M., Raiteri, C. M., Larionov, V. M., et al. 2008, A&A, 481, L79

[515] Villata, M., Raiteri, C. M., Gurwell, M., et al. 2009a, A&A Letters, in press [arXiv:0908.2722]

[516] Villata, M., Raiteri, C. M., Larionov, V. M., et al. 2009b, Astronomer's Telegram, 2325

[517] Villata, M., Raiteri, C. M., Larionov, V. M., et al. 2009c, A&A, 501, 455

[518] Vittorini, V., Tavani, M., Paggi, A., et al. 2009, ApJ, 706, L1433

[519] Volk, H. K. 1987, in eds. Proc. 20th ICRC, 157

[520] von Montigny, C., et al. 1995, ApJ, 440, 525

[521] von Montigny, C., Aller, H., Aller, M., et al. 1997, ApJ, 483, 161

[522] Wagner, S. J., & Witzel, A. 1995, ARA&A, 33, 163

[523] Wagner, S. J., Witzel, A., Heidt, J. 1996, AJ, 111, 2187

[524] Wagner, R. M. 2008, Proceedings of Science, 63, 13 [arXiv:0809.2843]

[525] Wall, J. V., & Peacock, J. A. 1985, MNRAS, 216, 173

[526] Walter, R., & Fink, H. H. 1993, A&A, 274, 105

[527] Wandel, A., Peterson, B. M., Malkan, M. A. 1999, ApJ, 526, 579

[528] Wardle, J. F. C., Homan, D. C., Cheung, C. C., et al. 2005, ASPC, 340, 67

[529] Weekes, T. C., et al. 1989, ApJ, 373, 289

[530] Wehrle, A. E., Pian, E., Urry, C. M., et al. 1997, AIPC, 410, 1417

[531] Wehrle, A. E., Pian, E., Urry, C. M., et al. 1998, ApJ 497, 178

[532] Wehrle, A. E., Piner, B. G., Unwin, S. C., et al. 2001, ApJS, 133, 297

[533] Werner, M. W., et al. 2004, ApJS, 154, 1

[534] Whitney, A. R., et al. 1971, Science, 173, 225

[535] Wilks, S. S. 1938, Ann. Math. Stat., 9, 60

[536] Wills, B. J, Netzer, H., Wills, D. 1985, ApJ, 288, 94

[537] Winkler, C., Gehrels, N., Schonfelder, V., et al. 2003, A&A, 411, L349

[538] Wold, M., Lacy, M., Lilje, P. B., Serjeant, S. 2000, MNRAS, 316, 267

[539] Woo, J., & Urry, C. M. 2002, ApJ, 579, 530

[540] Wood, A., & Mao, S. 2005, MNRAS, 362, 945

[541] Worrall, D. M., & Wilkes, B. J. 1990, ApJ, 360, 396

[542] Wurtz, R., Stocke, J. T., Ellingson, E., and Yee, H. K. C. 1997, ApJ, 480, 547

[543] Yaqoob, T., Serlemitsos, P. 2000, ApJ, 544, L95

[544] Zerbi, F. M., Chincarini, G., Ghisellini, G., et al. 2004, SPIE, 5492, 1590

[545] Zhang, Y. H., Treves, A., Celotti, A., Qin, Y. P., & Bai, J. M. 2005, ApJ, 629, 686